Intramolecular hydrogen-shift reactions of peroxy radicals

Thesis by

Eric Praske

In Partial Fulfillment of the Requirements for

the degree of

Doctor of Philosophy

Caltech

CALIFORNIA INSTITUTE OF TECHNOLOGY

Pasadena, California

2019

Defended September 20, 2018

Eric Praske
ORCID: 0000-0001-7169-4423

ACKNOWLEDGEMENTS

ABSTRACT

Straight chain alkanes with more than five carbons, emitted in cities due to incomplete combustion and fuel evaporation, undergo atmospheric gas-phase oxidation with the hydroxyl radical to produce alkyl radicals. These alkyl radicals subsequently add O_2, leading to the formation of peroxy radicals. Following further reaction of these radicals in urban areas, hydroxy-substituted peroxy radicals are formed. Previously, the fate of these peroxy radicals was assumed to be dominated by reaction with nitric oxide, a common air pollutant. Computational and experimental investigations of the oxidation mechanism of 2-hexanol, however, demonstrate that hydrogens α to the hydroxy group exhibit a significantly reduced energetic barrier toward intramolecular hydrogen shifts to the peroxy radical. The barrier reduction for these hydrogen shift reactions results in rate constants that are orders of magnitude larger than for alkyl hydrogens that lack α substitution. Due to significant reductions of nitric oxide emissions in North America, these rate constants are sufficiently large to suggest that this chemistry is competitive even in large cities, particularly during warm summer days. Gas-phase alkyl hydroperoxides, a class of compounds previously expected to exist in negligible quantities in cities, are major products of this chemistry.

Further oxidation of alkyl hydroperoxides leads to the formation of hydroperoxy-substituted peroxy radicals. The chemistry of such peroxy radicals is evaluated through the oxidation of 2-hydroperoxy-2-methylpentane. Experimental observations confirm the previously reported computational result that these peroxy radicals rapidly isomerize by intramolecular hydrogen shift of the hydroperoxide hydrogen. This isomerization occurs on timescales that are much faster than those of bimolecular reaction in essentially all regions of the troposphere. As a consequence of the isomerization, one peroxy radical isomer produced in the oxidation of 2-hydroperoxy-2-methylpentane exhibits an α hydroperoxide hydrogen shift. This reaction rate constant is similar to that reported for the α hydroxy hydrogen shift in the 2-hexanol system.

Alkoxy radicals produced in the oxidation of 2-hydroperoxy-2-methylpentane are similarly shown to undergo a very rapid hydrogen shift of the hydroperoxide hydrogen. One of these

shifts results in a peroxy radical that exhibits an α hydroxy hydrogen shift. Thus, the rapid scrambling of hydroperoxy-subsituted alkoxy and peroxy radicals is a key process that can enable additional unimolecular pathways that are otherwise inaccessible. This chemistry has the potential to introduce significant mechanistic complexity and, due to the rapid nature of the reactions, cannot be neglected even under typical "high NO" conditions employed in chamber studies.

PUBLISHED CONTENT AND CONTRIBUTIONS

Praske, E. et al. (2018). "Atmospheric autoxidation is increasingly important in urban and suburban North America". In: *Proc. Natl. Acad. Sci. U.S.A.* 115.1, pp. 64-69. doi: 10.1073/pnas.1715540115.
   E.P. performed experiments, analyzed data, and wrote the paper.

Praske, E. et al. (2015). "Atmospheric Fate of Methyl Vinyl Ketone: Peroxy Radical Reactions with NO and HO_2". In: *J. Phys. Chem. A.* 119.19, pp. 4562-4572. doi: 10.1021/jp5107058.
   E.P. performed experiments, analyzed data, and wrote the paper.

TABLE OF CONTENTS

LIST OF ILLUSTRATIONS

Chapter IV

LIST OF TABLES

C h a p t e r   1

INTRODUCTION

Atmospheric chemistry involves the study of gas and particle phase emissions and their subsequent transformation and fate. Most atmospheric chemists spend their time studying the reactivity and physical properties of trace gases and particles that comprise less than 0.1% by volume of Earth's atmosphere. Despite their low abundance, these trace constituents profoundly influence air quality and climate. Due to the strong oxidizing nature of Earth's atmosphere, a significant aspect of atmospheric chemistry involves the elucidation of oxidation mechanisms of hydrocarbons, important components of these trace species. The gas-phase oxidation of hydrocarbons is typically initiated by the hydroxyl radical (OH), nitrate radical, or ozone.

This thesis is broadly concerned with the OH-initiated oxidation mechanism of hydrocarbons. This mechanism generally entails the formation of alkyl radicals, which promptly add O_2 in air to produce peroxy radicals (RO_2). During the early years of atmospheric chemistry, research was primarily devoted to understanding the interaction of oxides of nitrogen ($NO_x = NO + NO_2$) with RO_2. Research at Caltech in the 1950s led to the discovery that RO_2 react with NO to produce NO_2. NO_2 promptly photolyzes in sunlight and air to yield ozone, one of the main pollutants contributing to photochemical smog. Due to this finding, a multitude of air quality regulations over the past several decades have aimed to reduce NO_x levels. As NO_x emissions have steadily decreased, a greater share of the research has been devoted to understanding the effect of this transition on the fate of RO_2. Typically, as NO_x is decreased, the complexity of the oxidation mechanism increases. Additionally, reactions in this lower NO_x regime tend to produce unstable compounds (e.g. peroxides) that are difficult to quantify. For these reasons, considerable effort must be expended to ensure that these mechanisms are properly assigned.

The reaction of RO_2 with the hydroperoxyl radical (HO_2) is one pathway that is accessible in the lower NO_x regime. Chapter 1 reports the oxidation mechanism of methyl vinyl ketone (3-buten-2-one, MVK) under conditions in which the RO_2 fate is dominated by HO_2. MVK is an important atmospheric degradation product of isoprene, a hydrocarbon emitted in large quantities by the biosphere. OH reacts with MVK almost exclusively by addition across the olefin to produce two distinct β-hydroxy RO_2. We discovered reaction channels that recycle OH and HO_2, which together comprise the HO_x family. Thus, the chemistry of MVK in the $RO_2 + HO_2$ channel was found to be much less HO_x consuming than previously thought. A chemical transport model was used to demonstrate that this chemistry has an impact on oxidant budgets over large forested regions such as the Amazon.

Chapter 2 significantly departs from the theme of the previous chapter and focuses on the title of this thesis. New experimental and computational approaches were applied to determine the effect of the transition to lower NO_x regimes in urban areas. Specifically, we studied OH-initiated n-alkane oxidation under varying abundances of NO. Alkanes are emitted in cities from natural gas distribution and are present in vehicle tailpipe exhaust. In general, small alkanes (C_1-C_4) arise from natural gas, medium sized alkanes (C_4-C_8) arise from gasoline vehicles, and large alkanes ($\geq C_8$) arise from diesel vehicles. As alkanes with more than five carbons oxidize in the presence of NO, hydroxy-substituted RO_2 are produced. Our study focused on the chemistry of these hydroxy-substituted RO_2. As NO decreased in our experiments, some of these RO_2 isomers began to react through intramolecular hydrogen shifts (H-shifts). We discovered that the hydroxy group lowers the intramolecular H-shift barrier for α hydrogens and, consequently, significantly increases the rate constants of these reactions. As a result, the rate constants are sufficiently large that these reactions directly compete against the $RO_2 + NO$ chemistry, even under modestly polluted conditions. The overall significance of the chemistry is attributed to the formation of hydroperoxy-substituted alkanes, a class of compounds previously not thought to be formed in urban gas-phase oxidation.

Chapter 3 applies the same experimental and computational method to study H-shifts in a hydroperoxy-substituted alkane. The alkane employed in this study lacked a hydrogen α to the hydroperoxy moiety due to tertiary carbon substitution. Therefore, the initially produced RO_2 were unable to undergo fast alkyl H-shifts. However, theoretical work had previously suggested that RO_2 undergo rapid isomerization with nearby hydroperoxy hydrogens such that a pair of RO_2 isomers is formed (e.g. $HOOROO\cdot \rightleftharpoons \cdot OOROOH$). Our study confirmed this result and demonstrated that an equilibrium within the RO_2 pair is established on timescales much faster than those typical of bimolecular chemistry. Due to asymmetry in the substrate, the RO_2 that comprised these pairs were distinct and, therefore, each possessed unique reaction channels. One of the RO_2 in the pair had an accessible α-OOH H-shift pathway. This configuration resulted in an activated hydrogen and therefore enhanced the H-shift rate constants in a manner similar to that observed with α-OH hydrogens in Chapter 2. Thus, this study clearly demonstrated the importance of the rapid isomerization of hydroperoxy-substituted RO_2.

Overall, this thesis contributes to a comprehensive understanding of the oxidation mechanisms of hydrocarbons. Specifically, gas-phase alkane oxidation in the lower NO_x regime is reported, although the findings almost certainly apply to a much broader array of substrates. As this thesis demonstrates, it is important to account for intramolecular H-shifts due to the formation of organic hydroperoxides, as well as the unique reaction channels enabled in the further oxidation of these species.

C h a p t e r   2

ATMOSPHERIC FATE OF METHYL VINYL KETONE: PEROXY RADICAL
REACTIONS WITH NO AND HO$_2$

Abstract

First generation product yields from the OH-initiated oxidation of methyl vinyl ketone (3-buten-2-one, MVK) under both low and high NO conditions are reported. In the low NO chemistry, three distinct reaction channels are identified, leading to the formation of 1) OH, glycolaldehyde, and acetyl peroxy (R2a), 2) a hydroperoxide (R2b), and 3) an α-diketone (R2c). The α-diketone likely results from HO$_x$-neutral chemistry previously only known to occur in reactions of HO$_2$ with halogenated peroxy radicals. Quantum chemical calculations demonstrate that all channels are kinetically accessible at 298 K. In the high NO chemistry, glycolaldehyde is produced with a yield of 74 ± 6.0%. Two alkyl nitrates are formed with a combined yield of 4.0 ± 0.6%. We revise a 3-D chemical transport model to assess what impact these modifications in the MVK mechanism have on simulations of atmospheric oxidative chemistry. The calculated OH mixing ratio over the Amazon increases by 6%, suggesting that the low NO chemistry makes a non-negligible contribution toward sustaining the atmospheric radical pool.

Introduction

MVK is one of the most abundant oxygenated volatile organic compounds in the Earth's atmosphere. It is a major product of the gas-phase oxidation of isoprene, a compound emitted by terrestrial vegetation to the atmosphere at a rate of approximately 500 Tg/yr.[1] Oxidation of isoprene by the hydroxyl radical (OH) produces MVK with a yield that depends on the concentrations of NO and HO_2, and temperature. MVK is also produced during the oxidation of isoprene by ozone and has been quantified in car exhaust.[2-3] Globally, approximately 100 Tg of MVK are produced annually from isoprene according to the simulations described here.[4]

MVK has an atmospheric lifetime of approximately 10 hours with respect to oxidation by OH ([OH] = 1.5 x 10^6 molecules/cm^3), which constitutes its principal atmospheric loss process.[5] OH adds to either of the two olefinic carbon atoms forming distinct alkyl radicals. In the atmosphere, these alkyl radicals rapidly react with O_2 forming peroxy radicals (RO_2):

R1a

R1b
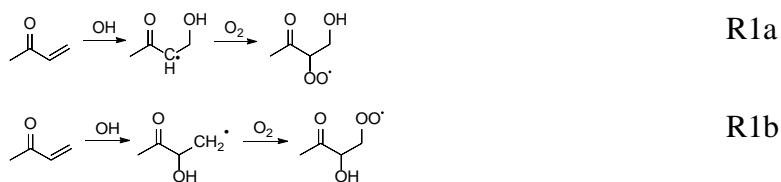
Tuazon et al. studied the OH-initiated MVK oxidation in the gas phase and determined that R1a accounts for $72 \pm 21\%$ of the OH reactivity with the remaining following pathway R1b.[6] The dominant fate of RO_2 radicals in the atmosphere is reaction with either HO_2 or NO. The reaction of MVK-derived RO_2 and NO to produce NO_2, HO_2, and carbonyl products has been previously characterized. Glycolaldehyde, methylglyoxal, formaldehyde, and peroxyacetyl nitrate have all been quantified as the primary first generation products of MVK oxidation under conditions where reaction with NO dominates the RO_2 fate.[6-7] The yields of glycolaldehyde and methylglyoxal through NO-mediated chemistry were determined to be $64 \pm 8\%$ and $25 \pm 4\%$, respectively.[6] The yield of organic nitrates has been estimated to be $10 \pm 10\%$.[8] Alkyl nitrates are of interest due to their interactions with aerosol as well as their

ability to act as temporary reservoirs of NO_x, which can be transported and lead to ozone formation downwind.[9]

The primary focus of this study is the chemistry of the reaction of the RO_2 radicals formed in R1a and R1b with HO_2. This chemistry is notably distinct given the diverse set of reactions that $RO_2 + HO_2$ may undergo.[10] Traditionally, these reactions have been viewed as sinks for atmospheric radicals through the formation of organic hydroperoxides.[11] As demonstrated here, however, this chemistry is largely HO_x neutral in the case of MVK. Two reaction channels (R2a-R2b), previously described for the reaction of acetonyl RO_2 and HO_2[12-15], are observed to occur for MVK RO_2 with substantial yields. We have also identified a carbonyl forming channel (R2c), which has only been reported in the reactions of halogenated RO_2 with HO_2.[16-18] The reaction pathways are shown below:

$$CH_3C(O)CH(O_2^{\bullet})CH_2OH + HO_2 \quad \rightarrow CH(O)CH_2OH + CH_3C(O) + OH + O_2 \qquad \text{R2a}$$
$$\rightarrow CH_3C(O)CH(OOH)CH_2OH + O_2 \qquad \text{R2b}$$
$$\rightarrow CH_3C(O)C(O)CH_2OH + OH + HO_2 \qquad \text{R2c}$$
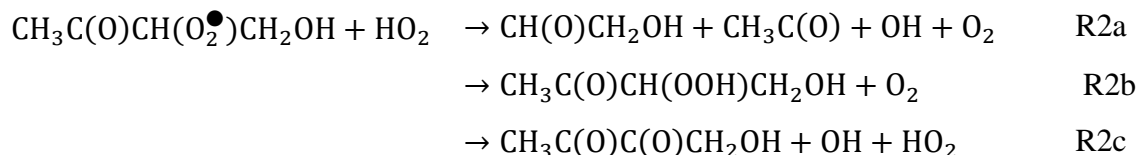
The discovery of efficient HO_x recycling in MVK chemistry adds to the growing number of new findings that the oxidation of isoprene and other biogenic alkenes in low NO environments is less HO_x consuming than previously understood.[19-22] Here, we use the GEOS-Chem atmospheric chemical transport model to evaluate the impact of this chemistry on simulated OH levels within the lower atmosphere.

Experimental methods

We performed a series of photo-oxidation experiments in a small Teflon-walled chamber (Table 1). Experiments were designed to evaluate the products of reactions of the peroxy radicals formed in R1a and R1b with both NO and HO_2. To evaluate the importance of unimolecular reactions of these peroxy radicals, we also investigated the dependence of the product distribution on peroxy radical lifetime.

CHEMICALS

Methyl vinyl ketone (99%, Sigma Aldrich), 3-hydroxy-2-butanone ($\geq$ 96%, Sigma-Aldrich), 4-hydroxy-2-butanone (95%, Sigma-Alrich), glycolaldehyde dimer (Sigma-Aldrich), H_2O_2

(30% w/w, Macron), nitric oxide (1993 ± 20 ppmv NO in N_2, Matheson), and isopropanol (≥ 99%, Macron) were all used as purchased.

CHAMBER AND INSTRUMENTS

Experiments were carried out in a 1 m^3 fluorinated ethylene propylene copolymer (Teflon-FEP, DuPont) environmental chamber at ambient laboratory pressure (~993 hPa), as previously described.[20] The chamber was connected to instrumentation via ~2 m of 6.35 mm OD PFA tubing. Instrumentation included a Time of Flight Chemical Ionization Mass Spectrometer (ToF-CIMS), a triple quadrupole MS-MS CIMS, and a gas chromatograph with a flame ionization detector (GC-FID).

MVK was monitored by GC-FID, with product determination via CIMS. The GC-FID (Agilent 5890 II) had a run cycle of approximately 30 minutes and was equipped with a megabore 0.53 μm PLOT-Q column (JW Chemicals).

CIMS. The CIMS techniques have been previously described in detail.[23-25] Reaction products were quantified using the CF_3O^- reagent ion (m/z = 85) at temporal resolution of 10 Hz. CF_3O^- was formed by passing 1 ppm CF_3OOCF_3 in N_2 through a ^{210}Po radioactive source. The reagent ion was then introduced to a flow tube where the chamber sample was diluted (dry N_2, 1675 standard cubic centimeters per minute). Due to clustering with the reagent ion, most masses reported here are represented as the sum of the nominal compound mass and m/z 85. Fluoride transfer can occur for acidic analytes. For example, nitric and acetic acids were detected primarily at m/z 82 and m/z 79, respectively. Observed ion signals were normalized to that of the reagent ion to account for variations in CF_3O^- fluence. The reagent ion was represented as the sum of m/z = 86, 104, and 120, which correspond to $^{13}CF_3O^-$ and its cluster with water and H_2O_2, respectively. Detection limits are typically ~10 pptv.

GC-CIMS

The CIMS was periodically connected to a GC column to enable the separation and quantification of isomers. The GC-CIMS technique has been previously described.[26-28] Briefly, both prior to and after photo-oxidation, samples of chamber air were analyzed using a gas chromatograph with the output of a 4 meter Restek RTX-1701 column connected to the ToF-CIMS. The analytes were cryogenically trapped on the head of the column using an isopropanol bath at approximately -20 °C. Sample collection lasted 4 minutes to yield a total

sample volume of about 150 cm^3, after which a temperature ramp program was initiated (30 °C for 0.1 min, +3 °C/min until 60 °C, and +10 °C/min to 130 °C).

CALIBRATION

Where available, synthetic standards were used to determine the sensitivity of the CIMS. For several of the products where standards are not available, we estimated the sensitivity using reagent ion-molecule collision rates, calculated using dipole moments and polarizabilities (see SI).[29-30] Isomer specific sensitivities for the MVK-derived alkyl nitrates were previously determined by thermal dissociation LED-induced fluorescence coupled to the output of a GC column.[26] Glycolaldehyde, the principal MVK oxidation product upon which other yields are based, was calibrated using an authentic standard. Gas phase standards were prepared by methods involving either the evaporation of a solution containing glycolaldehyde or by decomposition of crystalline glycolaldehyde dimer. In the first method, a gravimetric standard of glycolaldehyde dimer was dissolved in methanol to yield a 2.8% w/w glycolaldehyde solution. A known quantity of this solution was injected via syringe into a sealed glass three-way vial, which was then transferred to the chamber by flushing with a known volume of dry zero air. In a second method, crystalline glycolaldehyde dimer was placed into a vial and heated to 100 °C and vacuum purged to remove high volatility species as well as water and air. After 10 minutes, the vial was cooled to room temperature. A steady flow of dry N$_2$ transferred the headspace over the remaining glycolaldehyde dimer into a 50 L Teflon bag. Between the vial and the bag, a cold trap (-15 °C) was used to reduce the transmission of dimer and other low volatility impurities. After the bag was filled, an aliquot was transferred into a glass sample cell and the absolute concentration of glycolaldehyde was determined by FTIR (Nicolet 560 Magna-IR) using tabulated absorption cross sections.[31] The referenced Pacific Northwest National Laboratory glycolaldehyde cross-sections agree with those determined by Tuazon et al. to better than 10%.[6] A 500 cm^3 bulb was filled with the mixture and then flushed into the chamber with a known volume of air. The reproducibility of the calibration was verified twice for each technique, which confirmed that systematic and random error were below 7%. During each calibration, the signal on the chamber was monitored for 2-3 hours in order to constrain wall loss processes and determine

the effect of increasing relative humidity in the chamber. Over the timeframe in which the sensitivity was derived, the signal was stable to within $\pm 0.1\%$.

Standards for several of the proposed products of the oxidation of MVK are not commercially available. To identify these products, we synthesized several of the proposed compounds in the gas phase from commercially available precursors. 3-hydroxy-2-butanone and 4-hydroxy-2-butanone were oxidized in the presence of H_2O_2. Both compounds were first diluted in water to yield ~10% w/w solutions that were then volatized into the chamber using the three-way glass vial addition method described above. The experiments (see Table 2) were performed in both the HO_2 and NO dominated regimes. The oxidation products (see Figure 1) were analyzed by GC-CIMS to compare retention times with those of the products of MVK oxidation.
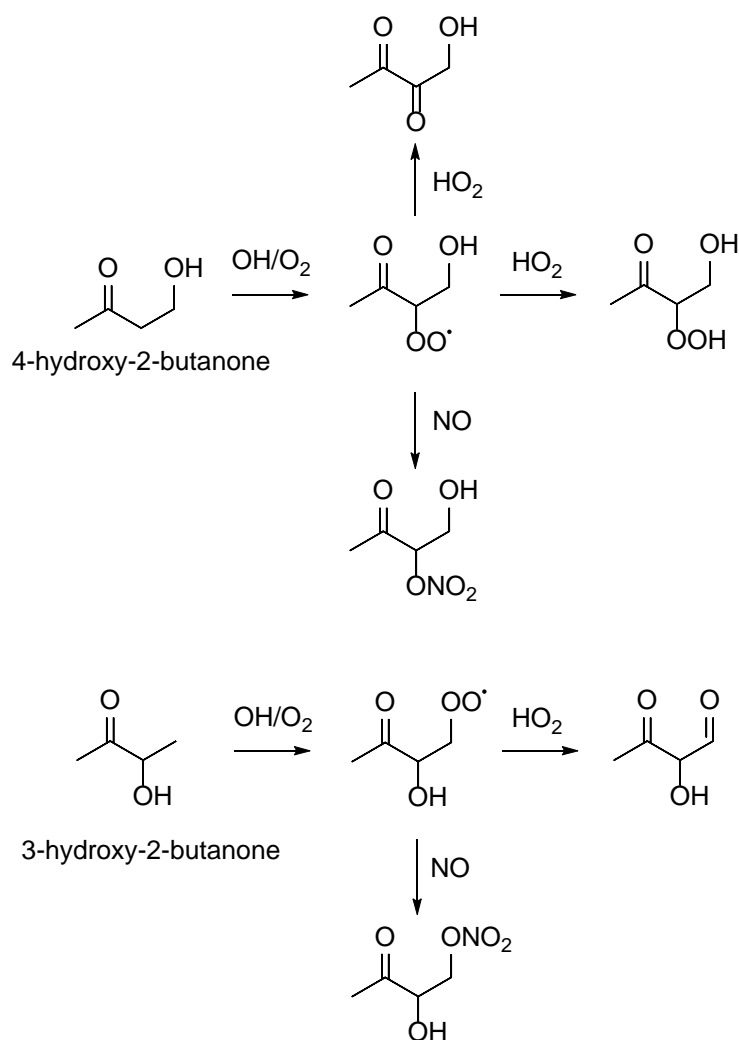
Figure 1. Diagnostic experiments using commercially available precursors were conducted to identify structures associated with mass signals in MVK oxidation. The detected products resulting from NO/HO$_2$ reaction are shown.

MVK PHOTO-OXIDATION EXPERIMENTS

The experiments performed are listed in Table 1. Experiments were conducted at 296 ± 2 K, with the exception of experiments 5, 6, 9, and 10 in which the chamber enclosure was heated and maintained at 323 K. Additions of MVK and oxidant were introduced sequentially to the chamber. MVK standards were prepared by serial dilution. First, a vapor pressure of ~13 hPa of MVK was siphoned into an evacuated 500 cm^3 glass bulb. An atmosphere of nitrogen was

added to the bulb, which was subsequently pumped to ~13 hPa before being refilled with N$_2$. All pressures were measured by an MKS Baratron. The resulting MVK mixing ratio (~100 ppm) was verified by FTIR using tabulated absorption cross sections.[31] The sample was then introduced to the chamber and diluted with a regulated flow (20 L min^{-1}, MKS mass flow controller) of dry zero air.

H$_2$O$_2$ was used as a HO$_x$ precursor in some experiments, while CH$_3$ONO was used in others. A known amount (~8 mg) of H$_2$O$_2$ (30% w/w in water) was transferred into a three-way glass vial and evaporated into the chamber using a stream of dry zero air for about 20 minutes to yield 2.50 ± 0.25 ppm H$_2$O$_2$. The residual mass of the vial was measured to ensure complete transfer of the contents to the chamber.

OH and HO$_2$ are produced via the photolysis of H$_2$O$_2$ under full chamber UV lights (8 Sylvania 350 blacklights with $J_{H2O2} \sim 1.7$ x 10^{-6} s^{-1}, $J_{NO2} \sim 2.5$ x 10^{-3} s^{-1}, and $J_{glycolaldehyde} \sim 1.5$ x 10^{-6} s^{-1}):

$$H_2O_2 + h\nu \rightarrow 2OH$$

$$OH + H_2O_2 \rightarrow HO_2 + H_2O$$
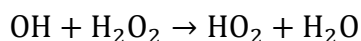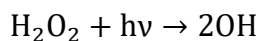
CH$_3$ONO was used as a radical precursor to create conditions where the peroxy radicals react at approximately equal rates with HO$_2$ and NO. Methyl nitrite was synthesized using a procedure similar to that outlined in Taylor et al.[32] A known pressure of CH$_3$ONO was added to a 500 cm^3 glass bulb, following a method similar to the addition of MVK. Only 2 UV lights were used in these experiments because the photolysis rate of CH$_3$ONO is much greater than that of H$_2$O$_2$ for the radiation emitted by our chamber lights. Radical generation proceeds by:

$$CH_3ONO + h\nu + O_2 \rightarrow HO_2 + NO + HCHO$$

$$HO_2 + NO \rightarrow OH + NO_2$$
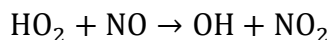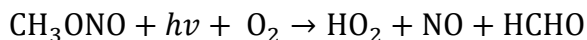
For experiments designed to measure the alkyl nitrate yield (7, 8, 9 and 10), ~1 ppm NO was added to the chamber at the start of the experiments using the primary standard described above.

After filling the chamber with all reactants and diluting to the desired volume, background signals were quantified via direct (without chromatographic separation) and GC-CIMS sampling. UV lights were then switched on until the mixing ratio of MVK had decayed ~10%. This amount was chosen to minimize the influence of secondary reactions and other loss processes while producing quantifiable yields of products. The product yields reported here are derived from this initial oxidation period.

Experiments 5 and 6 were performed to probe unimolecular pathways in the mechanism. Similar to previous experiments detailing the oxidation of methacrolein described by Crounse et al.,[21] the peroxy radical lifetimes were extended by halving the concentration of both MVK and oxidant and employing very low light flux conditions. Additionally, the chamber was heated to 50 °C to increase the rate of any RO_2 isomerization processes.

Finally, experiments 15 and 16 were performed to measure the photolysis of the products of MVK oxidation. MVK was oxidized in the presence of H_2O_2 until a sufficient signal level was attained for the product compounds of interest. At this point, oxidation was halted by switching the lights off. Isopropanol, an OH scrubber, was added to the chamber via a 500 cm^3 glass bulb to yield a ~50 ppm mixing ratio. According to evaluated gas phase kinetic data,[5] >99% of OH present or subsequently produced preferentially reacted with the scrubber under these conditions. The chamber was fully illuminated once again for ~10 hours. Photolysis experiments were conducted both with (experiment 16) and without (experiment 15) the presence of the OH scavenger.

Table 1. List of photo-oxidation experiments performed.

experiment #	objective	[MVK] initial (ppbv)	oxidant (ppmv)	[NO] initial (ppmv)	temperature ($\pm$ 2 K)	UV (%) [a]
1	$RO_2 + HO_2$	85	H_2O_2, 2.5	-	296	100
2	$RO_2 + HO_2$	79	H_2O_2, 2.5	-	296	100
3	$RO_2 + HO_2$	62	H_2O_2, 2.5	-	296	100
4	$RO_2 + HO_2$ hot	95	H_2O_2, 2.5	-	323	100
5	$RO_2 + HO_2$ slow, hot	60	CH_3ONO, 0.050	-	323	12.5
6	$RO_2 + HO_2$ slow, hot	28	H_2O_2, 1.6	-	323	12.5
7	$RO_2 + NO$	75	CH_3ONO, 0.100	1.3	296	25
8	$RO_2 + NO$	440	H_2O_2, 2.5	1.2	296	100
9	$RO_2 + NO$ hot	75	CH_3ONO, 0.100	1.2	323	25
10	$RO_2 + NO$ hot	78	CH_3ONO, 0.100	1.2	323	25

[a] $J_{NO2} = 2.5 \times 10^{-3}$ s^{-1} at 100% illumination

Table 2. List of diagnostic experiments performed. Parentheses are used to indicate the isolation of peroxy radicals produced by reactions R1a or R1b.

experiment #	objective			hydrocarbon	oxidant	NO added (ppmv)	OH scavenger
11	RO_2 (R1a) + HO_2			4-hydroxy-2-butanone	H_2O_2	-	No
12	RO_2 (R1a) + NO			4-hydroxy-2-butanone	H_2O_2	0.8	No
13	RO_2 (R1b) + HO_2			3-hydroxy-2-butanone	H_2O_2	-	No
14	RO_2 (R1b) + NO			3-hydroxy-2-butanone	H_2O_2	0.8	No
15	Photolysis			MVK	H_2O_2	-	No
16	Photolysis			MVK	H_2O_2	-	Yes

Quantum chemical methods

We employed theoretical calculations to evaluate the thermodynamics of the three proposed reaction pathways for the reaction of MVK-derived RO_2 and HO_2 (R2a-R2c). The lowest energy conformer for each of the stationary points along the reaction was found using the systematic search in Spartan'14[33] except for the transitions states (TS) where the structures were inferred based on previous calculations in the literature.[12, 16-18] The B3LYP hybrid density functional with the standard 6-31+G(d) double zeta basis set was used in these initial calculations. The optimized structure of each stationary point was subsequently refined with the wB97XD functional[34] and the aug-cc-pVDZ and aug-cc-pVTZ, double and triple zeta basis set, respectively (wB97XD/aVDZ and wB97XD/aVTZ). Only minor differences in structures are found between the wB97XD/aVDZ and wB97XD/aVTZ optimized structures. Harmonic vibrational frequencies are calculated for both wB97XD methods to confirm that each structure is either a minimum or a transition state (one imaginary frequency). The transition state (TS) structures are shown to connect the reactant or reactant intermediate and product on either side via intrinsic reaction coordinate (IRC) calculations with the wB97XD/aVDZ method. For all calculations we used the unrestricted Kohn-Sham

formalism with the spin symmetry of the initial guess wavefunction broken (Guess=Mix). The wB97XD DFT calculations are calculated using the Gaussian09 program suite with the default convergence criteria.[35]

We improved the accuracy of the thermochemistry by calculating single point energies with the explicitly-correlated CCSD(T)-F12a/VDZ-F12 method (F12) at the wB97XD/aug-cc-pVTZ optimized structures.[36] The F12 calculations on open-shell species are restricted open coupled cluster [ROCCSD(T)-F12] calculations based on a restricted-open Hartree-Fock (ROHF) determinant. The T1 diagnostic is less than 0.034 in all F12 calculations, which indicates that multiconfiguration effects are limited. All the F12 coupled cluster calculations are performed using the MOLPRO2010 program suite with the default convergence criteria.[37]

We obtain ΔG for each structure with the F12 energies and the thermal contribution from the wB97XD/aug-cc-pVTZ calculation.

Results and discussion
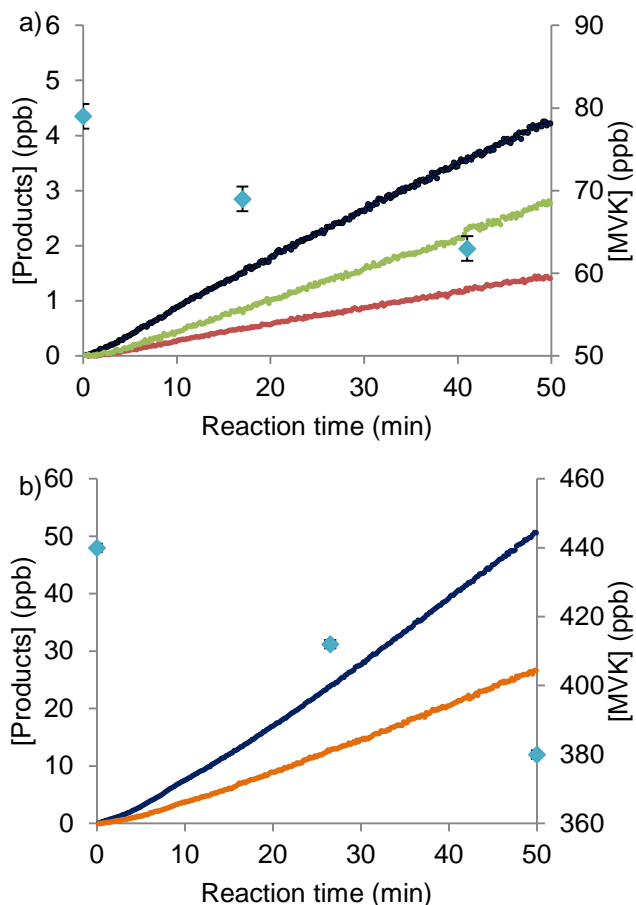
Figure 2. Reaction profiles demonstrating the HO$_2$ and NO dependence of the chemistry. Species shown are glycolaldehyde (dark blue), a 4,3-hydroxy hydroperoxide (green), an α-diketone (red), organic nitrates (×10, orange), and MVK (light blue diamonds). Data are derived from a) experiment 2 in the low NO regime and b) experiment 8 in the high NO regime. Error bounds reflect the uncertainty in the GC-FID quantification of MVK.

PRODUCT YIELDS

The product yields from the reaction of the hydroxy peroxy radicals formed via R1a and R1b with NO or HO$_2$ are shown in Table 3. Example time traces of the decay of MVK and the growth of these products are shown in Figure 2.

The yield of glycolaldehyde is computed from the rate of its formation divided by the loss rate of MVK. The yields of the other products are determined relative to glycolaldehyde. The tabulated uncertainty in the yield of glycolaldehyde includes error in its measurement and from error in the amount of MVK oxidized (due to uncertainty in the GC-FID measurements and in the initial concentration of MVK resulting from error in the infrared cross sections). The uncertainty in the yields of the other products includes error in the absolute yield of glycolaldehyde in addition to error in the slope of the linear regression of the relative rate of product formation. Uncertainty in the calibration of glycolaldehyde is ~7% and for the hydroxy nitrates is ~12%. Calibration of the remaining compounds is significantly more uncertain (30%) due to the lack of authentic standards (see Table S1). The error bounds in Table 3 also include uncertainty in both measured and calculated calibration factors. Due to uncertainty in the calibrations, the yields do not necessarily achieve carbon parity.

Table 3. Measured yields based on experiments 7 and 8 for the high NO regime and experiments 1-3 for the $RO_2 + HO_2$ regime. Methylglyoxal was not measured in these experiments.

regime	glycolaldehyde	methylglyoxal	C_4 α-diketone	C_4 4,3 hydroxy hydroperoxide	MVKN	MVKN'
$RO_2 + NO$	74 ± 6.0 %	24.12 ± 0.14 % [a]	-	-	2.4 ± 0.4 %	1.6 ± 0.4 %
$RO_2 + HO_2$	38 ± 4.6 %	4 ± 1 % [b]	14 ± 5.3 %	27 ± 9.7 %	-	-

[a] Galloway et al.[7]

[b] Personal communication from Keutsch, F. N.[38]

In direct sampling from the chamber, the signal from both hydroxy nitrate isomers produced from MVK, 4-hydroxy-3-nitrooxy-2-butanone (MVKN) and 4-nitrooxy-3-hydroxy-2-butanone (MVKN'), is measured as the cluster with CF_3O^- (*m/z* 234). The isomer specific yields were determined using GC-CIMS. We assigned the chromatographic peaks by

comparing the individual retention times with those of the hydroxy nitrate carbonyls produced in experiments 12 and 14 (Figure S2).

The yield and identification of the dicarbonyl compound was based on analysis of experiments 11, 13, 15, and 16. As discussed below, there are two possible compounds detected as a CF_3O^- cluster with $C_4O_3H_6$ at m/z 187: an α-diketone (1-hydroxy-2,3-butanedione) or an aldehyde (2-hydroxy-3-oxobutanal). However, the oxidation of 4-hydroxy-2-butanone in experiment 11 produced a yield of the m/z 187 compound relative to glycolaldehyde identical to that shown in Table 3. On the other hand, the m/z 187 signal observed from 3-hydroxy-2-butanone oxidation in experiment 13 was produced as a second-generation product and was not accompanied by co-production of glycolaldehyde. Thus, we conclude that the observed m/z 187 signal primarily arises from the α-diketone and that the contribution of the aldehyde is likely small (<2%).

Only a single hydroxy hydroperoxide was observed in GC-CIMS chromatograms obtained following the low NO oxidation of MVK (experiments 1-3). The elution time of this compound matched that of the hydroperoxide formed in experiment 11. The hydroxy hydroperoxides produced in experiments 1-3 and 11 also share identical and characteristic ion chemistry. Three major product ions are observed: m/z 205 results from the cluster of CF_3O^-; m/z 139 ($FC_4H_8O_4^-$) results from fluoride transfer; m/z 101 ($C_4H_5O_3^-$) likely results from loss of water and HF; and FCO_2^- (m/z 63) is a fragment of m/z 205 characteristic of CF_3O^- chemical ionization of hydroxy hydroperoxides.[24] The product ions (m/z 205:139:101:63) are produced in a ratio of 5:10:6.5:1. This analysis is further detailed in Figure S2. Given the identical elution time and similar product ion distribution between the MVK hydroperoxide and those derived from the oxidation of 4-hydroxy-2-butanone, we identify this hydroperoxide as the 4,3-hydroxy hydroperoxide.

REACTION OF RO_2 WITH NO: CONSTRAINING THE RATIO R1a:R1b

In the reaction of the two peroxy radicals produced in R1a and R1b with NO, two alkoxy radicals and two alkyl nitrates are produced (see Scheme 1). Tuazon et al. and Galloway et al. suggested that the internal and external alkoxy radicals decompose to glycolaldehyde and methylglyoxal with 100% yield, respectively.[6-7] Consistent with this hypothesis, we have

calculated the energy barriers associated with decomposition of the alkoxy formed from the reaction of the peroxy radical produced in R1a with NO. We find that fragmentation to methylglyoxal is likely uncompetitive with fragmentation to acetyl peroxy (PA) and glycolaldehyde (8.2 vs. 1.5 kcal/mole in electronic energy, see SI). This is consistent with the structure-activity relationship of Vereecken and Peeters which suggests these barriers to be 8.1 vs. 3.7 kcal/mole, respectively.[39] Thus, the product yields shown in Table 3 suggest that the branching to R1a, derived by adding the glycolaldehyde yield and that of the corresponding hydroxy nitrate, is $76 \pm 14\%$, while that to R1b is $24 \pm 14\%$. The branching of R1b is defined as the difference between unity and the branching to R1a. Our estimation of the branching ratio is consistent with previous estimates.[6-7]

Scheme 1. Proposed mechanism for the high NO regime (after Tuazon and Atkinson).[6]

Observed species are indicated in blue. Branching and yields (T = 296 K, P = 993 hPa) are

in red.
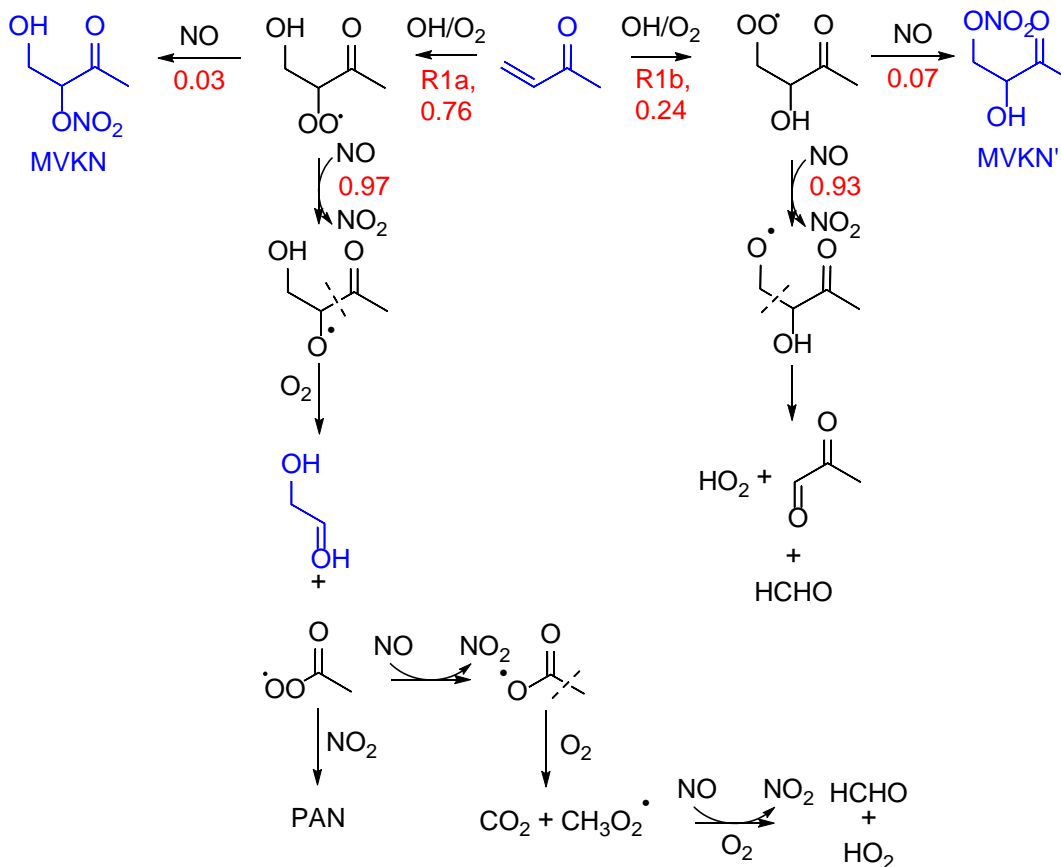
REACTION OF RO_2 WITH NO: FORMATION OF ALKYL NITRATES

The alkyl nitrate branching ratio from the reaction of the RO_2 produced in R1a with NO is

$3.2 \pm 0.6\%$ at 296 K, while the branching ratio from the RO_2 produced in R1b is more than

a factor of two larger ($6.6 \pm 1.5\%$). The combined yield at 296 K is $4.0 \pm 0.6\%$, much lower

than previously suggested.[6, 8] Comparing the yields from experiments 7 and 8 with those of

9 and 10, we find that the combined yield is a factor of ~1.8 times lower at 323 K than at 296

K. Furthermore, at 323 K, the production ratio of MVKN to MVKN' is 1.10 ± 0.05.

Alkyl nitrates likely form in a roaming radical mechanism. This mechanism proceeds following destabilization of the ROONO moiety. In some cases, the nascent radicals do not separate but rather reform an activated $RONO_2$ complex, which then undergoes collisional stabilization to form the nitrate.[40-43] As such, the yield will depend on the lifetime of the complex. This general mechanism is consistent with findings that alkyl nitrate yields tend to increase with the size of molecule,[44] and decrease with increasing temperature.[45] In addition, several studies have suggested that the formation of nitrates becomes less favorable when neighboring groups weaken the RO-ONO bond enhancing the rate of decomposition.[43, 46-47] Using the β-hydroxy nitrate yields quantified in our recent study of nitrates formed in the oxidation of alkenes,[27] we expect, based on the molecular size alone, that the alkyl nitrate yield from MVK would be ~14%. The much lower yield measured likely reflects destabilization of the RO-ONO moiety by the electron withdrawing characteristics of the ketone group. Additionally, the lower yield and stronger temperature dependence of the nitrate formed from the RO_2 produced in R1a suggests that a β-ketone is more destabilizing than a γ-ketone.

The atmospheric fate of these nitrates remains unclear. A recent theoretical study has reported that the atmospheric lifetime of MVKN and MVKN' will be limited by photolysis (~5 hours).[48] Upon further oxidation by OH, the nitrates have been proposed to generate formic and pyruvic acid.[24]

Scheme 2. Proposed mechanism for the OH-initiated oxidation of MVK following R1a

in the HO_2-dominated regime. Observed products are indicated in blue. Yields (T = 296 K,

P = 993 hPa) are in red.
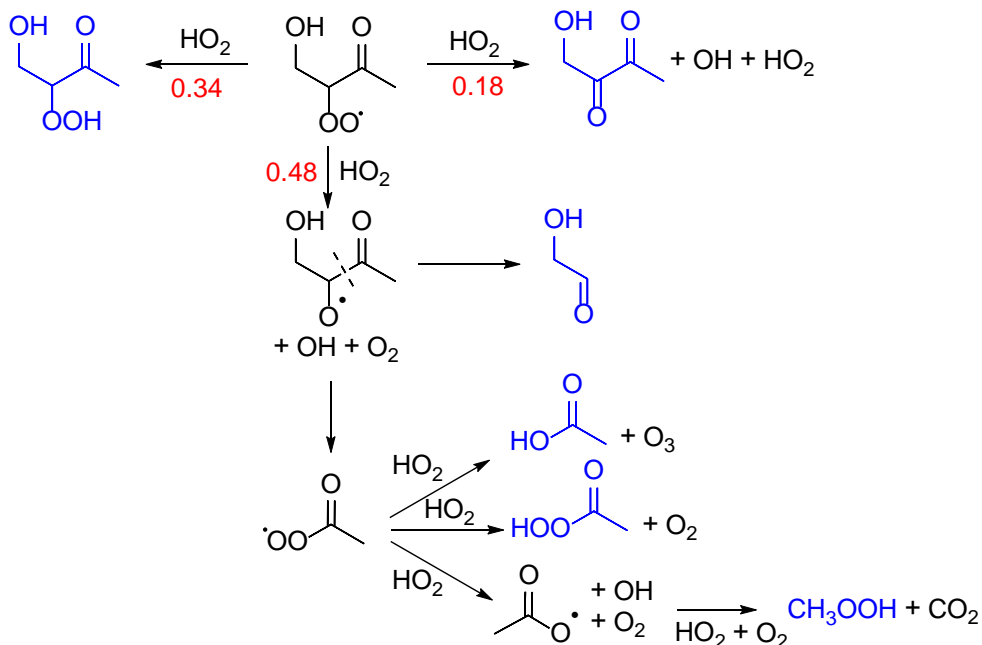
REACTION OF RO_2 WITH HO_2: NEW CHEMISTRY AND RADICAL RECYCLING

Reaction of the peroxy radicals with HO_2 is remarkably efficient in the recycling of radicals.

We identified R2a-R2c for the reaction of HO_2 with the MVK RO_2 arising from R1a (see

Scheme 2).

The large yield of glycolaldehyde (~40%) suggests that the OH radical is recycled efficiently

via R2a. This chemistry is not unprecedented. Recent studies have demonstrated that OH

generation occurs in several similar systems.[12-14] For example, reaction of HO_2 with PA

radical, produced in R2a upon addition of O_2 to the $CH_3C(O)$ radical, has been shown to

follow three pathways. The dominant channel (R3a, yield = 0.61 ± 0.09 [49]) produces OH and

acetoxy radicals, while peracetic acid (R3b) and acetic acid and O_3 (R3c) are produced in

smaller yields:[12-14, 50-51]

$$CH_3C(O)O_2 + HO_2 \quad \rightarrow CH_3C(O)O + OH + O_2 \qquad \text{R3a}$$
$$\rightarrow CH_3C(O)OOH + O_2 \qquad \text{R3b}$$

$$\rightarrow CH_3C(O)OH + O_3 \qquad\qquad R3c$$
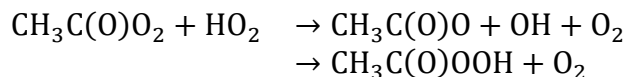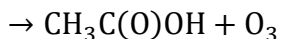
In the presence of HO_2, the radical produced in R3a leads to formation of methyl hydroperoxide (MHP):

$$CH_3C(O)O \rightarrow CH_3 + CO_2 \qquad\qquad R4$$

$$CH_3 + O_2 + M \rightarrow CH_3O_2 + M \qquad\qquad R5$$

$$CH_3O_2 + HO_2 \rightarrow CH_3OOH + O_2 \qquad\qquad R6$$
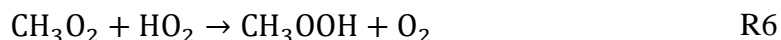
All stable organic end products identified in R3-R6 were detected in the HO_2-mediated reaction of MVK RO_2 and suggest greater radical recycling occurring beyond the initial OH reformation in R2a.

The 4,3-hydroxy hydroperoxide produced via R2b was found to promptly photolyze (Figure 3). Independent of whether an OH scrubber was added (experiments 15 and 16), the hydroperoxide decayed with a first-order loss rate of 3.0 ± 0.1 x 10^{-5} s^{-1}. Scaling the J_{NO2} in our chamber (2.5 x 10^{-3} s^{-1}) to that of a typical noontime atmosphere (0.01 s^{-1}) suggests that the atmospheric lifetime of this hydroxy hydroperoxide is short ($<< 1$ day). Assuming cleavage of the O-OH bond as the primary photolytic decomposition pathway, R2b will also recycle OH radicals efficiently.

The α-diketone produced via R2c likely results from a mechanism previously thought to be exclusive to halogenated RO_2. As we show below, this route likely produces OH + HO_2 in addition to the carbonyl. Similar chemistry was originally proposed by Wallington et al. to explain the formation of HC(O)F in the reaction of CH_2FO_2 and HO_2.[52] More recent theoretical studies have demonstrated that the energetic barrier for formation of OH and HO_2 from single-carbon fluorinated and chlorinated RO_2 is lower than the pathway to formation of H_2O and O_2 as originally proposed.[16-18] To our knowledge, the MVK system provides the first evidence for this chemistry in non-halogenated peroxy species.

Rapid photolysis has been previously reported for α-diketones.[53] We designed experiments 15 and 16 to measure the rate of photolysis for the hydroxy diketone (*m/z* 187). Both prior to and after the initiation of photolysis, the signal was monitored for a period of 2 hours to measure the wall loss rates. These were determined to be 2 x 10^{-7} s^{-1} and 2 x 10^{-6} s^{-1} before

and after photolysis, respectively. Upon illumination by UV light, the *m/z* 187 signal decayed ~20% at a consistent rate. After 4 hours, however, the loss ended such that an exponential decay no longer fit the data. This is likely due to the formation of a third-generation isobaric compound. Whether production of this compound existed during the initial period, although at a lower rate, is uncertain. Thus, we can only determine a loosely constrained value of ~1 x 10^{-5} s^{-1}, which includes corrections for wall loss and reaction with OH (< 1% due to the presence of an OH scrubber). This rate is lower than the calculated photolysis rate of a similar α-diketone, methylglyoxal, under similar conditions (4.1 x 10^{-5} s^{-1}).
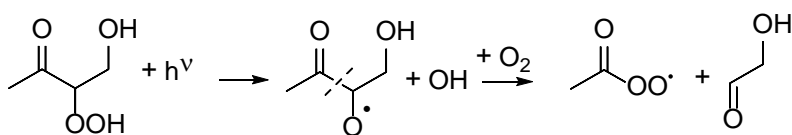
Figure 3. Photolysis the 4,3-hydroxy hydroperoxide, assuming cleavage of the O-OH bond, is expected to form PA, glycoladehyde, and recycle OH. Rapid photolysis of this species was observed.

INTERNAL OH ADDITION

We are unable to identify the majority of the products of the reaction of HO_2 with the terminal RO_2 (formed via R1b). By reference to the reactions arising from external OH addition (R1a), the products are likely methylgloxal, a hydroperoxide, and an aldehyde. The instruments employed in this study are insensitive to methylglyoxal and thus we turn to unpublished data collected in the HO_2-dominated regime during the same set of experiments reported by Galloway et al.[7] Preliminary analysis of this data via personal communication from the authors suggests an overall methylglyoxal yield of ~4%.[38] In the current study, only a single *m/z* 205 peak, identified as the 4,3-hydroxy hydroperoxide, was observed in GC-CIMS analysis. No other peaks resembling a fragmentation pattern characteristic to hydroperoxide functionality were located in the vicinity of the elution time of the observed *m/z* 205 compound. It is possible that ionization of the 3,4-hydroxy hydroperoxide results in fragmentation into undetectable products. Alternatively, the hydroperoxide may decompose

rapidly on the chamber walls. The C_4 aldehyde, as explained earlier, appears to be produced in, at most, a small yield. It may also be possible to form other products which are not observed by our CIMS.
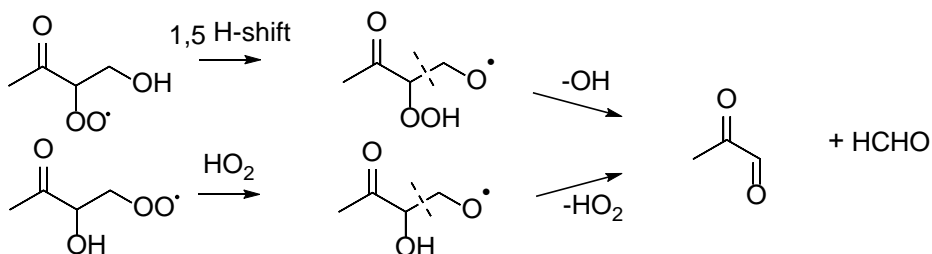
Figure 4. A 1,5 H-shift, as suggested by Peeters et al. and Asatryan et al.,[19, 54] is difficult to detect by the end products alone, as two pathways exist to their formation.

UNIMOLECULAR RO_2 CHANNELS

Functionalized peroxy radicals are known to undergo unimolecular hydrogen shifts from neighboring substituents.[10, 55] Recent theoretical studies have suggested that a unimolecular pathway involving a 1,5 H-shift from the terminal hydroxy group to the RO_2 (R1a) could be of significance in the production of methylglyoxal and formaldehyde (see Figure 4).[19, 54] While this mechanism proceeds through different intermediates, the end products are likely identical to the pathway involving HO_2 reaction with the terminal RO_2 to produce RO. Thus, the detection of this mechanism is complicated. Experiments 5 and 6 were designed to promote isomerization processes through active heating of the chamber to 50 °C and extension of RO_2 lifetimes. The product distributions and yields observed in these experiments were very similar to those seen in experiments 1-3. While the majority of products arising from R1b are poorly characterized, the ratio of MVKN to MVKN' in experiment 5 was consistent with those obtained in experiments 9 and 10. This suggests that neither of the RO_2 radicals had a significant unimolecular channel under the experimental conditions probed here.
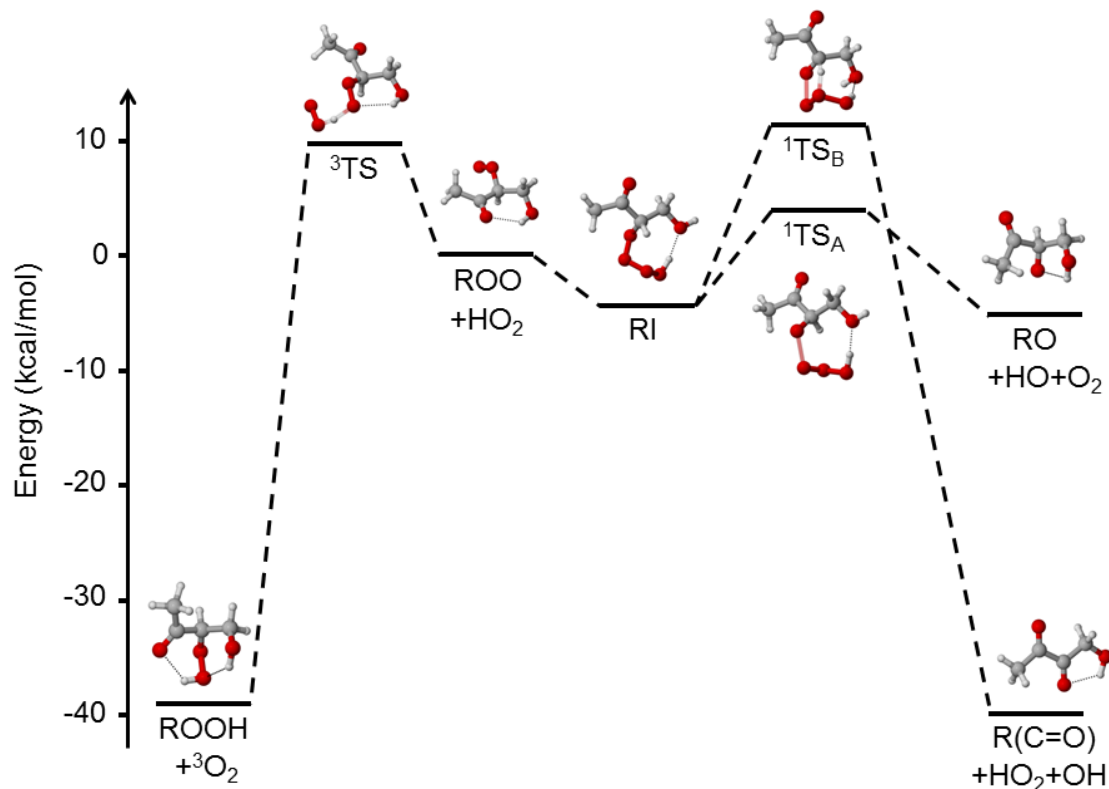
Figure 5. Relative energies (ΔG_{298K}) for the three $RO_2 + HO_2$ channels. We have used wB97XD/aug-cc-pVTZ thermochemistry with ROHF-ROCCSD(T)-F12/VDZ-F12 energies. The wB97XD/aug-cc-pVTZ geometries for each of the stationary points are shown.

Quantum chemical calculations

Figure 5 and Table 4 show that all three postulated reaction pathways (R2a-R2c) in the reaction of HO_2 with RO_2 (R1a) are kinetically accessible at 298 K. Transition states for the reactions leading to the hydroperoxide (ROOH) and the alkoxy (RO) corresponded to those found for acetonyl RO_2 in the literature.[12] In addition, a new channel leading to a diketone (R(C=O)) has been found. For all but TS_A of the reaction leading to RO, there is no significant spin contamination observed, with $<S^2>$ being within 0.02 of the expected values for singlet (0), doublet (¾), and triplet (2), respectively (see Table S5).

The ROOH reaction producing ground state O_2 takes place on the triplet surface via the transition state ^3TS (almost iso-energetic with the reactants) with a moderate free energy barrier of about 10 kcal/mol. Tunneling will slightly enhance the reaction rate along this surface by a factor similar to that of the R(C=O) channel.

The RO reaction occurs via a tetroxide intermediate (labeled RI) and a low-energy, open-shell singlet transition state TS_A with a free energy barrier of about 4 kcal/mol. The immediate products of TS_A are RO and an HO_3 radical, which further decomposes to OH and O_2. The structure and stability of HO_3 is a challenging problem for quantum chemical methods. Even high level methods such as CCSD(T)-F12 do not describe it accurately (see Zhou et al.,[56] Varandas et al.,[57] and references therein).

We have also identified a reaction path leading to the α-diketone (R(C=O)). This channel also proceeds via the tetroxide intermediate RI but to TS_B with a free energy barrier of about 12 kcal/mol and leads to the diketone and an H_2O_3 radical; the latter decomposes to OH + HO_2. Decomposition to H_2O and triplet O_2 would be even more energetically favorable, but is spin-forbidden as the reaction takes place along the singlet potential energy surface.

We have also found an alternative tetroxide structure about 2 kcal/mol below RI in electronic and free energy. This tetroxide can also decompose to both RO and R(C=O) products, although through a higher energy TS than the ones shown in Figure 5. The two tetroxides differ only in their H-bonding pattern (see SI).

We were unable to locate a transition state between the free reactants and either of the tetroxides, and we thus assume they form without a significant energy barrier.

The free energy barriers computed for the three reaction routes, as shown in Table 4, are within a few kcal/mol of each other. The electronic energy of all the transition states is around or below the electronic energy of the reactants. Furthermore, the routes with the largest free energy barrier (leading to R(C=O) and ROOH) are slightly assisted by tunneling. The effect of tunneling with the Eckart tunneling correction was calculated to be a factor of 3 for the diketone channel and insignificant for the RO channel.[58]

The uncertainty of the computed energy barriers is possibly higher than the usual few kcal/mol for CCSD(T)-F12/VDZ-F12 energies due to the spin issues in particular for TS_A and multireference issues (c.f. the discussion of the HO_3 intermediate product above; see also

SI). Thus, quantitative predictions of product yields are not reliable. Qualitatively, however, the calculations are consistent with the experimental observations, with the highest yields observed for the RO channel, followed by the ROOH and R(C=O) channels.

Table 4. Energetics of the Different $RO_2 + HO_2$ Channels.

	ΔE^a (kcal/mol)	ΔE^b (kcal/mol)	ΔG^c (kcal/mol)	TS (imaginary frequency, cm^{-1})
$ROO + HO_2$	0.0	0.0	0.0	-
^{3}TS	-3.2	+0.7	+10.2	934i
$ROOH + O_2$	-39.2	-43.1	-38.9	-
RI	-12.2	-20.4	-4.1	-
^{1}TS$_A$	2.5	-8.3	+4.1	212i
$RO + OH + O_2$	+5.7	+8.1	-5.0	-
^{1}TS$_B$	11.2	-0.7	+12.0	905i
$R(C=O) + OH + HO_2$	-22.3	-26.2	-40.0	-

[a]Calculated with wB97XD/aug-cc-pVTZ.

[b]Calculated with ROHF-ROCCSD(T)-F12/VDZ-F12//wB97XD/aug-cc-pVTZ.

[c]Calculated with the wB97XD/aug-cc-pVTZ thermochemistry with CCSD(T)-F12/VDZ-F12 single point energy correction.

Atmospheric implications

To assess the importance of the chemistry described here, we employed GEOS-Chem, a widely used chemical transport model.[4] A 1 year simulation (January to December 2012) of the model was conducted on a global 4° latitude x 5° longitude grid. The alkyl nitrate yield reported in this work was incorporated into the base chemistry to isolate the impact of HO_2 chemistry. Changes to the mechanism were applied separately to the base model to evaluate

the impact of each modification of the chemistry. We began by implementing the yields of first generation products described by R2a-R2c (MVK scenario). An additional scenario (MVK + RCO₃), was created to assess the impact of PA radical production through R2a. The default GEOS-Chem 2012 mechanism does not treat PA according to recent findings. Hence, the most recent measurement of the OH yield from the reaction of PA + HO$_2$ was incorporated into both the base and the revised mechanism so as not to bias the results.[49] Given the considerable yield of PA in R2a, we believe this scenario to be most representative of the findings reported in this work. In order to provide an external benchmark, the OH production resulting from methacrolein (MACR) isomerization was included in a separate run.[21] The final simulation incorporated all revisions of the previous scenarios and the fast photolysis of MVK ROOH. We find these changes result in a greater than 1% increase in the global mean boundary layer concentration of OH (Table 5). Locally, the impact is larger. In the forested tropical boundary layer, simulated OH concentrations are up to 6% larger (Figure 6).
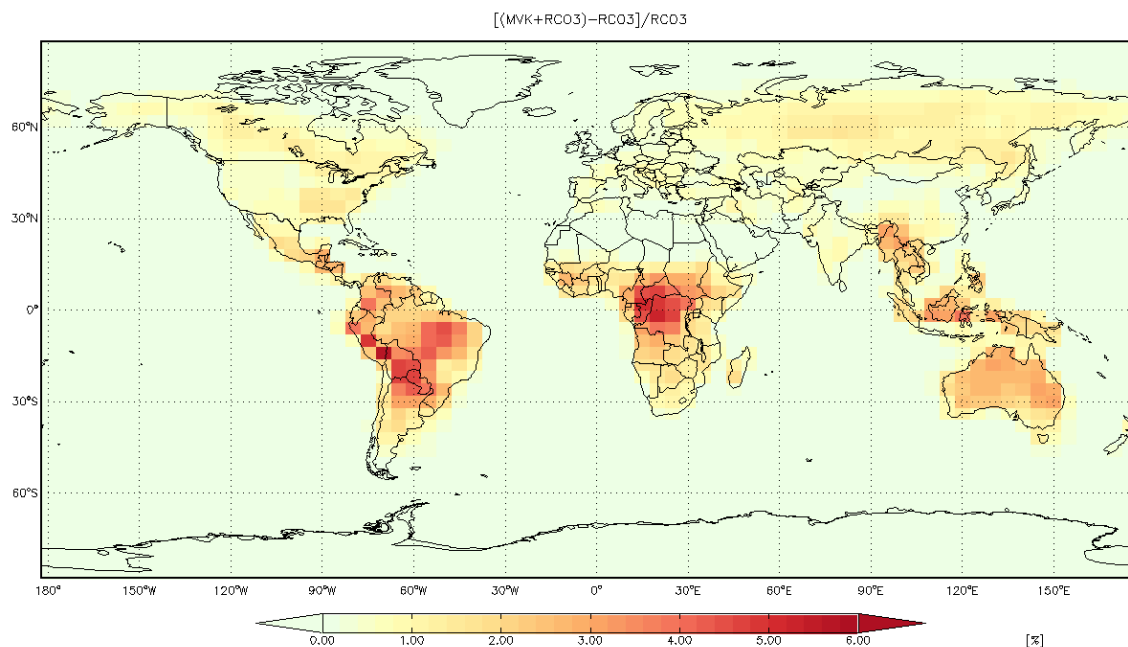
Figure 6. Annual-averaged OH mixing ratio difference for 2012 resulting from the revised MVK mechanism (MVK + RCO₃). Results are reported for 0-1 km above the surface.

Table 5. Comparison of various model scenarios with the increase determined relative to the base chemistry (see SI for scenario definitions). Global mean OH values were determined by averaging over all space between 0-1 km above the surface.

scenario	OH (ppt)	increase over base (%)
Base	0.0539	0.00
MVK	0.0541	0.30
MVK + RCO$_3$	0.0544	0.89
MACR	0.0541	0.35
All + J$_{ROOH}$	0.0547	1.33

Conclusions

HO$_x$ recycling channels have been proposed to explain first generation products arising from the oxidation of isoprene in pristine environments[19-20] as well as the production of hydroxyacetone from MVK's atmospheric sister compound, methacrolein.[21] Yet the atmospheric chemistry of MVK, particularly in environments with low concentrations of NO, has been largely unexplored. Here we demonstrate a number of new radical recycling channels that contribute to sustaining the oxidizing capacity of the atmosphere. We further illustrate dicarbonyl formation in a novel mechanism previously identified only for halogenated peroxy species. This finding suggests that carbonyl products may arise from reaction of HO$_2$ with other substituted peroxy radicals in an overall HO$_x$ neutral process.

REFERENCES
1. Guenther, A. B.; Jiang, X.; Heald, C. L.; Sakulyanontvittaya, T.; Duhl, T.; Emmons, L. K.; Wang, X., The Model of Emissions of Gases and Aerosols from Nature Version 2.1 (Megan2.1): An Extended and Updated Framework for Modeling Biogenic Emissions. *Geosci. Model Dev.* **2012,** *5* (6), 1471-1492.

2. Zhang, D.; Lei, W. F.; Zhang, R. Y., Mechanism of OH Formation from Ozonolysis of Isoprene: Kinetics and Product Yields. *Chem. Phys. Lett.* **2002,** *358* (3-4), 171-179.

3. Biesenthal, T. A.; Shepson, P. B., Observations of Anthropogenic Inputs of the Isoprene Oxidation Products Methyl Vinyl Ketone and Methacrolein to the Atmosphere. *Geophys. Res. Lett.* **1997,** *24* (11), 1375-1378.

4. Bey, I.; Jacob, D. J.; Yantosca, R. M.; Logan, J. A.; Field, B. D.; Fiore, A. M.; Li, Q. B.; Liu, H. G. Y.; Mickley, L. J.; Schultz, M. G., Global Modeling of Tropospheric Chemistry with Assimilated Meteorology: Model Description and Evaluation. *J. Geophys. Res.-Atmos.* **2001,** *106* (D19), 23073-23095.

5. Atkinson, R.; Baulch, D. L.; Cox, R. A.; Crowley, J. N.; Hampson, R. F.; Hynes, R. G.; Jenkin, M. E.; Rossi, M. J.; Troe, J., Evaluated Kinetic and Photochemical Data for Atmospheric Chemistry: Volume II - Gas Phase Reactions of Organic Species. *Atmos. Chem. Phys.* **2006,** *6*, 3625-4055.

6. Tuazon, E. C.; Atkinson, R., A Product Study of the Gas-Phase Reaction of Methyl Vinyl Ketone with the OH Radical in the Presence of NO_x. *Int. J. Chem. Kinet.* **1989,** *21* (12), 1141-1152.

7. Galloway, M. M.; Huisman, A. J.; Yee, L. D.; Chan, A. W. H.; Loza, C. L.; Seinfeld, J. H.; Keutsch, F. N., Yields of Oxidized Volatile Organic Compounds During the OH Radical Initiated Oxidation of Isoprene, Methyl Vinyl Ketone, and Methacrolein under High-NO_x Conditions. *Atmos. Chem. Phys.* **2011,** *11* (21), 10779-10790.

8. Chuong, B.; Stevens, P., Measurements of the Kinetics of the OH-Initiated Oxidation of Methyl Vinyl Ketone and Methacrolein. *Int. J. Chem. Kinet.* **2004,** *36* (1), 12-25.

9. Perring, A. E.; Pusede, S. E.; Cohen, R. C., An Observational Perspective on the Atmospheric Impacts of Alkyl and Multifunctional Nitrates on Ozone and Secondary Organic Aerosol. *Chem. Rev.* **2013,** *113* (8), 5848-5870.

10. Orlando, J. J.; Tyndall, G. S., Laboratory Studies of Organic Peroxy Radical Chemistry: An Overview with Emphasis on Recent Issues of Atmospheric Significance. *Chem. Soc. Rev.* **2012,** *41* (19), 6294-6317.

11. Seinfeld, J. H. P. S. N., *Atmospheric Chemistry and Physics : From Air Pollution to Climate Change*. Wiley: New York, 1998.

12. Hasson, A. S.; Kuwata, K. T.; Arroyo, M. C.; Petersen, E. B., Theoretical Studies of the Reaction of Hydroperoxy Radicals (HO_2 Center Dot) with Ethyl Peroxy ($CH_3CH_2O_2$ Center Dot), Acetyl Peroxy ($CH_3C(O)O_2$(Center Dot)) and Acetonyl Peroxy ($CH_3C(O)CH_2O_2$ Center Dot) Radicals. *J. Photochem. Photobiol. A-Chem.* **2005,** *176* (1-3), 218-230.

13. Hasson, A. S.; Tyndall, G. S.; Orlando, J. J., A Product Yield Study of the Reaction of HO_2 Radicals with Ethyl Peroxy ($C_2H_5O_2$), Acetyl Peroxy ($CH_3C(O)O_2$), and Acetonyl Peroxy ($CH_3C(O)CH_2O_2$) Radicals. *J. Phys. Chem. A* **2004,** *108* (28), 5979-5989.

14. Dillon, T. J.; Crowley, J. N., Direct Detection of OH Formation in the Reactions of HO_2 with $CH_3(O)O_2$ and Other Substituted Peroxy Radicals. *Atmos. Chem. Phys.* **2008,** *8* (16), 4877-4889.

15. Jenkin, M. E.; Hurley, M. D.; Wallington, T. J., Investigation of the Radical Product Channel of the $CH_3C(O) CH_2O_2+HO_2$ Reaction in the Gas Phase. *Phys. Chem. Chem. Phys.* **2008,** *10* (29), 4274-4280.

16. Hou, H.; Deng, L. Z.; Li, J. C.; Wang, B. S., A Systematic Computational Study of the Reactions of HO_2 with RO_2: The $HO_2+CH_2ClO_2$, $CHCl_2O_2$, and CCl_3O_2 Reactions. *J. Phys. Chem. A* **2005,** *109* (41), 9299-9309.

17. Hou, H.; Li, J.; Song, X. L.; Wang, B. S., A Systematic Computational Study of the Reactions of HO_2 with RO_2: The $HO_2+C_2H_5O_2$ Reaction. *J. Phys. Chem. A* **2005,** *109* (49), 11206-11212.

18. Hou, H.; Wang, B. S., A Systematic Computational Study on the Reactions of HO_2 with RO_2: The $HO_2+CH_3O_2(CD_3O_2)$ and $HO_2+CH_2FO_2$ Reactions. *J. Phys. Chem. A* **2005,** *109* (3), 451-460.

19. Peeters, J.; Nguyen, T. L.; Vereecken, L., HO_x Radical Regeneration in the Oxidation of Isoprene. *Phys. Chem. Chem. Phys.* **2009,** *11* (28), 5935-5939.

20. Crounse, J. D.; Paulot, F.; Kjaergaard, H. G.; Wennberg, P. O., Peroxy Radical Isomerization in the Oxidation of Isoprene. *Phys. Chem. Chem. Phys.* **2011,** *13* (30), 13607-13613.

21. Crounse, J. D.; Knap, H. C.; Ornso, K. B.; Jorgensen, S.; Paulot, F.; Kjaergaard, H. G.; Wennberg, P. O., Atmospheric Fate of Methacrolein. 1. Peroxy Radical Isomerization Following Addition of OH and O_2. *Journal of Physical Chemistry A* **2012,** *116* (24), 5756-5762.

22. Surratt, J. D., Radical Regeneration from Isoprene. *Nat. Geosci.* **2013,** *6* (12), 995-996.

23. Crounse, J. D.; McKinney, K. A.; Kwan, A. J.; Wennberg, P. O., Measurement of Gas-Phase Hydroperoxides by Chemical Ionization Mass Spectrometry. *Anal. Chem.* **2006,** *78* (19), 6726-6732.

24. Paulot, F.; Crounse, J. D.; Kjaergaard, H. G.; Kroll, J. H.; Seinfeld, J. H.; Wennberg, P. O., Isoprene Photooxidation: New Insights into the Production of Acids and Organic Nitrates. *Atmos. Chem. Phys.* **2009,** *9* (4), 1479-1501.

25. St. Clair, J. M.; McCabe, D. C.; Crounse, J. D.; Steiner, U.; Wennberg, P. O., Chemical Ionization Tandem Mass Spectrometer for the in Situ Measurement of Methyl Hydrogen Peroxide. *Rev. Sci. Instrum.* **2010,** *81* (9), 6.

26. Lee, L.; Teng, A. P.; Wennberg, P. O.; Crounse, J. D.; Cohen, R. C., On Rates and Mechanisms of OH and O_3 Reactions with Isoprene-Derived Hydroxy Nitrates. *J. Phys. Chem. A* **2014,** *118* (9), 1622-1637.

27. Teng, A. P.; Crounse, J. D.; Lee, L.; St. Clair, J. M.; Cohen, R. C.; Wennberg, P. O., Hydroxy Nitrate Production in the OH-Initiated Oxidation of Alkenes. *Atmos. Chem. Phys. Discuss.* **2014,** *14* (5), 6721-6757.

28. Bates, K. H.; Crounse, J. D.; St Clair, J. M.; Bennett, N. B.; Nguyen, T. B.; Seinfeld, J. H.; Stoltz, B. M.; Wennberg, P. O., Gas Phase Production and Loss of Isoprene Epoxydiols. *J. Phys. Chem. A* **2014,** *118* (7), 1237-1246.

29. Garden, A. L.; Paulot, F.; Crounse, J. D.; Maxwell-Cameron, I. J.; Wennberg, P. O.; Kjaergaard, H. G., Calculation of Conformationally Weighted Dipole Moments Useful in Ion-Molecule Collision Rate Estimates. *Chem. Phys. Lett.* **2009,** *474* (1-3), 45-50.

30. Su, T.; Chesnavich, W. J., Parametrization of the Ion-Polar Molecule Collision Rate-Constant by Trajectory Calculations. *J. Chem. Phys.* **1982,** *76* (10), 5183-5185.

31. Sharpe, S. W.; Johnson, T. J.; Sams, R. L.; Chu, P. M.; Rhoderick, G. C.; Johnson, P. A., Gas-Phase Databases for Quantitative Infrared Spectroscopy. *Appl. Spectrosc.* **2004,** *58* (12), 1452-1461.

32. Taylor, W. D.; Allston, T. D.; Moscato, M. J.; Fazekas, G. B.; Kozlowski, R.; Takacs, G. A., Atmospheric Photo-Dissociation Lifetimes for Nitromethane, Methyl Nitrite, and Methyl Nitrate. *Int. J. Chem. Kinet.* **1980,** *12* (4), 231-240.

33. *Spartan'14*, Wavefunction Inc.: Irvine, CA, 2014.

34. Chai, J. D.; Head-Gordon, M., Long-Range Corrected Hybrid Density Functionals with Damped Atom-Atom Dispersion Corrections. *Phys. Chem. Chem. Phys.* **2008,** *10* (44), 6615-6620.

35. Frisch, M. J.; Trucks, G. W.; Schlegel, H. B.; Scuseria, G. E.; Robb, M. A.; Cheeseman, J. R.; Scalmani, G.; Barone, V.; Mennucci, B.; Petersson, G. A., et al. *Gaussian 09*, Gaussian, Inc.: Wallingford, CT, USA, 2009.

36. Knizia, G.; Adler, T. B.; Werner, H. J., Simplified CCSD(T)-F12 Methods: Theory and Benchmarks. *J. Chem. Phys.* **2009,** *130* (5), 20.

37. Werner, H. J.; Knowles, P. J.; Knizia, G.; Manby, F. R.; Schtz, M., Molpro: A General-Purpose Quantum Chemistry Program Package. *WIREs Comput Mol Sci* **2012,** *2*, 242--253.

38. Keutsch, F. N., University of Wisconsin, Madison. Personal Communication. 2014.

39. Vereecken, L.; Peeters, J., Decomposition of Substituted Alkoxy Radicals-Part I: A Generalized Structure-Activity Relationship for Reaction Barrier Heights. *Phys. Chem. Chem. Phys.* **2009,** *11* (40), 9062-9074.

40. Butkovskaya, N. I.; Kukui, A.; Le Bras, G.; Rayez, M. T.; Rayez, J. C., Pressure Dependence of Butyl Nitrate Formation in the Reaction of Butylperoxy Radicals with Nitrogen Oxide. *The Journal of Physical Chemistry A* **2014**.

41. Herath, N.; Suits, A. G., Roaming Radical Reactions. *J. Phys. Chem. Lett.* **2011**, *2* (6), 642-647.

42. Dibble, T. S., Failures and Limitations of Quantum Chemistry for Two Key Problems in the Atmospheric Chemistry of Peroxy Radicals (Vol 42, Pg 5837, 2008). *Atmos. Environ.* **2009**, *43* (8), 1590-1590.

43. O'Brien, J. M.; Czuba, E.; Hastie, D. R.; Francisco, J. S.; Shepson, P. B., Determination of the Hydroxy Nitrate Yields from the Reaction of C(2)-C(6) Alkenes with OH in the Presence of NO. *J. Phys. Chem. A* **1998**, *102* (45), 8903-8908.

44. Carter, W. P. L.; Atkinson, R., Alkyl Nitrate Formation from the Atmospheric Photooxidation of Alkanes - a Revised Estimation Method. *J. Atmos. Chem.* **1989**, *8* (2), 165-173.

45. Atkinson, R.; Carter, W. P. L.; Winer, A. M., Effects of Temperature and Pressure on Alkyl Nitrate Yields in the NO_x Photooxidations of Normal-Pentane and Normal-Heptane. *J. Phys. Chem.* **1983**, *87* (11), 2012-2018.

46. Matsunaga, A.; Ziemann, P. J., Yields of Beta-Hydroxynitrates and Dihydroxynitrates in Aerosol Formed from OH Radical-Initiated Reactions of Linear Alkenes in the Presence of NO_x. *J. Phys. Chem. A* **2009**, *113* (3), 599-606.

47. Matsunaga, A.; Ziemann, P. J., Yields of Beta-Hydroxynitrates, Dihydroxynitrates, and Trihydroxynitrates Formed from OH Radical-Initiated Reactions of 2-Methyl-1-Alkenes. *Proc. Natl. Acad. Sci. U. S. A.* **2010**, *107* (15), 6664-6669.

48. Muller, J. F.; Peeters, J.; Stavrakou, T., Fast Photolysis of Carbonyl Nitrates from Isoprene. *Atmos. Chem. Phys.* **2014**, *14* (5), 2497-2508.

49. Gross, C. B. M.; Dillon, T. J.; Schuster, G.; Lelieveld, J.; Crowley, J. N., Direct Kinetic Study of OH and O_3 Formation in the Reaction of $CH_3C(O)O_2$ with HO_2. *J. Phys. Chem. A* **2014**, *118* (6), 974-985.

50. Hasson, A. S.; Tyndall, G. S.; Orlando, J. J.; Singh, S.; Hernandez, S. Q.; Campbell, S.; Ibarra, Y., Branching Ratios for the Reaction of Selected Carbonyl-Containing Peroxy Radicals with Hydroperoxy Radicals. *J. Phys. Chem. A* **2012**, *116* (24), 6264-6281.

51. Jenkin, M. E.; Hurley, M. D.; Wallington, T. J., Investigation of the Radical Product Channel of the $CH_3C(O)O_2+HO_2$ Reaction in the Gas Phase. *Phys. Chem. Chem. Phys.* **2007**, *9* (24), 3149-3162.

52. Wallington, T. J.; Hurley, M. D.; Schneider, W. F.; Sehested, J.; Nielsen, O. J., Mechanistic Study of the Gas-Phase Reaction of CH_2FO_2 Radicals with HO_2. *Chem. Phys. Lett.* **1994,** *218* (1-2), 34-42.

53. Bouzidi, H.; Fittschen, C.; Coddeville, P.; Tomas, A., Photolysis of 2,3-Pentanedione and 2,3-Hexanedione: Kinetics, Quantum Yields, and Product Study in a Simulation Chamber. *Atmos. Environ.* **2014,** *82*, 250-257.

54. Asatryan, R.; da Silva, G.; Bozzelli, J. W., Quantum Chemical Study of the Acrolein (CH_2CHCHO) + OH + O_2 Reactions. *J. Phys. Chem. A* **2010,** *114* (32), 8302-8311.

55. Crounse, J. D.; Nielsen, L. B.; Jørgensen, S.; Kjaergaard, H. G.; Wennberg, P. O., Autoxidation of Organic Compounds in the Atmosphere. *The Journal of Physical Chemistry Letters* **2013,** *4* (20), 3513-3520.

56. Zhou, Y. Y.; Hu, H.; Li, L.; Hou, H.; Wang, B. S., Ab Initio Study of the Elusive $HO_3(X(2)A'')$ Radical and the HO(X-2 Pi) + O_2(X-3 Sigma(-)(G)) Double Left Right Arrow $HO_3(X(2)A'')$ Reaction. *Comput. Theor. Chem.* **2013,** *1026*, 24-30.

57. Varandas, A. J. C., Ab Initio Treatment of Bond-Breaking Reactions: Accurate Course of HO_3 Dissociation and Revisit to Isomerization. *J. Chem. Theory Comput.* **2012,** *8* (2), 428-441.

58. Eckart, C., The Penetration of a Potential Barrier by Electrons. *Phys. Rev.* **1930,** *35* (11), 1303-1309.

C h a p t e r   3

ATMOSPHERIC AUTOXIDATION IS INCREASINGLY IMPORTANT IN URBAN
AND SUBURBAN NORTH AMERICA

Abstract

Gas-phase autoxidation – regenerative peroxy radical formation following intramolecular hydrogen shifts – is known to be important in the combustion of organic materials. The relevance of this chemistry in the oxidation of organics in the atmosphere has received less attention due, in part, to the lack of kinetic data at relevant temperatures. Here, we combine computational and experimental approaches to investigate the rate of autoxidation in RO_2 radicals produced in the oxidation of a prototypical atmospheric pollutant, n-hexane. We find that the reaction rate depends critically on the molecular configuration of the RO_2 radical undergoing hydrogen transfer (H-shift). RO_2 H-shift rate coefficients via transition states involving 6 and 7 membered rings (1,5 and 1,6 H-shifts, respectively) of α-OH hydrogens (HOC-**H**) formed in this system are of order 0.1 s^{-1} at 296 K, while the 1,4 H-shift is calculated to be orders of magnitude slower. Consistent with H-shift reactions over a substantial energetic barrier, we find that the rate coefficients of these reactions increase rapidly with temperature and exhibit a large, primary, kinetic isotope effect. The observed H-shift rate coefficients are sufficiently fast that, as a result of ongoing NO_x emission reductions, autoxidation is now competing with bimolecular chemistry even in the most polluted North American cities, particularly during summer afternoons when NO levels are low and temperatures are elevated.

Introduction

The gas-phase oxidation of organic compounds in the atmosphere proceeds through a number of reactive pathways. It is well established that reactions are initiated by oxidants including OH, NO_3, and O_3 and that, in the presence of oxygen, organic peroxy radicals (RO_2) are usually formed (1). The subsequent chemistry of RO_2 is diverse and depends on the chemical state of the atmosphere. Traditionally, bimolecular reaction with NO, HO_2, or other RO_2 has been assumed to dominate the fate of these radicals. Gas-phase autoxidation previously received significant attention only in combustion chemistry where high temperatures promote the process by permitting the reactants to overcome sizeable energetic barriers. The critical reaction in autoxidation, which generally governs the overall kinetics, is an intramolecular hydrogen shift to the RO_2. This reaction produces hydroperoxyalkyl radicals (often denoted QOOH), which are known intermediates in autoignition (2, 3). QOOH have only recently been observed (4). While several studies conducted at elevated temperatures have suggested that autoxidation is important in tropospheric chemistry (5-9), experimental kinetic measurements at atmospherically relevant temperatures have been lacking.

Several studies now report the atmospheric significance of RO_2 H-shift chemistry (10-24). Crounse et al. suggested that this mechanism may explain the rapid oxygenation of hydrocarbons that contribute to particle growth (15). Subsequently, autoxidation was implicated in the generation of low-volatility molecules resulting from a single addition of OH or O_3 to monoterpenes (25-30). In these systems, autoxidation reactions proceed through successive isomerizations and O_2 additions, resulting in the formation of molecules with high O/C ratios and, often, multiple hydroperoxide groups. Such compounds have recently been observed to undergo gas-particle transfer (31), and have been shown to be important in particle nucleation (32-49).

While appreciation for the importance of autoxidation is increasing, significant shortcomings exist that preclude adequate characterization of its impact. Research to date has failed to fully describe the autoxidation mechanism of monoterpenes. Attempts have been made to explore autoxidation using cyclohexene as a model system (50, 51). Even in such simplified systems,

however, multiple QOOH are formed, each of which can proceed through a large number of possible pathways to produce closed-shell products. Thus, elucidation of the mechanisms has proved challenging (50, 51).

Here, we use both experimental and computational methods to determine the room temperature rate constants for autoxidation in a simple system - peroxy radicals produced via photoxidation of n-hexane in the presence of NO. The existence of an autoxidation pathway in this system has previously been demonstrated at elevated temperature (5). In the atmosphere, oxidation of hexane by the hydroxyl radical (OH) in the presence of NO produces alkoxy radicals, an example of which is shown in Scheme 1. These alkoxy radicals can isomerize and react with O_2 to yield hydroxyperoxy radicals. For simplicity, our experiments use 2-hexanol as the precursor to produce a suite of these hydroxyperoxy radicals. In urban regions, the expectation is that these RO_2 react further with NO ultimately producing hydroxy carbonyls, HO_2, and NO_2. Autoxidation, on the other hand, competes with the second NO reaction as shown in Scheme 1. In contrast to the mechanism proposed to explain the highly oxidized products observed in the OH and O_3 initiated oxidation of monoterpenes (25-30), the RO_2 in the hexane system primarily proceed through only a single H-shift yielding QOOH, which react with O_2 to produce ketohydroperoxides and HO_2. This simplification enables less ambiguous experimental constraints for the specific RO_2 H-shift rate coefficients.
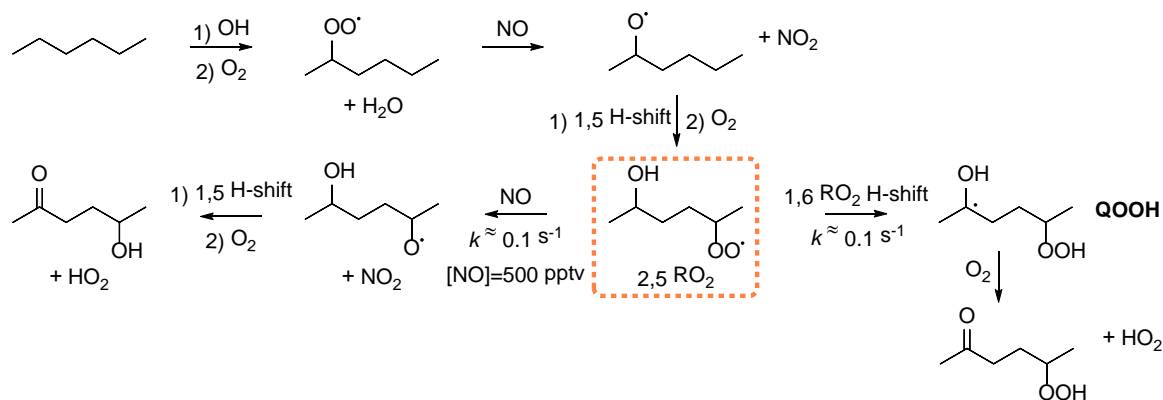
Scheme 1. The mechanism to produce the 2,5 RO_2 (orange box) from n-hexane in the atmosphere is shown. This RO_2 reacts with NO to produce a hydroxy ketone ($RONO_2$ – as shown in Scheme 3, are also produced in a minor channel). Competing with this chemistry

is a unimolecular 1,6 RO_2 H-shift (autoxidation), which produces a ketohydroperoxide and HO_2, after further reaction with O_2. The first order rate constants are provided at 300 K and one atmosphere of pressure.
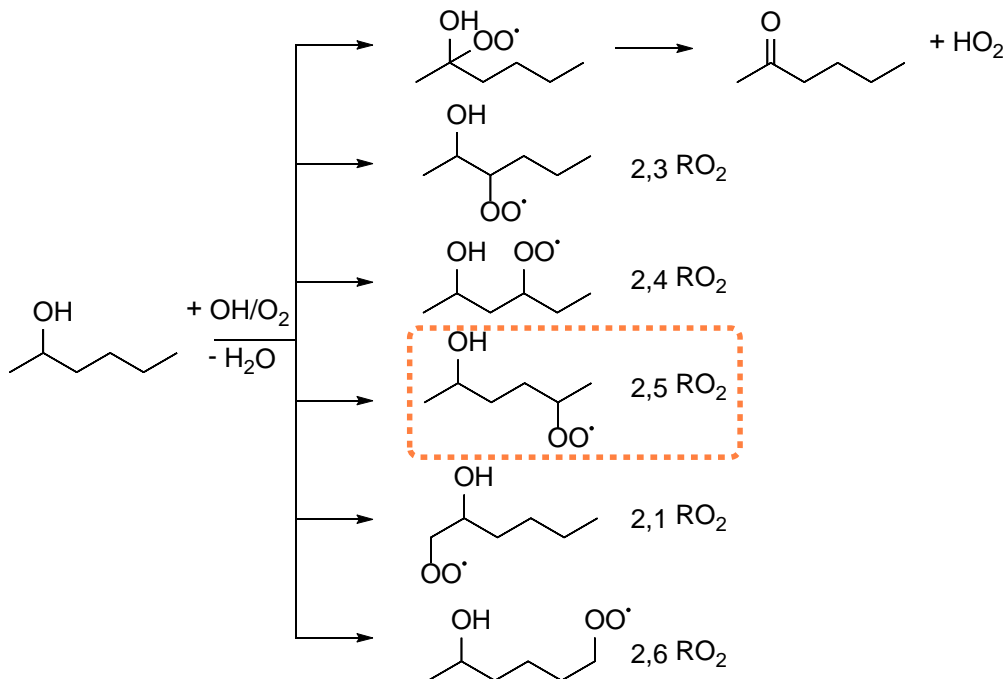
Scheme 2. We oxidize 2-hexanol with OH in air to produce a suite of RO_2 radicals including the 2,5 RO_2 (orange box) shown in Scheme 1.

Results and Discussion

Computational approach. We calculate the rate constants of the H-shift reactions using Multi-Conformer Transition State Theory (MC-TST) (52-55). The MC-TST expression for a rate constant is given by:

$$k_{MC-TST} = \kappa \frac{k_B T}{h} \frac{\sum_i^{all\ TS\ conf.} \exp\left(\frac{-\Delta E_i}{k_B T}\right) Q_{TS,i}}{\sum_j^{all\ R\ conf.} \exp\left(\frac{-\Delta E_j}{k_B T}\right) Q_{R,j}} \exp\left(-\frac{E_{TS,0} - E_{R,0}}{k_B T}\right)$$

where k_B is the Boltzmann constant, h is planck's constant, T is the temperature, $Q_{TS,i}$ is the partition function for the i'th transition state (TS) conformer, and ΔE_i is the difference in zero-point corrected energy between the i'th TS conformer and the lowest energy TS conformer.

$E_{TS,0}$ is the zero-point corrected energy of the lowest energy TS conformer. The analogous symbols apply for the reactant conformers. κ is the tunneling correction factor. Here, we use the 1D Eckart tunneling approximation which takes the forward and reverse barrier height and the imaginary frequency of the TS as input (56). The partition functions, energies, barrier heights, and imaginary frequencies needed to calculate k_{MC-TST} are obtained following the approach described by Møller et al. (55). Briefly, ωB97X-D/aug-cc-pVTZ was used for the geometries, frequencies, partition functions, zero-point energy corrections, and relative energies between unique conformers located by a systematic conformer search using molecular mechanics methods (57-59). CCSD(T)-F12a/VDZ-F12 single point energy calculations were performed for more accurate electronic energies in the barrier heights (60-64). See the SI for a detailed description.
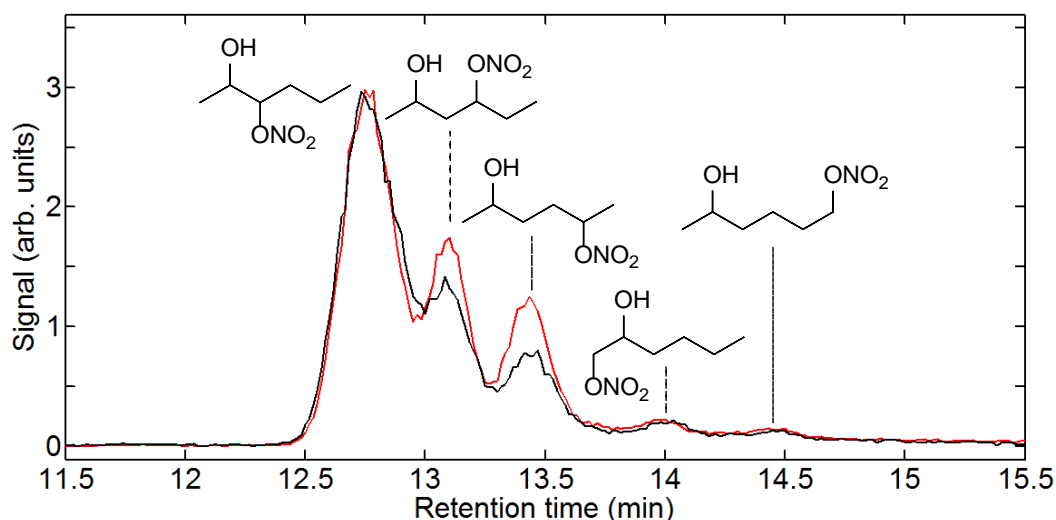
Figure 1. A chromatogram of five first generation organonitrate ($RONO_2$) isomers formed in the OH oxidation of 2-hexanol. We measure the isomer distribution relative to the 2,3 isomer at different bimolecular lifetimes ($\tau_{bimolecular}$). Loss of the 2,4 and 2,5 $RONO_2$ is evident in the experiment at $\tau_{bimolecular} \approx 4$ s (black) compared to the experiment at $\tau_{bimolecular} < 0.03$ s (red). Details on structural assignment can be found in the SI.
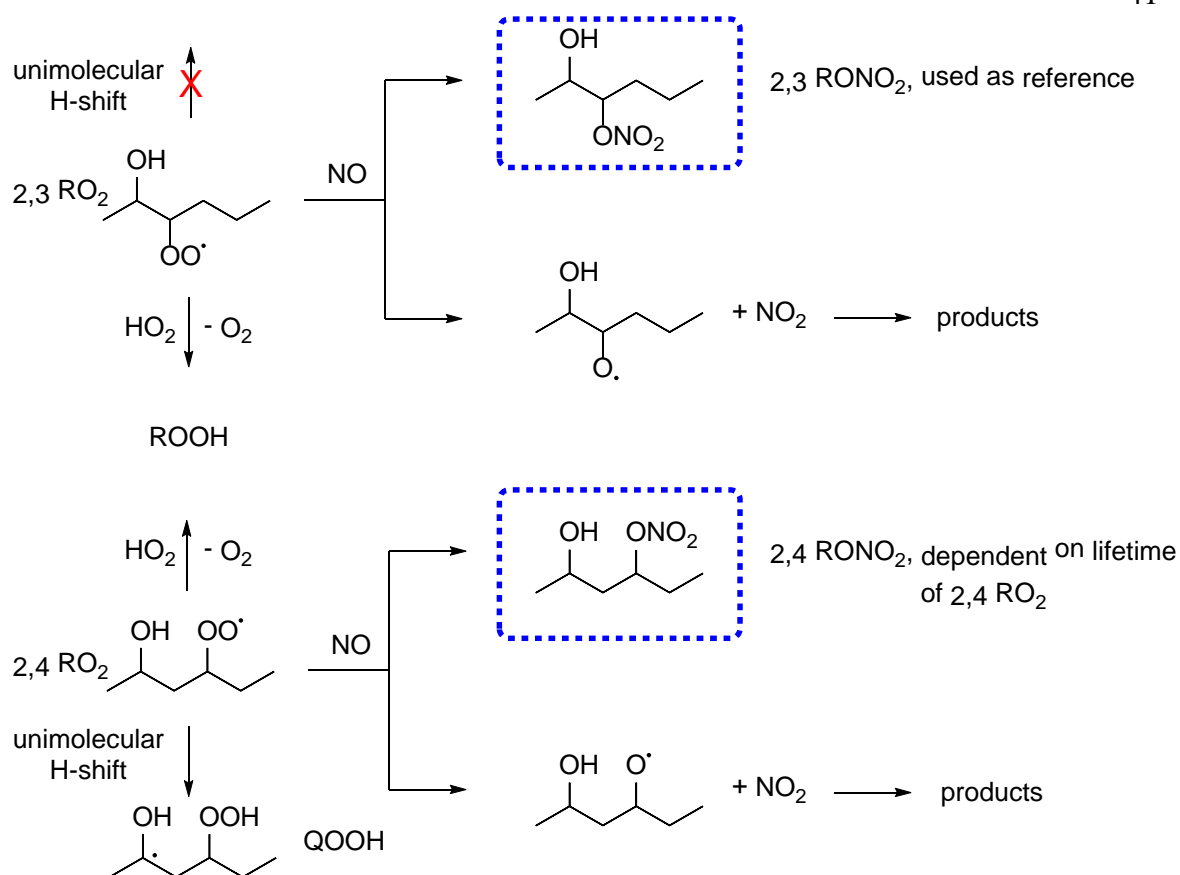
Scheme 3. Peroxy radicals produced in the reaction of OH with 2-hexanol produce organonitrates (RONO$_2$, blue boxes) after reaction with NO, in a branching ratio measured here to be ~25% at 296 K. Reaction with HO$_2$ produces hydroperoxides (ROOH). In competition with bimolecular chemistry, the 2,4 RO$_2$ undergoes a unimolecular H-shift to produce QOOH. By measuring the changing yield of the 2,4 and 2,5 RONO$_2$ isomers relative to that of the 2,3 RONO$_2$, an isomer that isomerizes negligibly under the conditions of these experiments, we experimentally constrain the H-shift rate constant. The chemistry of the 2,5 RO$_2$ radical (not shown) parallels that of the 2,4 isomer.

Experimental approach. The RO$_2$ studied in this work were prepared via oxidation of 2-hexanol by OH (Scheme 2) in a ~1 m^3 environmental chamber made of Teflon. To determine the rate constants of the H-shifts, we studied the competition between bimolecular and unimolecular chemistry in a suite of experiments with differing concentrations of NO (and HO$_2$), thereby producing a range of RO$_2$ bimolecular lifetimes ($\tau_{bimolecular}$):

$$\tau_{\text{bimolecular}} = \frac{1}{k_{RO_2+NO}[NO] + k_{RO_2+HO_2}[HO_2]}$$

Determination of the concentrations of NO and HO_2 in our experiments is described in the SI. The rate constants (k_{RO2+NO} and $k_{RO2+HO2}$) are taken from the literature (65) and described further in the SI. We assume the ratio of the rate constants ($\frac{k_{RO_2+NO}}{k_{RO_2+HO_2}}$) is isomer independent. We use measurements of the organonitrates ($RONO_2$), produced as minor products in the $RO_2 + NO$ channel, to probe the bimolecular chemistry. Following oxidation, the $RONO_2$ isomers were separated by gas chromatography and detected with chemical ionization mass spectrometry (GC-CIMS) using CF_3O^- ($m/z = 85$) as a reagent ion (Figure 1). GC-CIMS has been documented extensively (14, 15, 24, 66-69). A deconvolution algorithm described in the SI was required to analyze the chromatograms as it was not possible to increase the column length to fully separate the $RONO_2$ isomers without suffering significant isomer-specific transmission losses. Quantification became more difficult (with resulting higher uncertainty) for experiments at elevated temperature and/or long bimolecular lifetimes due to the higher water vapor concentration (~300 ppmv) that results from diffusion of water through the Teflon chamber walls.

The H-shifts from the 2,3 RO_2 are calculated to be much slower than bimolecular chemistry for all experiments reported here (see Table 1 and Table S5). We therefore assume that $\tau_{2,3\ RO_2} = \tau_{\text{bimolecular}}$. For the 2,4 and 2,5 RO_2 isomers, however, we find that the amount of time available to react with NO is shortened by unimolecular chemistry:

$$\tau_{RO_2} = \frac{1}{k_{RO_2+NO}[NO] + k_{RO_2+HO_2}[HO_2] + k_{\text{unimolecular}}}$$

As a result, the yields of the 2,4 and 2,5 $RONO_2$ relative to that of the 2,3 $RONO_2$ serve as a sensitive probe of unimolecular chemistry. A depiction of the method is shown in Scheme 3.
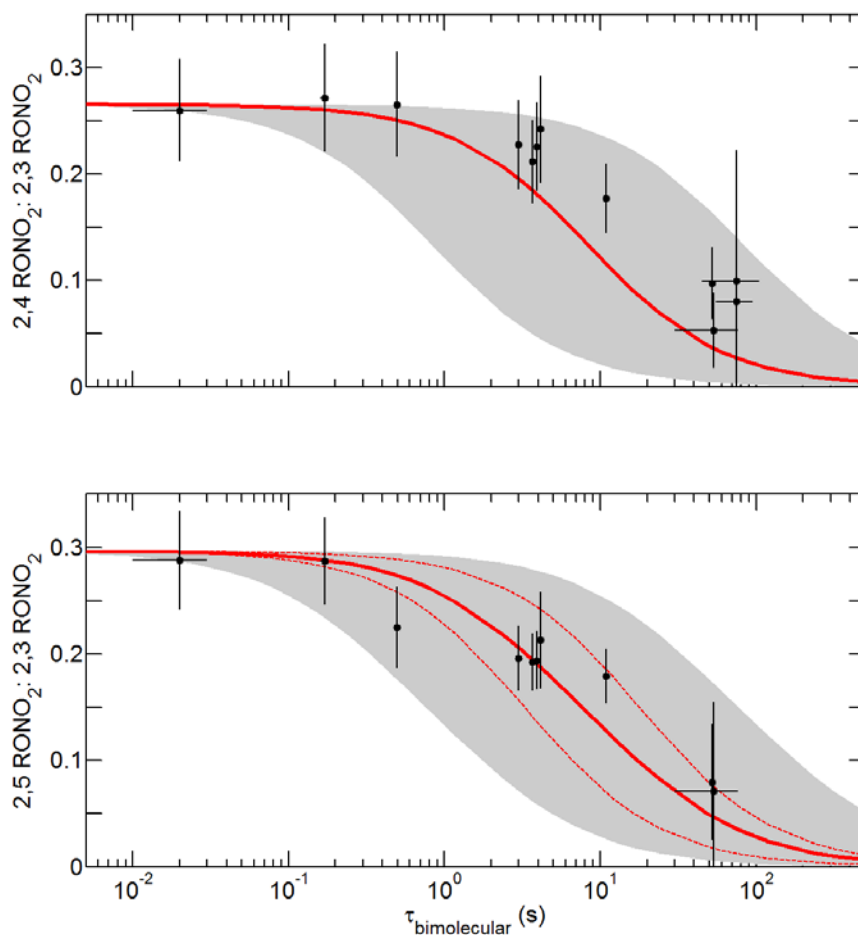
Figure 2. Comparison of experimental (black dots) and computational (red lines) results at 296 K for the 1,5 H-shift (top) and 1,6 H-shift (bottom). We demonstrate the difference in calculated 2,5 RO_2 H-shift rate coefficients between S,R and S,S diastereomers with the two dashed red lines that, when combined assuming an initial racemic mixture, produce the solid red line. The gray shaded region represents the range of uncertainty in the calculated rates.

H-shift Rate Coefficients. As shown in Figure 2, the observed ratio of the 2,4 and 2,5 $RONO_2$ to the 2,3 $RONO_2$ decreases as bimolecular lifetimes extend beyond 1 s. The equivalence point in the ratio of the 2,4 and 2,5 $RONO_2$ relative to the 2,3 $RONO_2$ observed at $\tau_{bimolecular} \approx 10$ s is consistent with unimolecular chemistry occurring at a rate of approximately 0.1 s^{-1}.

Consistent with a large energetic barrier encountered along the H-shift reaction coordinate, the falloff occurs at a shorter bimolecular lifetime at elevated temperature (see SI and Table 1) (70). Providing further evidence for our assignment of the mechanism, the falloff occurs at a bimolecular lifetime more than 20 times greater when deuterium is substituted α to the OH group (HOC-**D**; see SI). This is consistent with the expected primary kinetic isotope effect for RO_2 H-shifts (25, 51, 71).
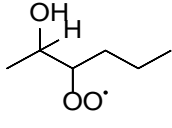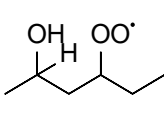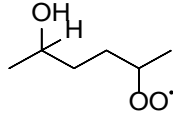
In Figure 2, comparisons are shown between the measurements and a model using the calculated rate coefficients for the H-shift reactions (Table 1). The 1,4 H-shift from the 2,3 isomer is calculated to be very slow ($<10^{-4}$ s^{-1} at T=296 K) and, as discussed in the SI, a 1,5 H-shift from this isomer was considered but is also expected to be slow. In contrast, the calculated rate coefficients of the 1,5 and 1,6 H-shifts from the 2,4 and 2,5 RO_2 are orders of magnitude faster. Surprisingly, the calculated H-shift rate coefficients of the S,S and S,R isomers of the 2,5 RO_2 differ significantly. As seen in Figure 3, the origin of this difference is a change in the hydrogen bond-like interaction between the hydroxy group and the carbon-bonded oxygen atom of the peroxy radical moiety between the reactant and the transition state (TS) in the S,R diastereomer. This produces a ~1 kcal/mol difference in barrier height and enhances the rate constant of the S,R diastereomer by a factor of ~5. Illustrating the difficulty in generalizing such behavior, however, opposing effects related to the barrier height, partition functions, and tunneling result in similar calculated rate coefficients for the 1,5 H-shift from S,R and S,S isomers of the 2,4 RO_2 (see SI).

In the model used in Figure 2 (solid red line), we assume that a racemic mixture is produced when O_2 adds to the alkyl radical and that the rate coefficients of RO_2 H-shifts for enantiomeric pairs are identical (Table 1). Simulations where the peroxy radicals are either entirely (R,R; S,S) or (R,S; S,R) are shown as dashed lines.

The experimental factors in Table 1 are the multiplicative scaling of the calculated rate constants required to best fit the experimental data (see SI, Figure S10-S10). For instance, a factor of 1.0 would indicate that a best fit was achieved without scaling the calculated rate constants. The best fit to the experimental data at 296 K require scaling of the calculated values by less than a factor of 3 for both the 1,5 and 1,6 H-shifts, well-within the combined uncertainties. The reasonable agreement between the experimental and computational results

for these H-shifts suggests that the computational approach used here, and described fully by Møller et al. (55), provides an efficient method applicable to a much broader range of substrates than can plausibly be investigated in the laboratory.

Table 1. H-shift rate coefficients (s^{-1}) and factors derived from theory and experiment.

			2,3 RO$_2$	2,4 RO$_2$	2,5 RO$_2$
	Reactant				
296 K	Theory [a]	S,R	5.4×10^{-5}	0.13	0.30
		S,S	1.3×10^{-5}	0.11	0.055
	Expt. (factor) [b]		-	0.4 +0.3/-0.2	0.8 +0.4/-0.3
318 K	Theory [a]	S,R	3.4×10^{-4}	0.64	1.3
		S,S	9.1×10^{-5}	0.58	0.27
	Expt. (factor) [b,c]		-	0.5 +0.3/-0.1	0.7 ± 0.2

[a] For the temperature dependent rate expressions, refer to the SI. Uncertainty in the calculated rates is estimated to be less than a factor of 10.

[b] Reported values correspond to scaling factors that afforded the best fit to the experimental data, assuming a fixed ratio between the calculated diastereomer rate constants and an initial racemic mixture of isomers. Uncertainty is estimated as described in the SI. The experiments are unable to differentiate the S,R and S,S isomers.

[c] Data for 318 K are available in the SI.
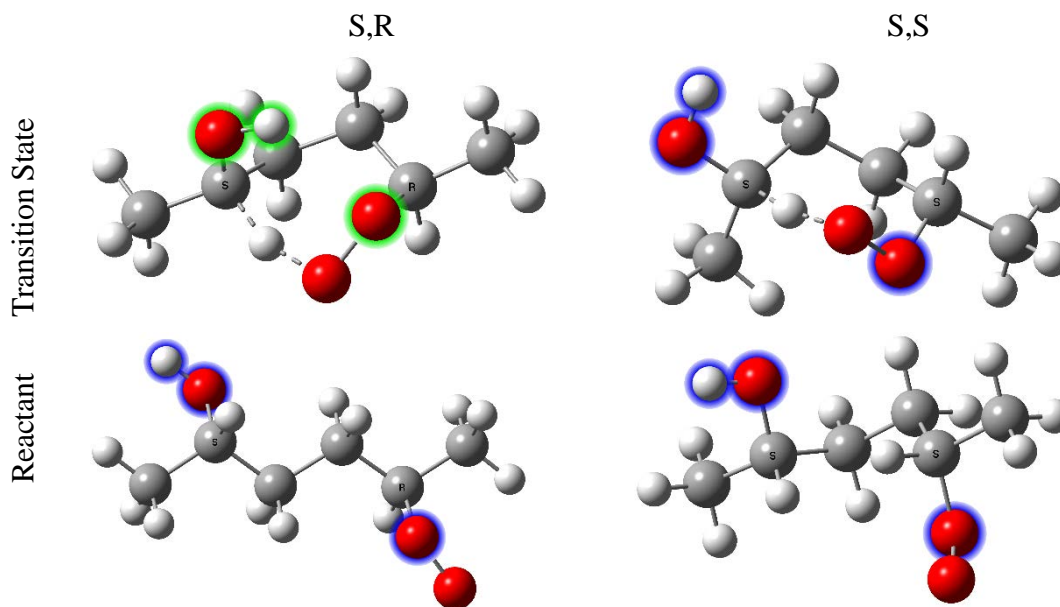
Figure 3. ωB97X-D/aug-cc-pVTZ optimized structures of the lowest energy conformers of the reactant and transition state. The S,R diastereomer of the 2,5 RO_2 exhibits a hydrogen bond-like interaction which stabilizes the TS. Consequently, the H-shift rate of this isomer is enhanced by a factor of ~5. Green halos indicate atoms involved in the hydrogen bond-like interaction. Blue halos are used when no such interaction exists.

Autoxidation products. We observe a CIMS signal at *m/z* 217 (a cluster of CF_3O^- with a compound of molecular weight 132 amu), corresponding to the mass of expected products, ketohydroperoxides. We assign this signal to the two RO_2 α-OH H-shift reactions shown in Scheme 4. Consistent with an autoxidation mechanism, the absolute yield of *m/z* 217 ($\frac{\Delta m/z\ 217}{\Delta 2-\text{hexanol}}$) at similar bimolecular lifetimes increases with temperature.

An additional signal at *m/z* 233 (*m/z* 234 with D-substitution) was observed, consistent with formation of a hydroxy ketohydroperoxide that arises from the 2,5 RO_2 through successive isomerizations as indicated in Scheme 4. The formation of this compound was enhanced by deuterium substitution at the α-OH center, which slows the 1,6 H-shift channel. The signal is much smaller in the non-deuterated experiments as the 1,6 H-shift outruns this chemistry. See the Supporting Information (SI) for further details.

Similar ketohydroperoxides were previously detected in the low NO oxidation of C_{12} alkanes (72-74). Although autoxidation was not discussed, second generation alkoxy radicals form hydroxyperoxy radicals that almost certainly undergo H-shifts at rates comparable to those reported here. The ketohydroperoxides were observed to partition to the particle phase with simultaneous conversion to peroxyhemiacetals. Additionally, a cyclization pathway from γ-ketohydroperoxides to form endoperoxides was suggested, and is similar to a pathway discussed in the SI and observed elsewhere (9, 75).
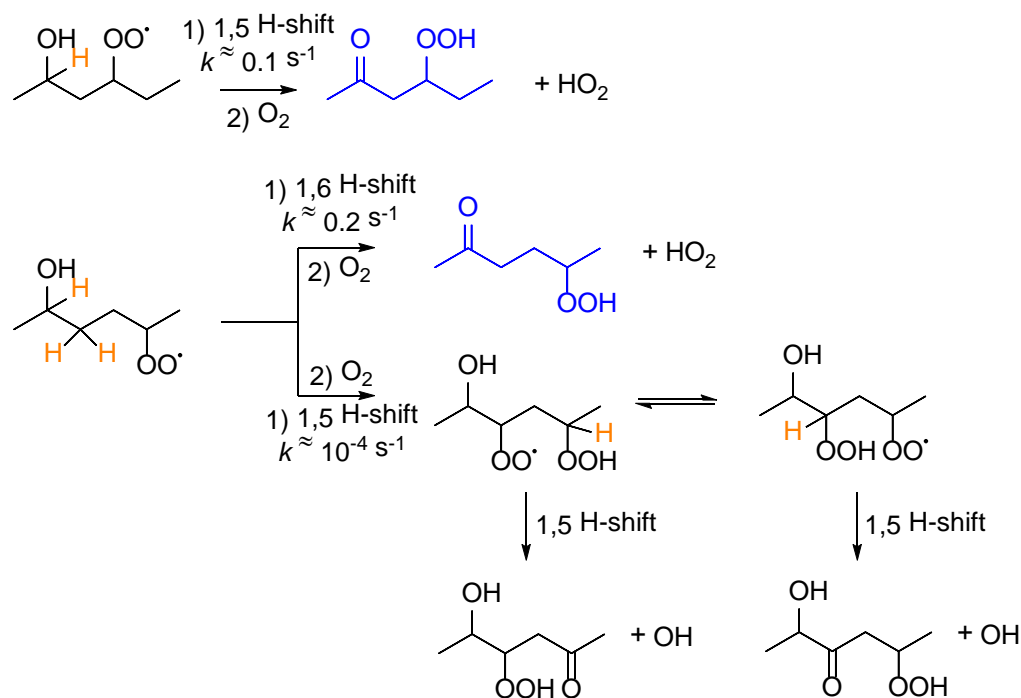
Scheme 4. Formation mechanism of ketohydroperoxides (blue highlighted). Hydrogen atoms involved in the H-shifts are orange highlighted. Also shown is the route to hydroxy ketohydroperoxides, suspected products of a 1,5 H-shift from the 2,5 RO_2. Approximate calculated rate coefficients are provided where available at 296 K.

Atmospheric Implications

In the atmosphere, the bimolecular lifetimes of peroxy radicals typically range from 1s to more than 100s. The lowest radical abundances (and therefore long bimolecular RO_2 lifetimes) are characteristic of attenuated UV environments (e.g., at night or in shaded

regions below thick cloud or tree canopies), or regions remote from anthropogenic NO_x emissions. Due to emission reductions from power generation and transportation, however, NO_x levels are declining rapidly across North America, reaching levels unprecedented in the past several decades (76, 77). The 2013 SENEX and SEAC4RS aircraft campaigns, for example, sampled large swaths of the Southeastern U.S. including areas significantly influenced by urban emissions. NO mixing ratios were often < 100 pptv and nearly always < 1 ppbv (78, 79). Even more impressive, NO_x levels in Pasadena, CA declined by more than a factor of two between 2010 and 2017 (80). In August 2017, we measured [NO] below 500 pptv on several weekend afternoons, corresponding to RO_2 lifetimes longer than 10 s. With afternoon temperatures typically exceeding 305 K, the autoxidation chemistry described here is now competing with reactions between peroxy radicals and NO in the middle of one of North America's most polluted cities.

While the rate of autoxidation is highly dependent on the substrate, this chemistry is undoubtedly important for many of the organic compounds emitted into the urban atmosphere. A recent review of vehicle emissions and urban aerosol formation speculated that autoxidation might play a role in the degradation of certain unsaturated compounds (81), but its role in alkane oxidation was not appreciated. Alkanes constitute a substantial fraction of urban non-methane hydrocarbon emissions (82-86), and n-alkanes with greater than five carbons are known emissions from gasoline and diesel powered vehicles arising from both incomplete combustion and fuel evaporation (87, 88). These compounds will undergo oxidation pathways that are nearly identical to those reported here for n-hexane.

The importance of organic hydroperoxide formation via autoxidation will depend on the fate and toxicity of these compounds. Peroxides are reactive oxygen species that are known to produce oxidative stress in plants and animals (89-91). Additionally, the rate of oxidant (e.g., ozone) and aerosol formation is almost certainly sensitive to autoxidation. Because autoxidation leads to the degradation of volatile organic compounds without converting NO to NO_2, ozone formation will be slower when this chemistry is important. While the impact on aerosol formation is less clear, it is likely to be enhanced because autoxidation adds oxygen with minimal fragmentation. For example, Zhao and coworkers recently showed that while NO_x emissions are lower with the latest vehicle emissions control technology, the

organic aerosol yield is greater than from the emissions using older generation technology (92). Although the authors do not provide a mechanistic explanation, the higher yields are likely attributable, in part, to hydroperoxide formation via an autoxidation mechanism.

As a result of highly successful policies to reduce emissions of NO_x, our results suggest that autoxidation is now becoming an important pathway for urban photochemistry across North America. Yet the photochemical models that have been used to inform these policies have little if any validation in the low NO regimes we are now experiencing. Thus, there is a risk that attainment of ozone compliance may occur at the expense of other air quality goals because of more efficient hydroperoxide and aerosol formation. It is thus imperative that our understanding of the low NO chemistry for the suite of organic compounds typically found in the atmosphere advance quickly and that monitoring efforts to quantify low NO processes, such as autoxidation, be undertaken with haste.

Methods. The experimental apparatus, including the GC-CIMS technique, has been previously described and is outlined in the SI for these experiments (14, 15, 66-69). Experiments are performed in a ~1 m^3 Teflon environmental chamber. In nearly all experiments, the precursor used was 2-hexanol, while CH_3ONO was used as a photolytic source of HO_2 and NO (and thus OH). NO was added prior to oxidation for experiments focusing on short RO_2 lifetimes and was quantified using a Teledyne 200EU chemilluminesence NO_x analyzer. For experiments without additional NO added, we use established methods to estimate its abundance (and that of HO_2) as detailed in the SI. We attempted to replicate near room temperature the method Jorand et al. (5) used to determine the autoxidation rate but, for reasons described in the SI, these experiments were not successful.

Experimental uncertainty. Considerable (>50%) experimental uncertainty arises in our estimate of $\tau_{\text{bimolecular}}$ for $\tau > 10$ s, due to imprecision in the interpretation of chromatographic peaks, and temperature fluctuations in our chamber. Details are provided in the SI.

Computational uncertainty. We estimate the uncertainty of the calculated rate constants to be less than a factor of 10. The uncertainties arise primarily from the barrier height, tunneling

correction, and the partition functions. Due to error cancelation, the ratio of the theoretical rate constants for these different H-shifts are likely more accurate than the absolute rate coefficients. This is especially true for reactions of the same or very similar molecules. See the SI for details.

References

1.Seinfeld JH & Pandis SN (1998) *Atmospheric chemistry and physics: from air pollution to climate change* (Wiley, New York).

2.Zádor J, Taatjes CA, & Fernandes RX (2011) Kinetics of elementary reactions in low-temperature autoignition chemistry. *Prog. Energy Combust. Sci.* 37(4):371-421.

3.Taatjes CA (2006) Uncovering the Fundamental Chemistry of Alkyl + O2 Reactions via Measurements of Product Formation. *J. Phys. Chem. A* 110(13):4299-4312.

4.Savee JD*, et al.* (2015) Direct observation and kinetics of a hydroperoxyalkyl radical (QOOH). *Science* 347(6222):643-646.

5.Jorand F*, et al.* (2003) Isomeric hexyl-ketohydroperoxides formed by reactions of hexoxy and hexylperoxy radicals in oxygen. *Int. J. Chem. Kinet.* 35(8):354-366.

6.Perrin O, Heiss A, Doumenc F, & Sahetchian K (1998) Homogeneous and heterogeneous reactions of the n-$C_5H_{11}O$, n-$C_5H_{10}OH$ and $OOC_5H_{10}OH$ radicals in oxygen. Analytical steady state solution by use of the Laplace transform. *J. Chem. Soc. Faraday Trans.* 94(16):2323-2335.

7.Blin-Simiand N*, et al.* (2001) Hydroperoxides with zero, one, two or more carbonyl groups formed during the oxidation of n-dodecane. *Combust. Flame* 126(1-2):1524-1532.

8.Heiss A & Sahetchian K (1996) Isomerization reactions of the n-C_4H_9O and n-OOC_4H_8OH radicals in oxygen. *Int. J. Chem. Kinet.* 28(7):531-544.

9.Perrin O, Heiss A, Sahetchian K, Kerhoas L, & Einhorn J (1998) Determination of the isomerization rate constant $HOCH_2CH_2CH_2CH(OO\cdot)CH_3$ →$HOC\cdot HCH_2CH_2CH(OOH)CH_3$. Importance of intramolecular hydroperoxy isomerization in tropospheric chemistry. *Int. J. Chem. Kinet.* 30(12):875-887.

10.Peeters J, Nguyen TL, & Vereecken L (2009) HO_x radical regeneration in the oxidation of isoprene. *Phys. Chem. Chem. Phys.* 11(28):5935-5939.

11.Asatryan R, da Silva G, & Bozzelli JW (2010) Quantum chemical study of the acrolein (CH_2CHCHO) + OH + O_2 reactions. *J. Phys. Chem. A* 114(32):8302-8311.

12.Crounse JD, Paulot F, Kjaergaard HG, & Wennberg PO (2011) Peroxy radical isomerization in the oxidation of isoprene. *Phys. Chem. Chem. Phys.* 13(30):13607-13613.

13.Vereecken L & Francisco JS (2012) Theoretical studies of atmospheric reaction mechanisms in the troposphere. *Chem. Soc. Rev.* 41(19):6259-6293.

14.Crounse JD*, et al.* (2012) Atmospheric fate of methacrolein. 1. Peroxy radical isomerization following addition of OH and O_2. *J. Phys. Chem. A* 116(24):5756-5762.

15. Crounse JD, Nielsen LB, Jørgensen S, Kjaergaard HG, & Wennberg PO (2013) Autoxidation of organic compounds in the atmosphere. *J. Phys. Chem. Lett.* 4(20):3513-3520.

16. Knap HC, Jørgensen S, & Kjaergaard HG (2015) Theoretical investigation of the hydrogen shift reactions in peroxy radicals derived from the atmospheric decomposition of 3-methyl-3-buten-1-ol (MBO331). *Chem. Phys. Lett.* 619:236-240.

17. Jokinen T, *et al.* (2014) Rapid autoxidation forms highly oxidized RO_2 radicals in the atmosphere. *Angew. Chem. Int. Ed.* 53(52):14596-14600.

18. Kurtén T, *et al.* (2015) Computational study of hydrogen shifts and ring-opening mechanisms in α-Pinene ozonolysis products. *J. Phys. Chem. A* 119(46):11366-11375.

19. Hyttinen N, *et al.* (2016) Unimolecular HO_2 loss from peroxy radicals formed in autoxidation is unlikely under atmospheric conditions. *J. Phys. Chem. A* 120(20):3588-3595.

20. Jørgensen S, *et al.* (2016) Rapid hydrogen shift scrambling in hydroperoxy-substituted organic peroxy radicals. *J. Phys. Chem. A* 120(2):266-275.

21. Richters S, Herrmann H, & Berndt T (2016) Highly oxidized RO_2 radicals and consecutive products from the ozonolysis of three sesquiterpenes. *Environ. Sci. Technol.* 50(5):2354-2362.

22. Knap HC & Jørgensen S (2017) Rapid hydrogen shift reactions in acyl peroxy radicals. *J. Phys. Chem. A* 121(7):1470-1479.

23. Wang S, Wu R, Berndt T, Ehn M, & Wang L (2017) Formation of highly oxidized radicals and multifunctional products from the atmospheric oxidation of alkylbenzenes. *Environ. Sci. Technol.* 51(15):8442-8449.

24. Teng AP, Crounse JD, & Wennberg PO (2017) Isoprene peroxy radical dynamics. *J. Am. Chem. Soc.* 139(15):5367-5377.

25. Ehn M, *et al.* (2014) A large source of low-volatility secondary organic aerosol. *Nature* 506(7489):476-479.

26. Zhang X, *et al.* (2015) Formation and evolution of molecular products in α-pinene secondary organic aerosol. *Proc. Natl. Acad. Sci. U.S.A.* 112(46):14168-14173.

27. Berndt T, *et al.* (2016) Hydroxyl radical-induced formation of highly oxidized organic compounds. *Nat. Commun.* 7:13677.

28. Jokinen T, *et al.* (2015) Production of extremely low volatile organic compounds from biogenic emissions: Measured yields and atmospheric implications. *Proc. Natl. Acad. Sci. U.S.A.* 112(23):7123-7128.

29. Mentel TF, *et al.* (2015) Formation of highly oxidized multifunctional compounds: autoxidation of peroxy radicals formed in the ozonolysis of alkenes – deduced from structure–product relationships. *Atmos. Chem. Phys.* 15(12):6745-6765.

30. Zhang X, *et al.* (2017) Highly oxygenated multifunctional compounds in α-Pinene secondary organic aerosol. *Environ. Sci. Technol.* 51(11):5932-5940.

31. Mutzel A, *et al.* (2015) Highly oxidized multifunctional organic compounds observed in tropospheric particles: A field and laboratory study. *Environ. Sci. Technol.* 49(13):7754-7761.

32. Kirkby J, *et al.* (2016) Ion-induced nucleation of pure biogenic particles. *Nature* 533(7604):521-526.

33.Schobesberger S, *et al.* (2013) Molecular understanding of atmospheric particle formation from sulfuric acid and large oxidized organic molecules. *Proc. Natl. Acad. Sci. U.S.A.* 110(43):17223-17228.

34.Riccobono F, *et al.* (2014) Oxidation products of biogenic emissions contribute to nucleation of atmospheric particles. *Science* 344(6185):717-721.

35.Zhao J, Ortega J, Chen M, McMurry PH, & Smith JN (2013) Dependence of particle nucleation and growth on high-molecular-weight gas-phase products during ozonolysis of α-pinene. *Atmos. Chem. Phys.* 13(15):7631-7644.

36.Bianchi F, *et al.* (2016) New particle formation in the free troposphere: A question of chemistry and timing. *Science* 352(6289):1109-1112.

37.Kulmala M, *et al.* (2013) Direct observations of atmospheric aerosol nucleation. *Science* 339(6122):943-946.

38.Jimenez JL, *et al.* (2009) Evolution of organic aerosols in the atmosphere. *Science* 326(5959):1525-1529.

39.Shrivastava M, *et al.* (2017) Recent advances in understanding secondary organic aerosol: Implications for global climate forcing. *Rev. Geophys.* 55(2):509-559.

40.Kroll JH & Seinfeld JH (2008) Chemistry of secondary organic aerosol: Formation and evolution of low-volatility organics in the atmosphere. *Atmos. Environ.* 42(16):3593-3624.

41.Chacon-Madrid HJ & Donahue NM (2011) Fragmentation vs. functionalization: chemical aging and organic aerosol formation. *Atmos. Chem. Phys.* 11(20):10553-10563.

42.Donahue NM, *et al.* (2013) How do organic vapors contribute to new-particle formation? *Faraday Discuss.* 165(0):91-104.

43.Huang R-J, *et al.* (2014) High secondary aerosol contribution to particulate pollution during haze events in China. *Nature* 514(7521):218-222.

44.Ng NL, *et al.* (2010) Organic aerosol components observed in northern hemispheric datasets from aerosol mass spectrometry. *Atmos. Chem. Phys.* 10(10):4625-4641.

45.Donahue NM, *et al.* (2012) Aging of biogenic secondary organic aerosol via gas-phase OH radical reactions. *Proc. Natl. Acad. Sci. U.S.A.* 109(34):13503-13508.

46.Monge ME, *et al.* (2012) Alternative pathway for atmospheric particles growth. *Proc. Natl. Acad. Sci. U.S.A.* 109(18):6840-6844.

47.Barsanti KC, Kroll JH, & Thornton JA (2017) Formation of low-volatility organic compounds in the atmosphere: Recent advancements and insights. *J. Phys. Chem. Lett.* 8(7):1503-1511.

48.Daumit KE, Kessler SH, & Kroll JH (2013) Average chemical properties and potential formation pathways of highly oxidized organic aerosol. *Faraday Discuss.* 165:181-202.

49.Elm J, Myllys N, & Kurtén T (2017) What is required for highly oxidized molecules to form clusters with sulfuric acid? *J. Phys. Chem. A* 121(23):4578-4587.

50.Rissanen MP, *et al.* (2015) Effects of chemical complexity on the autoxidation mechanisms of endocyclic alkene ozonolysis products: From methylcyclohexenes toward understanding α-Pinene. *J. Phys. Chem. A* 119(19):4633-4650.

51.Rissanen MP, *et al.* (2014) The formation of highly oxidized multifunctional products in the ozonolysis of cyclohexene. *J. Am. Chem. Soc.* 136(44):15596-15606.

52.Eyring H (1935) The activated complex and the absolute rate of chemical reactions. *Chem. Rev.* 17(1):65-77.

53.Evans MG & Polanyi M (1935) Some applications of the transition state method to the calculation of reaction velocities, especially in solution. *J. Chem. Soc. Faraday Trans.* 31(0):875-894.

54.Vereecken L & Peeters J (2003) The 1,5-H-shift in 1-butoxy: A case study in the rigorous implementation of transition state theory for a multirotamer system. *J. Chem. Phys.* 119(10):5159-5170.

55.Møller KH, Otkjær RV, Hyttinen N, Kurtén T, & Kjaergaard HG (2016) Cost-effective implementation of multiconformer transition state theory for peroxy radical hydrogen shift reactions. *J. Phys. Chem. A* 120(51):10072-10087.

56.Eckart C (1930) The penetration of a potential barrier by electrons. *Phys. Rev.* 35(11):1303-1309.

57.Chai J-D & Head-Gordon M (2008) Long-range corrected hybrid density functionals with damped atom-atom dispersion corrections. *Phys. Chem. Chem. Phys.* 10(44):6615-6620.

58.Dunning TH (1989) Gaussian basis sets for use in correlated molecular calculations. I. The atoms boron through neon and hydrogen. *J. Chem. Phys.* 90(2):1007-1023.

59.Kendall RA, Dunning TH, & Harrison RJ (1992) Electron affinities of the first-row atoms revisited. Systematic basis sets and wave functions. *J. Chem. Phys.* 96(9):6796-6806.

60.Watts JD, Gauss J, & Bartlett RJ (1993) Coupled-cluster methods with noniterative triple excitations for restricted open-shell Hartree–Fock and other general single determinant reference functions. Energies and analytical gradients. *J. Chem. Phys.* 98(11):8718-8733.

61.Adler TB, Knizia G, & Werner H-J (2007) A simple and efficient CCSD(T)-F12 approximation. *J. Chem. Phys.* 127(22):221106.

62.Knizia G, Adler TB, & Werner H-J (2009) Simplified CCSD(T)-F12 methods: Theory and benchmarks. *J. Chem. Phys.* 130(5):054104.

63.Werner H-J, Knizia G, & Manby FR (2011) Explicitly correlated coupled cluster methods with pair-specific geminals. *Mol. Phys.* 109(3):407-417.

64.Peterson KA, Adler TB, & Werner H-J (2008) Systematically convergent basis sets for explicitly correlated wavefunctions: The atoms H, He, B–Ne, and Al–Ar. *J. Chem. Phys.* 128(8):084102.

65.Saunders SM, Jenkin ME, Derwent RG, & Pilling MJ (2003) Protocol for the development of the Master Chemical Mechanism, MCM v3 (Part A): tropospheric degradation of non-aromatic volatile organic compounds. *Atmos. Chem. Phys.* 3:161-180.

66.St. Clair JM, *et al.* (2016) Kinetics and products of the reaction of the first-generation isoprene hydroxy hydroperoxide (ISOPOOH) with OH. *J. Phys. Chem. A* 120(9):1441-1451.

67.Bates KH, *et al.* (2014) Gas phase production and loss of isoprene epoxydiols. *J. Phys. Chem. A* 118(7):1237-1246.

68.Praske E, *et al.* (2015) Atmospheric fate of methyl vinyl ketone: Peroxy radical reactions with NO and HO$_2$. *J. Phys. Chem. A* 119(19):4562-4572.

69.Crounse JD, McKinney KA, Kwan AJ, & Wennberg PO (2006) Measurement of gas-phase hydroperoxides by chemical ionization mass spectrometry. *Anal. Chem.* 78(19):6726-6732.

70.Orlando JJ & Tyndall GS (2012) Laboratory studies of organic peroxy radical chemistry: an overview with emphasis on recent issues of atmospheric significance. *Chem. Soc. Rev.* 41(19):6294-6317.

71. Muchalski H, Levonyak AJ, Xu L, Ingold KU, & Porter NA (2015) Competition H(D) kinetic isotope effects in the autoxidation of hydrocarbons. *J. Am. Chem. Soc.* 137(1):94-97.

72. Yee LD*, et al.* (2013) Effect of chemical structure on secondary organic aerosol formation from C_{12} alkanes. *Atmos. Chem. Phys.* 13(21):11121-11140.

73. Yee LD*, et al.* (2012) Secondary organic aerosol formation from low-NO_x photooxidation of dodecane: Evolution of multigeneration gas-phase chemistry and aerosol composition. *J. Phys. Chem. A* 116(24):6211-6230.

74. Shiraiwa M*, et al.* (2013) Size distribution dynamics reveal particle-phase chemistry in organic aerosol formation. *Proc. Natl. Acad. Sci. U.S.A.* 110(29):11746-11750.

75. Jalan A*, et al.* (2013) New pathways for formation of acids and carbonyl products in low-temperature oxidation: the korcek decomposition of γ-ketohydroperoxides. *J. Am. Chem. Soc.* 135(30):11100-11114.

76. US Environmental Protection Agency (2011) Benefits and costs of the clean air act 1990-2020, the second prospective study. Available at www.epa.gov/clean-air-act-overview/benefits-and-costs-clean-air-act-1990-2020-second-prospective-study. Accessed August 8, 2017

77. Russell AR, Valin LC, & Cohen RC (2012) Trends in OMI NO_2 observations over the United States: effects of emission control technology and the economic recession. *Atmos. Chem. Phys.* 12(24):12197-12209.

78. Wolfe GM*, et al.* (2016) Formaldehyde production from isoprene oxidation across NO_x regimes. *Atmos. Chem. Phys.* 16(4):2597-2610.

79. Yu K*, et al.* (2016) Sensitivity to grid resolution in the ability of a chemical transport model to simulate observed oxidant chemistry under high-isoprene conditions. *Atmos. Chem. Phys.* 16(7):4369-4378.

80. California Air Resources Board (2017) Air quality and meteorological information system. Available at https://www.arb.ca.gov/aqmis2/aqdselect.php. Accessed August 8, 2017

81. Gentner DR*, et al.* (2017) Review of urban secondary organic aerosol formation from gasoline and diesel motor vehicle emissions. *Environ. Sci. Technol.* 51(3):1074-1093.

82. Baker AK*, et al.* (2008) Measurements of nonmethane hydrocarbons in 28 United States cities. *Atmos. Environ.* 42(1):170-182.

83. Warneke C*, et al.* (2007) Determination of urban volatile organic compound emission ratios and comparison with an emissions database. *J. Geophys. Res. Atmos.* 112(D10).

84. Warneke C*, et al.* (2012) Multiyear trends in volatile organic compounds in Los Angeles, California: Five decades of decreasing emissions. *J. Geophys. Res. Atmos.* 117(D21).

85. von Schneidemesser E, Monks PS, & Plass-Duelmer C (2010) Global comparison of VOC and CO observations in urban areas. *Atmos. Environ.* 44(39):5053-5064.

86. Boynard A*, et al.* (2014) Spatial and seasonal variability of measured anthropogenic non-methane hydrocarbons in urban atmospheres: Implication on emission ratios. *Atmos. Environ.* 82:258-267.

87. Watson JG, Chow JC, & Fujita EM (2001) Review of volatile organic compound source apportionment by chemical mass balance. *Atmos. Environ.* 35(9):1567-1584.

88. Schauer JJ, Kleeman MJ, Cass GR, & Simoneit BRT (1999) Measurement of emissions from air pollution sources. 2. C1 through C30 organic compounds from medium duty diesel trucks. *Environ. Sci. Technol.* 33(10):1578-1587.

89. Gebicki JM (1997) Protein hydroperoxides as new reactive oxygen species. *Redox Report* 3(2):99-110.

90. Yin H, Xu L, & Porter NA (2011) Free radical lipid peroxidation: Mechanisms and analysis. *Chem. Rev.* 111(10):5944-5972.

91. Zielinski ZAM & Pratt DA (2017) Lipid peroxidation: Kinetics, mechanisms, and products. *J. Org. Chem.* 82(6):2817-2825.

92. Zhao Y*, et al.* (2017) Reducing secondary organic aerosol formation from gasoline vehicle exhaust. *Proc. Natl. Acad. Sci. U.S.A.* 114(27):6984-6989.

C h a p t e r   4

INTRAMOLECULAR HYDROGEN SHIFT CHEMISTRY OF HYDROPEROXY-SUBSTITUTED PEROXY RADICALS

Abstract

Gas-phase autoxidation – the sequential regeneration of peroxy radicals (RO_2) via intramolecular hydrogen shifts (H-shifts) followed by oxygen addition – leads to the formation of organic hydroperoxides. The atmospheric fate of these peroxides remains unclear, including the potential for further H-shift chemistry. Here, we report H-shift rate coefficients for a system of RO_2 with hydroperoxide functionality produced in the OH-initiated oxidation of 2-hydroperoxy-2-methylpentane. The initial RO_2 formed in this chemistry are unable to undergo α-OOH H-shift (HOOC-**H**) reactions. However, these RO_2 rapidly isomerize (> 100 s^{-1} at 296 K) by H-shift of the hydroperoxy hydrogen (ROO-**H**) to produce a hydroperoxy-substituted RO_2 with an accessible α-OOH hydrogen. First order rate coefficients for the 1,5 H-shift of the α-OOH hydrogen are measured to be ~0.04 s^{-1} (296 K) and ~0.1 s^{-1} (318 K), within 50% of the rate coefficients calculated using multiconformer transition state theory. Reaction of the RO_2 with NO produces alkoxy radicals which also undergo rapid isomerization via 1,6 and 1,5 H-shift of the hydroperoxy hydrogen (ROO-**H**) to produce RO_2 with alcohol functionality. One of these hydroxy-substituted RO_2 exhibits a 1,5 α-OH (HOC-**H**) H-shift, measured to be ~0.2 s^{-1} (296 K) and ~0.6 s^{-1} (318 K), again in agreement with the calculated rates. Thus, the rapid shift of hydroperoxy hydrogens in alkoxy and peroxy radicals enables intramolecular reactions that would otherwise be inaccessible.

Introduction

In the atmosphere, organic peroxy radicals (RO_2) are formed following the reaction of OH, NO_3, or O_3 with hydrocarbons.[1] These RO_2 undergo bimolecular reaction with NO, HO_2, and other RO_2.[2] In addition, unimolecular reactions of RO_2 have recently been shown to be important in the atmospheric chemistry of a growing number of hydrocarbons.[3-14] These reactions form the basis of gas-phase autoxidation, which involves the regenerative formation of RO_2 via intramolecular RO_2 H-shifts followed by O_2 addition. These reactions proceed through hydroperoxy alkyl radical intermediates, often denoted QOOH.[15] Such chemistry has long been known to be relevant in combustion.[16-17]

Atmospheric autoxidation has been implicated in the rapid oxygenation of hydrocarbons, contributing to new particle formation and growth.[18-31] Autoxidation was recently shown to play a role in the oxidation of alkanes emitted in urban areas.[32] Hydroxy-substituted RO_2 are produced in this chemistry and exhibit sufficiently low energetic barriers for H-shift reactions that compete with bimolecular reactions in the atmosphere.[33] Indeed, some of these H-shift rates are sufficiently fast (~0.1 s^{-1}) that multifunctional organic hydroperoxides can be produced via this mechanism even under modestly polluted conditions. The fate of these hydroperoxides in urban air, however, remains largely unexplored. It is possible that these hydroperoxides partition to the aerosol phase or photolyze due to enhanced absorption cross sections.[34-35] In the gas phase, organic hydroperoxides will undergo further reaction with OH to produce hydroperoxy-substituted RO_2. Intramolecular H-shifts in these radicals have been the subject of previous studies, but only at elevated temperature.[36-43]
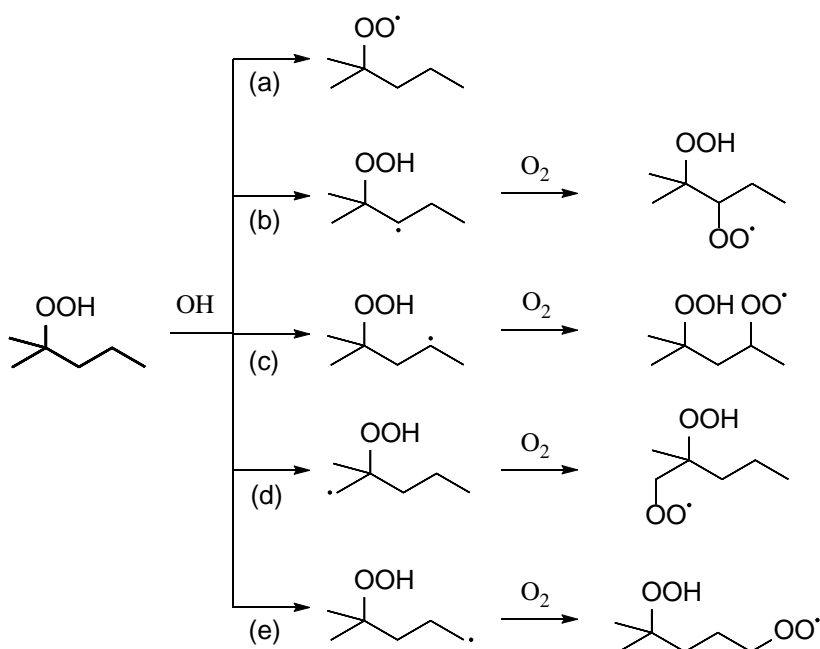
Scheme 5. Peroxy radicals (RO$_2$) formed following OH-initiated oxidation of 2-hydroperoxy-2-methylpentane. Abstraction of the hydroperoxide hydrogen is a major channel (a). Abstraction of secondary alkyl hydrogens, (b)-(c), dominates over that of primary alkyl hydrogens, (d)-(e).

In this study, we oxidize 2-hydroperoxy-2-methylpentane with OH under conditions relevant to the atmosphere. As shown in Scheme 1, the RO$_2$ formed following hydrogen abstraction and O$_2$ addition lack an abstractable α-OOH hydrogen due to the presence of the methyl substituent. However, due to rapid and reversible H-shifts between the ROO-**H** and the RO$_2$ radical centers, an RO$_2$ with an accessible α-OOH hydrogen is produced. The dominant channels (b) and (c) are illustrated in Scheme 2. In the presence of NO, these RO$_2$ form distinct hydroperoxynitrates (HPN) that are quantified in this work (shown in boxes).

In addition to HPN, reaction of the RO$_2$ with NO produces alkoxy radicals (Scheme 3). These alkoxy radicals undergo a very rapid H-shift with hydroperoxy hydrogens to produce hydroxy-substituted RO$_2$. One of these hydroxy-substituted RO$_2$ possesses an accessible 1,5 α-OH H-shift. Due to the ability to unlock alkyl H-shifts that would otherwise be inaccessible (or very slow), the rapid isomerization of hydroperoxy-substituted alkoxy and peroxy radicals represents a critical process in the oxidation mechanism of the substrate used here as well as many other compounds found in the urban atmosphere. This rapid isomerization

between ROOH and RO$_2$, first described in a computational study by Jørgensen and coworkers,[44-45] is similar to the interconversion of alcohols and alkoxy radicals reported in computational studies by Dibble.[46-47]
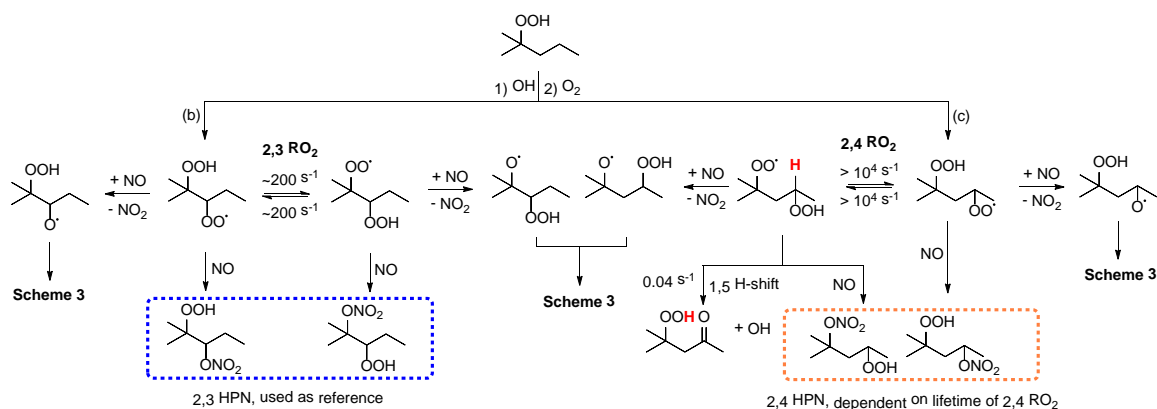
Scheme 6. RO$_2$ formed following pathways (b) and (c) in Scheme 1 undergo rapid H-shifts of the hydroperoxy hydrogen producing two pairs of RO$_2$ (denoted here as 2,3 and 2,4 RO$_2$). In the presence of NO, these RO$_2$ form distinct hydroperoxynitrates (HPN) that are quantified in this work (shown in boxes). For the 4-hydroperoxy-2-methyl-2-peroxy isomer of the 2,4 RO$_2$, a unimolecular 1,5 α-OOH H-shift competes with the bimolecular reaction with NO. The forward rate coefficients shown are those measured at 296 K. The reverse rate coefficients for the 2,3 and 2,4 RO$_2$ are similar given the measured distribution of the products of the two sets of isomers.
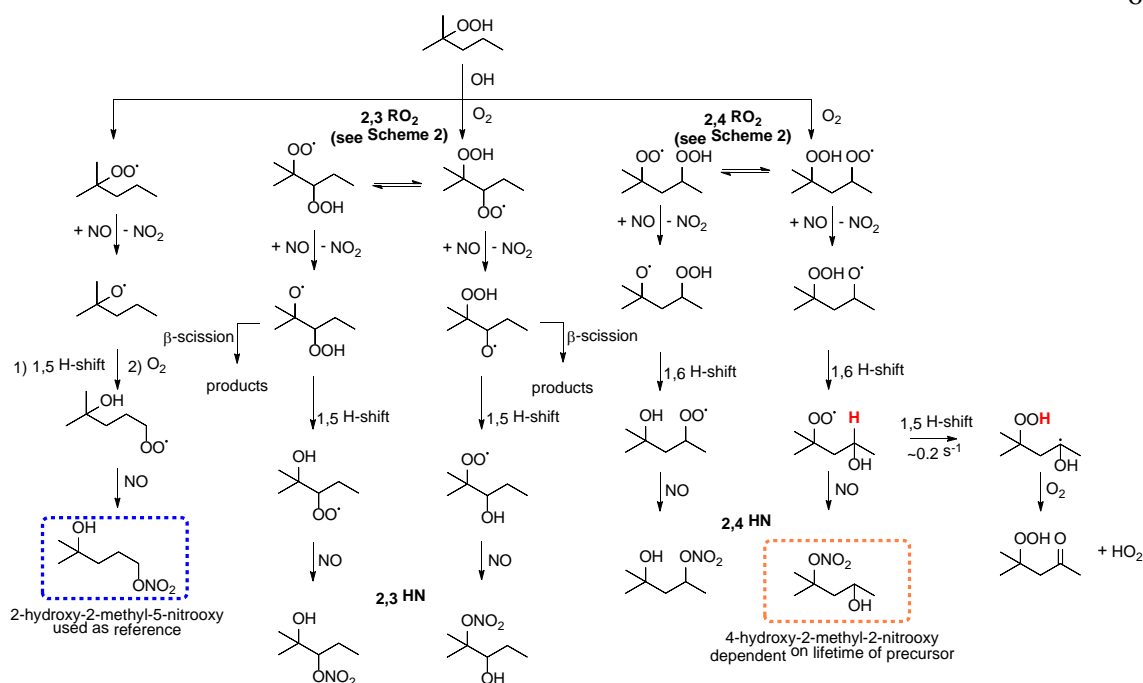
Scheme 7. Pathways following reaction of RO$_2$ with NO. In addition to the organonitrate pathway shown in Scheme 2, the reaction of RO$_2$ with NO produces alkoxy radicals. These alkoxy radicals rapidly isomerize to produce hydroxy RO$_2$ which react with NO to produce hydroxy nitrates (HN - boxes) and other products. The 4-hydroxy-2-methyl-2-peroxy RO$_2$ can also undergo a 1,5 α-OH H-shift. β-scission is only expected to be competitive for the 2,3 alkoxy radicals and thus this pathway is omitted in the scheme for the remaining alkoxy radicals.

Methods

Theory. Multiconformer Transition State Theory (MC-TST) is used to calculate the rate coefficients in this work.[48-51] MC-TST is well-suited to characterize intramolecular RO$_2$ chemistry due to the large number of reactant conformers typically encountered. We follow the MC-TST approach of Møller et al.,[51] which has been shown to provide good agreement with the few available measured H-shift rate coefficients.[32] The MC-TST expression for the rate coefficient is:

$$k_{MC-TST} = \kappa \frac{k_B T}{h} \frac{\sum_i^{all\ TS\ conf.} \exp\left(-\frac{\Delta E_i}{k_B T}\right) Q_{TS,i}}{\sum_j^{all\ R\ conf.} \exp\left(-\frac{\Delta E_j}{k_B T}\right) Q_{R,j}} \exp\left(-\frac{E_{TS,0} - E_{R,0}}{k_B T}\right)$$

where h is Planck's constant, k_B is Boltzmann's constant, and T is the temperature. ΔE_i is the zero-point corrected energy difference between TS conformer i and the lowest energy TS conformer, $Q_{TS,i}$ is the partition function of TS conformer i, and $E_{TS,0}$ is the zero-point corrected energy of the lowest energy TS conformer. The symbols are analogously defined for the reactant conformers. κ is the Eckart tunneling correction factor (see SI for further details).[52]

Conformers are located with a systematic MMFF[53-58] conformer search in Spartan'14,[59] with the radical atom forced to have no charge.[51] Conformers are then optimized with B3LYP/6-31+G(d) in Gaussian 09.[60-65] We calculate the vibrational frequencies of the conformers to verify that a minimum or first-order saddle point was found as desired. Duplicate conformers are removed by a custom bash-wrapped python script, by comparing dipole moments and energies.[66] Zero-point energy corrected conformers within 2 kcal/mol of the lowest energy conformer are re-optimized with ωB97X-D/aug-cc-pVTZ (ωB97) and their frequencies are calculated.[67-68] The energies and partition functions at this level are used for the ΔEs and Qs in the MC-TST expression. For the lowest energy conformer of reactant and TS, we calculate a ROHF-ROCCSD(T)-F12a/VDZ-F12//ωB97X-D/aug-cc-pVTZ[69-73] (F12) single-point energy with MOLPRO 2012[74] to use with the ωB97 zero-point correction for accurate values of $E_{TS,0}$ and $E_{R,0}$. For the rapid alkoxy (RO) and peroxy (RO$_2$) ROO-**H** H-shift reactions, the reaction barriers were calculated at the ωB97 level due to convergence problems with the F12 energies in the TS of these reactions. This causes an increase in the uncertainty of the barrier (and, to a minor extent, tunneling) of these calculated H-shifts and the rate coefficients are accurate to about a factor of 100. The ratios of the equilibrated RO$_2$ isomers are independent of the TS and are obtained at the F12 level. The calculation output files used in this work are available at https://sid.erda.dk/wsgi-bin/ls.py?share_id=fgP2YXJCPg.

Experiment. Using a method analogous to that of our earlier study of hexane oxidation,[32] we use isomer-specific measurements of multifunctional organonitrates (RONO$_2$) to study the rate coefficients of unimolecular chemistry. RO$_2$ undergoing unimolecular chemistry will have smaller yields of HPN at longer bimolecular lifetimes. For the hydroperoxy-substituted RO$_2$, the equilibrated isomer will also have smaller yields of HPN. By quantifying the yields

of the HPN as a function of the bimolecular lifetime, we determine the rate coefficients of the H-shift chemistry.

Materials and hydroperoxide synthesis. 2-methyl-2-pentene (98%, Fluka), isopropanol (≥99%, Macron), and nitric oxide (1993 ± 20 ppmv NO in N_2, Matheson) are used as purchased. CH_3ONO is synthesized in a manner similar to that described by Taylor et al.[75] 2-hydroperoxy-2-methylpentane is synthesized by addition of 2-methyl-2-pentanol (2.5 g, 24.5 mmol) as a solution in ether (8 mL) to a mixture of 30% aqueous hydrogen peroxide (30 mL) and 10 M H_2SO_4 (3 mL), and the mixture is stirred for 18 h. The reaction is quenched with saturated K_2CO_3 (10 mL), and the layers are separated. The organic layer is washed with brine (8 mL), dried (Na_2SO_4), and concentrated under reduced pressure. The crude reaction mixture, purified via flash column chromatography, elutes with CH_2Cl_2/Et_2O (25:1) on SiO_2 (50 mL) to provide 2.14 g (74%) of 2-hydroperoxy-2-methylpentane as a colorless liquid. Refer to the SI for the characterization of this compound.

Chamber Studies. 2-hydroperoxy-2-methylpentane is added to a ~1 m^3 Teflon chamber via evaporation of an aqueous solution prepared by mixing the neat peroxide with water (1:1 by volume). A small quantity (<4 μL) of this solution is placed in a 3-way vial and zero air transfers the headspace to the chamber. CH_3ONO is introduced to the chamber via a 500 mL glass bulb. FTIR (Nicolet 560 Magna IR) is used to quantify the contents of the bulb prior to addition using published absorption cross sections.[76] Nitric oxide is introduced in some experiments and is quantified using a Teledyne 200EU NO_x analyzer.

Sylvania blacklights (λ_{max} ~350 nm) illuminate the chamber for between 10 min and 16 hours following the collection of background chromatograms. Photolysis of CH_3ONO in air produces NO, HO_2, and OH:

$$CH_3ONO + h\nu + O_2 \rightarrow HO_2 + NO + HCHO$$

$$HO_2 + NO \rightarrow OH + NO_2$$
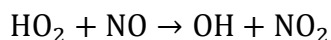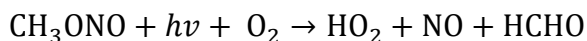
Experiments are conducted with different [NO] and [HO_2], yielding a range of RO_2 bimolecular lifetimes ($\tau_{bimolecular}$):

$$\tau_{bimolecular} = \frac{1}{k_{RO_2+NO}[NO] + k_{RO_2+HO_2}[HO_2]} = \frac{1}{k_{bimolecular}} \quad \text{(Eq. 1)}$$

By using a low abundance of the organic peroxide (~20-80 ppbv), the impact of RO_2 + RO_2 chemistry is minimized. Determination of $\tau_{bimolecular}$ is described in the SI. The ratio $\frac{k_{RO_2+NO}}{k_{RO_2+HO_2}}$ is assumed to be the same for RO_2 isomers.

Following oxidation of a small amount (5-20%) of the 2-hydroperoxy-2-methylpentane, the lights are turned off and isomer specific measurement of $RONO_2$ is performed using a gas chromatograph chemical ionization mass spectrometer (GC-CIMS),[77] following the method described previously in Praske et al.[32] Briefly, the output of a GC equipped with an 11.5 m Restek RTX-200 column is coupled to the CIMS, using CF_3O^- (*m/z* 85) as the reagent ion.[78-82] Following cryofocusing of the analytes on the head of the column, a temperature program is initiated. See the SI for further details.

Chromatographic assignment of RONO2. Four major HPN isomers are resolved following oxidation of 2-hydroperoxy-2-methylpentane by OH in the presence of NO (Figure 1A). As discussed below and shown in Scheme 2, these are produced from two pairs of interconverting hydroperoxy peroxy radicals with the functional groups either β (2,3) or γ (2,4). The two 2,3 HPN are assigned using the NO_3-initiated oxidation of 2-methyl-2-pentene (see Scheme 4A). This chemistry produces nitrooxy peroxy radicals that react with HO_2 produced via reaction of NO_3 with HCHO, as described by Schwantes et al.[83] NO_3 preferentially adds to the secondary carbon of the olefin.[83] As shown in Figure 1B, we observe the formation of two HPN in a ratio of ~10:1 and thus assign the first peak (largest) to the secondary nitrate. The remaining two peaks in Figure 1A are assigned to the 2,4 HPN isomers. This is consistent with previous observations that the retention time of analytes with the same functionality generally increases with increasing separation of the functional groups.[32, 84]

To assign the hydroxy-substituted nitrates (HN) produced in the oxidation of 2-hydroperoxy-2-methylpentane (Figure 1C), we use measurements of the products of the OH-initiated oxidation of 4-methyl-2-pentanol (see Scheme 4B and Figure 1D). The tertiary HN is the major HN produced from this chemistry and allows assignment of the HN eluting at this time as the 4-hydroxy-2-methyl-2-nitrooxy isomer. The remaining isomers are assigned based on elution order. We assume, as shown in the oxidation of 2-methyl-2-pentene, that secondary

nitrates elute first. Thus, the preceding peak in Figure 1C is inferred to correspond to the 2-hydroxy-2-methyl-4-nitrooxy isomer while the later eluting isomer is assigned to the 2-hydroxy-2-methyl-5-nitrooxy isomer. Finally, we assume that the first two smaller peaks correspond to the 2,3 HN. As discussed below, we interpret their much smaller abundance (compared with that of the 2,3 HPN) as reflecting competition between β-scission and the ROO-H shift to the alkoxy radical (Scheme 3). Further evidence for the assignments in both the hydroperoxides (and alcohols) is shown in the SI (Figure S7) where, at very high NO concentrations, we are able to capture the distribution of 2,3 HPN and HN before the 2,3 RO_2 are fully equilibrated, and thereby assign the tertiary hydroperoxide (and secondary alcohol).
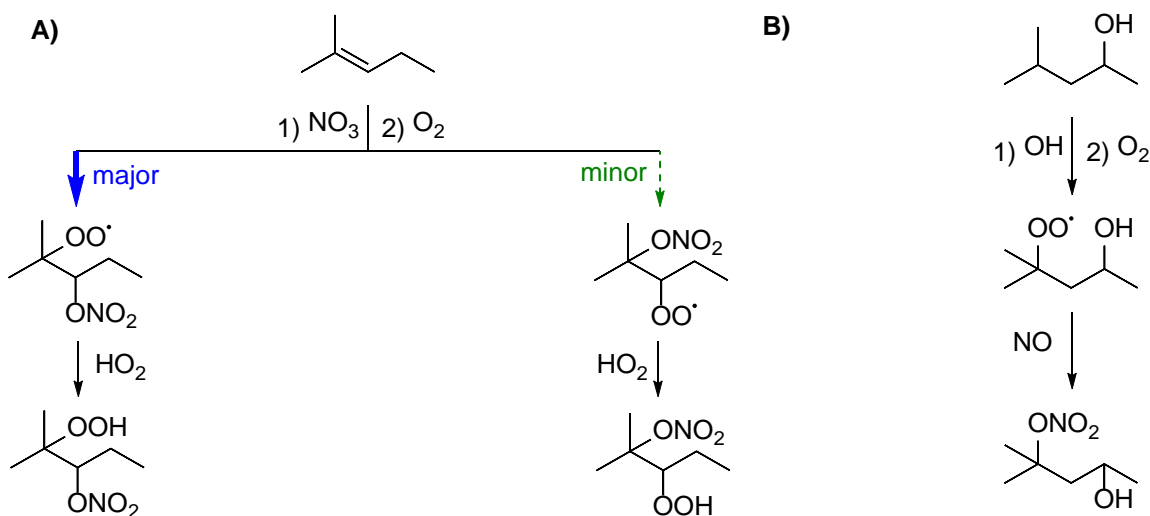
Scheme 8. Chromatographic assignment is based on the oxidation of commercially available precursors. A) The NO_3-initiated oxidation of 2-methyl-2-pentene produced the 2,3 HPN from 2-hydroperoxy-2-methylpentane. B) The OH-initiated oxidation of 4-methyl-2-

pentanol produces the HN isomer shown in the orange box in Scheme 3.
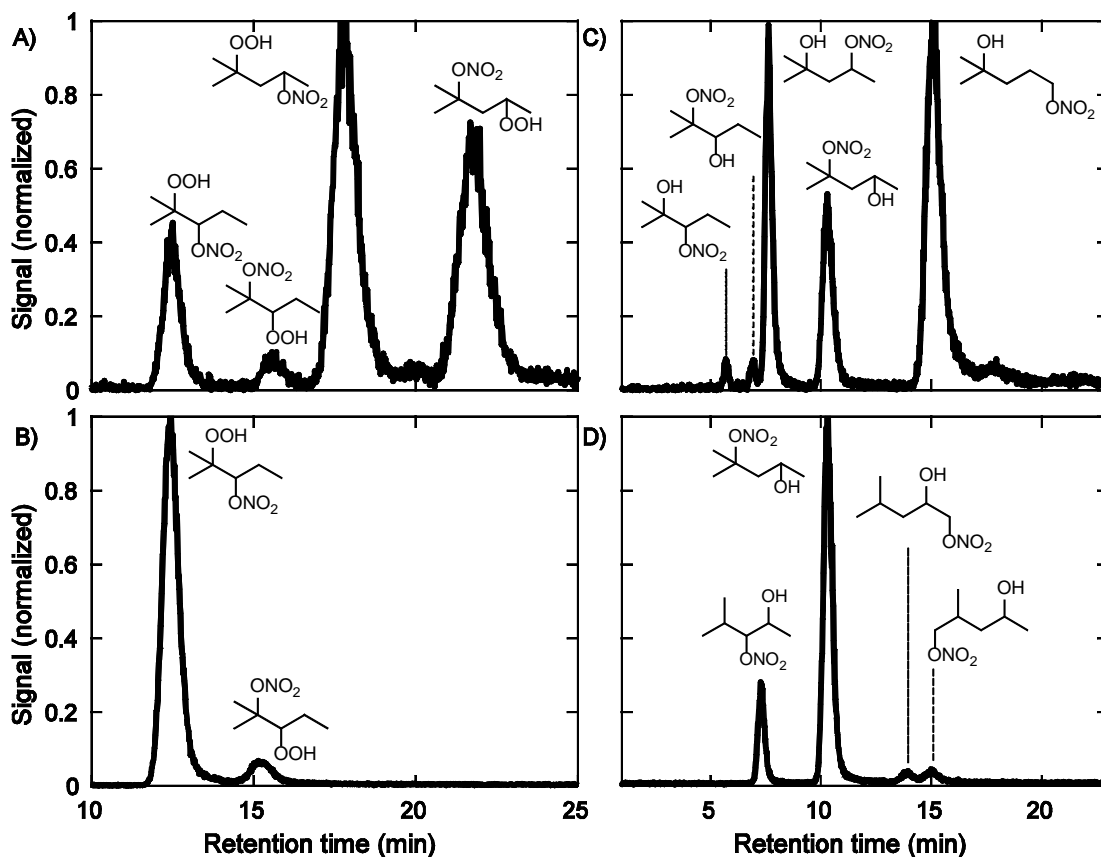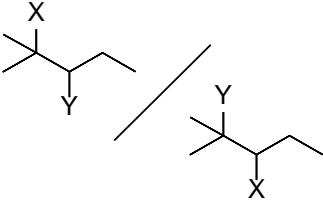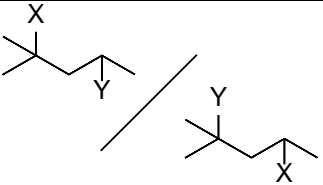
Figure 4. The RONO$_2$ are separated and identified by GC-CIMS. Chromatographic assignment of the HPN (clustered with CF$_3$O$^-$ at *m/z* 264): A) OH-initiated oxidation of 2-hydroperoxy-2-methylpentane B) NO$_3$-initiated oxidation of 2-methyl-2-pentene (see Scheme 4A) produced the 2,3 HPN isomers. Chromatographic assignment of the HN (*m/z* 248): C) OH-initiated oxidation of 2-hydroperoxy-2-methylpentane. Note the relatively lower abundance of the 2,3 HN as compared to the 2,3 HPN in panel A. As discussed in the text, we attribute this to the fast decomposition of the 2,3 alkoxy radicals, which outruns the 1,5 alkoxy H-shift of the hydroperoxide hydrogen (see Scheme 3). D) OH-initiated oxidation of 4-methyl-2-pentanol (see Scheme 4B) primarily produced the tertiary HN. In each of the chromatograms, the signal has been normalized to the intensity of the tallest peak.

Results and Discussion

Constraining the ROO-H RO$_2$ H-shift. As shown in the SI and Figure S6, only at very high [NO] are any changes in the ratio within the 2,3 HPN observed. From data obtained at [NO] > 1 ppmv, we infer that the forward and reverse rate coefficients for the H-shifts between the 2,3 hydroperoxy RO$_2$ are about 10^2 s^{-1} at 296 K and even faster (>10^4 s^{-1}, 296 K) for the 2,4 hydroperoxy RO$_2$. These are in agreement with the calculated rate coefficients of ~10^3 s^{-1} and ~10^6 s^{-1} for the 2,3 and 2,4 RO$_2$, respectively. The rapid RO$_2$ isomerization of hydroperoxy hydrogens was suggested in the computational study of Jørgensen et al.[44] but, to the best of our knowledge, this is the first experimentally-derived estimate of these rate coefficients. These rapid isomerization reactions are critical to our study as they enable the two alkyl H-shifts (shown in Schemes 2 and 3) that are inaccessible in the initially produced RO$_2$ (see Scheme 1).

RO$_2$ equilibrium. For [NO] < 100 ppb, we find that the ratios of the two HPN in the 2,3 and 2,4 RO$_2$ systems are invariant. The ratios of the HPN for the equilibrated 2,3 and 2,4 RO$_2$ systems are listed in Table 1. Because we do not know if both the branching ratio to form HPN and k_{RO_2+NO} are the same for the two isomers in each system, the ratio of the HPN signals (Table 1) may not be the same as the ratio of the concentrations of the peroxy radicals that produced them. Using the recommended branching ratio parametrization described in Wennberg et al.,[85] for example, the fraction of tertiary peroxy radicals is 25% smaller than estimated from the ratio of the HPNs. Table 1 also includes the equilibrium constants for the RO$_2$ calculated from the relative energies of the two RO$_2$ isomers. A 1 kcal/mol error in the difference in the free energies of the RO$_2$ (the expected accuracy of the F12 calculations) would correspond to a factor of ~5 in this ratio (at 296 K) suggesting that the calculations are consistent with the observed product distribution to within error.

Table 1. Comparison of calculated ratio of the equilibrated RO_2 isomers and the measured ratio of their products.

Ratio	Temperature (K)	RO_2 [a] (X=OO; Y=OOH)	HPN [b] (X=ONO$_2$; Y=OOH)	HN [c] (X=OH; Y=ONO$_2$)
	296	0.59	0.31 ± 0.02	-
	318	0.71	0.34 ± 0.04	-
	296	3.1	0.75 ± 0.06	1.3 ± 0.1
	318	3.3	0.77 ± 0.06	1.4 ± 0.1

[a] The ratio calculated from the F12 energies of the RO_2.

[b] The ratio of the measured hydroperoxy nitrates (Scheme 2).
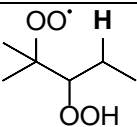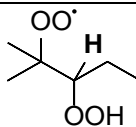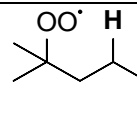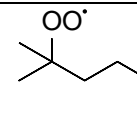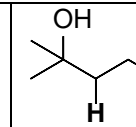
[c] The ratio of the measured hydroxy nitrates (Scheme 3).

Constraining the ROO-H to alkoxy H-shift. Recall from Scheme 2 that, in addition to HPN formation, alkoxy radicals are produced in the RO_2 + NO reaction. These alkoxy radicals undergo rapid H-shifts from the hydroperoxide to the alkoxy radicals, producing hydroxy-substituted RO_2 as shown in Scheme 3. Note that the reverse of this reaction (RO_2 abstraction of the hydroxy H) is too slow to compete over the range of lifetimes probed in our experiments.[86] The alkoxy H-shifts, however, are so fast that we are unable to provide a direct experimental constraint. We considered the possibility that chemical activation may play a role, but the rate coefficients derived from our calculations with the thermalized alkoxy radicals are consistent with experimental observations.

Reaction of the hydroxy-substituted RO_2 with NO yields the HN detected by the GC-CIMS. As shown in Figure 1C, we even observe the 2,3 HN, suggesting that these alkoxy H-shifts are at least partially competitive with β-scission. Using a structure-activity relationship, the energetic barrier for the 2,3 alkoxy β-scission is estimated to be small (< 3 kcal/mol) corresponding to $k_{\beta\text{-scission}} \sim 10^{11}$ s^{-1}.[87] For the 2,3 alkoxy radicals at 296 K, the fastest alkyl H-shift is orders of magnitude slower ($k_{\text{alkyl}-H-\text{shift}} \sim 10^5$ s^{-1}) and thus does not compete with either β-scission or the rapid ROO-H 1,5 H-shift.[88]

For the 2,4 alkoxy radicals at 296 K, $k_{\beta\text{-scission}}$ and $k_{\text{alkyl}-H-\text{shift}}$ are each estimated to be $<10^4$ s^{-1} and $<10^6$ s^{-1}, respectively.[87-88] Thus, the ROO-H 1,6 H-shift rate coefficients must be similar to, or greater than, $k_{\text{alkyl}-H-\text{shift}}$ in order to explain the observations. Consistent with this, the calculated rate coefficient for the 1,6 H-shift is $\sim 10^{10}$ s^{-1}. The similar ratio of HPN and HN described in Table 1 suggests that the ROO-H 1,6 H-shift is likely the only fate of the alkoxy radical.

Table 2. MC-TST calculated rate coefficients for selected H-shifts of alkyl hydrogens at 298.15 K for the reference RO_2, with the abstracted hydrogen shown explicitly in bold.

Origin	2,3 RO$_2$		ROO-**H** abstraction		
RO$_2$					
Rate coefficient (s^{-1})	5.3×10^{-4}	1.8×10^{-7}	2.8×10^{-4}	5.4×10^{-6}	2.4×10^{-4}

Determination of the 1,5 α-OOH H-shift. For both the hydroperoxy and hydroxy-substituted RO_2, we use MC-TST calculations to identify RO_2 isomers that do not undergo alkyl H-shifts over the range of $\tau_{\text{bimolecular}}$ probed in the experiments (see Table 2). The total lifetime of these RO_2 isomers (labeled 'reference' in Schemes 2 and 3) is $\tau_{\text{bimolecular}}$ (Eq. 1). The RO_2 that react via α-OOH or α-OH H-shifts ($k_{H-\text{shift}}$), however, have shorter lifetimes. For these RO_2, the yield of RONO$_2$ relative to that of the RONO$_2$ produced from the reference RO_2 will decrease as $\tau_{\text{bimolecular}}$ is extended. The changing ratio of the RONO$_2$

isomer yields as a function of $\tau_{bimolecular}$ is used to determine the rate coefficients of unimolecular chemistry. Enantiomeric RO_2 pairs are assumed to react with equal rate coefficients and are not distinguished here.

As shown in Figures 2 and 3, the ratio of both the 2,4 HPN isomers relative to the 2,3 HPN reference decreases at longer $\tau_{bimolecular}$ as a result of the α-OOH 1,5 H-shift (see Scheme 2). H-shifts arising from the 2,3 RO_2 are calculated to be negligible under the conditions of these experiments, and so $\tau_{2,3\ RO_2} = \tau_{bimolecular}$ (see the first two columns in Table 2). We use the observed change in the ratio of the 2,4 HPN normalized to the 2,3 HPN as a function of $\tau_{bimolecular}$ to infer the rate coefficient of the 1,5 α-OOH H-shift (Figure 3).

The rate of unimolecular chemistry inferred from the behavior shown in Figure 3, $k_{H-shift-effective}$, is less than the rate of the isomer-specific 1,5 α-OOH 4-hydroperoxy-2-methyl-2-peroxy (2-OO-4-OOH) H-shift, $k_{H-shift-2-OO-4-OOH}$, because of the rapid interconversion between the 2,4 RO_2 isomers (see Scheme 2). Due to this interconversion, the concentrations of both 2,4 RO_2 isomers, relative to the 2,3 RO_2 isomers, decline at the same rate (see Figure 2). Thus, the experimentally determined rate coefficient of unimolecular chemistry is proportional to the fraction of the 2,4 RO_2 that is capable of the α-OOH H-shift:

$$k_{H-shift-effective} = k_{H-shift-2-OO-4-OOH} \left(\frac{\text{2-OO-4-OOH}}{\text{2-OO-4-OOH} + \text{2-OOH-4-OO}} \right)$$

For example, as the two 2,4 RO_2 are nearly equally abundant at equilibrium, $k_{H-shift-effective}$ would be about half of $k_{H-shift-2-OO-4-OOH}$. In our experiments, the equivalence point, where the rate of unimolecular and bimolecular chemistry for the 2,4 RO_2 is the same, is ~0.02 s^{-1}. This is $k_{H-shift-effective}$. This challenge of estimating isomer-specific H-shift rate coefficients in the context of an interconnected pool of RO_2 is similar to that described in Teng et al. for the 1,6 H-shifts in the hydroxy peroxy radicals formed following addition of OH and O_2 to isoprene.[84]

The kinetic model, shown in the curved lines in Figure 3, uses the calculated rate coefficient for the 1,5 α-OOH RO_2 H-shift (Table 3) together with an estimate of the fraction of the 2,4 RO_2 that exists as the 2-OO-4-OOH isomer (about 50% given the nearly equal abundance of HPN (and HN) isomers). The small difference between the HPN and HN ratios (Table 1) can

be explained if the nitrate yield from the secondary RO_2 is 25% greater than that of the tertiary RO_2. Given the uncertainties in the nitrate yields, we assume the ratio of the 2-OO-4-OOH to the 2-OOH-4-OO is no smaller than 3:1 and no larger than 1:3. Thus, we assume

$$\frac{\text{2-OO-4-OOH}}{\text{2-OO-4-OOH+2-OOH-4-OO}} = 0.50 \pm 0.25.$$ As discussed below, the measured and calculated

$k_{\text{H-shift-effective}}$ are in good agreement.
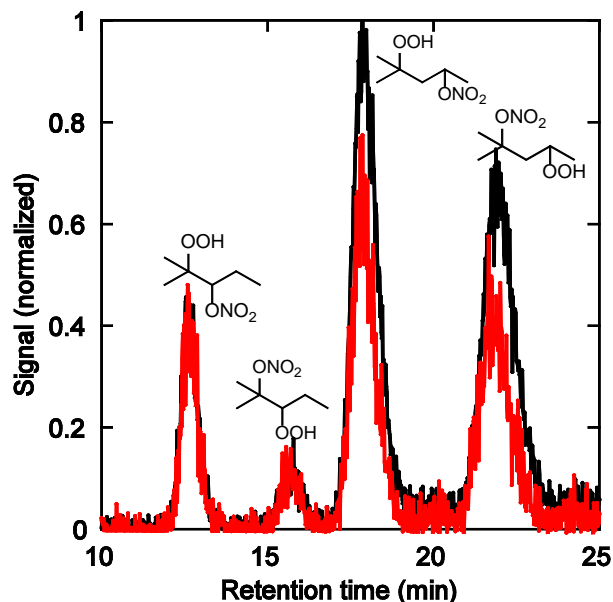
Figure 5. Two chromatograms following 2-hydroperoxy-2-methylpentane oxidation at 318 K are displayed. The loss of the 2,4 HPN is apparent in the experiment at $\tau_{\text{bimolecular}} \approx 5$ s (red) compared to the experiment at $\tau_{\text{bimolecular}} \approx 0.1$ s (black). Measurement of the ratio 2,4 HPN:2,3 HPN as a function of bimolecular lifetime is used to estimate the α-OOH H-shift. The black line chromatogram has been normalized to the intensity of the tallest peak, while that of the red line has been normalized to the 2,3 HPN reference.
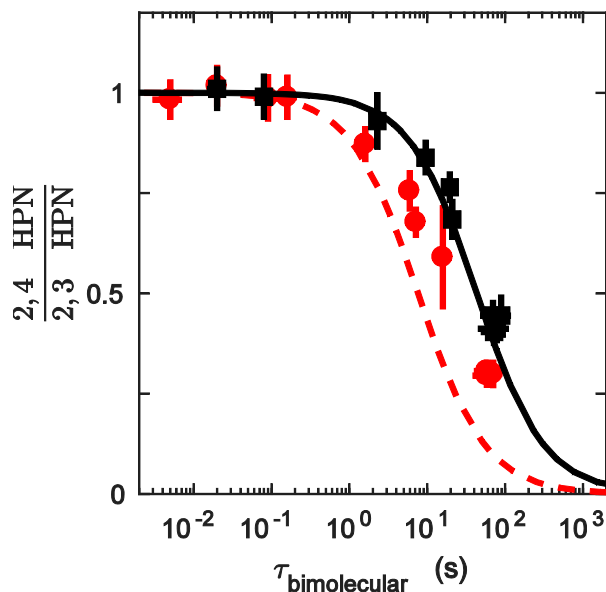
Figure 6. Experimental data used to constrain the 1,5 α-OOH H-shift at 296 K (black squares) and 318 K (red circles). The solid black (296 K) and dashed red (318 K) lines are simulations using the calculated 1,5 α-OOH H-shift rate together with the assumption that the concentration of the 2-OO-4-OOH isomer is equal to that of the 2-OOH-4-OO isomer. Both the model and experimental points have been normalized by the mean of the ratio obtained at the two shortest $\tau_{bimolecular}$. Due to the limitations of our method, it is not possible to lengthen $\tau_{bimolecular}$ beyond 100 s; thus, the sigmoidal tail at long lifetimes is poorly constrained.

The observed temperature dependence provides further confidence in our interpretation of the mechanism responsible for the reduced yields of the 2,4 HPN isomers at long $\tau_{bimolecular}$. The equivalence point, where $k_{RO_2+NO}[NO] + k_{RO_2+HO_2}[HO_2] = k_{\text{H-shift-effective}}$, occurs when $\tau_{bimolecular}$ is ~4 times shorter at 318 K than at 296 K, consistent with the large energetic barriers encountered by these H-shifts (see SI).

Determination of the 1,5 α-OH $k_{H-shift}$. The 1,5 α-OH H-shift of the 4-hydroxy-2-methyl-2-peroxy isomer is observed using measurements of the HN (Scheme 3), and the rate coefficient is quantified in a manner similar to that used in the determination of the 1,5 α-OOH H-shift. In this system, the 2-hydroxy-2-methyl-5-nitrooxy isomer is used as a reference. Our calculations (Table 2) demonstrate negligible H-shift channels for the RO₂

formed via the ROO-**H** abstraction of 2-hydroperoxy-2-methylpentane (left column in Scheme 3). This RO_2 reacts with NO and the resulting alkoxy undergoes a 1,5 H-shift to produce a hydroxy-substituted RO_2, which also exhibits a negligible H-shift pathway (Table 2). Thus, the HN arising from reaction of this RO_2 with NO serves as a suitable reference. As shown in Figure 4, the ratio of the yield of the 4-hydroxy-2-methyl-2-nitrooxy isomer to that of the 2-hydroxy-2-methyl-5-nitrooxy reference exhibits a strong dependence on $\tau_{bimolecular}$ and temperature. The process responsible for this dependence is assigned to a 1,5 H-shift proceeding via abstraction of the α-OH hydrogen (Scheme 3). In Figure 4, the kinetic model employs the theoretically calculated α-OH H-shift rate coefficient. However, the curve shown in Figure 4 also depends on both the rapid hydrogen scrambling between the RO_2 isomers as well as the α-OOH H-shift rate coefficient since the production of the 2,4 HN is tied to the 2,4 RO_2 system (Scheme 3). Here, we use the experimentally constrained 1,5 α-OOH H-shift rate coefficient, and the error bounds in Table 3 account for the full range of uncertainty in this value.
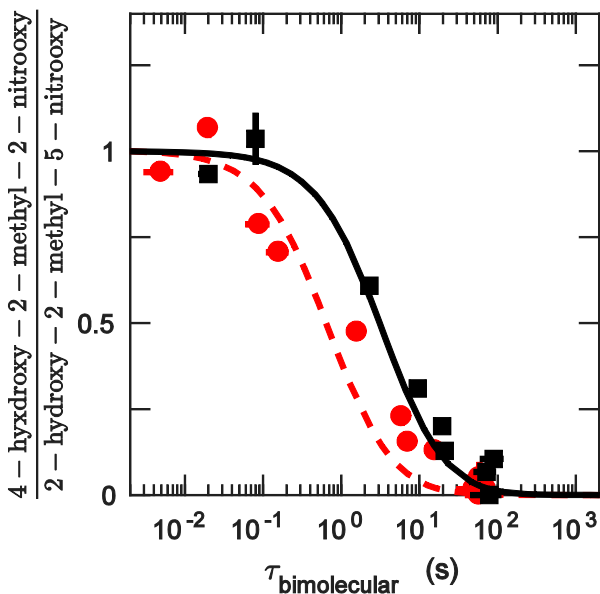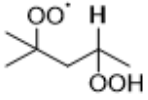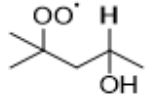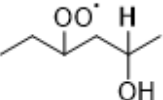
Figure 7. Experimental data used to constrain the 1,5 α-OH H-shift at 296 K (black squares) and 318 K (red circles). Simulated curves using computational results for the α-OH H-shift are shown at 296 K (solid black) and 318 K (dashed red). The simulations use the

experimentally constrained rate coefficient for the 1,5 α-OOH H-shift (Table 3), while the calculated rate coefficient is used for the 1,5 α-OH H-shift. Both the model and experimental points have been normalized by the mean of the ratio obtained at the two shortest $\tau_{bimolecular}$.

Products of the 1,5 H-shift chemistry. A significant CIMS signal is observed at *m/z* 217, corresponding to the cluster of a compound of nominal mass 132 amu and the CF_3O^- reagent ion, *m/z* 85. As in our previous study, this signal is attributed to the formation of the ketohydroperoxide,[32] a product of the autoxidation mechanism following hydrogen abstraction at α-OH and α-OOH centers as shown in Schemes 2 and 3. There is only one ketohydroperoxide isomer produced by both of these H-shifts.

Comparison of experimental and computational results. The experimental rate coefficients shown in Table 3 are derived by fitting the kinetic model to the experimental data (see SI, Figures S4-S5). The experimental and calculated values agree to better than a factor of 3. Furthermore, reasonable agreement is achieved by comparison of our results with those of Mohamed et al.[38] Although the study focused on temperature ranges relevant to combustion, the 1,5 α-OOH H-shift rate coefficient was calculated to be 0.07 s^{-1} at 296 K and 0.5 s^{-1} at 318 K, within a factor of 4 of our experimental and computational results (see Table 3). In combination with our previous results,[32] the reasonable agreement suggests that the computational approach used here, and described in detail by Møller et al.,[51] is a robust method for calculating the kinetic parameters of RO_2 H-shifts for the diverse substrates needed to be considered in chemical models.

Table 3. α-OOH and α-OH H-shift rate coefficients (s^{-1}) derived by theory and experiment

Temperature	Method	Reactant		
		1,5 α-OOH H-shift	1,5 α-OH H-shift	1,5 α-OH H-shift [a]
296 K	Theory [b]	0.045	0.28	0.12
	Expt. [c]	0.036 +0.077/-0.027	0.22 +0.14/-0.040	0.048 +0.036/-0.024
318 K	Theory [b]	0.25	1.4	0.61
	Expt. [c]	0.13 +0.23/-0.10	0.56 +0.44/-0.14	0.31 +0.18/-0.061

[a] Reported in Praske et al.[32] Rate coefficients correspond to the average of the S,R and S,S diastereomers.

[b] For the temperature dependent rate expressions, refer to the SI. Uncertainty in the calculated rates is estimated to be less than a factor of 10.[32]

[c] Uncertainty is estimated as described in the SI. Additionally, the 1,5 α-OOH H-shift is sensitive to our estimate of K_{eq}. We include the uncertainty in this parameter in the reported error bounds.

Role of structure. At 296 K, the experimentally determined rate coefficient of the α-OH 1,5 H-shift is ~5 times greater than that of the α-OH 1,5 H-shift in a peroxy radical produced in the oxidation of 2-hexanol (see Table 3).[32] The difference in these rate coefficients for nominally similar H-shifts clearly demonstrates that structure plays a key role in the kinetics. The effect of structure has previously been investigated computationally in unimolecular reactions involved in fuel combustion at elevated temperatures. Miyoshi, for example, determined that increasing the methyl substitution of the RO$_2$ center increases the reaction barrier in 1,7 H-shifts.[37] This effect was attributed to an increase in the ring strain energy of the transition state, likely caused by the spatial configuration of the methyl substituents. Similarly, Davis and Francisco computationally investigated H-shifts in n-alkyl and branched methyl alkyl radicals,[89-90] and found that the spatial configuration of the methyl substituent influenced the energy of the transition state. This effect was correlated to a shift of the methyl group from a gauche to anti configuration, which produced lower barrier

heights. Otkjær et al. computationally studied a systematic set of peroxy radicals with a range of different substituents.[33] They calculated that the presence of an α-OH or α-OOH group can increase the rate coefficient of an H-shift by factors up to 1000, in agreement with the experimental results of our current and previous work.[32] Finally, hydrogen bond-like interactions in the reactant and transition state influence the barrier height, as previously demonstrated.[32, 86]

Atmospheric Implications

In this study, we demonstrate the migration of hydroperoxy hydrogens in alkoxy and peroxy radicals. The rate coefficients are sufficiently large that this chemistry may outrun bimolecular reaction in the atmosphere for similar radicals. Additionally, these processes are competitive even under typical "high NO" conditions employed in chamber studies, suggesting a possible role for these reactions in explaining the shortcomings of previous mechanistic interpretations. Perhaps of equal importance is the ability of alkoxy radicals to abstract hydroperoxy hydrogens fast enough to compete against fast unimolecular processes including β-scission and alkyl isomerization.

The rapid scrambling of the radical center enables subsequent autoxidation pathways that are otherwise inaccessible. For example, the α-OH and α-OOH H-shifts quantified in this work are not accessible without this chemistry due to the presence of the α-methyl substituent in the precursor. This suggests that reaction mechanisms must account for the migration of hydroperoxy hydrogens in order to capture the atmospheric fate of these species. Due to ongoing NO_x emission reductions,[91] such organic hydroperoxides formed through both HO_2 chemistry and autoxidation will comprise an increasingly large share of reactive atmospheric trace gases.

This study emphasizes the need to understand the fate of these autoxidation products. In alkane oxidation, we have shown that ketohydroperoxides are significant products. In order to better assess their role in the urban atmosphere as it relates to air quality, a study that quantitatively examines the fate of ketohydroperoxides (e.g. photolysis, deposition, oxidation, or aerosol transfer) is needed.

ASSOCIATED CONTENT

Supporting Information

Calibration factors, NMR spectra, chromatographic analysis, uncertainty, additional computational results, and temperature-dependent rate expressions. This material is available free of charge via the Internet at http://pubs.acs.org.

Corresponding Author

*E-mail: wennberg@caltech.edu and hgk@chem.ku.dk

Notes

The Authors declare no competing financial interest.

References

1. Seinfeld, J. H.; Pandis, S. N., *Atmospheric Chemistry and Physics: From Air Pollution to Climate Change*. Wiley: New York, 1998.
2. Orlando, J. J.; Tyndall, G. S., Laboratory Studies of Organic Peroxy Radical Chemistry: An Overview with Emphasis on Recent Issues of Atmospheric Significance. *Chem. Soc. Rev.* **2012,** *41* (19), 6294-6317.
3. Peeters, J.; Nguyen, T. L.; Vereecken, L., HO_x Radical Regeneration in the Oxidation of Isoprene. *Phys. Chem. Chem. Phys.* **2009,** *11* (28), 5935-5939.
4. Asatryan, R.; da Silva, G.; Bozzelli, J. W., Quantum Chemical Study of the Acrolein (CH_2CHCHO) + OH + O_2 Reactions. *J. Phys. Chem. A* **2010,** *114* (32), 8302-8311.
5. Crounse, J. D.; Paulot, F.; Kjaergaard, H. G.; Wennberg, P. O., Peroxy Radical Isomerization in the Oxidation of Isoprene. *Phys. Chem. Chem. Phys.* **2011,** *13* (30), 13607-13613.
6. Vereecken, L.; Francisco, J. S., Theoretical Studies of Atmospheric Reaction Mechanisms in the Troposphere. *Chem. Soc. Rev.* **2012,** *41* (19), 6259-6293.
7. Crounse, J. D.; Knap, H. C.; Ørnsø, K. B.; Jørgensen, S.; Paulot, F.; Kjaergaard, H. G.; Wennberg, P. O., Atmospheric Fate of Methacrolein. 1. Peroxy Radical Isomerization Following Addition of OH and O_2. *J. Phys. Chem. A* **2012,** *116* (24), 5756-5762.
8. Crounse, J. D.; Nielsen, L. B.; Jørgensen, S.; Kjaergaard, H. G.; Wennberg, P. O., Autoxidation of Organic Compounds in the Atmosphere. *J. Phys. Chem. Lett.* **2013,** *4* (20), 3513-3520.
9. Knap, H. C.; Jørgensen, S.; Kjaergaard, H. G., Theoretical Investigation of the Hydrogen Shift Reactions in Peroxy Radicals Derived from the Atmospheric Decomposition of 3-methyl-3-buten-1-ol (MBO331). *Chem. Phys. Lett.* **2015,** *619*, 236-240.
10. Jokinen, T.; Sipilä, M.; Richters, S.; Kerminen, V.; Paasonen, P.; Stratmann, F.; Worsnop, D.; Kulmala, M.; Ehn, M.; Herrmann, H., et al., Rapid Autoxidation Forms

Highly Oxidized RO_2 Radicals in the Atmosphere. *Angew. Chem. Int. Ed.* **2014,** *53* (52), 14596-14600.

11. Kurtén, T.; Rissanen, M. P.; Mackeprang, K.; Thornton, J. A.; Hyttinen, N.; Jørgensen, S.; Ehn, M.; Kjaergaard, H. G., Computational Study of Hydrogen Shifts and Ring-Opening Mechanisms in α-Pinene Ozonolysis Products. *J. Phys. Chem. A* **2015,** *119* (46), 11366-11375.

12. Richters, S.; Herrmann, H.; Berndt, T., Highly Oxidized RO_2 Radicals and Consecutive Products from the Ozonolysis of Three Sesquiterpenes. *Environ. Sci. Technol.* **2016,** *50* (5), 2354-2362.

13. Wang, S.; Wu, R.; Berndt, T.; Ehn, M.; Wang, L., Formation of Highly Oxidized Radicals and Multifunctional Products from the Atmospheric Oxidation of Alkylbenzenes. *Environ. Sci. Technol.* **2017,** *51* (15), 8442-8449.

14. Xu, L.; Møller, K. H.; Crounse, J. D.; Otkjær, R. V.; Kjaergaard, H. G.; Wennberg, P. O., Unimolecular Reactions of Peroxy Radicals Formed in the Oxidation of α-Pinene and β-Pinene by Hydroxyl Radical, in prep for *J. Phys. Chem. A.*

15. Savee, J. D.; Papajak, E.; Rotavera, B.; Huang, H.; Eskola, A. J.; Welz, O.; Sheps, L.; Taatjes, C. A.; Zádor, J.; Osborn, D. L., Direct Observation and Kinetics of a Hydroperoxyalkyl Radical (QOOH). *Science* **2015,** *347* (6222), 643-646.

16. Taatjes, C. A., Uncovering the Fundamental Chemistry of Alkyl + O_2 Reactions Via Measurements of Product Formation. *J. Phys. Chem. A* **2006,** *110* (13), 4299-4312.

17. Zádor, J.; Taatjes, C. A.; Fernandes, R. X., Kinetics of Elementary Reactions in Low-Temperature Autoignition Chemistry. *Prog. Energy Combust. Sci.* **2011,** *37* (4), 371-421.

18. Ehn, M.; Thornton, J. A.; Kleist, E.; Sipila, M.; Junninen, H.; Pullinen, I.; Springer, M.; Rubach, F.; Tillmann, R.; Lee, B., et al., A Large Source of Low-Volatility Secondary Organic Aerosol. *Nature* **2014,** *506* (7489), 476-479.

19. Zhang, X.; Lambe, A. T.; Upshur, M. A.; Brooks, W. A.; Gray Bé, A.; Thomson, R. J.; Geiger, F. M.; Surratt, J. D.; Zhang, Z.; Gold, A., et al., Highly Oxygenated Multifunctional Compounds in α-Pinene Secondary Organic Aerosol. *Environ. Sci. Technol.* **2017,** *51* (11), 5932-5940.

20. Berndt, T.; Richters, S.; Jokinen, T.; Hyttinen, N.; Kurtén, T.; Otkjær, R. V.; Kjaergaard, H. G.; Stratmann, F.; Herrmann, H.; Sipilä, M., et al., Hydroxyl Radical-Induced Formation of Highly Oxidized Organic Compounds. *Nat. Commun.* **2016,** *7*, 13677.

21. Jokinen, T.; Berndt, T.; Makkonen, R.; Kerminen, V.-M.; Junninen, H.; Paasonen, P.; Stratmann, F.; Herrmann, H.; Guenther, A. B.; Worsnop, D. R., et al., Production of Extremely Low Volatile Organic Compounds from Biogenic Emissions: Measured Yields and Atmospheric Implications. *Proc. Natl. Acad. Sci. U.S.A.* **2015,** *112* (23), 7123-7128.

22. Mentel, T. F.; Springer, M.; Ehn, M.; Kleist, E.; Pullinen, I.; Kurtén, T.; Rissanen, M.; Wahner, A.; Wildt, J., Formation of Highly Oxidized Multifunctional Compounds: Autoxidation of Peroxy Radicals Formed in the Ozonolysis of Alkenes – Deduced from Structure–Product Relationships. *Atmos. Chem. Phys.* **2015,** *15* (12), 6745-6765.

23. Zhang, X.; McVay, R. C.; Huang, D. D.; Dalleska, N. F.; Aumont, B.; Flagan, R. C.; Seinfeld, J. H., Formation and Evolution of Molecular Products in α-Pinene Secondary Organic Aerosol. *Proc. Natl. Acad. Sci. U.S.A.* **2015,** *112* (46), 14168-14173.

24. Mutzel, A.; Poulain, L.; Berndt, T.; Iinuma, Y.; Rodigast, M.; Böge, O.; Richters, S.; Spindler, G.; Sipilä, M.; Jokinen, T., et al., Highly Oxidized Multifunctional Organic Compounds Observed in Tropospheric Particles: A Field and Laboratory Study. *Environ. Sci. Technol.* **2015,** *49* (13), 7754-7761.

25. Kirkby, J.; Duplissy, J.; Sengupta, K.; Frege, C.; Gordon, H.; Williamson, C.; Heinritzi, M.; Simon, M.; Yan, C.; Almeida, J., et al., Ion-Induced Nucleation of Pure Biogenic Particles. *Nature* **2016,** *533* (7604), 521-526.

26. Schobesberger, S.; Junninen, H.; Bianchi, F.; Lönn, G.; Ehn, M.; Lehtipalo, K.; Dommen, J.; Ehrhart, S.; Ortega, I. K.; Franchin, A., et al., Molecular Understanding of Atmospheric Particle Formation from Sulfuric Acid and Large Oxidized Organic Molecules. *Proc. Natl. Acad. Sci. U.S.A.* **2013,** *110* (43), 17223-17228.

27. Riccobono, F.; Schobesberger, S.; Scott, C. E.; Dommen, J.; Ortega, I. K.; Rondo, L.; Almeida, J.; Amorim, A.; Bianchi, F.; Breitenlechner, M., et al., Oxidation Products of Biogenic Emissions Contribute to Nucleation of Atmospheric Particles. *Science* **2014,** *344* (6185), 717-721.

28. Zhao, J.; Ortega, J.; Chen, M.; McMurry, P. H.; Smith, J. N., Dependence of Particle Nucleation and Growth on High-Molecular-Weight Gas-Phase Products During Ozonolysis of α-Pinene. *Atmos. Chem. Phys.* **2013,** *13* (15), 7631-7644.

29. Bianchi, F.; Tröstl, J.; Junninen, H.; Frege, C.; Henne, S.; Hoyle, C. R.; Molteni, U.; Herrmann, E.; Adamov, A.; Bukowiecki, N., et al., New Particle Formation in the Free Troposphere: A Question of Chemistry and Timing. *Science* **2016,** *352* (6289), 1109-12.

30. Kulmala, M.; Kontkanen, J.; Junninen, H.; Lehtipalo, K.; Manninen, H. E.; Nieminen, T.; Petäjä, T.; Sipilä, M.; Schobesberger, S.; Rantala, P., et al., Direct Observations of Atmospheric Aerosol Nucleation. *Science* **2013,** *339* (6122), 943-946.

31. Stolzenburg, D.; Fischer, L.; Vogel, A. L.; Heinritzi, M.; Schervish, M.; Simon, M.; Wagner, A. C.; Dada, L.; Ahonen, L. R.; Amorim, A., et al., Rapid Growth of Organic Aerosol Nanoparticles over a Wide Tropospheric Temperature Range. *Proc. Natl. Acad. Sci. U.S.A.* **2018,** *115* (37), 9122-9127.

32. Praske, E.; Otkjær, R. V.; Crounse, J. D.; Hethcox, J. C.; Stoltz, B. M.; Kjaergaard, H. G.; Wennberg, P. O., Atmospheric Autoxidation Is Increasingly Important in Urban and Suburban North America. *Proc. Natl. Acad. Sci. U.S.A.* **2018,** *115* (1), 64-69.

33. Otkjær, R. V.; Jakobsen, H. H.; Tram, C. M.; Kjaergaard, H. G., Calculated Hydrogen Shift Rate Constants in Substituted Alkyl Peroxy Radicals. *J. Phys. Chem. A* **2018**, *122* (43), 8665-8673.

34. Jorand, F.; Heiss, A.; Perrin, O.; Sahetchian, K.; Kerhoas, L.; Einhorn, J., Isomeric Hexyl-Ketohydroperoxides Formed by Reactions of Hexoxy and Hexylperoxy Radicals in Oxygen. *Int. J. Chem. Kinet.* **2003,** *35* (8), 354-366.

35. Liu, Z.; Nguyen, V. S.; Harvey, J.; Muller, J.-F.; Peeters, J., The Photolysis of α-Hydroperoxycarbonyls. *Phys. Chem. Chem. Phys.* **2018,** *20* (10), 6970-6979.

36. Goldsmith, C. F.; Green, W. H.; Klippenstein, S. J., Role of O_2 + QOOH in Low-Temperature Ignition of Propane. 1. Temperature and Pressure Dependent Rate Coefficients. *J. Phys. Chem. A* **2012,** *116* (13), 3325-3346.

37. Miyoshi, A., Systematic Computational Study on the Unimolecular Reactions of Alkylperoxy (RO$_2$), Hydroperoxyalkyl (QOOH), and Hydroperoxyalkylperoxy (O$_2$QOOH) Radicals. *J. Phys. Chem. A* **2011,** *115* (15), 3301-3325.

38. Mohamed, S. Y.; Davis, A. C.; Al Rashidi, M. J.; Sarathy, S. M., High-Pressure Limit Rate Rules for α-H Isomerization of Hydroperoxyalkylperoxy Radicals. *J. Phys. Chem. A* **2018,** *122* (14), 3626-3639.

39. Sharma, S.; Raman, S.; Green, W. H., Intramolecular Hydrogen Migration in Alkylperoxy and Hydroperoxyalkylperoxy Radicals: Accurate Treatment of Hindered Rotors. *J. Phys. Chem. A* **2010,** *114* (18), 5689-5701.

40. Yao, Q.; Sun, X.-H.; Li, Z.-R.; Chen, F.-F.; Li, X.-Y., Pressure-Dependent Rate Rules for Intramolecular H-Migration Reactions of Hydroperoxyalkylperoxy Radicals in Low Temperature. *J. Phys. Chem. A* **2017,** *121* (16), 3001-3018.

41. Asatryan, R.; Bozzelli, J. W., Chain Branching and Termination in the Low-Temperature Combustion of n-Alkanes: 2-Pentyl Radical + O$_2$, Isomerization and Association of the Second O$_2$. *J. Phys. Chem. A* **2010,** *114* (29), 7693-7708.

42. Wang, Z.; Popolan-Vaida, D. M.; Chen, B.; Moshammer, K.; Mohamed, S. Y.; Wang, H.; Sioud, S.; Raji, M. A.; Kohse-Höinghaus, K.; Hansen, N., et al., Unraveling the Structure and Chemical Mechanisms of Highly Oxygenated Intermediates in Oxidation of Organic Compounds. *Proc. Natl. Acad. Sci. U.S.A.* **2017,** *114* (50), 13102-13107.

43. Sha, Y.; Dibble, T. S., Tunneling Effect in 1,5 H-Migration of a Prototypical OOQOOH. *Chem. Phys. Lett.* **2016,** *646*, 153-157.

44. Jørgensen, S.; Knap, H. C.; Otkjær, R. V.; Jensen, A. M.; Kjeldsen, M. L. H.; Wennberg, P. O.; Kjaergaard, H. G., Rapid Hydrogen Shift Scrambling in Hydroperoxy-Substituted Organic Peroxy Radicals. *J. Phys. Chem. A* **2016,** *120* (2), 266-275.

45. Knap, H. C.; Jørgensen, S., Rapid Hydrogen Shift Reactions in Acyl Peroxy Radicals. *J. Phys. Chem. A* **2017,** *121* (7), 1470-1479.

46. Dibble, T. S., Intramolecular Hydrogen Bonding and Double H-Atom Transfer in Peroxy and Alkoxy Radicals from Isoprene. *J. Phys. Chem. A* **2004,** *108* (12), 2199-2207.

47. Dibble, T. S., Prompt Chemistry of Alkenoxy Radical Products of the Double H-Atom Transfer of Alkoxy Radicals from Isoprene. *J. Phys. Chem. A* **2004,** *108* (12), 2208-2215.

48. Eyring, H., The Activated Complex and the Absolute Rate of Chemical Reactions. *Chemical Reviews* **1935,** *17* (1), 65-77.

49. Evans, M. G.; Polanyi, M., Some Applications of the Transition State Method to the Calculation of Reaction Velocities, Especially in Solution. *Trans. Faraday Soc.* **1935,** *31* (0), 875-894.

50. Vereecken, L.; Peeters, J., The 1,5-H-Shift in 1-Butoxy: A Case Study in the Rigorous Implementation of Transition State Theory for a Multirotamer System. *J. Chem. Phys.* **2003,** *119* (10), 5159-5170.

51. Møller, K. H.; Otkjær, R. V.; Hyttinen, N.; Kurtén, T.; Kjaergaard, H. G., Cost-Effective Implementation of Multiconformer Transition State Theory for Peroxy Radical Hydrogen Shift Reactions. *J. Phys. Chem. A* **2016,** *120* (51), 10072-10087.

52. Eckart, C., The Penetration of a Potential Barrier by Electrons. *Phys. Rev.* **1930,** *35* (11), 1303-1309.

53. Halgren, T. A., Merck Molecular Force Field. I. Basis, Form, Scope, Parameterization, and Performance of MMFF94. *J. Comput. Chem.* **1996,** *17* (5-6), 490-519.

54. Halgren, T. A., Merck Molecular Force Field. II. MMFF94 Van Der Waals and Electrostatic Parameters for Intermolecular Interactions. *J. Comput. Chem.* **1996,** *17* (5-6), 520-552.

55. Halgren, T. A., Merck Molecular Force Field. III. Molecular Geometries and Vibrational Frequencies for MMFF94. *J. Comput. Chem.* **1996,** *17* (5-6), 553-586.

56. Halgren, T. A.; Nachbar, R. B., Merck Molecular Force Field. IV. Conformational Energies and Geometries for MMFF94. *J. Comput. Chem.* **1996,** *17* (5-6), 587-615.

57. Halgren, T. A., Merck Molecular Force Field. V. Extension of MMFF94 Using Experimental Data, Additional Computational Data, and Empirical Rules. *J. Comput. Chem.* **1996,** *17* (5-6), 616-641.

58. Halgren, T. A., MMFF VII. Characterization of MMFF94, MMFF94s, and Other Widely Available Force Fields for Conformational Energies and for Intermolecular-Interaction Energies and Geometries. *J. Comput. Chem.* **1999,** *20* (7), 730-748.

59. Spartan'14; Wavefunction Inc.: Irvine, CA, 2014.

60. Becke, A. D., Density-Functional Thermochemistry. III. The Role of Exact Exchange. *J. Chem. Phys.* **1993,** *98* (7), 5648-5652.

61. Lee, C.; Yang, W.; Parr, R. G., Development of the Colle-Salvetti Correlation-Energy Formula into a Functional of the Electron Density. *Phys. Rev. B* **1988,** *37* (2), 785-789.

62. Hehre, W. J.; Ditchfield, R.; Pople, J. A., Self—Consistent Molecular Orbital Methods. XII. Further Extensions of Gaussian—Type Basis Sets for Use in Molecular Orbital Studies of Organic Molecules. *J. Chem. Phys.* **1972,** *56* (5), 2257-2261.

63. Clark, T.; Chandrasekhar, J.; Spitznagel, G. W.; Schleyer, P. V. R., Efficient Diffuse Function-Augmented Basis Sets for Anion Calculations. III. The 3-21+G Basis Set for First-Row Elements, Li–F. *J. Comput. Chem.* **1983,** *4* (3), 294-301.

64. Frisch, M. J.; Pople, J. A.; Binkley, J. S., Self-Consistent Molecular Orbital Methods 25. Supplementary Functions for Gaussian Basis Sets. *J. Chem. Phys.* **1984,** *80* (7), 3265-3269.

65. Frisch, M. J.; Trucks, G. W.; Schlegel, H. B.; Scuseria, G. E.; Robb, M. A.; Cheeseman, J. R.; Scalmani, G.; Barone, V.; Petersson, G. A.; Nakatsuji, H., et al. *Gaussian 09 Revision D.01*, Wallingford, CT, 2009.

66. Otkjær, R. V.; Møller, K. H. Github: Removal of Duplicate Conformers V1.0. https://github.com/rasmusotkjaer/Removal-of-Duplicate-Conformers/ (accessed August 23, 2018).

67. Kendall, R. A.; Dunning Jr., T. H.; Harrison, R. J., Electron Affinities of the First-Row Atoms Revisited. Systematic Basis Sets and Wave Functions. *J. Chem. Phys.* **1992,** *96* (9), 6796-6806.

68. Chai, J.-D.; Head-Gordon, M., Long-Range Corrected Hybrid Density Functionals with Damped Atom-Atom Dispersion Corrections. *Phys. Chem. Chem. Phys.* **2008,** *10* (44), 6615-6620.

69. Peterson, K. A.; Adler, T. B.; Werner, H.-J., Systematically Convergent Basis Sets for Explicitly Correlated Wavefunctions: The Atoms H, He, B–Ne, and Al–Ar. *J. Chem. Phys.* **2008,** *128* (8), 084102.

70. Werner, H.-J.; Knizia, G.; Manby, F. R., Explicitly Correlated Coupled Cluster Methods with Pair-Specific Geminals. *Mol. Phys.* **2011,** *109* (3), 407-417.

71. Adler, T. B.; Knizia, G.; Werner, H.-J., A Simple and Efficient CCSD(T)-F12 Approximation. *J. Chem. Phys.* **2007,** *127* (22), 221106.

72. Knizia, G.; Adler, T. B.; Werner, H.-J., Simplified CCSD(T)-F12 Methods: Theory and Benchmarks. *J. Chem. Phys.* **2009,** *130* (5), 054104.

73. Watts, J. D.; Gauss, J.; Bartlett, R. J., Coupled-Cluster Methods with Noniterative Triple Excitations for Restricted Open-Shell Hartree–Fock and Other General Single Determinant Reference Functions. Energies and Analytical Gradients. *J. Chem. Phys.* **1993,** *98* (11), 8718-8733.

74. Werner H.J.; Knowles P.J.; Knizia G.; Manby F.R.; Schutz M., MOLPRO, Version 2012.1, a Package of Ab Initio Programs. **2012**.

75. Taylor, W. D.; Allston, T. D.; Moscato, M. J.; Fazekas, G. B.; Kozlowski, R.; Takacs, G. A., Atmospheric Photo-Dissociation Lifetimes for Nitromethane, Methyl Nitrite, and Methyl Nitrate. *Int. J. Chem. Kinet.* **1980,** *12* (4), 231-240.

76. Sharpe, S. W.; Johnson, T. J.; Sams, R. L.; Chu, P. M.; Rhoderick, G. C.; Johnson, P. A., Gas-Phase Databases for Quantitative Infrared Spectroscopy. *Appl. Spectrosc.* **2004,** *58* (12), 1452-1461.

77. Vasquez, K. T.; Allen, H. M.; Crounse, J. D.; Praske, E.; Xu, L.; Noelscher, A. C.; Wennberg, P. O., Low-Pressure Gas Chromatography with Chemical Ionization Mass Spectrometry for Quantification of Multifunctional Organic Compounds in the Atmosphere. *Atmos. Meas. Tech. Discuss.* **2018,** in review.

78. Crounse, J. D.; McKinney, K. A.; Kwan, A. J.; Wennberg, P. O., Measurement of Gas-Phase Hydroperoxides by Chemical Ionization Mass Spectrometry. *Anal. Chem.* **2006,** *78* (19), 6726-6732.

79. Paulot, F.; Crounse, J. D.; Kjaergaard, H. G.; Kroll, J. H.; Seinfeld, J. H.; Wennberg, P. O., Isoprene Photooxidation: New Insights into the Production of Acids and Organic Nitrates. *Atmos. Chem. Phys.* **2009,** *9* (4), 1479-1501.

80. Praske, E.; Crounse, J. D.; Bates, K. H.; Kurtén, T.; Kjaergaard, H. G.; Wennberg, P. O., Atmospheric Fate of Methyl Vinyl Ketone: Peroxy Radical Reactions with NO and HO$_2$. *J. Phys. Chem. A* **2015,** *119* (19), 4562-4572.

81. Bates, K. H.; Crounse, J. D.; St Clair, J. M.; Bennett, N. B.; Nguyen, T. B.; Seinfeld, J. H.; Stoltz, B. M.; Wennberg, P. O., Gas Phase Production and Loss of Isoprene Epoxydiols. *J. Phys. Chem. A* **2014,** *118* (7), 1237-1246.

82. St. Clair, J. M.; Rivera-Rios, J. C.; Crounse, J. D.; Knap, H. C.; Bates, K. H.; Teng, A. P.; Jørgensen, S.; Kjaergaard, H. G.; Keutsch, F. N.; Wennberg, P. O., Kinetics and Products of the Reaction of the First-Generation Isoprene Hydroxy Hydroperoxide (ISOPOOH) with OH. *J. Phys. Chem. A* **2016,** *120* (9), 1441-1451.

83. Schwantes, R. H.; Teng, A. P.; Nguyen, T. B.; Coggon, M. M.; Crounse, J. D.; St. Clair, J. M.; Zhang, X.; Schilling, K. A.; Seinfeld, J. H.; Wennberg, P. O., Isoprene NO$_3$

Oxidation Products from the RO_2 + HO_2 Pathway. *J. Phys. Chem. A* **2015,** *119* (40), 10158-10171.

84. Teng, A. P.; Crounse, J. D.; Wennberg, P. O., Isoprene Peroxy Radical Dynamics. *J. Am. Chem. Soc.* **2017,** *139* (15), 5367-5377.

85. Wennberg, P. O.; Bates, K. H.; Crounse, J. D.; Dodson, L. G.; McVay, R. C.; Mertens, L. A.; Nguyen, T. B.; Praske, E.; Schwantes, R. H.; Smarte, M. D., et al., Gas-Phase Reactions of Isoprene and its Major Oxidation Products. *Chem. Rev.* **2018,** *118* (7), 3337-3390.

86. Peeters, J.; Müller, J.-F.; Stavrakou, T.; Nguyen, V. S., Hydroxyl Radical Recycling in Isoprene Oxidation Driven by Hydrogen Bonding and Hydrogen Tunneling: The Upgraded LIM1 Mechanism. *J. Phys. Chem. A* **2014,** *118* (38), 8625-8643.

87. Vereecken, L.; Peeters, J., Decomposition of Substituted Alkoxy Radicals-Part I: A Generalized Structure-Activity Relationship for Reaction Barrier Heights. *Phys. Chem. Chem. Phys.* **2009,** *11* (40), 9062-9074.

88. Atkinson, R., Rate Constants for the Atmospheric Reactions of Alkoxy Radicals: An Updated Estimation Method. *Atmos. Environ.* **2007,** *41* (38), 8468-8485.

89. Davis, A. C.; Francisco, J. S., Ab Initio Study of Hydrogen Migration across n-Alkyl Radicals. *J. Phys. Chem. A* **2011,** *115* (14), 2966-2977.

90. Davis, A. C.; Francisco, J. S., Ab Initio Study of Key Branching Reactions in Biodiesel and Fischer–Tropsch Fuels. *J. Am. Chem. Soc.* **2011,** *133* (47), 19110-19124.

91. Russell, A. R.; Valin, L. C.; Cohen, R. C., Trends in OMI NO_2 Observations over the United States: Effects of Emission Control Technology and the Economic Recession. *Atmos. Chem. Phys.* **2012,** *12* (24), 12197-12209.

Chapter 5

OUTLOOK AND FUTURE WORK

This thesis describes laboratory studies performed to elucidate the oxidation mechanisms of hydrocarbons. While significant contributions were made, there remain lines of investigation that merit further research.

In Chapter 1, the mechanism reported for the internal addition of OH to MVK in the RO_2 + HO_2 channel is largely speculative. For this RO_2, the recent study of Fuchs et al. suggests the existence of a 1,4 H-shift to yield a hydroperoxy diketone.[1] Also of interest is a recent computational study reporting the likely mechanism for the photolysis of the α-hydroperoxyketone.[2] The mechanism suggested involves a 1,5 H-shift following excitation to yield an enol. Subsequent review of the experimental data suggests that this mechanism is feasible, as a product ion possibly corresponding to that of the enol was detected.

Chapters 2 and 3 investigate the importance of intramolecular RO_2 chemistry in alkane oxidation. The findings add to a growing body of evidence suggesting that RO_2 H-shifts play a role in the oxidation of a broad range of atmospheric hydrocarbons. It will be important to continue to evaluate, either computationally or experimentally, the prevalence of these H-shifts in gas-phase hydrocarbon oxidation mechanisms. As NO_x levels decline in response to regulation, the significance of autoxidation will increase and therefore drive the need to assess its implications for air quality.

Ultimately, the impact of this chemistry will be determined by the fate of autoxidation products. For alkanes, ketohydroperoxides are significant products, yet little is quantitatively known about their atmospheric fate. Studies that examine the various loss pathways and epidemiologically assess exposure to these species are warranted. Only once progress has been made in these areas will regulators have actionable data to consider the implementation of mitigation policies.

The mobility of hydroperoxide hydrogens in both peroxy and alkoxy radicals represents another important discovery that certainly has implications for a large number of reaction mechanisms. The large rate constants for these reactions suggest that this chemistry will nearly always outrun bimolecular reaction for species similar to those reported here. Overall, this reaction will add complexity to chemical models, particularly when it enables pathways that did not exist in the initially produced RO_2.

Currently, chemical models possess only a limited treatment of autoxidation. One challenge is that many models do not explicitly treat individual reactions for every hydrocarbon due to computational constraints. Instead, parmeterizations are implemented that require similar molecules to be treated equally. The dependence of chemical structure on H-shift rate constants and the mobility of hydroperoxide hydrogens, however, provide clear examples of where such parameterizations will fail to accurately describe the oxidation sequence. In some instances, this failure may lead to significantly different conclusions that do not correspond with observations. This "tug of war" between experimentalists and modelers is nothing new to the field of atmospheric chemistry. Ultimately, a careful balance between computational cost and accurate description of the chemistry must be sought.

SUPPORTING INFORMATION: ATMOSPHERIC FATE OF METHYL VINYL
KETONE: PEROXY RADICAL REACTIONS WITH NO AND HO$_2$

INSTRUMENTAL CALIBRATION. CIMS sensitivity factors are determined by the specific molecule-ion collision rates and the binding energy of the resulting clusters. The rate of collision can be estimated from the dipole moment and polarizability of the analyte.[1] These properties were calculated using DFT for the C_4 compounds produced in the oxidation of MVK. Because the dipole moment depends on the structural conformation of the molecule, we calculate the population density and dipole of all conformers with a relative population of >5% at 298 K to estimate the conformationally-weighted property. The polarizability was not found to exhibit significant conformational dependence and the calculation was therefore based on the lowest energy structure. Further detail of similar calculations is provided by Garden et al.[2] A summary of these properties along with calibration factors for MVK systems is shown in Table S1.

Table S1. Calculated conformer-weighted dipole moments (μ) and polarizabilites (α) served as the basis for sensitivity determination (see Paulot et al.,[3] unless otherwise noted). k_x is the weighted average of the calculated collision rates (see Su et al.[1]) for conformers having an abundance greater than 5%. These are normalized to the average of the calculated collision rates for CF_3O^- with MVKN and MVKN' at 298 K ($k = 1.8$ x 10^{-9} cm^3 molecule^{-1} s^{-1}) and the mean of the experimentally determined MVKN and MVKN' sensitivities was used to infer the sensitivity for compounds for which no standards were available. Masses (m/z) represent the cluster mass with CF_3O^-. For compounds reacting with CF_3O^- to form multiple product ions, the sum of all known product ions have been used for quantification. Isoprene nitrate (1-hydroxy-3-methylbut-3-en-2-yl nitrate, ISOPN-4,3) has been included for additional comparison between theory and experiment.

molecule	m/z	μ (D)	α (Å^3)	k_x (10^{-9} cm^3 molecule^{-1} s^{-1})	calculated sensitivity (x 10^{-4}) [a]	experimental sensitivity (x 10^{-4}) [a]
ISOPN-4,3	232	2.5	11	1.9	3.1	3.7
glycolaldehyde	145	2.3	4.5	2.0	3.1	3.0 ± 0.2 [b]
hydroxy diketone	187	2.1 [c]	7.2 [c]	1.8	2.7	-
4,3-hydroxy-hydroperoxide	205+139 +101+63	2.6 [c]	8.1 [c]	2.0	3.1	-
MVKN	234	2.3	9.9	1.8	2.8	2.6 ± 0.3 [b]
MVKN'	234	2.2	9.7	1.8	2.7	3.0 ± 0.3 [b]

[a] CF_3O^- CIMS sensitivity (norm. cts. pptv^{-1})

[b] Hydroxy nitrate sensitivities were determined using thermal dissociation LED-induced fluorescence[4] and glycolaldehyde was calibrated as described in the current work. Uncertainties are indicated for measured sensitivities.

[c] Calculated in support of this work by HGK at the B3LYP/6-31G(d) level.
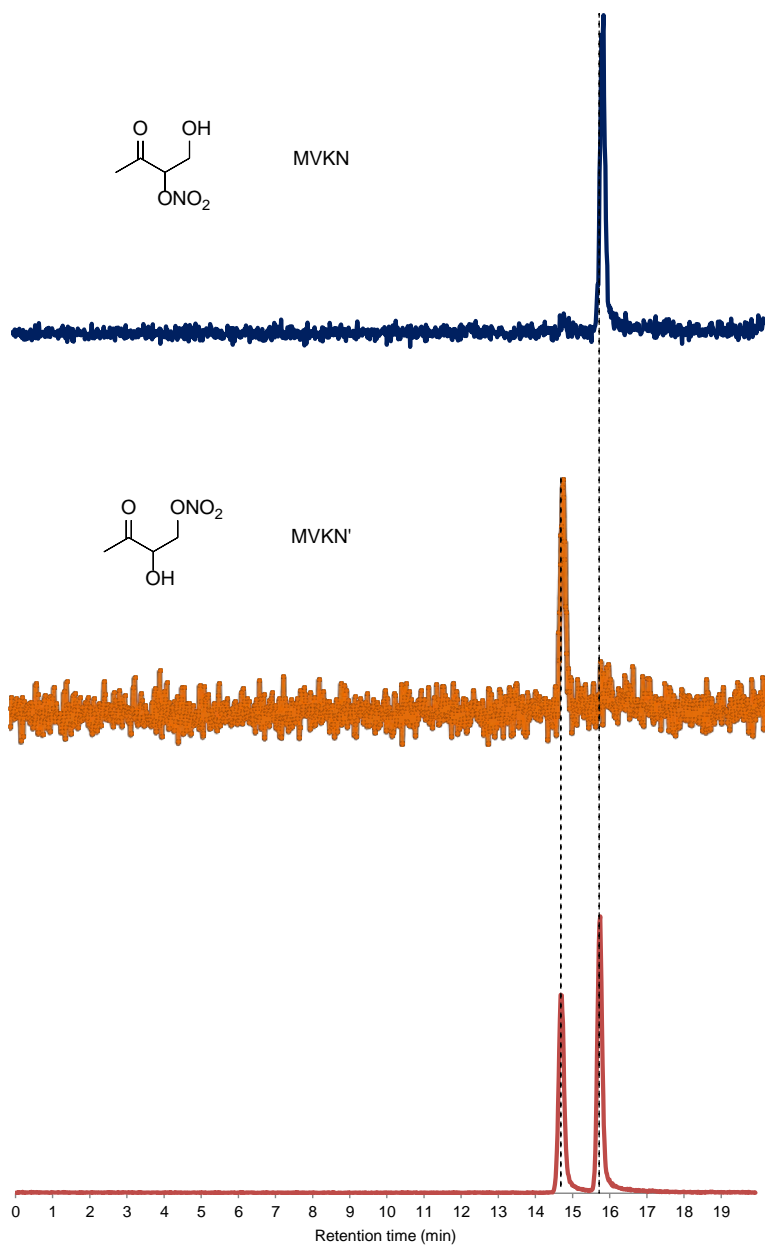
Figure S1. Chromatographic analysis used for the identification of MVKN and MVKN'.

Data are derived from experiments 8 (bottom panel), 14 (mid panel), and 12 (top panel).

The latter two experiments isolated the chemistry of individual RO_2, enabling the structures

and retention times of the individual organic nitrates to be discerned. This assignment also matches the elution order previously reported using a similar column.[5]
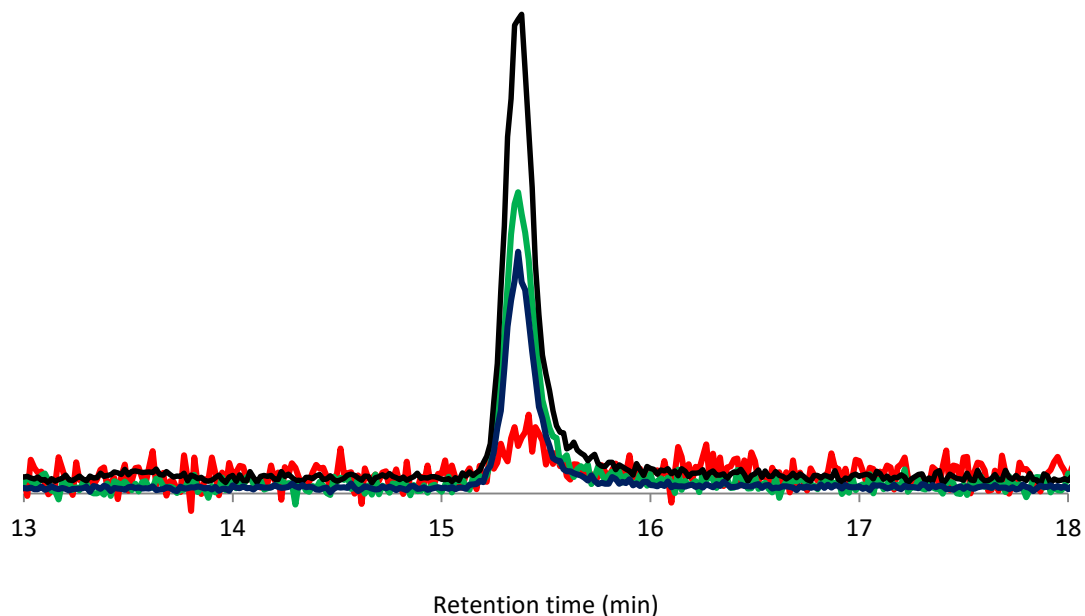
Figure S2. Chromatographic analysis of the 4,3 hydroxy hydroperoxide derived from experiment 1. Shown are the major product ions in order of descending area: *m/z* 139 (black), *m/z* 101 (green), *m/z* 205 (blue), *m/z* 63 (red).

CHEMICAL TRANSPORT MODEL. The following section describes changes made to the GEOS-Chem mechanism (Table S2 – Table S3).[6] The maps (Figure S3 – Figure S5) illustrate the output of the model resulting from the changes. These simulations employ GEOS-Chem v9-02 using GEOS5 meteorology and initialize the model with a 1.5 year spinup before the January – December 2012 final simulation. The Rosenbrock Rodas-3 with Kinetic PreProcessing software was used as the solver.

Table S2. Revisions incorporated into the GEOS-Chem mechanism. The scenarios are consistent with those described by Table 5. The base scenario includes the alkyl nitrate branching determined in this work. Naming conventions used below can be found at http://wiki.seas.harvard.edu/geos-chem.

scenario	base model	revised model
Base (VRO_2 + NO →)	$0.88NO_2$ + $0.35HO_2$ + $0.35CH_2O$ + $0.53MCO_3$ + $0.53GLYC$ + $0.35MGLY$ + $0.12MVKN$; k=2.7 x 10^{-12} x exp(350/T)	$0.965NO_2$ + $0.249HO_2$ + $0.249CH_2O$ + $0.716MCO_3$ + $0.716GLYC$ + $0.249MGLY$ + $0.035MVKN$; k=2.7 x 10^{-12} x exp(350/T)
MVK (VRO_2 + HO_2 →)	1.000 VRP; k=1.82 x 10^{-13} x exp(1300/T)	0.38VRP + 0.62OH + 0.37GLYC + $0.37MCO_3$ + 0.13MEK + $0.25HO_2$ + 0.12MGLY + $0.12CH_2O$; k=1.82 x 10^{-13} x exp(1300/T)
MVK + RCO_3 (MCO_3 + HO_2 →; RCO_3 + HO_2 →; MAO_3 + HO_2 →; VRO_2 + HO_2 →)	0.16 ACTA + 0.16 O_3 + 0.61 OH + 0.61 MO_2 + 0.23 MAP; k=5.2 x 10^{-13} exp(980/T) 0.16 RCOOH + 0.16 O_3 + 0.61 OH + 0.61 ETO_2 + 0.23 PP; k=4.3 x 10^{-13} exp(1040/T) 0.16 O_3 + 0.61 OH + 0.61 CO_2 + 0.61 CH_2O + 0.21 MCO_3 + 0.40 MO_2 + 0.4 CO + 0.23 MAOP; k=4.3 x 10^{-13} exp(1040/T) 1.000 VRP; k=1.82 x 10^{-13} x exp(1300/T)	0.16 ACTA + 0.16 O_3 + 0.61 OH + 0.61 MO_2 + 0.23 MAP; k=5.2 x 10^{-13} exp(980/T) 0.16 RCOOH + 0.16 O_3 + 0.61 OH + 0.61 ETO_2 + 0.23 PP; k=4.3 x 10^{-13} exp(1040/T) 0.16 O_3 + 0.61 OH + 0.61 CO_2 + 0.61 CH_2O + 0.21 MCO_3 + 0.40 MO_2 + 0.4 CO + 0.23 MAOP; k=4.3 x 10^{-13} exp(1040/T) 0.38VRP + 0.62OH + 0.37GLYC + $0.37MCO_3$ + 0.13MEK + $0.25HO_2$ + 0.12MGLY + $0.12CH_2O$; k=1.82 x 10^{-13} x exp(1300/T)
MACR (MRO_2 →)	1.000CO + 1.000HAC + 1.000OH; k=0	1.000CO + 1.000HAC + 1.000OH; k=2.90 x 10^7 x exp(-5297/T)

Table S3. Revised wavelength bins utilized to define the photolysis frequency of the MVK hydroperoxide in the model.

Lower-bound wavelength (nm)	289	298.25	307.45	312.45	320.30	345	412.45
Upper-bound wavelength (nm)	298.25	307.45	312.45	320.30	345	412.45	850
Base cross section (cm^2)	5.621 x 10^{-21}	3.573 x 10^{-21}	2.441 x 10^{-21}	1.755 x 10^{-21}	7.405 x 10^{-22}	4.261 x 10^{-23}	0
New cross section (cm^2)	5.665 x 10^{-20}	4.000 x 10^{-20}	2.740 x 10^{-20}	2.140 x 10^{-20}	7.085 x 10^{-21}	5.634 x 10^{-22}	0

[(MVK+RCO3)−RCO3]/RCO3
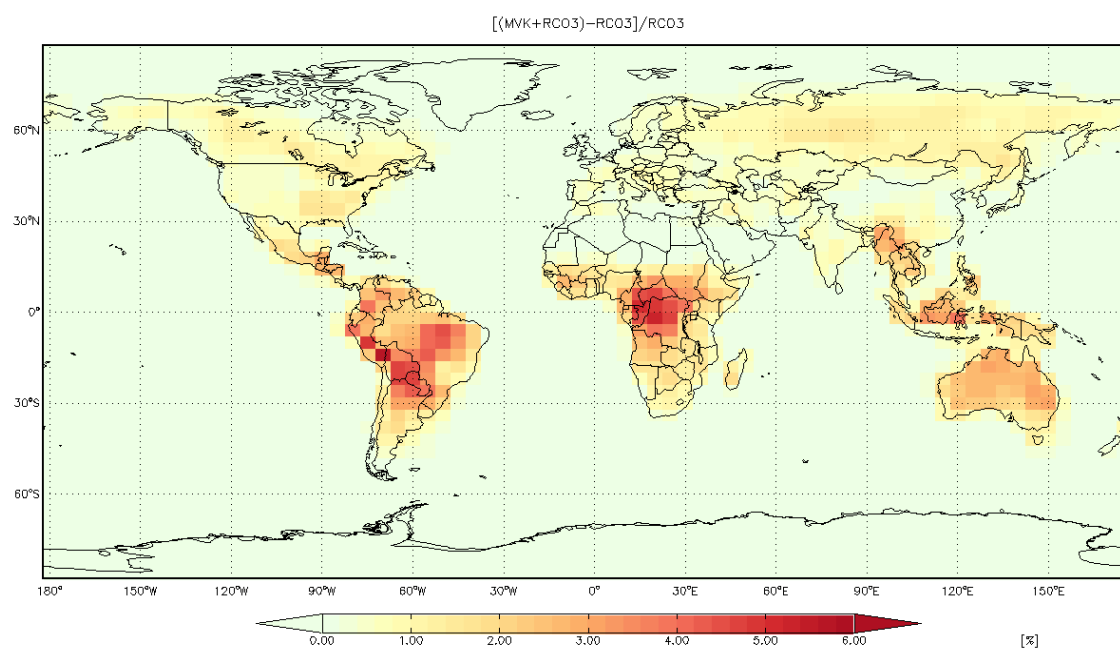
Figure S3. Relative difference in the OH mixing ratio for MVK + RCO$_3$ in the boundary layer (0-1 km).

(MACR−Base)/Base
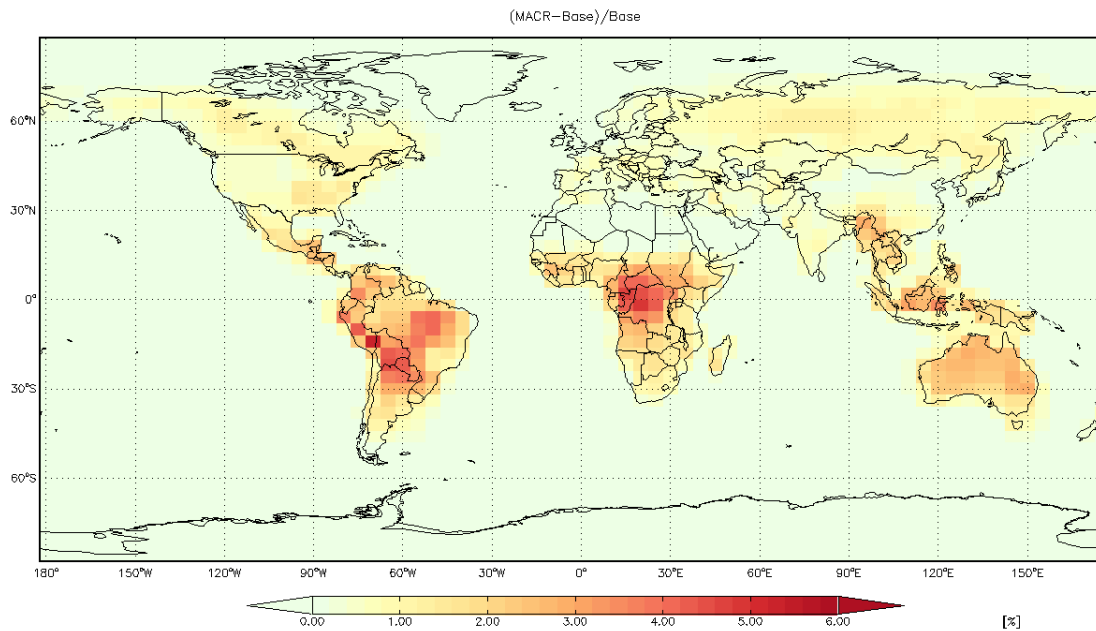
Figure S4. Relative difference in the OH mixing ratio for MACR in the boundary layer (0-1 km).
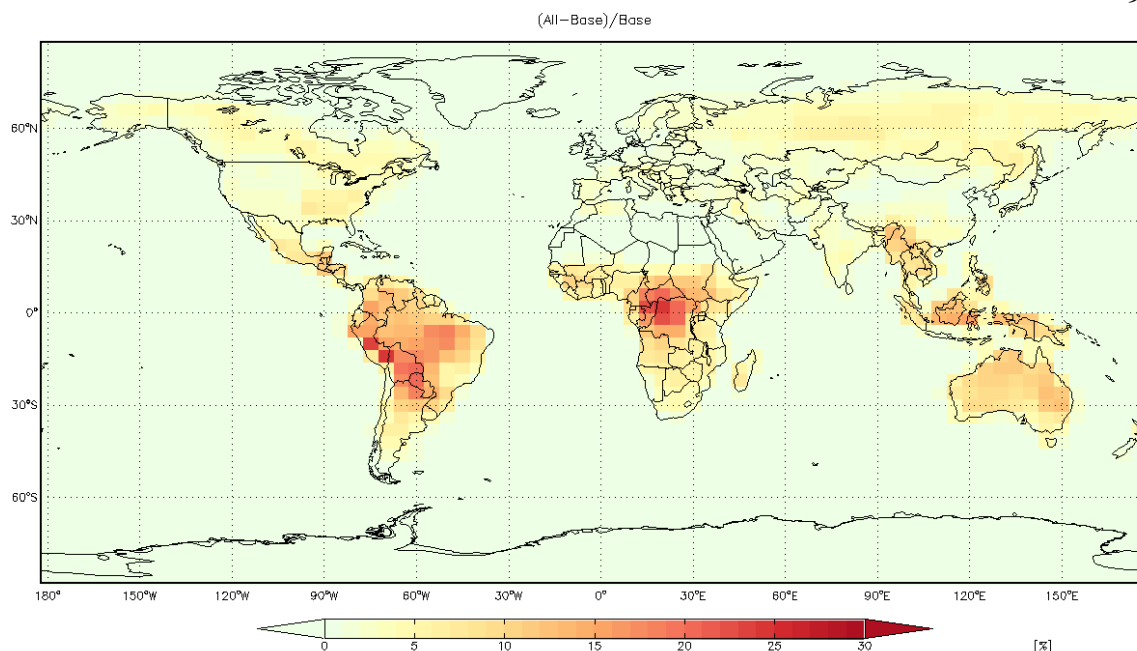
Figure S5. All inclusive: MVK, MACR isomerization, RCO_3, J_{ROOH}; relative difference in the boundary layer (0-1 km).

QUANTUM CHEMICAL CALCULATIONS. To test whether using a UHF reference wave function would lower the coupled-cluster energies for the spin-contaminated transition state TS_A, we performed qualitative RHF-RCCSD(T)/6-31+G(d) and UHF-UCCSD(T)/6-31+G(d) single-point energy calculations with the Gaussian 09 program on the wB97xd/aug-cc-pVTZ - optimized geometry. While the UHF energy was 60.5 kcal/mol below the RHF energy, the UHF-UCCSD energy was 344.0 kcal/mol and the UHF-UCCSD(T) energy 272.9 kcal/mol above the RHF-RCCSD and RHF-RCCSD(T) energies, respectively. Inspection of the CCSD iterations (over 300 were required for convergence) indicates that the UCCSD probably converged to the wrong state. A similar comparison for the alternative TS_A isomer, for which CCSD convergence problems did not occur, yielded more modest energy differences, but the UHF-UCCSD(T) energy was still 5.3 kcal/mol above the RHF-RCCSD(T) energy. Spin contamination at the UHF level was extreme for both of the TS_A isomers; $<S^2> = 0.93…0.95$ before and $0.19…0.20$ after annihilation. This indicates that using a UHF reference in the coupled cluster calculations would neither lower the barrier, nor improve the reliability of the results and suggests that

multireference calculations are required to attain better accuracy. These problems are likely related to the difficulties of even advanced methods like CCSD(T) or even MRCISD in describing the structure and stability of the HO_3 intermediate product. Varandas et al. has suggested that a quantitative prediction of the dissociation energy of HO_3 would require FCI calculations.[7]

The DFT relative energies for reactant and products are within 4 kcal/mol of the ROHF-ROCCSD(T)-F12/VDZ-F12//wB97XD/aug-cc-pVTZ energies and give an idea of the uncertainty expected in these calculations. For the RI and the TS's the difference is higher than usual and, in conjunction with the spin and T1 values, an indication that multireference calculations are needed to obtain accurate values. The DFT barrier values for the ROOH and R(C=O) channels are such that these products would not be observed. The F12 barriers for these channels are lower and thus in better agreement with experiment.

The formation of intermediate product complexes of energies comparable to that of the reactants allow for back reactions that further complicate determination of yields.

Table S4. Spin contamination and T1 diagnostic in the calculations from the different

$RO_2 + HO_2$ channels.

	$<S^2>$ before annihilation [a]	$<S^2>$ after annihilation [a]	T1[b]
ROO	0.7546	0.7500	0.023
OOH	0.7543	0.7500	0.034
^{3}TS	2.0124	2.0001	0.032
ROOH	0.0	0.0	0.013
O_2	2.0101	2.0001	0.008
RI	0.0	0.0	0.016
^{1}TS$_A$	0.5729	0.0167	0.020
RO	0.7577	0.7500	0.028
OH	0.7529	0.7500	0.007
^{1}TS$_B$	0.0	0.0	0.021
R(C=O)	0.0	0.0	0.014

[a] In the UwB97XD/aug-cc-pVTZ calculation.

[b] In the ROHF-ROCCSD(T)-F12/VDZ-F12//wB97XD/aug-cc-pVTZ calculation.

SECOND TETROXIDE. We have found a second tetroxide that also leads to both RO and R(C=O). It is lower in energy than the one in Figure 4, however the TS leading to the products are higher in energy. These pathways are shown below in Figure S6.
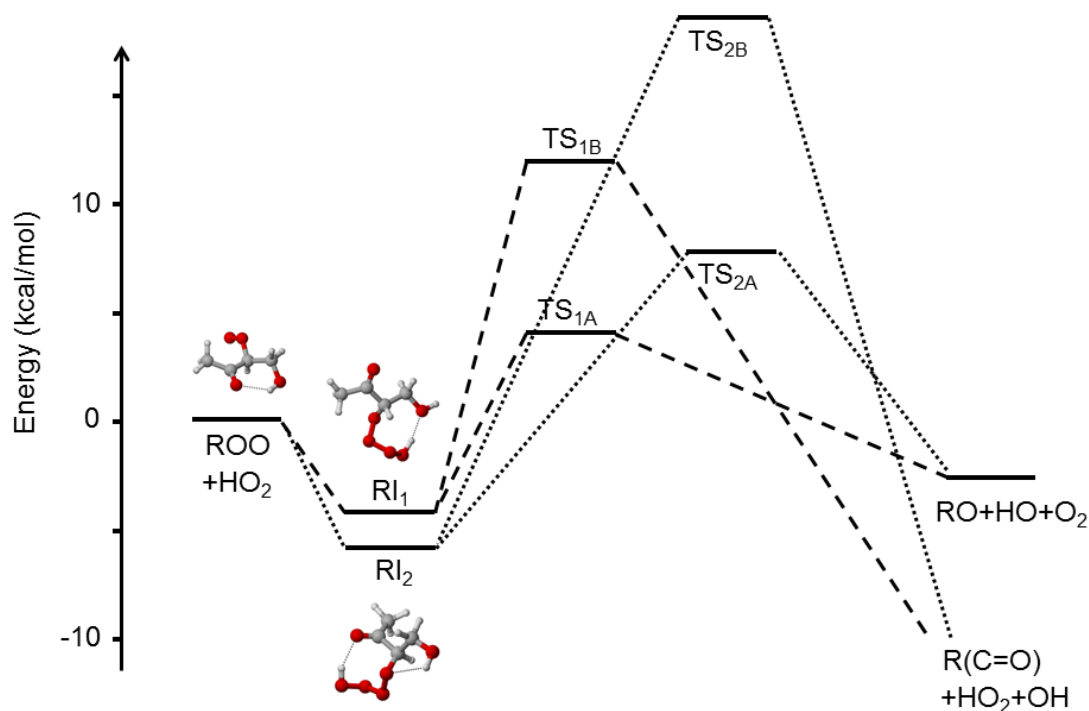
Figure S6. Relative energies (ΔG_{298K}) for the two singlet $RO_2 + HO_2$ channels, including the second tetroxide (RI_2). RI_1 is identical to RI in the manuscript. We have used wB97XD/aug-cc-pVTZ thermochemistry with ROHF-ROCCSD(T)-F12/VDZ-F12 energies. The wB97XD/aug-cc-pVTZ geometries for each of the stationary points are shown.

Table S5. Comparison of the energetics of the channels associated with the two different tetroxides.

	ΔE^a (kcal/mol)	ΔE^b (kcal/mol)	$\Delta G_{298K}{}^c$ (kcal/mol)	TS (imaginary frequency, cm^{-1})
ROO + HO$_2$	0.0	0.0	0.0	-
RI≡RI$_1$	-12.2	-20.4	-4.1	-
RI$_2$	-13.7	-21.7	-6.0	-
TS$_{1A}$≡TS$_A$	+2.5	-8.3	+4.1	212i
TS$_{2A}$	+3.9	-5.1	+7.8	169i
TS$_{1B}$≡ TS$_B$	+11.2	-0.7	+12.0	905i
TS$_{2B}$	+18.1	+6.7	+18.9	1011i

[a] Calculated with wB97XD/aug-cc-pVTZ.

[b] Calculated with ROHF-ROCCSD(T)-F12/VDZ-F12//wB97XD/aug-cc-pVTZ.

[c] Calculated with the wB97XD/aug-cc-pVTZ thermochemistry with CCSD(T)-F12/VDZ-F12 single point energy correction.

TABLE S6. Spin contamination and T1 diagnostic associated with the second tetroxide

RI$_2$ and its TS.

	$<S^2>$ before annihilation [a]	$<S^2>$ after annihilation [a]	T1[b]
RI$_2$	0.0	0.0	0.016
TS$_{2A}$	0.6813	0.0250	0.021
TS$_{2B}$	0.0	0.0	0.022

[a] In the UwB97XD/aug-cc-pVTZ calculation.

[b] In the ROHF-ROCCSD(T)-F12/VDZ-F12//wB97XD/aug-cc-pVTZ calculated.

DECOMPOSITION OF ALKOXY RADICAL FORMED FROM EXTERNAL OH ADDITION TO MVK (R1a). The decomposition of the alkoxy radical formed in the reaction of NO with the peroxy radical produced in R1a can lead to either methylglyoxal ($CH_3(C=O)CHO$) and the CH_2OH radical or glycolaldehyde (CH_2OHCHO) and the $CH_3C=O$ radical. The calculated energies and stationary points are shown in Figure S7 and Table S7. The barrier of the internal alkoxy decomposition will likely be dominated by glycolaldehyde formation.
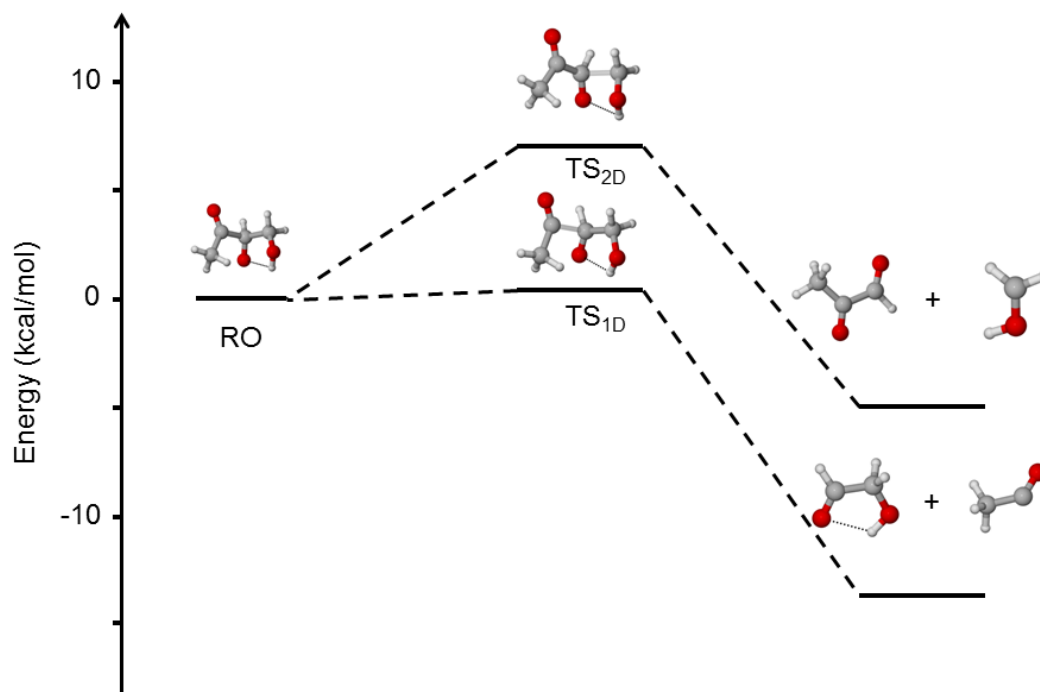
Figure S7. Relative energies (ΔG_{298K}) for the two decomposition channels of the alkoxy formed from external OH addition to MVK. We have used wB97XD/aug-cc-pVTZ thermochemistry with ROHF-ROCCSD(T)-F12/VDZ-F12 energies. The wB97XD/aug-cc-pVTZ geometries for each of the stationary points are shown.

Table S7. Energetics of the different RO decomposition channels

	ΔE^a (kcal/mol)	ΔE^b (kcal/mol)	ΔG_{298K}^c (kcal/mol)	TS (imaginary frequency, cm^{-1})
RO	0.0	0.0	0.0	-
TS$_{1D}$[d]	+3.3	+1.5	+0.4	199.4i
Glycolaldehyde+ CH$_3$(C=O)	+14.2	+10.5	-5.1	-
TS$_{2D}$	+9.0	+8.2	+6.9	237.6i
Methylglyoxal+ CH$_2$OH	+3.9	+0.2	-14.2	-

[a] Calculated with wB97XD/aug-cc-pVTZ.

[b] Calculated with ROHF-ROCCSD(T)-F12/VDZ-F12//wB97XD/aug-cc-pVTZ.

[c] Calculated with the wB97XD/aug-cc-pVTZ thermochemistry with CCSD(T)-F12/VDZ-F12 single point energy correction.

[d] Structure optimized and frequencies and thermal contributions to $\Delta G298K$ calculated using tight optimization criteria and an ultrafine integration grid in order to remove a spurious near-zero imaginary frequency. For consistency, the DFT energy has been computed with a single-point energy evaluation using the normal integration grid.

Table S8. Spin contamination and T1 diagnostic associated with the second RI and its

TS.

	$<S^2>$ before annihilation [a]	$<S^2>$ after annihilation [a]	T1[b]
TS$_{1D}$	0.7617	0.7500	0.018
CH3(C=O)CHO	0.0	0.0	0.014
CH$_2$OH	0.7534	0.7500	0.020
TS$_{2D}$	0.7650	0.7501	0.018
CH$_2$OHCHO	0.0	0.0	0.015
CH$_3$(C=O)	0.7542	0.7500	0.016

[a] In the UwB97XD/aug-cc-pVTZ calculation.

[b] In the ROHF-ROCCSD(T)-F12/VDZ-F12//wB97XD/aug-cc-pVTZ calculation.

Cartesian coordinates for all wB97XD/aug-cc-pVTZ optimized structures, where the electronic energy is in kcal/mol:

```
:::::::::::::::
HO₂
:::::::::::::::
3
Energy:   -94704.3569035
O         0.05500      0.70969       0.00000
O         0.05500     -0.60177       0.00000
H        -0.87995     -0.86335       0.00000

:::::::::::::::
O₂
:::::::::::::::
2
Energy:   -94336.1957928
O         0.00000      0.00000       0.59799
O         0.00000      0.00000      -0.59799

:::::::::::::::
OH
:::::::::::::::
2
Energy:   -47528.0389744
O         0.00000      0.00000       0.10780
H         0.00000      0.00000      -0.86242

:::::::::::::::
R(C=O)
:::::::::::::::
13
Energy: -239529.5526856
C         2.30914     -0.66919      -0.04255
C         1.18192      0.31301       0.00906
C        -0.24329     -0.27535       0.01132
C        -1.39271      0.69344      -0.03597
O        -2.62017      0.03653      -0.01120
H        -2.43716     -0.90952       0.01335
O         1.31295      1.50856       0.04493
O        -0.42236     -1.46679       0.04879
H        -1.29524      1.38686       0.80611
H        -1.28369      1.30066      -0.94242
H         2.25549     -1.23220      -0.97580
H         2.20934     -1.39831       0.76132
H         3.25754     -0.14538       0.02616
```

```
:::::::::::::::
RO
:::::::::::::::
14
Energy: -239869.6979721
C        -1.37690      1.22621       -0.42550
C        -1.09636     -0.18405       -0.02779
C         0.29602     -0.43875        0.78587
C         1.34311     -0.75576       -0.32010
H         0.94661     -1.49381       -1.01589
O        -1.76645     -1.13412       -0.26446
O         0.58962      0.64168        1.47266
H         0.07548     -1.33555        1.38137
H         2.20782     -1.19154        0.19185
H        -0.57105      1.56190       -1.07872
H        -1.35224      1.84999        0.46770
H        -2.33661      1.28831       -0.93013
O         1.69503      0.38722       -1.04428
H         1.88927      1.07665       -0.40252

:::::::::::::::
ROO
:::::::::::::::
15
Energy: -287035.2495299
C         1.55878      1.57985        0.13201
C         0.15972      1.07175       -0.03230
C        -0.05696     -0.43610       -0.19581
O         1.01474     -1.17941        0.41824
O         1.98885     -1.43520       -0.40921
O        -0.80323      1.80041       -0.06267
C        -1.37076     -0.91139        0.42921
O        -2.47270     -0.45315       -0.30298
H        -2.43629      0.50882       -0.29392
H         1.98052      1.20208        1.06463
H         2.19355      1.20020       -0.66966
H         1.55217      2.66538        0.13605
H        -0.05089     -0.66573       -1.26303
H        -1.41653     -0.59664        1.47764
H        -1.38847     -1.99990        0.40264
```

```
:::::::::::::::
ROOH
:::::::::::::::
16
Energy: -287442.6139997
C        -0.46165      1.49173       0.41834
C        -0.13173      0.05885       0.84402
C         1.03478     -0.52184       0.04309
C         2.31811      0.25780       0.05789
O         0.90387     -1.54482      -0.58396
O        -0.54196      1.65401      -0.97611
O        -1.25093     -0.79757       0.83759
O        -1.75897     -0.88717      -0.49368
H        -1.14374     -1.53625      -0.86893
H        -1.19226      1.02115      -1.29412
H         0.32350      2.16328       0.76692
H        -1.39347      1.77623       0.91605
H         0.15907      0.07220       1.89953
H         2.21587      1.07767      -0.65650
H         2.51748      0.69203       1.03731
H         3.14043     -0.38123      -0.25102

:::::::::::::::
TSA
:::::::::::::::
18
Energy: -381737.1368787
C        -2.43736     -1.52374      -0.03950
C        -2.02906     -0.09221      -0.22122
O        -2.77994      0.78015      -0.56490
C        -0.53571      0.22410       0.05887
O        -0.06481     -0.56417       1.06244
C        -0.27973      1.71000       0.27226
O         1.11489      1.94334       0.10283
O         1.51014     -1.56530       0.40213
O         1.93182     -1.05700      -0.67108
O         2.92437     -0.04137      -0.41327
H         1.33371      2.82829       0.39104
H        -0.85670      2.29015      -0.44713
H        -0.03848     -0.07099      -0.88719
H        -0.59247      1.97918       1.28347
H        -1.68241     -2.20031      -0.43780
H        -3.40234     -1.68833      -0.50998
H        -2.50755     -1.73311       1.02882
H         2.34558      0.72089      -0.18882
```

```
:::::::::::::::
TSB
:::::::::::::::
18
Energy: -381728.4030946
C        -2.48856       -1.20372        0.17708
C        -1.83792        0.07721       -0.24390
C        -0.42750        0.33818        0.30742
C         0.17843        1.73039        0.06786
O         1.52551        1.71623        0.50345
H         1.53339        1.31154        1.37837
O        -2.34003        0.91019       -0.95025
O        -0.05572       -0.27530        1.34851
O         1.34345       -1.60812        0.55163
H         0.16922        1.99709       -0.98523
H         0.21883       -0.39537       -0.58218
H        -0.40742        2.47484        0.61343
H        -2.65322       -1.18418        1.25480
H        -1.82264       -2.04571       -0.01576
H        -3.43152       -1.32854       -0.34624
O         1.20018       -1.25371       -0.65559
O         2.28173       -0.35006       -1.13142
H         2.20561        0.40420       -0.49863

:::::::::::::::
RI
:::::::::::::::
18
Energy: -381751.8518753
C        -2.35127       -1.48241        0.20507
C        -1.98578       -0.06833       -0.13886
C        -0.49290        0.27441       -0.14960
C        -0.21880        1.71319        0.23857
O         1.16077        1.96422        0.00685
H         1.35783        2.87288        0.23143
O        -2.79594        0.77607       -0.42560
O         0.24334       -0.55575        0.74207
O         0.97023       -1.55115        0.04983
H        -0.84911        2.36492       -0.36599
H        -0.12281        0.11361       -1.16495
H        -0.46646        1.86001        1.29365
H        -2.13096       -1.66883        1.25676
H        -1.74213       -2.18197       -0.36838
H        -3.40765       -1.64219        0.01172
O         1.93572       -0.91709       -0.73522
O         2.88274       -0.32752        0.10405
H         2.47893        0.55022        0.23885
```

:::::::::::::::
Triplet TS
:::::::::::::::
18
Energy: -381742.8499081
C	-0.74581	-2.19323	0.87641
C	-1.23424	-1.20273	-0.13674
O	-2.11251	-1.43482	-0.92517
C	-0.59284	0.18718	-0.18587
O	0.44296	0.24849	0.81876
O	1.24612	1.29041	0.63545
C	-1.62526	1.28826	0.05353
O	-1.16962	2.56159	-0.30700
O	2.96015	0.01590	-0.50810
O	2.33312	-1.09095	-0.53149
H	-0.33674	2.73425	0.13822
H	-2.48505	1.06110	-0.57399
H	-0.12388	0.32572	-1.16077
H	-1.94246	1.25012	1.10273
H	-0.86927	-1.78927	1.88249
H	0.32102	-2.36842	0.73760
H	-1.30246	-3.11925	0.77025
H	2.32603	0.70393	-0.00018

:::::::::::::::
RI$_2$
:::::::::::::::
18
Energy: -381753.3123935
C	0.44054	2.45723	-0.76096
C	0.08656	1.29446	0.11912
C	0.73501	-0.04229	-0.24026
C	2.11414	-0.14546	0.41802
O	2.82531	-1.26513	-0.02985
H	2.32702	-2.05166	0.20039
O	-0.64663	1.39942	1.07299
O	0.01066	-1.14363	0.27123
O	-1.01276	-1.52806	-0.62345
H	2.70714	0.73103	0.15898
H	0.84324	-0.14246	-1.32250
H	1.97618	-0.15350	1.50440
H	-0.10259	2.34462	-1.70205
H	1.50320	2.46644	-1.00475
H	0.15025	3.39032	-0.28771
O	-1.95554	-0.50215	-0.68355
O	-2.66617	-0.47099	0.51565
H	-2.10098	0.11597	1.05344

```
::::::::::::::
```
TS$_{2A}$
```
::::::::::::::
18
Energy: -381735.6583446
C          0.55967          2.37211         -0.78351
C          0.18419          1.22639          0.11372
C          0.81536         -0.13178         -0.20636
C          2.26894         -0.15347          0.36701
O          2.98943         -1.25373         -0.09400
H          2.53334         -2.05246          0.17852
O         -0.58549          1.36351          1.03489
O          0.20952         -1.19966          0.37865
O         -1.51098         -1.54532         -0.61499
H          2.79185          0.73924          0.02614
H          0.91408         -0.25286         -1.29336
H          2.19791         -0.12471          1.45804
H         -0.17130          2.39905         -1.59528
H          1.54325          2.24902         -1.23367
H          0.49835          3.31062         -0.23930
O         -2.16061         -0.46437         -0.67835
O         -2.83665         -0.20142          0.56271
H         -2.11814          0.26057          1.04245
```


```
::::::::::::::
```
TS$_{2B}$
```
::::::::::::::
18
Energy: -381721.4565748
C          1.39936         -1.15753         -0.68325
C          0.41387         -0.31038          0.12783
C          0.57710          1.22638          0.20328
C          1.83075          1.82552         -0.35632
O         -0.29888          1.88433          0.70962
O          2.60746         -1.34104          0.02057
O         -0.13770         -0.84897          1.12434
H          1.82818          1.71269         -1.44278
H          1.87563          2.88138         -0.10636
H          2.41440         -1.82606          0.82529
H          1.65856         -0.67636         -1.62509
H          0.91378         -2.11223         -0.90393
H          2.70629          1.29489          0.01709
H         -0.69213         -0.31141         -0.68434
O         -1.90813         -0.61401         -0.67848
O         -2.02804         -1.28667          0.38919
O         -2.49366          0.75609         -0.56472
H         -1.95962          1.13539          0.16684
```

```
::::::::::::::
TS1D
::::::::::::::
14
Energy: -239866.3562507
O          1.69185          0.27730         -1.14730
C          1.36489         -0.81495         -0.33447
C          0.58811         -0.35300          0.89480
O          0.80484          0.78406          1.33702
H          1.80675          1.02055         -0.54202
H          0.21918         -1.15476          1.55429
H          0.80708         -1.54489         -0.92083
H          2.26665         -1.31793          0.04476
C         -1.29245         -0.19057         -0.01170
O         -1.94284         -1.15853         -0.07919
C         -1.49468          1.21400         -0.44551
H         -1.27259          1.86361          0.39894
H         -0.74857          1.41971         -1.21412
H         -2.50462          1.35816         -0.82401


::::::::::::::
TS2D
::::::::::::::
14
Energy: -239860.6918345
C          1.36190          0.15292          1.33412
C          1.12802         -0.12375         -0.11871
C          0.02281          0.67935         -0.80750
C         -1.48575         -0.82041         -0.43964
O         -1.89654         -0.58299          0.80733
H         -2.23134          0.31857          0.86835
O          1.76327         -0.91305         -0.77433
O         -0.49768          1.66688         -0.28732
H         -2.08698         -0.43575         -1.25560
H          0.00176          0.50741         -1.89753
H         -0.99817         -1.77791         -0.56154
H          0.45808         -0.09059          1.89519
H          1.54125          1.21765          1.48211
H          2.20107         -0.43476          1.69403


::::::::::::::
CH3(C=O)
::::::::::::::
6
```

```
Energy:   -96126.6206046
C          0.24589       -0.42765        -0.00002
O          1.25615        0.17232         0.00001
C         -1.16495        0.09765         0.00001
H         -1.67722       -0.29349        -0.87768
H         -1.67724       -0.29373         0.87758
H         -1.18037        1.18867         0.00008
```

:::::::::::::

Glycolaldehyde

:::::::::::::

```
8
Energy: -143739.2004389
O         -1.33190       -0.57699         0.00009
C         -0.66700        0.64402        -0.00013
C          0.82590        0.48307         0.00013
O          1.35107       -0.59826        -0.00011
H         -0.65287       -1.26232         0.00028
H          1.41971        1.41434         0.00053
H         -0.93672        1.24348        -0.88003
H         -0.93687        1.24389         0.87943
```

:::::::::::::

CH$_2$OH

:::::::::::::

```
5
Energy:   -72208.1163135
C         -0.68029        0.02743        -0.05953
O          0.66649       -0.12522         0.01991
H          1.09619        0.72703        -0.05305
H         -1.11371        0.99497         0.15446
H         -1.23270       -0.88487         0.09649
```

:::::::::::::

Methylglyoxal

:::::::::::::

```
9
Energy: -167647.4185019
C          0.87116        1.27366         0.00004
C          0.52316       -0.18109         0.00000
C         -0.96810       -0.54788         0.00014
O          1.31733       -1.08564        -0.00011
O         -1.84394        0.26802        -0.00014
H         -1.15282       -1.63760         0.00058
H          0.42986        1.75545         0.87343
H          0.42896        1.75580        -0.87269
H          1.94955        1.39923        -0.00039
```

REFERENCES

1. Su, T.; Chesnavich, W. J., Parametrization of the Ion-Polar Molecule Collision Rate-Constant by Trajectory Calculations. *J. Chem. Phys.* **1982,** *76* (10), 5183-5185.

2. Garden, A. L.; Paulot, F.; Crounse, J. D.; Maxwell-Cameron, I. J.; Wennberg, P. O.; Kjaergaard, H. G., Calculation of Conformationally Weighted Dipole Moments Useful in Ion-Molecule Collision Rate Estimates. *Chem. Phys. Lett.* **2009,** *474* (1-3), 45-50.

3. Paulot, F.; Crounse, J. D.; Kjaergaard, H. G.; Kroll, J. H.; Seinfeld, J. H.; Wennberg, P. O., Isoprene Photooxidation: New Insights into the Production of Acids and Organic Nitrates. *Atmos. Chem. Phys.* **2009,** *9* (4), 1479-1501.

4. Teng, A. P.; Crounse, J. D.; Lee, L.; St. Clair, J. M.; Cohen, R. C.; Wennberg, P. O., Hydroxy Nitrate Production in the OH-Initiated Oxidation of Alkenes. *Atmos. Chem. Phys. Discuss.* **2014,** *14* (5), 6721-6757.

5. Lee, L.; Teng, A. P.; Wennberg, P. O.; Crounse, J. D.; Cohen, R. C., On Rates and Mechanisms of OH and O_3 Reactions with Isoprene-Derived Hydroxy Nitrates. *J. Phys. Chem. A* **2014,** *118* (9), 1622-1637.

6. Bey, I.; Jacob, D. J.; Yantosca, R. M.; Logan, J. A.; Field, B. D.; Fiore, A. M.; Li, Q. B.; Liu, H. G. Y.; Mickley, L. J.; Schultz, M. G., Global Modeling of Tropospheric Chemistry with Assimilated Meteorology: Model Description and Evaluation. *J. Geophys. Res.-Atmos.* **2001,** *106* (D19), 23073-23095.

7. Varandas, A. J. C., Ab Initio Treatment of Bond-Breaking Reactions: Accurate Course of HO_3 Dissociation and Revisit to Isomerization. *J. Chem. Theory Comput.* **2012,** *8* (2), 428-441.

A p p e n d i x   B

SUPPORTING INFORMATION: ATMOSPHERIC AUTOXIDATION IS
INCREASINGLY IMPORTANT IN URBAN AND SUBURBAN NORTH AMERICA

Experimental methods

We performed a series of oxidation experiments of 2-hexanol with varying NO and HO_2 mixing ratios (and thus varying $\tau_{\text{bimolecular}}$). Gas chromatography coupled with CF_3O^- CIMS was used to quantify the relative abundance of the individual $RONO_2$ isomers formed in these experiments.

Experiments began by adding reagents to a ~1 m^3 Teflon bag. A 500 cm^3 glass bulb with 2-hexanol vapor was prepared, which underwent serial dilution to achieve the desired mixing ratio and was backfilled with N_2. A separate bulb was similarly prepared containing CH_3ONO. FTIR (Nicolet 560 Magna IR) was used to quantify both gas mixtures using published cross sections (1). Addition of nitric oxide was necessary for certain experiments. For experiments without NO added to the chamber, $[NO]_0$ was less than 30 pptv in the zero air used to fill the chamber.

Following the collection of background signals in the CIMS instrument, the chamber was illuminated typically for 10-60 minutes depending on experimental conditions. For experiments with $\tau_{\text{bimolecular}} > 30$ s, however, longer oxidation periods ranging 12-16 hours were required to accumulate sufficient products for quantification while simultaneously ensuring that RO_2 self-reactions remained negligible.

Chemicals and synthesis

2-hexanol (99%, Sigma-Aldrich), nitric oxide (1993 ± 20 ppmv NO in N_2, Matheson), isopropanol (≥ 99%, Macron), 2-hexanone (Sigma-Aldrich, 98%), and lithium aluminum deuteride (Strem, 98%) were used as purchased. Deuterated 2-hexanol

was afforded in 89% yield upon treatment of 2-hexanone (0.500 g, 4.99 mmol) with lithium aluminum deuteride (0.230 g, 5.49 mmol) in THF (16 mL) as described elsewhere (2). Methyl nitrite was synthesized using a method similar to that described in Taylor et al. (3).

A synthetic sample of the 2,5 $RONO_2$ needed for chromatographic assignment was prepared from the addition of nitric acid to 2,5-dimethyltetrahydrofuran (2,5-diMeTHF, Santa Cruz Biotechnology) as detailed in earlier work (4). Briefly, ~5 mmol of 2,5-diMeTHF was dissolved in DCM, with the reaction vessel submerged in an ice bath, and concentrated HNO_3 was added in a 1.1:1 (HNO_3:2,5-diMeTHF) molar ratio. The vessel was removed from the ice bath and left to stir for 1 hour. The solvent was then removed by boiling under reduced pressure at 23 K.

Chamber and instruments

The chamber configuration and the Gas Chromatograph Chemical Ionization Mass Spectrometer (GC-CIMS) have been documented extensively (5-11). The chamber consists of a ~1 m^3 fluorinated ethylene propylene copolymer bag (Teflon-FEP, DuPont) connected to instrumentation by 6.35 mm OD PFA tubing. The chamber is housed inside an enclosure with UV reflective metal flashing. All experiments were conducted at ambient pressure (~745 torr) and at either 296 ± 2 K or 318 ± 5 K. The enclosure is equipped with 8 individually controlled UV blacklights (Sylvania 350). For some experiments, only one bulb was used and a front panel blocked direct illumination such that only the reflection illuminated the chamber. The placement of a back panel (a very poor UV reflector) in addition to the front panel enabled a further reduction of the light

flux in some experiments. Modulating the light enabled control over the photolysis of methyl nitrite, used as an oxidant source according to the following reactions:

$$CH_3ONO + h\nu + O_2 \rightarrow HO_2 + NO + HCHO$$

$$HO_2 + NO \rightarrow OH + NO_2$$
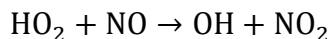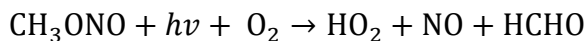
GC-CIMS, using CF_3O^- reagent ion ($m/z = 85$), was used to quantify multifunctional oxidation products with a detection limit of ~10 pptv with a 1 s integration period. The reagent ion was formed by passing 1 ppm CF_3OOCF_3 in N_2 through a radioactive ^{210}Po source. After dilution of the sample flow with N_2, gas analytes interact with CF_3O^- at a pressure of 35 mbar, forming charged clusters. In order to compensate for variation in the total ion signal, analyte signals were normalized to the sum of the isotope of the reagent ion, $^{13}CF_3O^-$, and its clusters with water and H_2O_2 (m/z 104 and m/z 120, respectively). CIMS signal backgrounds were determined prior to initiating photoxidation.

To enable separation of isobaric species, gas chromatography coupled with CF_3O^- CIMS was conducted following oxidation (5, 6, 9, 11-14). Analytes were collected on the head of a 4 m Restek RTX-1701 column using a -10 ℃ isopropanol bath. The collection temperature could not be significantly reduced without also trapping large quantities of water, which degrades the analysis. After trapping, elution was enabled using a flow of 8 sccm N_2 and a temperature ramping program (30 °C for 0.1 min, +3 °C/min until 60 °C, and +10 °C/min to 130 °C). The effluent of the column was further diluted with N_2 and transmitted into the CIMS ion-molecule reaction region. Chromatograms of chamber air were collected both before and after the oxidation period.

The concentration of NO present at the beginning of the high-NO experiments was quantified using a 200EU Teledyne-API chemiluminesence NO_x analyzer. Calibration was performed by sampling a 939 ppbv NO standard (Scott-Marrin, Inc.). For those experiments performed without addition of NO, we quantify the NO abundance as described below in the calculation of bimolecular lifetime. A gas chromatograph equipped with a flame ionization detector (GC-FID, Hewlett Packard 5890 series II Plus) was used to monitor 2-hexanol and the principal oxidation product, 2-hexanone.

Calculation of bimolecular RO_2 lifetime

For the conditions of our experiments, self-reaction of the peroxy radicals is much slower than reaction with either NO or HO_2. Thus, the bimolecular peroxy radical lifetime is given by:

$$\tau_{\text{bimolecular}} = \frac{1}{k_{RO_2+NO}[NO] + k_{RO_2+HO_2}[HO_2]}$$

For experiments where NO is not quantifiable using the chemilluminescence instrument (those without NO added), the bimolecular RO_2 lifetime is estimated using the method described in Crounse et al. (15) and Teng et al. (12). Briefly, we use the observed production rates and yields of hydrogen peroxide, $RONO_2$, and ROOH together with the recommended rate coefficients for $RO_2 + HO_2$ (1.8×10^{-11} cm^3 molec^{-1} s^{-1} at 296 K; 1.3×10^{-11} cm^3 molec^{-1} s^{-1} at 318 K), and $RO_2 + NO$ (8.6×10^{-12} cm^3 molec^{-1} s^{-1} at 296 K; 7.9×10^{-12} cm^3 molec^{-1} s^{-1} at 318 K) (16). The mixing ratio of HO_2 is estimated from the production rate of H_2O_2 ($P_{H_2O_2}$) and the recommended rate coefficient for the self-reaction of HO_2 ($k_{HO_2+HO_2}$) including a dependence on water vapor (17):

$$P_{H_2O_2} = k_{HO_2+HO_2} \times [HO_2]^2$$

$$k_{HO_2+HO_2} = \left(2.2 \text{ x } 10^{-13}\exp\left(\frac{600}{T}\right) + 1.9 \text{ x}10^{-33}[M] \exp\left(\frac{980}{T}\right)\right)$$

$$\times \left(1 + 1.4 \times 10^{-21}[H_2O] \exp\left(\frac{2200}{T}\right)\right)$$

$$[HO_2] = \sqrt{\frac{P_{H_2O_2}}{k_{H_2O_2}}}$$

Finally, [NO] was inferred based on known [HO2] and the observed production rates of the hydroxynitrates and peroxides, P_{RONO_2} and P_{ROOH}, respectively:

$$P_{RONO_2} = BR_{RONO_2} \times k_{RO_2+NO} \times [NO] \times [RO_2]$$

$$P_{ROOH} = Y_{ROOH} \times k_{RO_2+HO_2} \times [HO_2] \times [RO_2]$$

$$[NO] = \frac{P_{RONO_2}}{P_{ROOH}} \frac{Y_{ROOH}}{BR_{RONO_2}} \frac{k_{RO_2+HO_2}}{k_{RO_2+NO}} [HO_2]$$

We assume that the yield of the hydroperoxide, Y_{ROOH}, is 1.0 while the nitrate branching ratio (BR_{RONO_2}) is measured as described below. We also account for wall losses of these compounds.

Instrumental calibration

Most of the multifunctional species discussed in this work are not commercially available in pure form. For these species, direct calibration is not possible and an alternative method for the estimation of instrumental sensitivities is required for quantification. We estimate these sensitivities through the calculation of the ion-molecule collision rate coefficients using the parameterization of Su et al. (18), assuming that all collisions lead to formation of quantifiable product ions. We calculate the dipole moments and polarizabilities of closed-shell products arising from the 2,5 RO_2, in addition to all isomers of the 3 major $RONO_2$, using DFT (B3LYP/6-31+G(d)). Due to the dependence of the dipole moment on structural conformation, we use a weighted average of the located conformers. In contrast, the polarizability does not exhibit a large conformational dependence and the determination was based on the lowest energy conformer. A detailed description of this method is available (19). These properties for species derived from the 2-hexanol system are given in Table S1.

In our estimation of [NO] (see above), we use a ratio of production rates ($\frac{P_{RONO_2}}{P_{ROOH}}$), and therefore this expression is only sensitive to the relative calibration factors of these species. Because the calibration factor was only calculated for the 2,5 ROOH isomer, we use the ratio of the $RONO_2$ and ROOH sensitivities for this isomer. For the determination of the nitrate branching ratios, however, the isomer-specific calibration factors were used. In the case of differing sensitivity for a diastereomeric pair, the average was used.
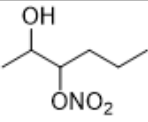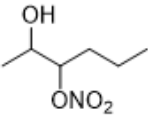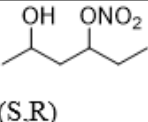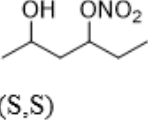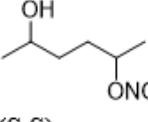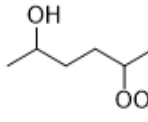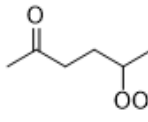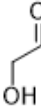
As discussed above, the production rate of H_2O_2 is used to estimate [HO_2] and thereby $\tau_{bimolecular}$. The efficiency of CF_3O^- clustering with H_2O_2 is affected by water vapor

according to competing effects: 1) $CF_3O^- \cdot H_2O$ reacts more efficiently by ligand exchange with H_2O_2 to form $CF_3O^- \cdot H_2O_2$ compared to the CF_3O^- ion and 2) $CF_3O^- \cdot H_2O_2$ likewise undergoes ligand exchange with water vapor:

$$CF_3O^- \cdot H_2O_2 + H_2O \rightleftharpoons H_2O_2 + CF_3O^- \cdot H_2O$$
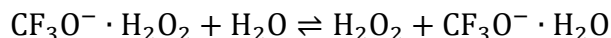
In order to account for the changing sensitivity, a calibration for H_2O_2 across a span of water vapor mixing ratios relevant to our experiments was performed. A measured quantity of dilute H_2O_2 was evaporated into our chamber and a small ~0.2 m^3 Teflon bag was prepared with ~1% water vapor in N_2. The small bag was connected through a critical orifice to the flow tube and a flow controller regulated a quantity of dry N_2. At the highest setting, dry N_2 overflowed the critical orifice and backflowed into the pillow bag such that no water vapor from the pillow bag was sampled. As the flow rate of N_2 was decreased, however, a mixture of dry N_2 and water vapor entered the flow tube which allowed us to vary the water vapor mixing ratio in the ion region. As discussed by Crounse et al. (6), the instrumental sensitivity toward H_2O_2 increased by 25% over the range of water vapor (30-300 ppm) observed in the 2-hexanol experiments.

Table S1. Calculated average dipole moments ($\bar{\mu}$) and polarizabilities (α) used to determine ion-molecule collision rate coefficients and instrumental sensitivity. k_x is the conformer weighted average collision rate coefficient. The instrumental sensitivity is derived from the ratio of this rate coefficient for each analyte against that of glycolaldehyde ($k = 2.0 \times 10^{-9}$ cm^3 molecule^{-1} s^{-1}), for which an experimental determination has been made. Dipole moments and polarizabilities are calculated at the B3LYP/6-31+G(d) level of theory.

molecule	m/z	$\bar{\mu}$ (D)	α (Å^3)	k_x (10^{-9} cm^3 molecule^{-1} s^{-1})	calculated sensitivity (x 10^{-4}) [a]	experimental sensitivity (x 10^{-4}) [a]
(structure: OH, ONO$_2$) (S,R)	248	3.2	15	2.4	1.8	-
(structure: OH, ONO$_2$) (S,S)	248	3.2	15	2.4	1.8	-
(structure: OH ONO$_2$) (S,R)	248	4.1	15	2.9	2.2	-
(structure: OH ONO$_2$) (S,S)	248	3.8	15	2.7	2.0	-
(structure: OH, ONO$_2$) (S,S)	248	4.1	15	2.9	2.2	-
(structure: OH, OOH) [b] (S,R)	219	3.8	13	2.8	2.1	-
(structure: O, OOH)	217	4.8	12	3.3	2.5	-
(structure: O, OH)	145	2.3	4.5	2.0	-	1.5

[a] CF$_3$O$^-$ CIMS sensitivity (ncts. pptv^{-1}), where ncts. includes normalization to ^{13}CF$_3$O$^-$ and its clusters with water and H$_2$O$_2$ m/z 86 + m/z 104 + m/z 120

[b] The dipole moment and polarizability was only calculated for the S,R diastereomer

Structural assignment of the RONO$_2$
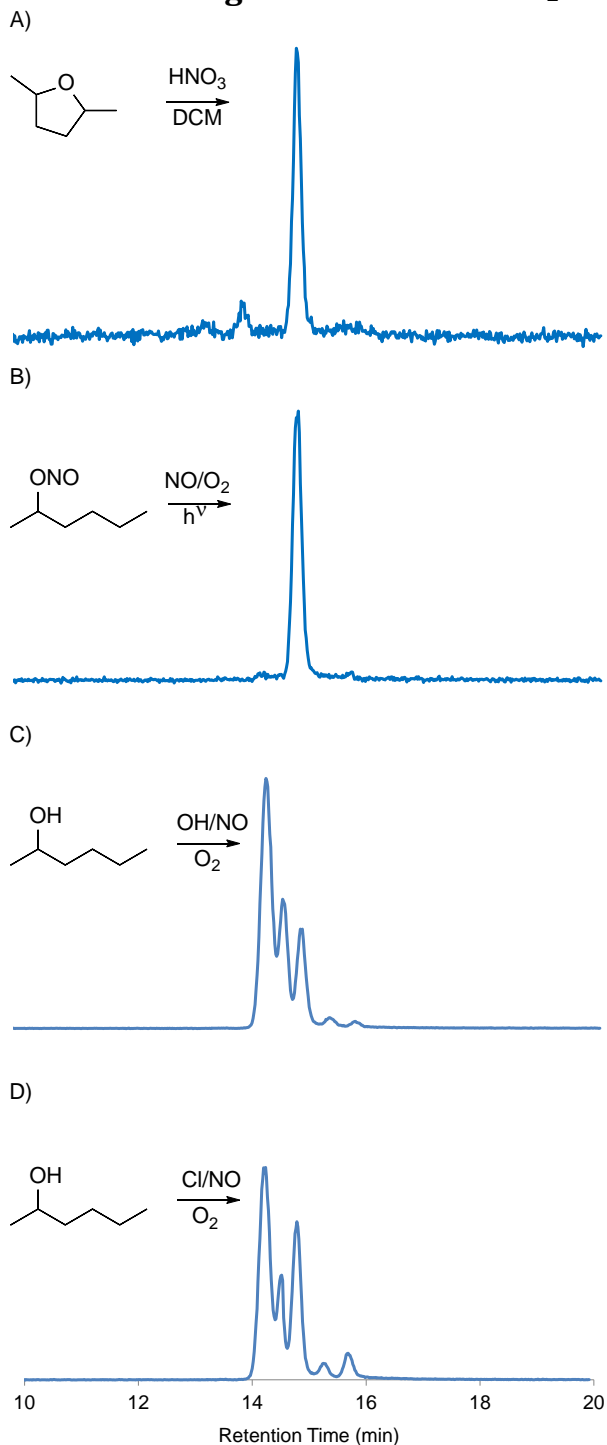
Figure S1. Structural assignment of RONO$_2$ was performed by chromatographic analysis. Panel A demonstrates GC-CIMS sampling of the dried product mixture following the condensed phase synthesis of 2,5 RONO$_2$ (see text). All gas-phase photoxidation

reactions (panels B-D) were performed under conditions of high NO ($[NO]_0 > 350$ ppbv), effectively eliminating contribution from unimolecular channels. The corresponding oxidation reactions are indicated. Note that retention times differ from chromatograms shown in the main article and elsewhere in the SI due to slight differences in the instrumental configuration.

The identities of the $RONO_2$ isomers were assigned following the collection of several chromatograms (see Figure S1). Among the three major peroxy radicals, the OH hydrogen abstraction preference from 2-hexanol as determined by SAR ($\sim$0.6,$\sim$0.2,$\sim$0.2 for β, γ, and δ abstraction, respectively) nominally agrees with the isomer distribution observed here (0.66 ± 0.20, 0.17 ± 0.06, 0.17 ± 0.06 at 296 K) (20, 21).

For the 2,5 $RONO_2$, a synthetic standard was synthesized as described above. The elution time of this peak was found to match that of the major product of 2-hexylnitrite photolysis. Thus, this isomer was conclusively identified. Additional assignments were made by performing oxidation of the alcohol initiated by Cl, exploiting distinct abstraction differences as compared with OH. According to SAR, while C-H bonds that are α and β to a hydroxy group are activated (20, 21), the extent of the activation at more distant sites (γ, δ, ...) is negligible. Abstraction at deactivated sites is enhanced by Cl compared to OH due to distinct activation barriers, producing substantially different chromatographic peak ratios (22, 23). As seen in Figure S1, this effect is most pronounced for the $RONO_2$ at the 5- and 6-carbon positions (3rd and 5th peaks, respectively; see Figure 1 of the main article for assignment).

Product yields and branching ratios

Table S2. Measured production of RONO$_2$ following OH reaction of 2-hexanol with [NO]$_0$ > 350 ppbv. Mixing ratios are expressed in ppbv. ΔRONO$_2$ represents the sum of all isomers detected during CIMS sampling using a weighted average of the calibration factors for the 3 dominant isomers. The individual isomer yields were calculated by dividing ΔRONO$_2$ by the GC fractional abundances assuming equal transmission of the isomers. The primary RONO$_2$ (2,1 and 2,6 RO$_2$; not shown in the table) were produced in ~5% and ~8% yields at 296 K and 313 K, respectively.

T (K)	ΔRONO$_2$	Δ2,3 RONO$_2$	Δ2,4 RONO$_2$	Δ2,5 RONO$_2$	Δ2-hexanol	BR$_{RONO_2}$
296 ± 2	1.7 ± 0.5	1.1 ± 0.4	0.27 ± 0.09	0.27 ± 0.09	17 ± 0.87	0.25 ± 0.10
313 ± 3	1.3 ± 0.4	0.72 ± 0.3	0.23 ± 0.08	0.25 ± 0.09	19 ± 1.9	0.17 ± 0.07

Experiments performed at [NO]$_0$ > 350 ppbv enable measurement of the branching ratios of hydroxy nitrates (BR$_{RONO_2}$) and 2-hexanone, the expected major product following α-OH abstraction in 2-hexanol.

We measured RONO$_2$ using CIMS, and accounted for a first-order wall loss coefficient of ~8 × 10^{-6} s^{-1}. A weighted average of the available calibration factors was used to determine ΔRONO$_2$. The abundance of the minor, primary RONO$_2$ was estimated using the same average calibration factor as the dipole moments and polarizabilities were not calculated for these isomers. GC-FID was used to quantify both the loss of alcohol (Δ2-hexanol) and formation of 2-hexanone, while accounting for differences in the FID response factors for the alcohol (1.1) versus the ketone (1.0) (24). The average organonitrate branching ratio for the hydroxyperoxy radicals was determined as:

$$BR_{RONO_2} = \frac{\Delta RONO_2}{\Delta 2\text{-hexanol} \times (1 - Y_{ketone})}$$

The results are shown in Table S2, and the error bounds reflect uncertainty in the calibration factors as well as measurement precision. The yield of 2-hexanone, Y_{ketone}, was determined to be 0.6 ± 0.2, consistent with the expected value based on SAR estimates of the abstraction preference (20, 21). Given the poor precision of the GC-FID measurements, the temperature dependence of the 2-hexanone yield was unresolved. The temperature dependence of BR_{RONO_2} is similar to that reported in Atkinson et al. for C_5 and C_7 alkanes (25).

Uncertainty
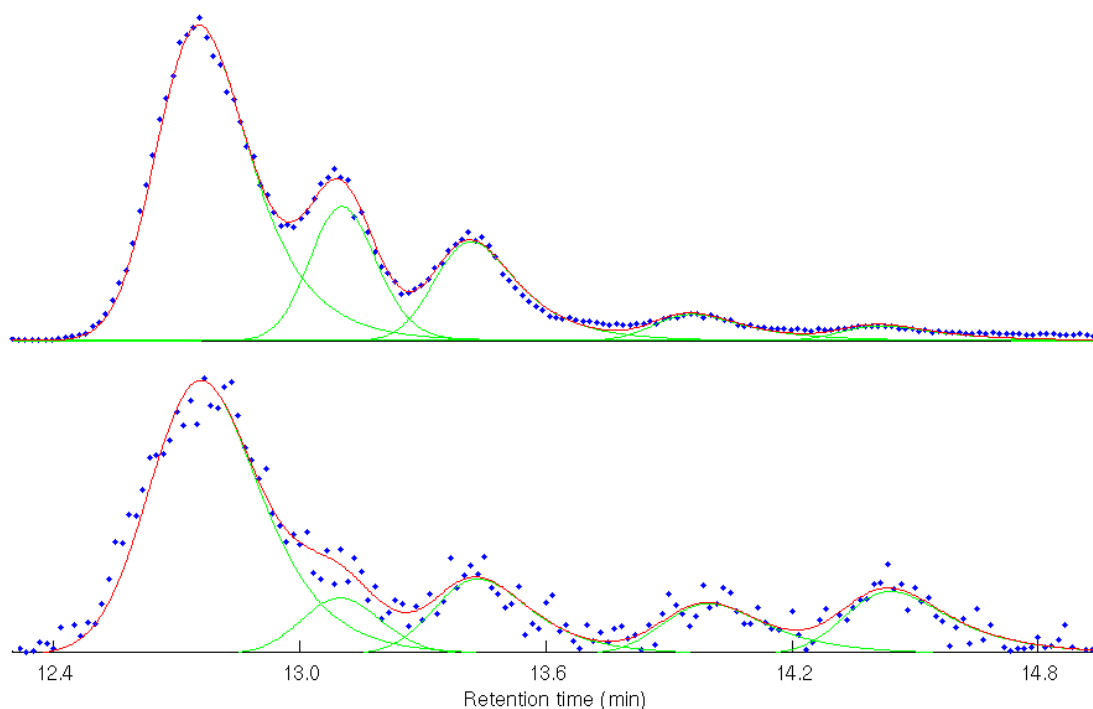
Figure S2. Representative chromatograms from a short (top, $\tau_{bimolecular} \approx 0.02$ s) and long (bottom, $\tau_{bimolecular} \approx 40$ s) lifetime experiment. The output of the peak deconvolution and fitting algorithm is shown for the peaks (green) and the sum (red). Background signals, particularly for the later eluting isomers, are apparent in the bottom chromatogram. These compounds have lower volatilities and persist in the experimental apparatus to a greater extent compared to the earlier eluting isomers.

There is significant uncertainty in our calculation of $\tau_{bimolecular}$ using observed

production rates of the hydroperoxides and hydroxynitrates. We include the standard 1σ

error incurred from the ordinary least-square fit to each production signal. Recommended

rate coefficients also carry associated error. For example, $k_{HO_2+HO_2}$ carries a stated

uncertainty of $\pm15\%$ (17), while k_{RO_2+NO} and $k_{RO_2+HO_2}$ presumably also carry uncertainty

but the quantity is not provided in the literature (16). Furthermore, calibration factors are

each estimated to carry $\pm30\%$ uncertainty. In our calculation of $\tau_{bimolecular}$, the ratio of

the $RONO_2$ and $ROOH$ sensitivities is used; thus, the cumulative uncertainty in the

calibration factors for this expression is ~40%. In addition, the hot experiments saw

the chamber temperature fluctuate on order ±5 ºC.

  As described in the main article, chromatography was used to quantify the isomers and

determine the abundance of the 2,4 and 2,5 $RONO_2$ relative to that of the 2,3 $RONO_2$.

Chromatographic challenges include poorly constrained peak shapes and sample

backgrounds that contribute to error in the measured ratios of $RONO_2$. We studied the

impact of different experimental conditions on the chromatography using the synthetic

2,5 $RONO_2$ standard. The peak shape of this single isomer is poorly represented by a

Gaussian, as pronounced tailing is apparent. An Exponentially Modified Gaussian (EMG)

provides a reasonable representation of the peak shape and was used to fit the

chromatograms (26). We employed the peakfit.m function for Matlab by Dr. Tom

O'Haver (27). The function was modified to enable treatment of the EMG with fixed

peak widths and distinct tailing constants for each isomer. The output of the algorithm is

shown for two representative chromatograms in Figure S2.

        As the other $RONO_2$ isomers were not well separated, peak parameters were

optimized as determined by the root mean square difference between the data and the

EMG model. In minimizing the residuals, we found that the best fits were achieved when

the isomers were allowed different tailing constants. Peak widths were also found to

increase with collection time, consistent with the expected spread of the sample on the

column. While these parameters were optimized to achieve the best fit, significant

uncertainty existed due to the lack of authentic standards for each isomer.

In order to characterize the uncertainty, we used a bootstrapping method to probe the sensitivity of the isomer ratios to the assumed EMG peak parameters. In the bootstrap, we varied the peak widths and tailing constants by ±40% of the default choices (used, for example, in the fits shown in Figure S2). 10,000 fitting trials were used; further increases in the number of trials did not change the result, suggesting that the space was adequately sampled. Trials that degraded the fit beyond 1σ of the root-mean-square error were rejected. The results of the bootstrap are summarized in Table S3.

Table S3. Bootstrap results expressed as % uncertainty (1σ) of measured $RONO_2$ isomer ratios resulting from the peak fits.

$\tau_{bimolecular} < 20$ s		$\tau_{bimolecular} > 20$ s	
2,4 $RONO_2$: 2,3 $RONO_2$	2,5 $RONO_2$: 2,3 $RONO_2$	2,4 $RONO_2$: 2,3 $RONO_2$	2,5 $RONO_2$: 2,3 $RONO_2$
16	12	25	14
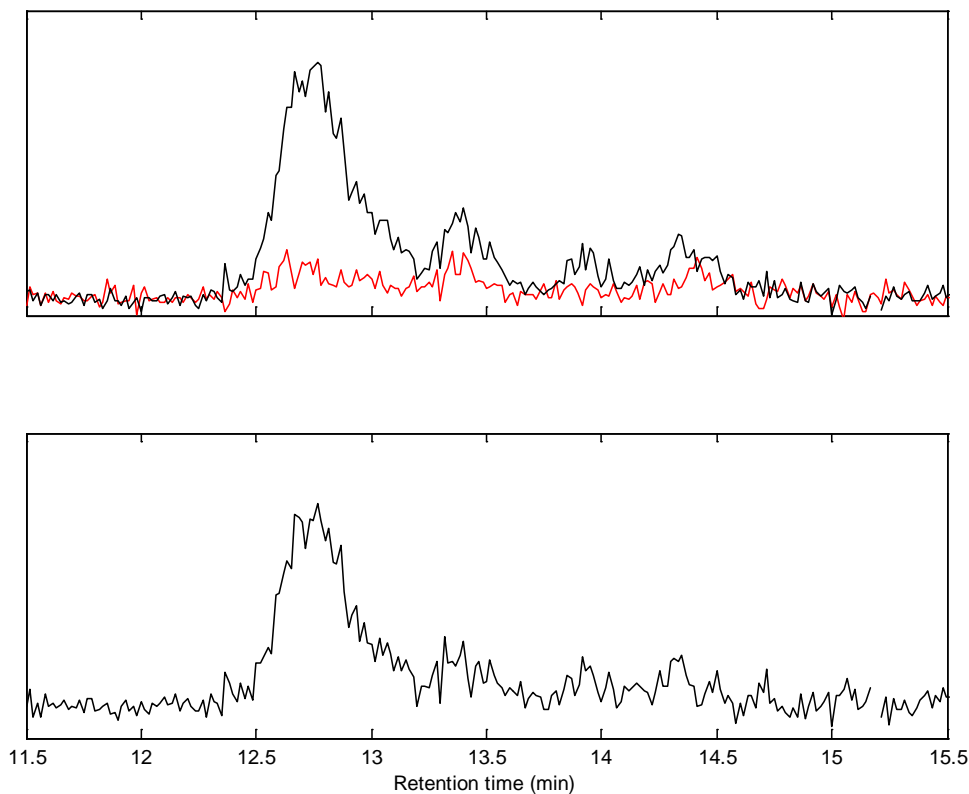
Figure S3. Top: a post-oxidation chromatogram (black) with the background (red) overlaid. Bottom: The background subtracted chromatogram. The data were extracted from an experiment at $\tau_{\text{bimolecular}} \approx 50$ s.

At the longest lifetimes, an additional source of error arises from uncertainty in the background signals in the GC. Backgrounds were typically negligible ($< 5\%$ of post-oxidation signal) for $\tau_{\text{bimolecular}} < 20$ s, but were quite significant (30% to 100% of post-oxidation signal) for long lifetime experiments. The uncertainty is further increased by low signal to noise. We show a background and post-oxidation chromatogram, along with the background subtracted signal, in Figure S3 for a long lifetime experiment. The isomers are retained differently in the experimental apparatus, producing substantial variability in the backgrounds for long lifetime experiments. To bound the potential error

in the measured RONO$_2$ isomer ratios due to these backgrounds, we collected several

pre-oxidation chromatograms as well as zero air blanks following the conclusion of the

experiment. We express the uncertainty (1σ) of the background peak areas at long

lifetimes in the uncertainty range for these points.

A smaller source of uncertainty impacting longer $\tau_{bimolecular}$ data points arises from

possible differences in our instrumental sensitivity toward the S,S vs. S,R stereoisomer.

While a racemic mixture is assumed at the shortest lifetimes, our calculations show that

this will not be the case as the RO$_2$ lifetimes increase, as indicated by the distinct rate

constants for the diastereomers of the 2,5 RO$_2$. This effect has the potential to influence

the distribution of RONO$_2$ we measure in our GC, as the column used here is not able to

separate these diastereomers. We have bounded this effect by calculating the difference

in instrumental sensitivity between the RONO$_2$ isomers, and we display the results in

Table S1. The calculated sensitivities did not appreciably differ for any pair of

diastereomers.

The determination of the experimental factor by fitting the data points with a

model carries additional uncertainty. The experimental factor represents the value that,

when multiplied by the calculated rate coefficient, afforded the best fit to the data. The

same factor was used for both diastereomers. A weighted least squares approach was

adopted to determine the best fit:

$$\sum_{i=1}^{n} \frac{1}{\sigma_i^2}(y_i - \hat{y}_i)^2$$

where σ_i^2 represents the point-wise variance and $y_i - \hat{y}_i$ denotes the residual between

the data points and the model. A Monte Carlo method was used in order to estimate the

uncertainty in the fit. 5,000 synthetic data sets were generated, with each point lying

within its respective range of uncertainty. The same procedure of weighted least squares

was used to determine the best fit for each of the synthetic data sets. The error bounds

provided with the experimental factors represent the full range of results that yielded a

best fit to the synthetic data sets.

Computational methods

We followed the approach described by Møller et al. (28) and only a brief

description is provided here. A sample TS conformer of the desired reaction was

optimized with B3LYP/6-31+G(d) (abbreviated as B3LYP) in Gaussian 09 Rev. D. (29-

34). That geometry was used as the input for a systematic conformer search in Spartan'14

with the MMFF force field (35-41). The TS conformer search was performed with the O-

O, O$\cdots$H and C-H bond distances locked. The input for the conformer search of the

reactant and product were drawn in Spartan'14. In all of the conformer searches the

MMFF force field was altered to enforce the correct charge on the radical center, with the

keyword 'FFHINT=X~~+0' where X is the atom number of the radical. The resulting

conformers were transferred to Gaussian 09, where constrained optimizations with

B3LYP were performed for the TS conformers. The same constraints as in the conformer

search were used. Afterwards, free optimizations for a saddle point were performed for

the TS with B3LYP. The reactant and product were optimized for a minimum, also with

B3LYP. The conformers were sorted according to electronic energy, and those within 2 kcal/mol of the lowest energy conformer were reoptimized with ωB97X-D/aug-cc-pVTZ (ωB97X-D) (42, 43). Their frequencies were calculated at the ωB97X-D level of theory as well. For the lowest zero-point-energy corrected conformer of the reactant, TS, and product, a single point energy calculation was performed in Molpro 2012.1 at the ROHF-ROCCSD(T)-F12a/VDZ-F12//ωB97X-D level of theory (F12) for an accurate value of $E_{TS,0}$ and $E_{R,0}$ (44-49).
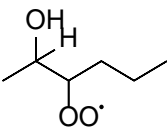
We used the lowest energy TS conformer at the ωB97X-D level of theory for the Eckart tunneling correction (50). An intrinsic reaction coordinate (IRC) calculation was performed starting from the corresponding B3LYP TS structure in both the forward and back reaction. The endpoints of the IRC were optimized and then reoptimized with ωB97X-D, and F12 single point energy calculations were performed at the final ωB97X-D geometry.
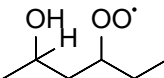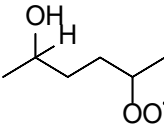
Output files from the ωB97X-D and F12 calculations are available electronically at:

http://www.erda.dk/public/archives/YXJjaGl2ZS1JX1ZJSHA=/published-archive.html

Expression of the rate coefficients

Table S4. Temperature dependence of the calculated rate coefficients.

Reactant		k (s^{-1})
	S,R	$1.5017 \times 10^{12} \times \exp\left(\dfrac{-13091}{T}\right)$ $\times \exp\left(\dfrac{1.6504 \times 10^{8}}{T^{3}}\right)$

	S,S	$1.7506 \times 10^{12} \times \exp\left(\dfrac{-13488}{T}\right)$ $\times \exp\left(\dfrac{1.5832 \times 10^8}{T^3}\right)$
OH, OO· (structure)	S,R	$5.0180 \times 10^{11} \times \exp\left(\dfrac{-9517.1}{T}\right)$ $\times \exp\left(\dfrac{8.1948 \times 10^7}{T^3}\right)$
	S,S	$1.9370 \times 10^{12} \times \exp\left(\dfrac{-10084}{T}\right)$ $\times \exp\left(\dfrac{9.2686 \times 10^7}{T^3}\right)$
OH (structure) OO·	S,R	$9.1036 \times 10^{10} \times \exp\left(\dfrac{-8688.0}{T}\right)$ $\times \exp\left(\dfrac{7.5470 \times 10^7}{T^3}\right)$
	S,S	$7.7343 \times 10^{10} \times \exp\left(\dfrac{-9144.2}{T}\right)$ $\times \exp\left(\dfrac{7.5879 \times 10^7}{T^3}\right)$

The expressions in Table S4 were obtained using data calculated at 5 K intervals in the range 290 K-320 K. The MC-TST rate coefficients without tunneling were plotted against 1/T and were fit with an exponential function. The Eckart tunneling correction factor was plotted against $1/T^3$ and fit to an exponential. The pre-exponential factor in the rate expressions are the product of the pre-exponential factors in the two fits. Within the specified temperature range, the fits reproduce the calculated MC-TST rate constants, including tunneling, to within 0.5%.

Uncertainty

The uncertainty in the calculated rate coefficients originates from three parts of the MC-TST equation: the barrier height, the tunneling correction, and the partition functions.

Werner et al. reports reaction energies calculated with CCSD(T)-F12a/VDZ-F12 for a set of 104 reactions with a mean average deviation of 0.70 kcal/mol from CCSD(T)/CBS results (51). The reactions studied by Werner et al. include primary small open- and closed-shell molecules. Some include second row atoms, but none of the reactions are unimolecular isomerizations. Møller et al. (28) reported barrier heights with CCSD(T)-F12a/VDZ-F12 to differ only by 0.25 and 0.33 kcal/mol from values obtained with CCSD(T)-F12/VDZ-F12//ωB97X-D/aug-cc-pVTZ. The latter is the same used in this study, and the reaction studied by Møller et al. is also a peroxy radical H-shift. We thus assign an uncertainty of 0.7 kcal/mol in the barrier heights, which would translate to a factor of 3 uncertainty in the rate coefficient at 298 K.

Sha and Dibble (52) reported a ratio between the Eckart tunneling correction and the microcanonically optimized multidimensional tunneling correction (μOMT) of 1.7 for a peroxy radical H-shift. Zhang and Dibble (53) reported ratios of 0.74 and 2.3 between the Eckart correction and small-curvature tunneling (SCT). All three ratios are at 300 K and calculated as the Eckart correction divided by either SCT or μOMT. μOMT is a more advanced approach than SCT as it includes effects from large-curvature tunneling (LCT) which leads to a higher value for the tunneling correction. As such, we assign a factor of 2 uncertainty in the rate constant at 298 K stemming from the tunneling estimate.

Since our approach to MC-TST includes a cut-off after B3LYP optimizations, where only the conformers within 2 kcal/mol of the lowest in energy are kept, we introduce an imprecision in the sum of partition functions. Møller et al. reported the error to be smaller than 20% for both the forward and reverse rate constant of four different

reactions (28). We used the harmonic oscillator (HO) approximation, which poorly reproduces the barrier to internal torsions, leading to an error in the partition functions used for the rate constants. Zhang and Dibble reported differences up to a factor of five at 300 K between rate constants calculated with harmonic oscillator and hindered rotor (HR) approximations, respectively (53). Lin et al. showed HO partition functions that deviated by 28% compared to values obtained with torsional eigenvalue summation (54). Some of this effect is expected to cancel, as hindered rotors are likely present in both the reactant and TS. Møller et al. showed that using the HR approximations implemented in Gaussian 09 had little effect on their system, with differences no larger than 33% at 298 K (28). Based on these reports we estimate our combined uncertainty from the cutoff and hindered rotations to be a factor of 2.

All of these factors combined would lead to a total uncertainty in the rate coefficient of a factor of 12. However, some of the effects (e.g., barrier height and tunneling) would likely cancel which leads us to estimate a factor of 10 uncertainty in the absolute values of the rate coefficients. However, previous applications of the approach used here produce agreement with experiment to better than a factor of five (28), a trend that is continued in this work. Since these uncertainties probably affect our rate coefficients in similar manners, the calculated rate coefficients are likely more accurate relative to each other. Increasing temperature changes the accuracy of the different approximations, HR becomes more important, and tunneling becomes less important. However, the temperature range considered here is likely too narrow to have a considerable effect on our uncertainty estimates.

High temperature data (318 K)
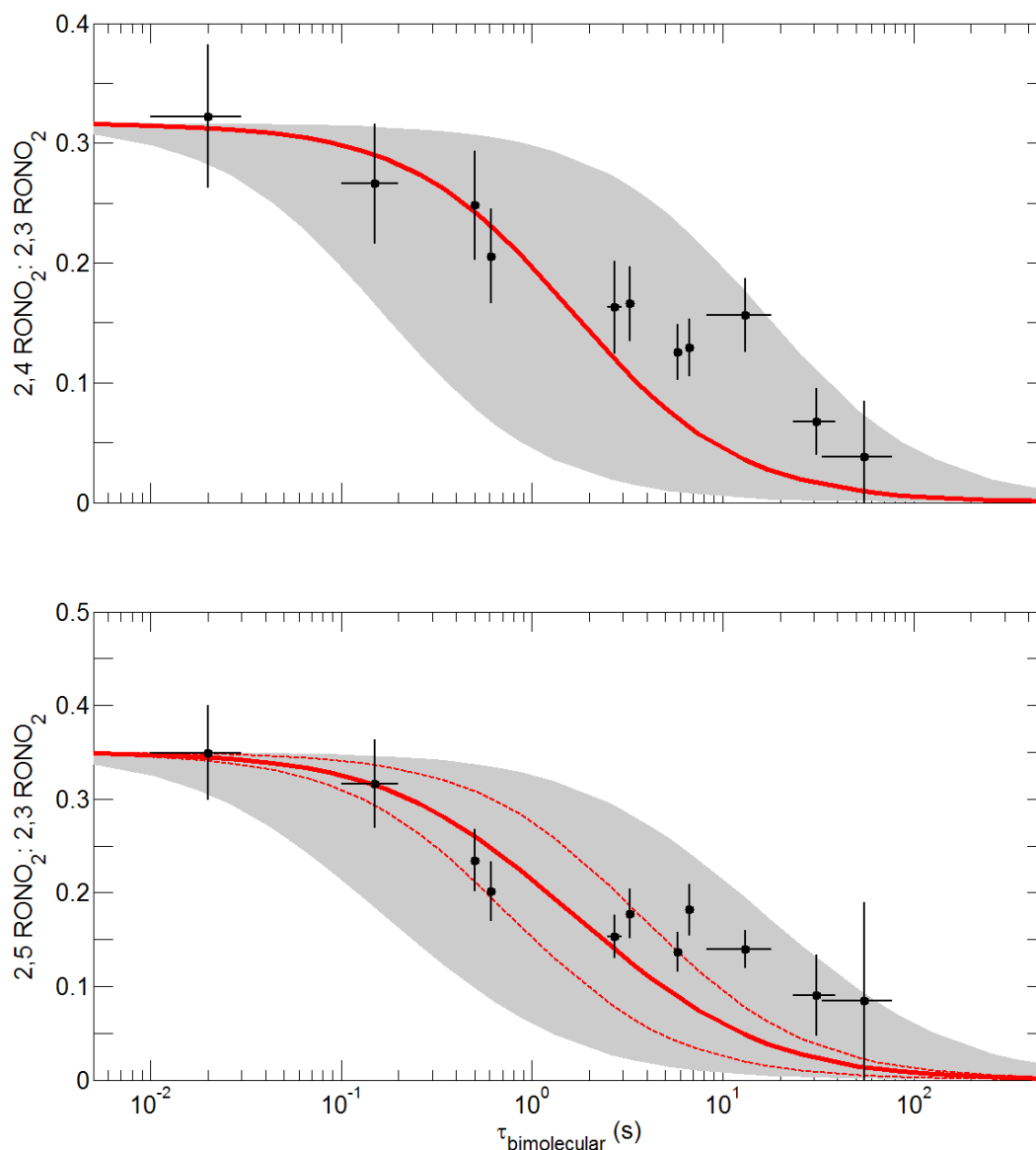
Figure S4. Comparison of experimental (black dots) and computational (red lines) results at 318 K. We demonstrate the difference between S,R and S,S for the 2,5 RO_2 H-shift in the two dashed red lines that, when combined assuming a racemic mixture, produce the solid red line. The gray shaded region represents the range of uncertainty in the calculated rate coefficients.

As discussed in the main article, we observe a significant decrease in the lifetimes of the

2,4 and 2,5 RO_2 at 318 K. This decrease is consistent with the expectation that the rate of

autoxidation increases with temperature (55), and provides confidence in our interpretation of the mechanism. The large scatter in the data compared to the data at 296 K is due, in part, to temperature fluctuations ($\pm$ 5 K) as well as increased water vapor diffusing into the chamber.
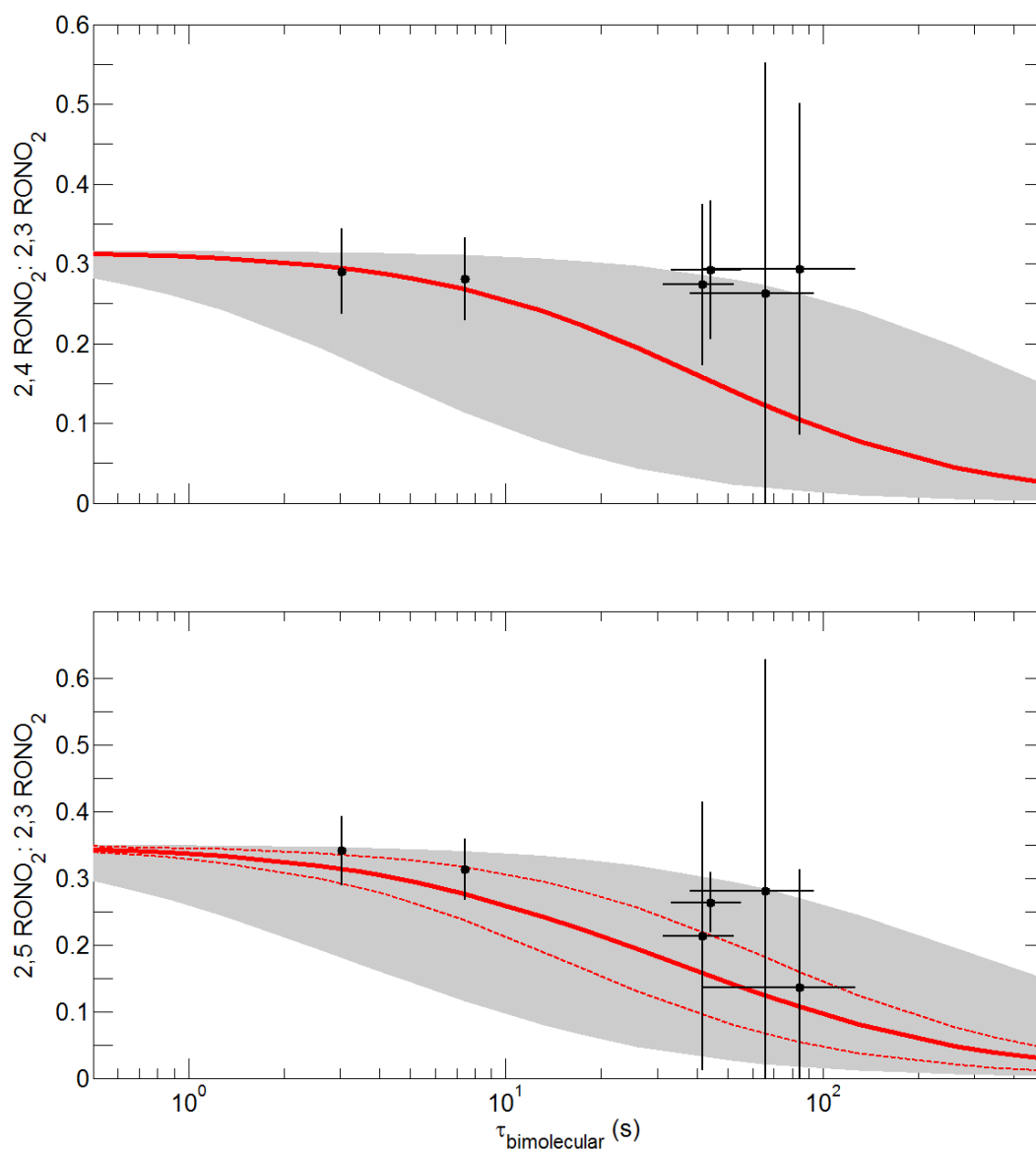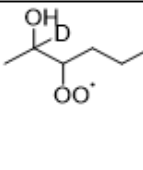
Deuterated 2-hexanol
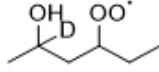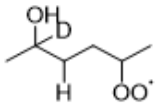
Figure S5. Comparison of experimental (black dots) and computational (red lines) results at 318 K for the deuterated compound. We demonstrate the difference between S,R and

S,S for the 1,5 and 1,6 H-shifts of the 2,5 RO$_2$ in the two dashed red lines that, when combined assuming a racemic mixture, produce the solid red line. The gray shaded region represents the range of uncertainty in the calculated rate coefficients.

Table S5. D(H)-shift rates (s^{-1}) and factors derived from theory and experiment, respectively, for deuterated 2-hexanol. Rate coefficients are calculated following the approach by Møller *et al.* at the CCSD(T)-F12a/cc-pVDZ-F12//ωB97X-D/aug-cc-pVTZ level of theory (28).

Reactant						
D(H)-shift			1,4	1,5	1,5	1,6
298 K	Theory [a]	S,R	4.3×10^{-7}	4.7×10^{-3}	2.9×10^{-4}	0.012
		S,S	1.2×10^{-7}	3.3×10^{-3}	2.0×10^{-4}	2.3×10^{-3}
318 K	Theory [a]	S,R	4.3×10^{-6}	0.028	1.9×10^{-3}	0.063
		S,S	1.3×10^{-6}	0.021	1.3×10^{-3}	0.013
	Expt. (factor) [b]		-	< 0.2 +0.8/-0.2	0.3 +0.6/-0.2	

[a] Uncertainty in the calculated rates is estimated to be a factor of ~10
[b] Reported values correspond to scaling factors that afforded the best fit to the experimental data. The experiments are unable to differentiate the S,R and S,S isomers, nor can they distinguish the 1,5 and 1,6 H-shifts from the 2,5 RO$_2$

Consistent with the proposed mechanism, we observe a primary kinetic isotope effect (KIE) following deuterium substitution at the α–OH center (HOC-**D**). We employed the same experimental method at 318 K for the deuterated substrate to estimate the KIE, and display the results in Figure S5 and Table S5. The best fits to the experimental data are displayed in Figure S10. The calculations suggest that the observed decrease in the RO$_2$ D-shift rate coefficient is due to a decrease in tunneling by a factor of 4–17 and a seemingly systematic ~1 kcal/mol increase in barrier height.

While the ketohydroperoxide product at *m/z* 217 continued to dominate in the

D-substitution experiments, the formation of *m/z* 234 was enhanced compared to the

formation of *m/z* 233 in H-substitution experiments at similar $\tau_{bimolecular}$. For two

experiments at $\tau_{bimolecular}$~7 s, *m/z* 234:*m/z* 217 ~ 0.25 (D-substitution) while *m/z*

233:*m/z* 217 < 0.10 (H-substitution). This signal is consistent with a hydroxy

ketohydroperoxide product, which we suspect results from successive 1,5 H-shifts from

both the 2,5 RO$_2$ (Scheme 4, main article) and 2,3 RO$_2$ (Scheme S1). Calculation of the

1,5 H-shift rate coefficient from the 2,3 RO$_2$ was not undertaken in this work. However,

previous studies have estimated the rate coefficient in similar systems to be of the same

order as the 1,5 H-shift from the 2,5 RO$_2$ reported in Table S5 (13, 66).
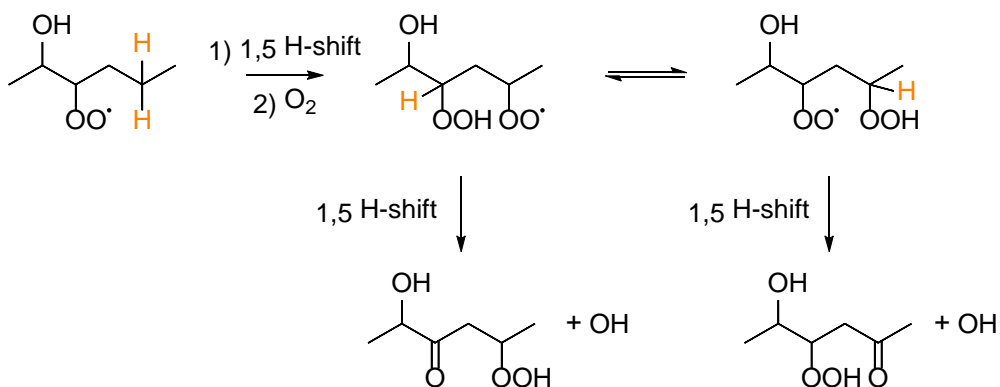
Scheme S1. An additional route to hydroxy ketohydroperoxides with the 2,3 RO$_2$ as the precursor. Hydrogen atoms involved in the H-shifts are orange highlighted.

Diastereoisomer effects

As can be seen from Table S6, there is a 1 kcal/mol difference in the barrier

height for the 1,6 H-shift of the S,R and S,S isomer of the 2,5 RO$_2$. The tunneling

corrections are very similar, as are the ratios between the partition functions of the TS

conformers and reactant conformers. Thus, the difference in barrier height is almost solely responsible for the factor of ~5 difference in the rate coefficients (see main article).

In the case of the 1,4 H-shift of the 2,3 RO_2, there is a factor of ~4 difference in the rate coefficient between the S,R and S,S isomer. The barrier height is ~0.5 kcal/mol lower for the S,R isomer, which increases the rate coefficient. A further increase for the S,R isomer is attained by a greater ratio between the partition functions as well as a higher tunneling correction factor, and cannot solely be ascribed to differences in the barrier height as for the 2,5 RO_2 system.

Table S6. Barrier heights, ratios between partition functions and Eckart tunneling correction factors for the reactions studied here. Calculated following the approach of Møller *et al.* at the CCSD(T)-F12a/cc-pVDZ-F12//ωB97X-D/aug-cc-pVTZ level of theory at 298 K (28).

Reaction	Isomer	$E_{TS,0} - E_{R,0}$ (kcal/mol)	$\dfrac{\sum_i^{TS\ conf.} \exp\left(\frac{-\Delta E_i}{k_B T}\right) Q_{TS,i}}{\sum_j^{R\ conf.} \exp\left(\frac{-\Delta E_j}{k_B T}\right) Q_{R,j}}$	κ_{Eckart}	$k_{H\text{-shift}}$ (s^{-1})
1,4 H-shift	(S,R) 2,3 RO_2	26.08	0.225	606	6.5×10^{-5}
	(S,S) 2,3 RO_2	26.52	0.145	473	1.6×10^{-5}
1,5 H-shift	(S,R) 2,4 RO_2	18.98	0.044	45	0.15
	(S,S) 2,4 RO_2	20.29	0.243	65	0.13
1,6 H-shift	(S,R) 2,5 RO_2	17.60	0.011	40	0.35
	(S,S) 2,5 RO_2	18.64	0.011	43	0.065

The 1,5 H-shift of the 2,4 RO_2 exhibits virtually identical rate constants for the S,R and S,S isomers. Again, the barrier height is lower for the S,R isomer, this time by ~1.3 kcal/mol. However, the ratio of the partition functions is low for the S,R isomer, because of a high number of low-energy reactant conformers. That is not the case for the S,S isomer where the ratio is higher by a factor of ~6. Additionally, the tunneling correction factor is ~50% larger for the S,S isomer. When these three effects are combined, the rate constants are nearly identical at 0.13 s^{-1} and 0.11 s^{-1} (T=296 K) for the S,R and S,S

isomer, respectively. We display the geometries of the lowest lying conformers of the reactant and TS of the 1,4 H-shift of the 2,3 RO_2 (Figure S6) and the 1,5 H-shift of the 2,4 RO_2 (Figure S7). Refer to the main article (Figure 3) for the geometries of the 1,6 H-shift of the 2,5 RO_2. By visual inspection, it is understandable that the barrier height is lower for the S,R isomer. For all three systems, hydrogen bond-like interactions serve to either stabilize the reactant of the S,S isomer or the TS of the S,R isomer. Both lead to a lower barrier height for the S,R isomer relative to the S,S isomer.
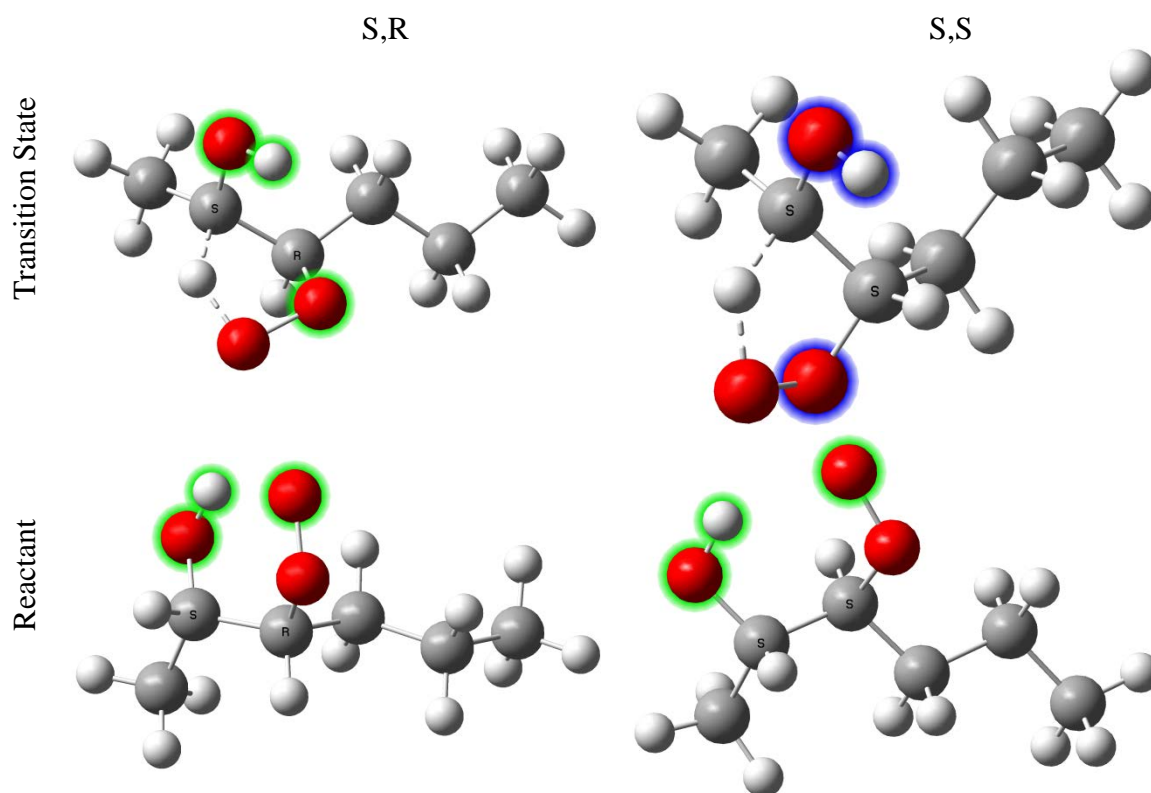
Figure S6. ωB97X-D/aug-cc-pVTZ optimized structures of the lowest energy conformers of the reactant and transition state of the 1,4 H-shift of the 2,3 RO_2. Green halos indicate

atoms involved in the hydrogen bond-like interaction. Blue halos are used when no such interaction exists.
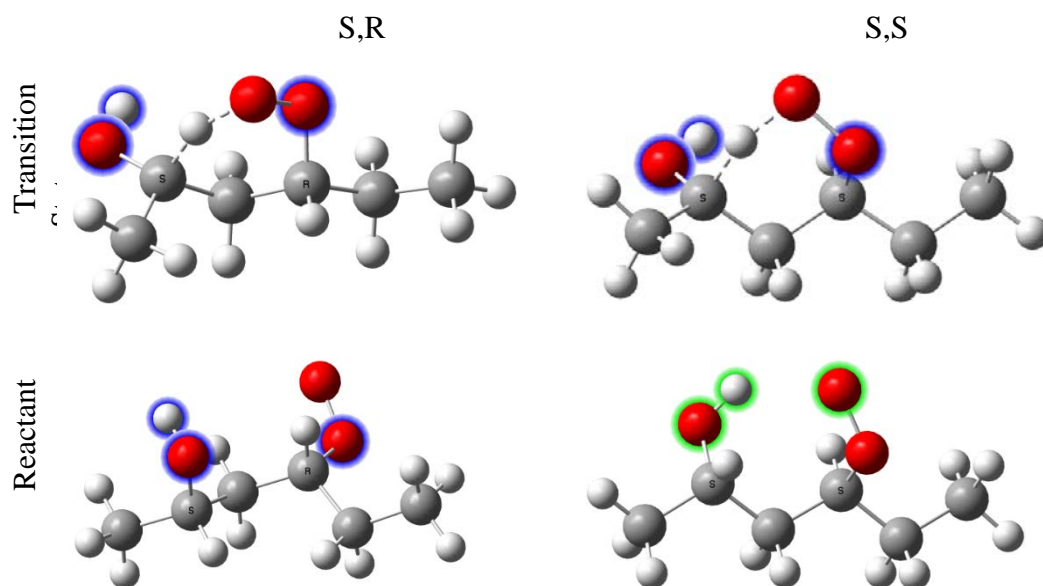
Figure S7. ωB97X-D/aug-cc-pVTZ optimized structures of the lowest energy conformers of the reactant and transition state of the 1,5 H-shift of the 2,4 RO_2. Green halos indicate atoms involved in the hydrogen bond-like interaction. Blue halos are used when no such interaction exists.

Best fits
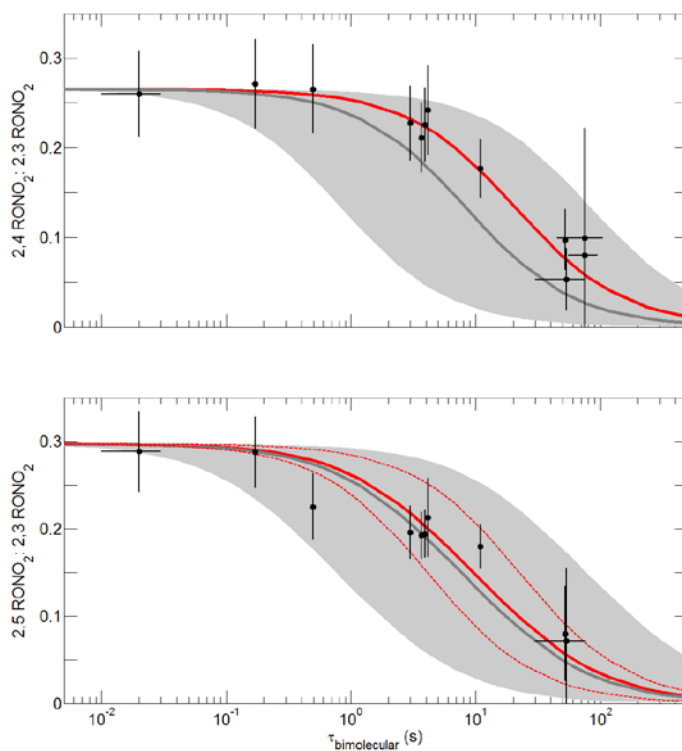
Figure S8. Best fits are shown for the 2-hexanol data at 296 K. Simulated curves (red lines) were generated by multiplying the calculated rate coefficients by the experimental factors displayed in Table 1. The gray line represents the result obtained using the calculated rate coefficients. The solid lines assume a racemic mixture, while the dashed lines assume either entirely S,R or entirely S,S.
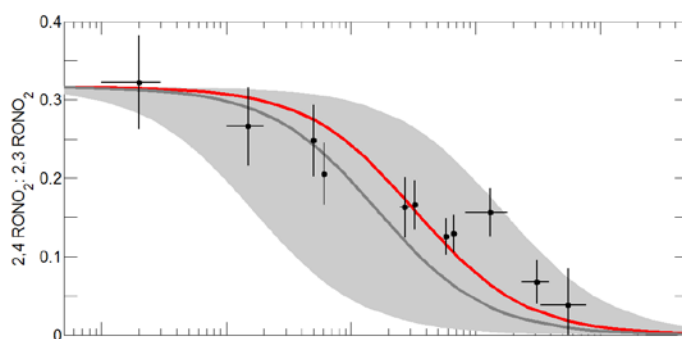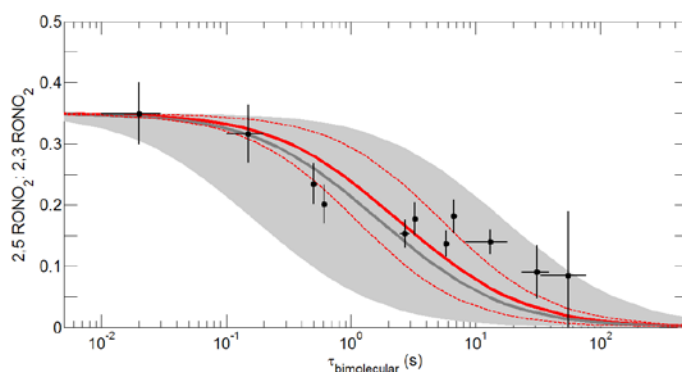
Figure S9. Best fits are shown for the 2-hexanol data at 318 K. Simulated curves (red lines) were generated by multiplying the calculated rate coefficients by the experimental factors displayed in Table 1. The gray line represents the result obtained using the calculated rate coefficients. The solid lines assume a racemic mixture, while the dashed lines assume either entirely S,R or entirely S,S.
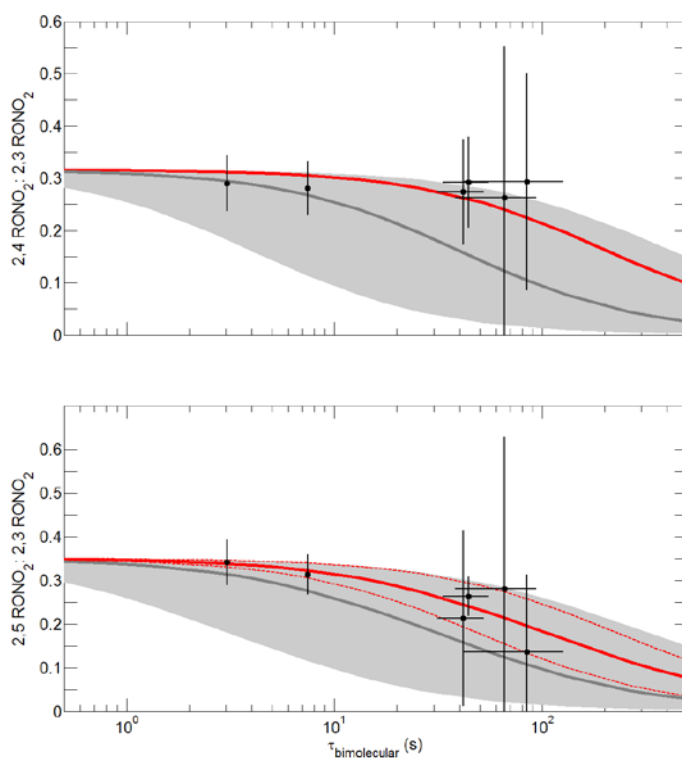
Figure S10. Best fits are shown for deuterated 2-hexanol at 318 K. Simulated curves (red lines) were generated by multiplying the calculated rate coefficients by the experimental factors displayed in Table S5. The gray line represents the result obtained using the calculated rate coefficients. The solid lines assume a racemic mixture, while the dashed lines assume either entirely S,R or entirely S,S.

Previous determination of the 1,6 RO$_2$ H-shift
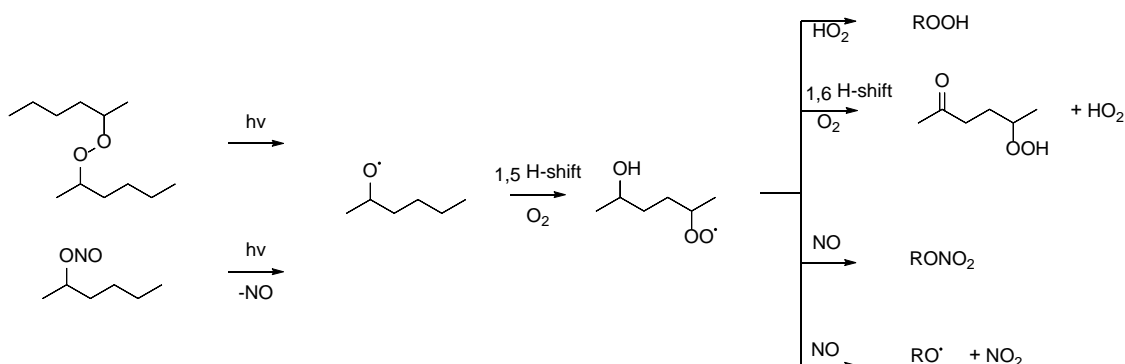
Scheme S2. Mechanism to produce the 2,5 hydroxy RO$_2$ using bis-hexylperoxide and 2-hexylnitrite precursors.

Jorand et al. previously reported rate coefficients for the 1,6 H-shift in this system at elevated temperatures (453 and 483 K) (56). To form the 2,5 RO$_2$ radical, di-2-hexylperoxide was pyrolyzed to produce the same RO$_2$ that undergoes the 1,6 H-shift reported here. For the very fast H-shift rates ($\sim10^3$ s^{-1}) observed at these temperatures, the peroxy radical lifetime is sufficiently short that RO$_2$ self-reactions are minimal despite the large RO$_2$ concentrations produced.

In an attempt to replicate their method, we photolyzed both 2-hexylnitrite and di-2-hexylperoxide (hereafter, hexoxy method) as shown in Scheme S2. However, as our experiments were conducted at room temperature, we needed to significantly reduce the RO$_2$ concentrations to avoid self-reaction. We therefore used a much slower photolysis rate than the pyrolysis rate of Jorand et al. Additionally, we found that photolysis did not constitute the sole loss of starting material. OH-initiated oxidation represented a large fraction of the 2-hexylnitrite and di-2-hexylperoxide loss, which further muddled interpretation of the data. In addition, as the hexoxy method did not produce the suite of

RONO$_2$ used here to diagnose the H-shift rate, our estimation of the rate coefficients in these experiments required absolute quantification of the bimolecular and unimolecular products. As a result of these limitations, attempts to quantify the 1,6 H-shift rate coefficient via this method were inconsistent and prone to error.

Calculations for the hexoxy method

  While assessing the hexoxy chemistry in the laboratory, we completed a series of complementary calculations. Scheme S3 shows the fastest H-shift reactions of 1-hexoxy and its subsequent products. The rate coefficients shown are calculated following the MC-TST approach of Møller et al. used for the other rate coefficients presented in this work and are at the CCSD(T)-F12a/cc-pVDZ-F12//ωB97X-D/aug-cc-pVTZ level of theory (28). The reactions of R• with O$_2$ are assumed to be fast with a pseudo first-order rate coefficient of 1.2×10^7 s^{-1}. This is based on a second-order rate coefficient of 2.3×10^{12} cm^3 molecule^{-1} s^{-1} and an O$_2$ concentration of 5.3×10^{18} molecule cm^{-3} (21% O$_2$ by volume at P=760 torr) (57, 58).

1-hexoxy

1,5 H-shift | 1,6 H-shift

11 s^{-1} | 1.1×10^6 s^{-1} | 26 s^{-1} | 1.0×10^5 s^{-1}

HO | HO

+O$_2$ | +O$_2$

1,4 RO$_2$ | OO$^\bullet$ | HO
HO

1,5 RO$_2$ | OO$^\bullet$

3.1×10^5 s^{-1} | 1,6 H-Shift
0.048 s^{-1}

OOH

HO

+O$_2$
-HO$_2$

OOH

O | HPA
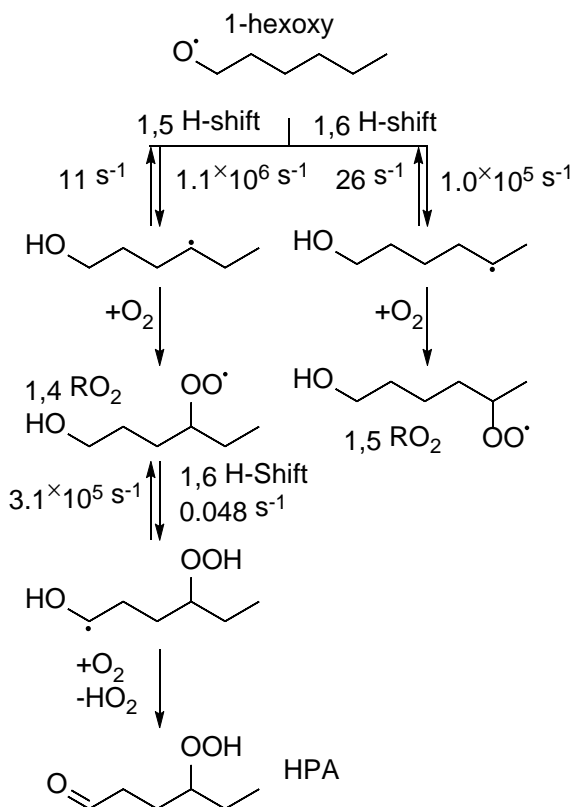
Scheme S3. H-Shift reactions of 1-hexoxy and its H-shift products. Rate coefficients are calculated with MC-TST and CCSD(T)-F12a/VDZ-F12//ωB97X-D/aug-cc-pVTZ.

As can be seen from the forward rate coefficients in Scheme S3, 1-hexoxy is most likely to undergo a 1,5 H-shift. The reverse rate constants are too slow compared to the reaction with O$_2$, leading to formation of the 1,4-hydroxy peroxy radical. The 1,6 H-shift of the 1,4-peroxy radical is the fastest H-shift of that species and forms a new alkyl radical, which finally forms a hydroperoxy-aldehyde (HPA) through H-abstraction by O$_2$. HPA is expected to be the major autoxidation product of 1-hexoxy. According to the MC-TST rate coefficients of the 1,5 and 1,6 H-shift of 1-hexoxy, approximately 10% of 1-hexoxy reacts through a 1,6 H-shift. This finding nominally agrees with the alkoxy SAR of Vereecken et al. (59), and was corroborated in the laboratory. Generally, the
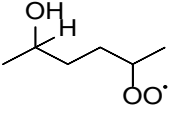
alkoxy radicals are much more reactive than their peroxy counterparts, which is

consistent with results in the literature (60, 61).
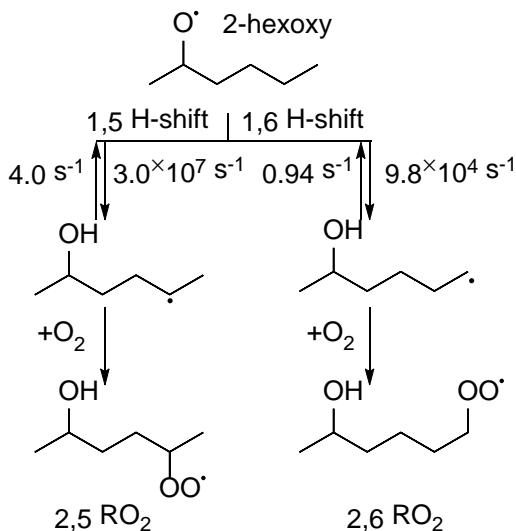
Scheme S4. H-Shift reactions of 2-hexoxy. Rate coeffiecients are calculated with MC-TST and CCSD(T)-F12a/VDZ-F12//ωB97X-D/aug-cc-pVTZ.
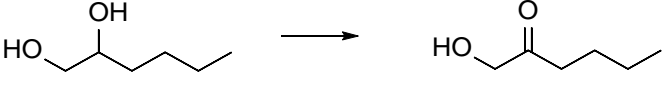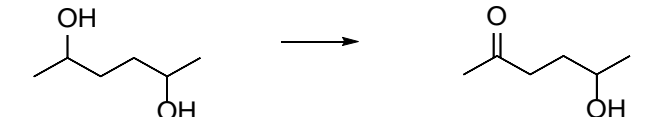
Scheme S4 shows the corresponding mechanism for 2-hexoxy. Based on the MC-TST rate coeffiecients, the 1,5 H-shift accounts for approximately 99% of all H-shift reactions, in agreement with the Vereecken et al. SAR (59). The 2,5 RO_2 is therefore expected to be the major autoxidation precursor, which can isomerize through a 1,6 RO_2 H-shift and form the ketohydroperoxide after reaction with O_2, as shown in the main article. In addition to the temperature range reported here, we calculated the 1,6 H-shift rate coefficient for the temperatures of the Jorand et al. experiments (Table S7). The approach of Møller et al. is optimized at 298 K and, due to hindered rotors and the conformer energy cutoff, becomes less reliable at elevated temperature (28). Nevertheless, reasonable agreement between theory and experiment is demonstrated.

Table S7. H-shift rate coefficients (s^{-1}) derived by theory and earlier experimental work (56). Rate coefficients are calculated following the approach of Møller et al. at the CCSD(T)-F12a/cc-pVDZ-F12//ωB97X-D/aug-cc-pVTZ level of theory.

		453 K	483 K
MC-TST	S,R	8.6×10^2	2.4×10^3
	S,S	2.5×10^2	7.4×10^2
Jorand et al. (2003)		2.3 (+5.6/-1.8) $\times10^3$	6.1 (+14/-4.8) $\times10^3$

Quantification of the 2,5 ketohydroperoxide

Table S8. Comparison of experimentally determined and predicted yields for hexanediol oxidation by OH.

reaction	SAR yield (20)	measured yield (approx.) [b]
	0.75 [a]	0.6 [a]
	0.85	< 0.1

[a] The yield represents the sum of the two β-hydroxycarbonyl isomers
[b] The yield was calculated by dividing the observed formation of the hydroxy carbonyl by the observed loss of the diol. We did not account for potential differences in sensitivity.
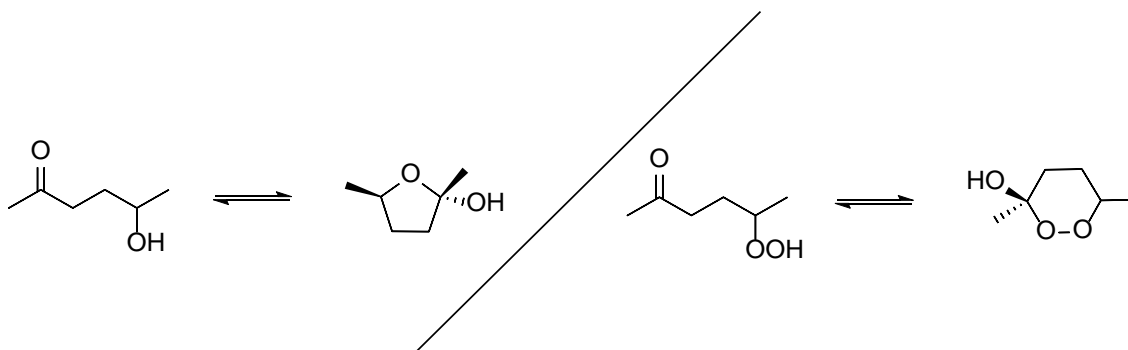
Figure S11. Depiction of the hypothesized cyclization process leading to hemiketal (left) and endoperoxide (right) formation.

One potential source of error in our determination of the H-shift rate using the hexoxy method is lack of carbon closure due to loss of the ketohydroperoxide. This could result, for example, from the formation of an endoperoxide (Figure S11). In a separate set of experiments, we found evidence that cyclization of 2,5 hydroxy ketones occurs. Following the oxidation of 2,5 hexanediol (see Table S8), the measured yield of 5-hydroxy-2-hexanone, the expected major product, was very low. This finding is consistent with hemiketal cyclization as depicted in Figure S11. This (likely heterogeneous) process has previously been suggested to occur in analogous systems (62, 63). In contrast, the observed hydroxy carbonyl yield following oxidation of 1,2 hexanediol was much higher (~0.6), consistent with the expectation that cyclization is minimal for β hydroxy carbonyls. The cyclic products possibly undergo CF_3O^- ion chemistry that results in fragmentation. The calculated sensitivity of the cyclic product was only a factor of 2 lower than the open-chain 5-hydroxy-2-hexanone. The greater than factor of 6 discrepancy in the measured yield is consistent with instrumental quantification challenges.

A similar mechanism is suspected of converting the 2,5 ketohydroperoxide in the hexoxy experiments as demonstrated in previous work (64, 65). Using production rates of the ketohydroperoxide as observed at the CF_3O^- cluster mass (m/z 217), we infer substantially lower H-shift rate coefficients (assuming a ketohydroperoxide yield of 1 following the RO_2 H-shift) than from the nitrate method. We were unable to locate ions consistent with a fragmentation process in the GC analyses, suggesting that the products were undetected.

References

1. Sharpe SW*, et al.* (2004) Gas-phase databases for quantitative infrared spectroscopy. *Appl. Spectrosc.* 58(12):1452-1461.
2. Meddour A, Atkinson D, Loewenstein A, & Courtieu J (1998) Enantiomeric analysis of homologous series of secondary alcohols by deuterium nmr spectroscopy in a chiral nematic liquid crystal: Influence of molecular geometry on chiral discrimination. *Chem. Eur. J.* 4(7):1142-1147.
3. Taylor WD*, et al.* (1980) Atmospheric photo-dissociation lifetimes for nitromethane, methyl nitrite, and methyl nitrate. *Int. J. Chem. Kinet.* 12(4):231-240.
4. Muthuramu K, Shepson PB, & O'Brien JM (1993) Preparation, analysis, and atmospheric production of multifunctional organic nitrates. *Environ. Sci. Technol.* 27(6):1117-1124.
5. Bates KH*, et al.* (2014) Gas phase production and loss of isoprene epoxydiols. *J. Phys. Chem. A* 118(7):1237-1246.
6. Crounse JD, McKinney KA, Kwan AJ, & Wennberg PO (2006) Measurement of gas-phase hydroperoxides by chemical ionization mass spectrometry. *Anal. Chem.* 78(19):6726-6732.
7. Paulot F*, et al.* (2009) Isoprene photooxidation: new insights into the production of acids and organic nitrates. *Atmos. Chem. Phys.* 9(4):1479-1501.
8. Teng AP*, et al.* (2014) Hydroxy nitrate production in the OH-initiated oxidation of alkenes. *Atmos. Chem. Phys. Discuss.* 14(5):6721-6757.
9. St. Clair JM*, et al.* (2016) kinetics and products of the reaction of the first-generation isoprene hydroxy hydroperoxide (ISOPOOH) with OH. *J. Phys. Chem. A* 120(9):1441-1451.
10. Teng AP, Crounse JD, & Wennberg PO (2017) Isoprene peroxy radical dynamics. *J. Am. Chem. Soc.* 139(15):5367-5377.

11. Praske E*, et al.* (2015) Atmospheric fate of methyl vinyl ketone: Peroxy radical reactions with NO and HO$_2$. *J. Phys. Chem. A* 119(19):4562-4572.

12. Teng AP, Crounse JD, & Wennberg PO (2017) Isoprene peroxy radical dynamics. *J. Am. Chem. Soc.* 139(15):5367-5377.

13. Crounse JD*, et al.* (2012) Atmospheric fate of methacrolein. 1. Peroxy radical isomerization following addition of OH and O$_2$. *J. Phys. Chem. A* 116(24):5756-5762.

14. Crounse JD, Nielsen LB, Jørgensen S, Kjaergaard HG, & Wennberg PO (2013) Autoxidation of organic compounds in the atmosphere. *J. Phys. Chem. Lett.* 4(20):3513-3520.

15. Crounse JD, Paulot F, Kjaergaard HG, & Wennberg PO (2011) Peroxy radical isomerization in the oxidation of isoprene. *Phys. Chem. Chem. Phys.* 13(30):13607-13613.

16. Saunders SM, Jenkin ME, Derwent RG, & Pilling MJ (2003) Protocol for the development of the Master Chemical Mechanism, MCM v3 (Part A): tropospheric degradation of non-aromatic volatile organic compounds. *Atmos. Chem. Phys.* 3:161-180.

17. Atkinson R*, et al.* (2004) Evaluated kinetic and photochemical data for atmospheric chemistry: Volume I - gas phase reactions of O$_x$, HO$_x$, NO$_x$ and SO$_x$ species. *Atmos. Chem. Phys.* 4:1461-1738.

18. Su T & Chesnavich WJ (1982) Parametrization of the ion-polar molecule collision rate-constant by trajectory calculations. *J. Chem. Phys.* 76(10):5183-5185.

19. Garden AL*, et al.* (2009) Calculation of conformationally weighted dipole moments useful in ion-molecule collision rate estimates. *Chem. Phys. Lett.* 474(1-3):45-50.

20. Kwok ESC & Atkinson R (1995) Estimation of hydroxyl radical reaction rate constants for gas-phase organic compounds using a structure-reactivity relationship: An update. *Atmos. Environ.* 29(14):1685-1695.

21. Bethel HL, Atkinson R, & Arey J (2001) Kinetics and products of the reactions of selected diols with the OH radical. *Int. J. Chem. Kinet.* 33(5):310-316.

22. Begum S & Subramanian R (2014) Reaction of chlorine radical with tetrahydrofuran: a theoretical investigation on mechanism and reactivity in gas phase. *J Mol Model* 20(6):1-11.

23. Atkinson R*, et al.* (2006) Evaluated kinetic and photochemical data for atmospheric chemistry: Volume II - gas phase reactions of organic species. *Atmos. Chem. Phys.* 6:3625-4055.

24. Scanlon JT & Willis DE (1985) Calculation of flame ionization detector relative response factors using the effective carbon number concept. *J. Chromatogr. Sci.* 23(8):333-340.

25. Atkinson R, Carter WPL, & Winer AM (1983) Effects of temperature and pressure on alkyl nitrate yields in the NO$_x$ photooxidations of normal-pentane and normal-heptane. *J. Phys. Chem.* 87(11):2012-2018.

26. Jeansonne MS & Foley JP (1991) Review of the Exponentially Modified Gaussian (EMG) function since 1983. *J. Chromatogr. Sci.* 29(6):258-266.

27. O'Haver T (2016) Interactive Peak Fitter. Available at https://terpconnect.umd.edu/~toh/spectrum/InteractivePeakFitter.htm. Accessed January 8, 2017.

28. Møller KH, Otkjær RV, Hyttinen N, Kurtén T, & Kjaergaard HG (2016) Cost-effective implementation of multiconformer transition state theory for peroxy radical hydrogen shift reactions. *J. Phys. Chem. A* 120(51):10072-10087.

29. Becke AD (1993) Density-functional thermochemistry. III. The role of exact exchange. *J. Chem. Phys.* 98(7):5648-5652.

30. Lee C, Yang W, & Parr RG (1988) Development of the Colle-Salvetti correlation-energy formula into a functional of the electron density. *Phys. Rev. B* 37(2):785-789.

31. Hehre WJ, Ditchfield R, & Pople JA (1972) Self-consistent molecular orbital methods. XII. Further extensions of gaussian-type basis sets for use in molecular orbital studies of organic molecules. *J. Chem. Phys.* 56(5):2257-2261.

32. Clark T, Chandrasekhar J, Spitznagel GW, & Schleyer PvR (1983) efficient diffuse function-augmented basis sets for anion calculations. III. The 3-21+G basis set for first-row elements, Li–F. *J. Comput. Chem.* 4(3):294--301.

33. Frisch MJ, Pople JA, & Binkley JS (1984) Self-consistent molecular orbital methods 25. Supplementary functions for Gaussian basis sets. *J. Chem. Phys.* 80(7):3265-3269.

34. Frisch MJ, *et al.* (2009) Gaussian 09 (Gaussian, Inc., Wallingford, CT, USA).

35. Spartan'14 (Wavefunction Inc., Irvine, CA).

36. Halgren TA (1996) Merck molecular force field. I. Basis, form, scope, parameterization, and performance of MMFF94. *J. Comp. Chem.* 17(5-6):490-519.

37. Halgren TA (1996) Merck molecular force field. II. MMFF94 van der Waals and electrostatic parameters for intermolecular interactions. *J. Comp. Chem.* 17(5-6):520-552.

38. Halgren TA (1996) Merck molecular force field. III. Molecular geometries and vibrational frequencies for MMFF94. *J. Comp. Chem.* 17(5-6):553-586.

39. Halgren TA & Nachbar RB (1996) Merck molecular force field. IV. conformational energies and geometries for MMFF94. *J. Comp. Chem.* 17(5-6):587-615.

40. Halgren TA (1996) Merck molecular force field. V. Extension of MMFF94 using experimental data, additional computational data, and empirical rules. *J. Comp. Chem.* 17(5-6):616-641.

41. Halgren TA (1999) MMFF VII. Characterization of MMFF94, MMFF94s, and other widely available force fields for conformational energies and for intermolecular-interaction energies and geometries. *J. Comp. Chem.* 20(7):730-748.

42. Kendall RA, Dunning, TH, & Harrison RJ (1992) Electron affinities of the first-row atoms revisited. Systematic basis sets and wave functions. *J. Chem. Phys.* 96(9):6796-6806.

43. Chai J-D & Head-Gordon M (2008) Long-range corrected hybrid density functionals with damped atom-atom dispersion corrections. *Phys. Chem. Chem. Phys.* 10(44):6615-6620.

44. Werner HJ, Knowles PJ, Knizia G, Manby FR, & Schtz M (2012) MOLPRO, version 2012.1, a package of ab initio programs.

45. Watts JD, Gauss J, & Bartlett RJ (1993) Coupled-cluster methods with noniterative triple excitations for restricted open-shell Hartree–Fock and other general single determinant reference functions. Energies and analytical gradients. *J. Chem. Phys.* 98(11):8718-8733.

46. Knizia G, Adler TB, & Werner HJ (2009) Simplified CCSD(T)-F12 methods: Theory and benchmarks. *J. Chem. Phys.* 130(5):20.

47. Adler TB, Knizia G, & Werner H-J (2007) A simple and efficient CCSD(T)-F12 approximation. *J. Chem. Phys.* 127(22):221106.

48. Werner H-J, Knizia G, & Manby FR (2011) Explicitly correlated coupled cluster methods with pair-specific geminals. *Mol. Phys.* 109(3):407-417.

49. Peterson KA, Adler TB, & Werner H-J (2008) Systematically convergent basis sets for explicitly correlated wavefunctions: The atoms H, He, B–Ne, and Al–Ar. *J. Chem. Phys.* 128(8):084102.

50. Eckart C (1930) The penetration of a potential barrier by electrons. *Phys. Rev.* 35(11):1303-1309.

51. Werner H-J, Knizia G, Adler Thomas B, & Marchetti O (2010) Benchmark studies for explicitly correlated perturbation and coupled cluster theories. in *Z. Phys. Chem.*, p 493.

52. Sha Y & Dibble TS (2016) Tunneling effect in 1,5 H-migration of a prototypical OOQOOH. *Chem. Phys. Lett.* 646:153-157.

53. Zhang F & Dibble TS (2011) Impact of tunneling on hydrogen-migration of the n-propylperoxy radical. *Phys. Chem. Chem. Phys.* 13(40):17969-17977.

54. Lin CY, Izgorodina EI, & Coote ML (2008) How accurate are approximate methods for evaluating partition functions for hindered internal rotations? *J. Phys. Chem. A* 112(9):1956-1964.

55. Orlando JJ & Tyndall GS (2012) Laboratory studies of organic peroxy radical chemistry: an overview with emphasis on recent issues of atmospheric significance. *Chem. Soc. Rev.* 41(19):6294-6317.

56. Jorand F*, et al.* (2003) Isomeric hexyl-ketohydroperoxides formed by reactions of hexoxy and hexylperoxy radicals in oxygen. *Int. J. Chem. Kinet.* 35(8):354-366.

57. Seinfeld JH & Pandis SN (1998) *Atmospheric chemistry and physics: from air pollution to climate change* (Wiley, New York).

58. Park J, Jongsma CG, Zhang R, & North SW (2004) OH/OD initiated oxidation of isoprene in the presence of O_2 and NO. *J. Phys. Chem. A* 108(48):10688-10697.

59.   Vereecken L & Peeters J (2010) A structure-activity relationship for the rate coefficient of H-migration in substituted alkoxy radicals. *Phys. Chem. Chem. Phys.* 12(39):12608-12620.

60.   Denisova TG & Denisov ET (2001) Kinetic parameters of alkyl, alkoxy, and peroxy radical isomerization. *Kinet. Catal.* 42(5):620-630.

61.   Dibble TS (2004) Intramolecular hydrogen bonding and double h-atom transfer in peroxy and alkoxy radicals from isoprene. *J. Phys. Chem. A* 108(12):2199-2207.

62.   Lim YB & Ziemann PJ (2009) Kinetics of the heterogeneous conversion of 1,4-hydroxycarbonyls to cyclic hemiacetals and dihydrofurans on organic aerosol particles. *Phys. Chem. Chem. Phys.* 11(36):8029-8039.

63.   Aschmann SM, Arey J, & Atkinson R (2003) Kinetics and products of the gas-phase reaction of OH radicals with 5-Hydroxy-2-Pentanone at 296± 2 K. *J. Atmos. Chem.* 45(3):289-299.

64.   Perrin O, Heiss A, Sahetchian K, Kerhoas L, & Einhorn J (1998) Determination of the isomerization rate constant $HOCH_2CH_2CH_2CH(OO\cdot)CH_3$ $\rightarrow HOC\cdot HCH_2CH_2CH(OOH)CH_3$. Importance of intramolecular hydroperoxy isomerization in tropospheric chemistry. *Int. J. Chem. Kinet.* 30(12):875-887.

65.   Jalan A*, et al.* (2013) New pathways for formation of acids and carbonyl products in low-temperature oxidation: the korcek decomposition of γ-ketohydroperoxides. *J. Am. Chem. Soc.* 135(30):11100-11114.

66.   Jørgensen S*, et al.* (2016) Rapid hydrogen shift scrambling in hydroperoxy-substituted organic peroxy radicals. *J. Phys. Chem. A* 120(2):266-275.

A p p e n d i x   C

SUPPORTING INFORMATION: INTRAMOLECULAR HYDROGEN SHIFT CHEMISTRY OF HYDROPEROXY-SUBSTITUTED PEROXY RADICALS

Experimental

We study the oxidation mechanism of 2-hydroperoxy-2-methylpentane. The reader is referred to the main article for an overview of the method.

Synthesis

2-hydroperoxy-2-methylpentane is synthesized and purified as described in the main article. The compound is characterized by NMR (see Figure S1) and HR-ToF: ^{1}H NMR (400 MHz, CDCl$_3$) δ 7.27 (br s, 1 H), 1.48-1.44 (m, 2 H), 1.33-1.23 (m, 2 H), 1.15 (s, 6 H), 0.86 (t, J = 7.5 Hz, 1H); ^{13}C NMR (100 MHz, CDCl$_3$) δ 82.9, 40.8, 23.8 (2C), 17.3, 14.7; IR (NaCl, film) 3382, 2934, 2872, 2355, 2339, 1455, 1363, 1235, 1175 cm^{-1}; HRMS (CI) m/z 203.0898 [C$_7$F$_3$H$_{14}$O$_3$ (M+CF$_3$O$^-$) requires 203.0895].
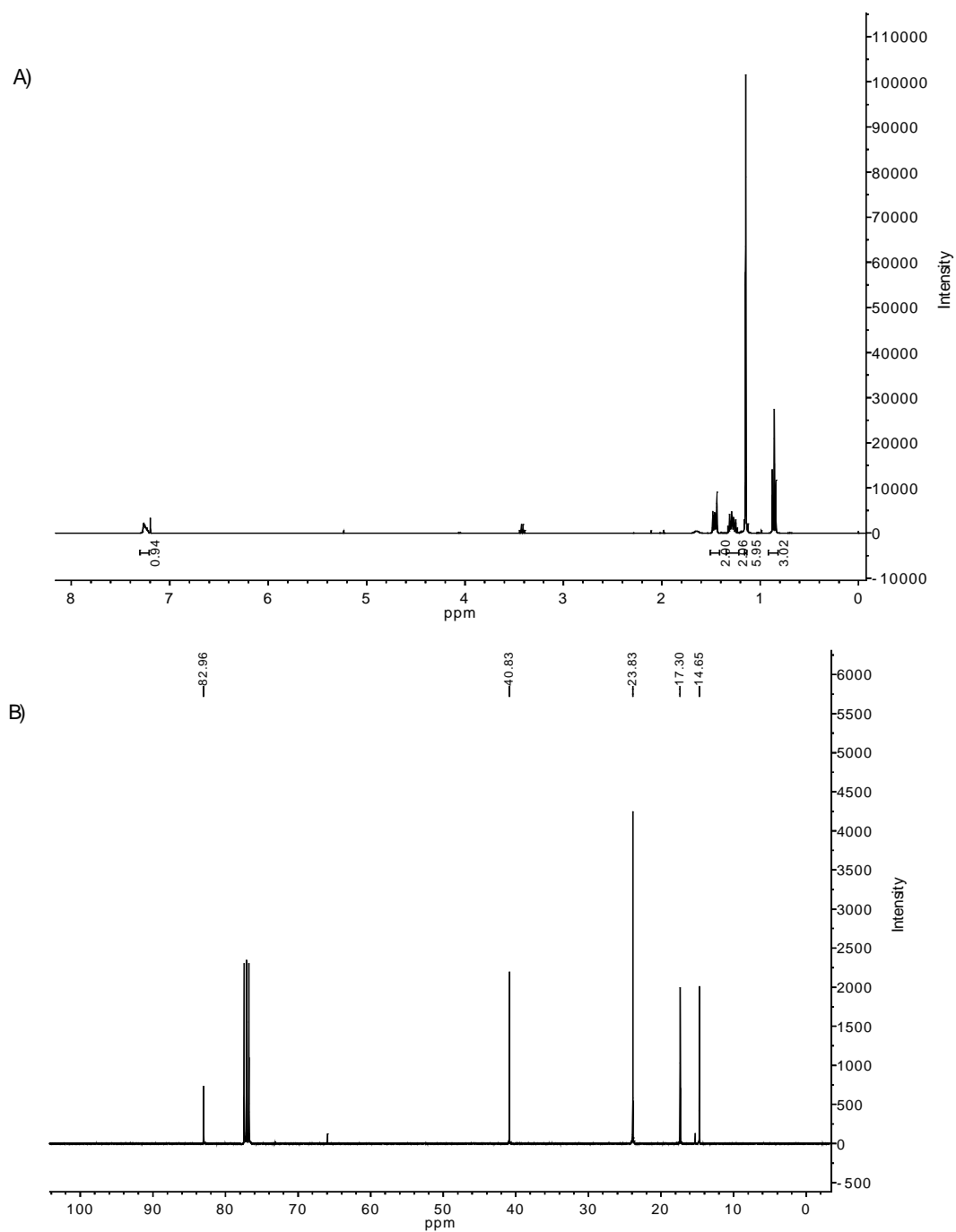
Figure S12. NMR spectra of 2-hydroperoxy-2-methylpentane: A) ^{1}H NMR (400 MHz, CDCl$_3$); B) ^{13}C NMR (100 MHz, CDCl$_3$)

RO₂ lifetime calculation

The concentrations of NO and HO₂ are systematically varied, thus producing a range of $\tau_{bimolecular}$. For experiments in which reaction with NO dominates the RO₂ fate, $\tau_{bimolecular}$ is calculated based on [NO] measurement. For the remainder, $\tau_{bimolecular}$ is calculated as described in Teng et al. and Praske et al.[1-2] This method incorporates an estimate of [NO], building upon the method for estimating [HO₂] originally described by Crounse et al.[3] Observed production rates of H_2O_2 ($P_{H_2O_2}$), the dihydroperoxide (P_{ROOH}), and hydroperoxy-substituted RONO₂ (P_{RONO_2}) are used to constrain [HO₂] and [NO]. This is achieved by using recommended values for k_{RO_2+NO}, $k_{RO_2+HO_2}$, and $k_{HO_2}+k_{HO_2}$.[4-5] The mixing ratio of HO₂ is given by:

$$P_{H_2O_2} = k_{HO_2+HO_2} \times [HO_2]^2$$

$$k_{HO_2+HO_2} = \left(2.2 \text{ x } 10^{-13} \exp\left(\frac{600}{T}\right) + 1.9 \text{ x} 10^{-33}[M] \exp\left(\frac{980}{T}\right)\right)$$

$$\times (1 + 1.4 \times 10^{-21}[H_2O] \exp\left(\frac{2200}{T}\right))$$

$$[HO_2] = \sqrt{\frac{P_{H_2O_2}}{k_{H_2O_2}}}$$

Using [HO₂] and the relative yields of ROOH and RONO₂ as input, [NO] can be approximated according to the following equations:

$$P_{RONO_2} = BR_{RONO_2} \times k_{RO_2+NO} \times [NO] \times [RO_2]$$

$$P_{ROOH} = BR_{ROOH} \times k_{RO_2+HO_2} \times [HO_2] \times [RO_2]$$

$$[NO] = \frac{P_{RONO_2}}{P_{ROOH}} \frac{BR_{ROOH}}{BR_{RONO_2}} \frac{k_{RO_2+HO_2}}{k_{RO_2+NO}} [HO_2]$$

The branching ratio in the reaction of RO_2+HO_2 to yield the hydroperoxide (BR_{ROOH}) is assumed to be unity and BR_{RONO_2} is calculated as described below.

Calculation of BR_{RONO_2}

The branching ratio of the hydroperoxy nitrates resulting from reaction of NO with the hydroperoxy RO_2 cannot be derived in a robust manner using the data. This is due to uncertainty related to the abstraction of the hydroperoxy hydrogen (ROO-**H**), which likely constitutes a significant reaction channel in the oxidation of 2-hydroperoxy-2-methylpentane by OH. Thus, we use the parameterization of Teng et al. to calculate the branching ratio to form hydroperoxy nitrates,[6] with corrections applied for β-hydroperoxy and tertiary RO_2 consistent with the recommendations of Wennberg et al.[5] Accordingly, BR_{RONO_2} is given by:

$$BR_{RONO_2} = (0.045 \pm 0.016) \times N - (0.11 \pm 0.05)$$

where N is the number of heavy atoms excluding the peroxy moiety. For the hydroperoxy-substituted RO_2, there are 10 heavy atoms (N = 10 - 2 = 8) and the nominal $BR_{RONO_2} = 0.25 \pm 0.08$ at 296 K (0.19 ± 0.06 at 318 K). The BR for the 2,3 RO_2 is decreased by 60% relative to the nominal BR_{RONO_2}, while the BR for the tertiary RO_2 is increased by 25%. We use the temperature dependence determined by Atkinson et al. for the organonitrate yield in the oxidation of n-heptane.[7]
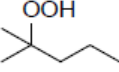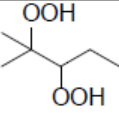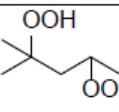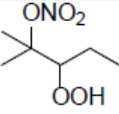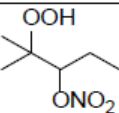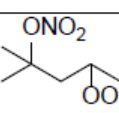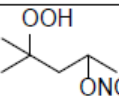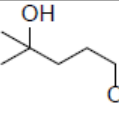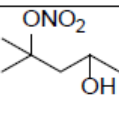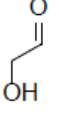
Instrumental calibration

Authentic standards for the multifunctional species presented in this work are not commercially available, thereby precluding a direct calibration for these species. The method of Garden et al. is used for the estimation of instrumental sensitivities.[8] This method employs the parameterization of Su et al. to calculate the ion-molecule collision rate coefficients assuming that all collisions lead to quantifiable product ions.[9] The dipole moments and polarizabilities of closed-shell products are calculated using density functional theory (B3LYP/6-31+G(d)). Due to the dependence of the dipole moment on structural conformation, we use a weighted average of the located conformers. In contrast, the polarizability does not exhibit a large conformational dependence and the determination is based on the lowest energy conformer. These properties for species derived from the 2-hydroperoxy-2-methylpentane system are given in Table S1.

As our estimation of [NO] uses a ratio of production rates $(\frac{P_{RONO_2}}{P_{ROOH}})$, the ratio of the calibration factors is also required. The ratio used is an average of the factors for the 2,3 and 2,4 $RONO_2$ and the 2,3 and 2,4 ROOH. As discussed above, the production rate of H_2O_2 is used to estimate [HO_2] and thereby $\tau_{bimolecular}$. The efficiency of CF_3O^- clustering with H_2O_2 is affected by water vapor, and the method described by Praske et al. was adopted to account for this effect.[2] In general, the growth rate of water vapor in our chamber experiments was significantly slower than those reported in Praske et al. due to the use of a dry air purge inside the chamber enclosure. Thus, the corrections for water vapor that were applied resulted in only minimal changes to [HO_2].

Table S9. Calculated average dipole moments ($\bar{\mu}$) and polarizabilities (α) used to determine ion-molecule collision rate coefficients and instrumental sensitivity. k_x is the conformer weighted average collision rate coefficient. The instrumental sensitivity is derived from the ratio of this rate coefficient for each analyte against that of glycolaldehyde ($k = 2.0 \times 10^{-9}$ cm^3 molecule^{-1} s^{-1}), for which an experimental determination has been made. Dipole moments and polarizabilities are calculated at the B3LYP/6-31+G(d) level of theory.
[a] CF$_3$O$^-$ CIMS sensitivity (norm. cts. pptv^{-1})

Molecule	m/z	$\bar{\mu}$ (D)	α (Å^3)	k_x (10^{-9} cm^3 molecule^{-1} s^{-1})	calculated sensitivity ($\times 10^{-4}$) [a]	experimental sensitivity ($\times 10^{-4}$) [a]
OOH	203	1.8	12	1.7	1.8	-
OOH / OOH	235	2.6	14	2.1	2.2	-
OOH / OOH	235	3.9	14	2.8	2.9	-
ONO$_2$ / OOH	264	4.1	15	2.9	3.0	-
OOH / ONO$_2$	264	4.2	15	2.9	3.0	-
ONO$_2$ / OOH	264	4.5	15	3.1	3.3	-
OOH / ONO$_2$	264	4.6	15	3.1	3.3	-
OH / ONO$_2$	248	4.3	15	3.0	3.2	-
ONO$_2$ / OH	248	4.3	15	3.0	3.2	-
O / OH	145	2.3	4.5	2.0	-	2.1 [b]

[b] This value is based on a recent calibration for glycolaldehyde and differs from that reported in Praske et al.[2] Multiple calibrations for various species demonstrated similar increases in sensitivity presumably due to slight differences in the instrumental configuration.

Chromatography
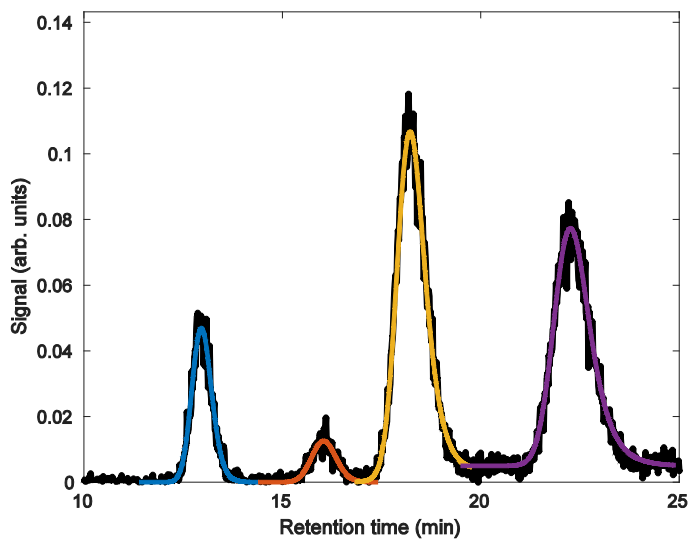
Figure S13. An example chromatogram (black line) for the hydroperoxy-substituted RONO$_2$ (m/z 264; neutral mass 179 amu) outlined in Scheme 2, showing the output of the peak fitting algorithm (colored Gaussians). The final two peaks use linear baseline subtraction. See Figure 1 of the main article for assignment.
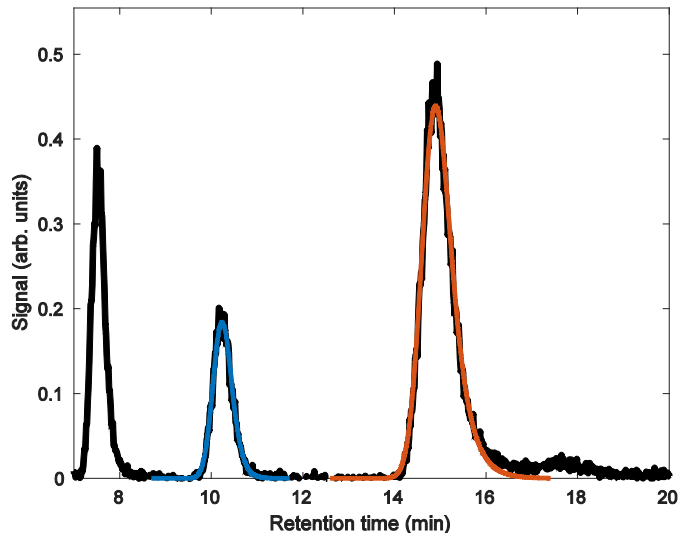
Figure S14. An example chromatogram (black line) for the hydroxy-substituted $RONO_2$ (m/z 248; neutral mass 163 amu) outlined in Scheme 3, showing the output of the peak fitting algorithm (colored Gaussians). See Figure 1 of the main article for assignment.

Following oxidation, the $RONO_2$ are separated by gas chromatography using a Restek RTX-200 11.5 m column with a column flow of 8 sccm N_2. Cryogenic trapping of the analytes is enabled by submersion of a ~20 cm loop of column in an isopropanol bath maintained at -20 ℃. It is not possible to significantly lower this temperature without also trapping water, which degrades the chromatography. Upon collection of the sample, the trap is removed and the temperature program is initiated (30 ℃ for 0.1 min, +20 ℃/min until 80 ℃, hold at 80 ℃ for 25 min, then +20 ℃/min until 130 ℃). The 80 ℃ isothermal elution is necessary to adequately separate the $RONO_2$ while minimizing decomposition. The effluent of the column is diluted with N_2 before being transmitted into the CIMS ion-molecule reaction region. Blank chromatograms are collected prior to the initiation of photoxidation.

Adequate separation of the $RONO_2$ is achieved and peak fitting is performed by using an Exponentially Modified Gaussian (EMG) function adapted from MATLAB code by Dr. Tom O'Haver.[10] The peak parameters are fixed and do not vary between experimental runs. A sample output of the fitting algorithm is shown in Figure S2 and Figure S3. The later eluting isomers exhibit longer tailing and the EMG time constant is adjusted accordingly. All parameters are chosen by minimizing the residuals between the EMG function and the data.

Uncertainty

Experimental uncertainty can be divided into three main categories: estimation of $\tau_{bimolecular}$, instrument calibration factors, and chromatography. The uncertainty is characterized in a manner similar to that described in Praske et al. and only a brief description is given here.[2] In accordance with the method used to calculate $\tau_{bimolecular}$, we use the observed production rates of hydroperoxides and organonitrates. Linear least-squares fits are used to derive the production rates and we include the 1σ error in the slope. Recommended rate coefficients are also used in the estimation of $\tau_{bimolecular}$ and these carry associated uncertainty.[4, 11] Finally, calibration factors are assigned a default uncertainty of $\pm30\%$.

Table S10. Bootstrap results expressed as % uncertainty of measured $RONO_2$ isomer ratios resulting from the peak fits.

	2,4 $RONO_2$:2,3 $RONO_2$	4-hydroxy-2-methyl-2-nitrooxy:2-hydroxy-2-methyl-5-nitrooxy
$\tau_{bimolecular} < 20$ s	25	13
$\tau_{bimolecular} > 20$ s	30	28

The chromatographic uncertainty in the peak fitting algorithm is summarized in Table S2. These values are determined according to a bootstrap method. Two chromatograms are selected for the bootstrap; one is representative of the large signal commonly observed in

short lifetime experiments ($\tau_{bimolecular} < 20$ s) and another is representative of the small signal observed in long lifetime experiments ($\tau_{bimolecular} > 20$ s). The bootstrap varies the default peak shape parameters (e.g. in Figure S2) by $\pm$ 40% over 10,000 fitting trials. Trials that degrade the fit beyond 1σ of the root-mean-square error are rejected. Of those that remain, the minimum and maximum areas are determined for each peak. Thus, the uncertainty is given by the range bounded by the minimum and maximum of the ratios 2,4 $RONO_2$:2,3 $RONO_2$ and 2-nitrooxy-4-hydroxy:2-hydroxy-5-nitrooxy.

The data points displayed in Figure 3 and Figure 4 carry the aforementioned chromatographic uncertainty as well as uncertainty in $\tau_{bimolecular}$. The best fit, used to derive the experimental rate coefficients in Table 2, is determined by a weighted least squares fit to the data (see Figure S4-S5). The sum of squares is given by:

$$\sum_{i=1}^{n} \frac{1}{\sigma_i^2} (y_i - \hat{y}_i)^2$$

where σ_i^2 represents the point-wise variance and $y_i - \hat{y}_i$ denotes the residual between the data points and the model. In order to characterize uncertainty in the experimental factors, a Monte Carlo simulation is conducted. 5,000 synthetic data sets are generated by varying the data points within their respective range of uncertainty and the least squares approach is again adopted to determine the best fit in each of these data sets. The error bounds given in Table 2 represent the full range of values that afforded best fits in the synthetic data sets.

Best fits

The kinetic model, which employed the calculated rate coefficients in Figure 3 and Figure 4, was used to determine the best fit to the experimental data using the weighted least squares procedure described in previous section. The results that afforded best fits are shown in Figure S4 and Figure S5.
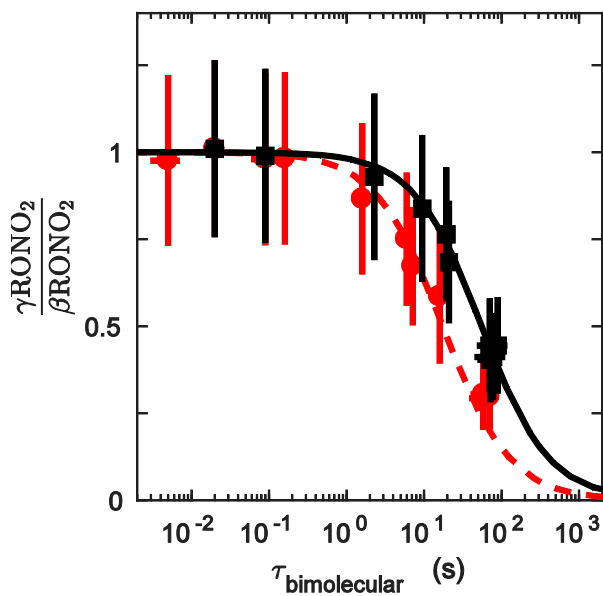
Figure S15. Experimental data used to constrain the α-OOH 1,5 H-shift at 296 K (black squares) and 318 K (red circles). Best fits are shown at 296 K (solid black line) and 318 K (dashed red line). These fits were used to determine the experimental rate coefficients displayed in Table 2.
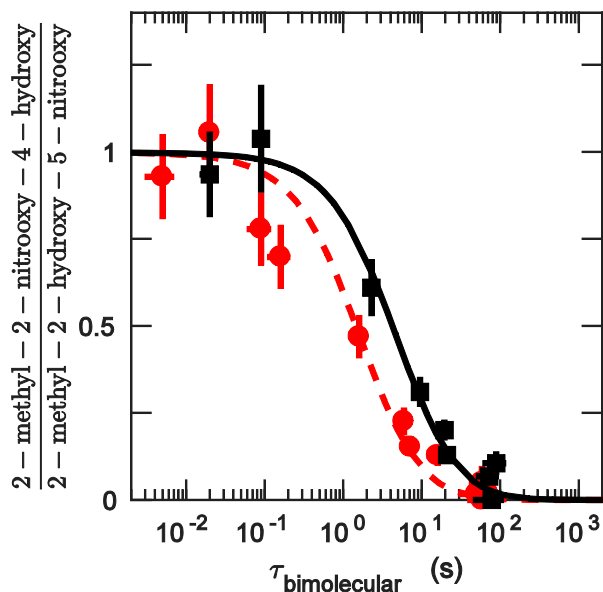
Figure S16. Experimental data used to constrain the α-OH 1,5 H-shift at 296 K (black squares) and 318 K (red circles). Best fits are shown at 296 K (solid black line) and 318 K (dashed red line). These fits were used to determine the experimental rate coefficients displayed in Table 2.

.

Computational

Multiconformer Transition State Theory (MC-TST) is used to calculate the rate coefficients in this work.[12-15] The reader is referred to the main article for an overview of the method.

Tunneling

The 1D Eckart tunneling correction is used in our calculations.[16] The Eckart correction uses the imaginary frequency of the TS and the forward and reverse barrier height as input. An intrinsic reaction coordinate (IRC) is calculated from the B3LYP/6-31+G(d) TS conformer corresponding to the conformer lowest in zero-point corrected energy after

optimization at the ωB97X-D/aug-cc-pVTZ level of theory. The endpoints of the IRC are optimized at the B3LYP/6-31+G(d) level of theory and reoptimized with ωB97X-D/aug-cc-pVTZ. Then, a ROHF-ROCCSD(T)-F12a/VDZ-F12//ωB97X-D/aug-cc-pVTZ single-point energy is calculated. The barrier heights use the single point energy and the ωB97X-D/aug-cc-pVTZ zero-point correction, and the imaginary frequency is calculated with the ωB97X-D functional and the aug-cc-pVTZ basis set.

In some cases, the H-shift leads to decomposition of the product and we could not use the optimized endpoint of the IRC as input for the Eckart correction. This is because the H-shift reaction leads to a radical carbon with an OOH group attached, which is not a minimum on the potential energy surface. It is followed by a second saddle point, which leads to dissociation of the O···O-H bond. Instead, we use the point on the IRC with the lowest RMS gradient before the OOH decomposition occurs. See Figure S5 for an example of the point chosen.
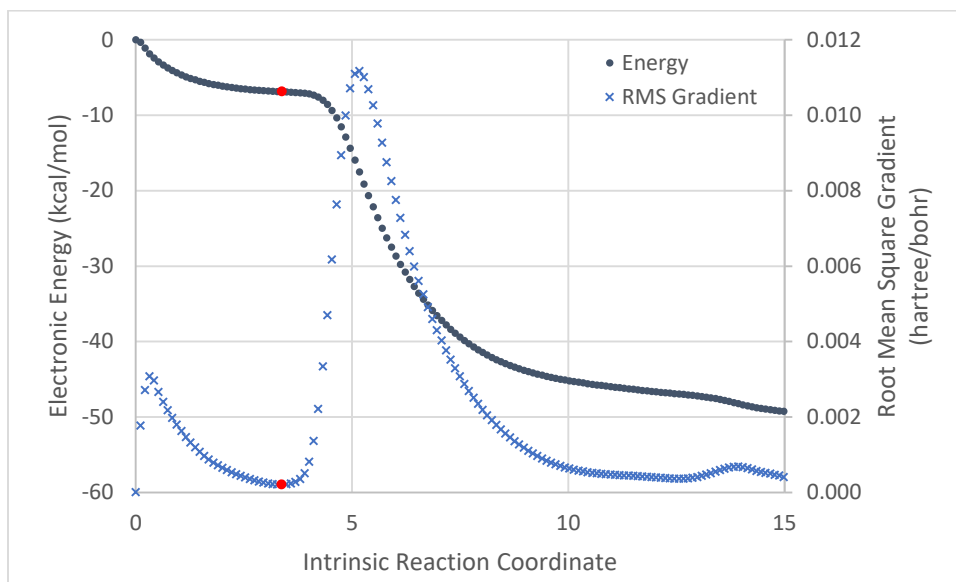
Figure S8. Example of the product side of an IRC leading to decomposition and the corresponding energy and RMS gradient. The electronic energy (grey dots) is plotted on the left axis, relative to the energy of the TS in kcal/mol. The RMS gradient (blue crosses) is on

the right axis in hartree/bohr. The point chosen for the constrained optimization is marked with a red dot.

The geometry at the point indicated on Figure S5 with a red dot is then optimized at the B3LYP/6-31+G(d) level of theory with a fixed O⋯O-H bond distance. It is then reoptimized with the same constraint at the ωB97X-D/aug-cc-pVTZ level of theory and its frequencies are calculated. Finally, a ROHF-ROCCSD(T)-F12a/VDZ-F12//ωB97X-D/aug-cc-pVTZ single-point energy is calculated. The barrier heights for the Eckart correction are derived from a combination of the zero-point correction from the ωB97X-D/aug-cc-pVTZ calculation and the electronic energy from the ROHF-ROCCSD(T)-F12a/VDZ-F12//ωB97X-D/aug-cc-pVTZ single-point calculation.

OH-Initiated Oxidation of 2-hydroperoxy-2-methylpentane
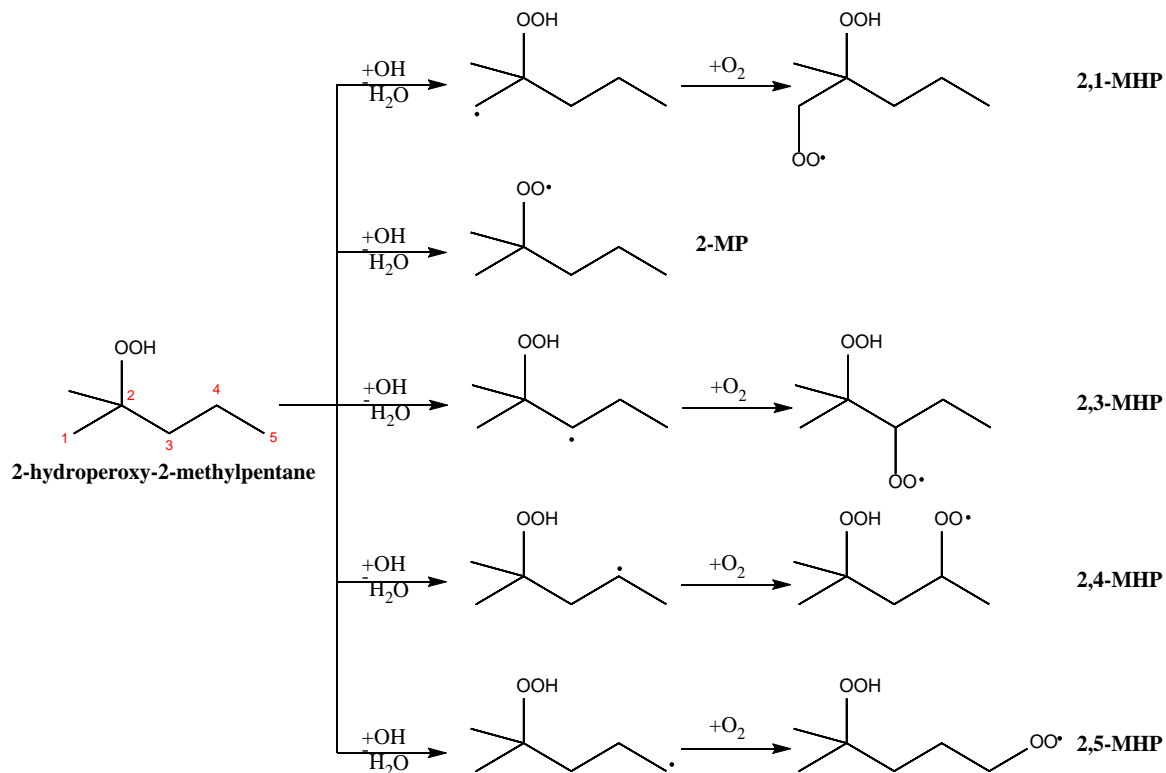
Figure S9. The RO₂ formed following OH-initiated oxidation of 2-hydroperoxy-2-methylpentane. The atom numbering used for naming the compounds is shown in red on 2-hydroperoxy-2-methylpentane.

The reaction of 2-hydroperoxy-2-methylpentane with OH gives rise to multiple alkyl radicals (see Figure S6). OH abstraction at the primary centers (C1 and C5) is expected to account for only a minor fraction of the total reactivity.[17] Abstraction at C3 and C4 leads to two RO₂ that we refer to as 2,3-MHP and 2,4-MHP. Under this naming convention, the first number is the position of the hydroperoxy group and the second is the position of the RO₂. Abstraction of the hydrogen atom in the hydroperoxy group leads to a monofunctional RO₂, which we refer to as 2-MP. We consider the possibility that the alkyl radicals undergo H-shift chemistry prior to O₂ addition. The alkyl radical preceding 2,4 MHP formation is investigated in order to rule out a fast H-shift proceeding by abstraction of the hydroperoxide

hydrogen (ROO-**H**). At 298.15 K, the rate coefficient is calculated to be $2.1 \cdot 10^5 \text{ s}^{-1}$ and, therefore, this reaction is not expected to compete with O_2 addition ($\sim 10^7 \text{ s}^{-1}$) under the conditions of these experiments (1 atm in air). We assume that the same is true of the other alkyl radicals.
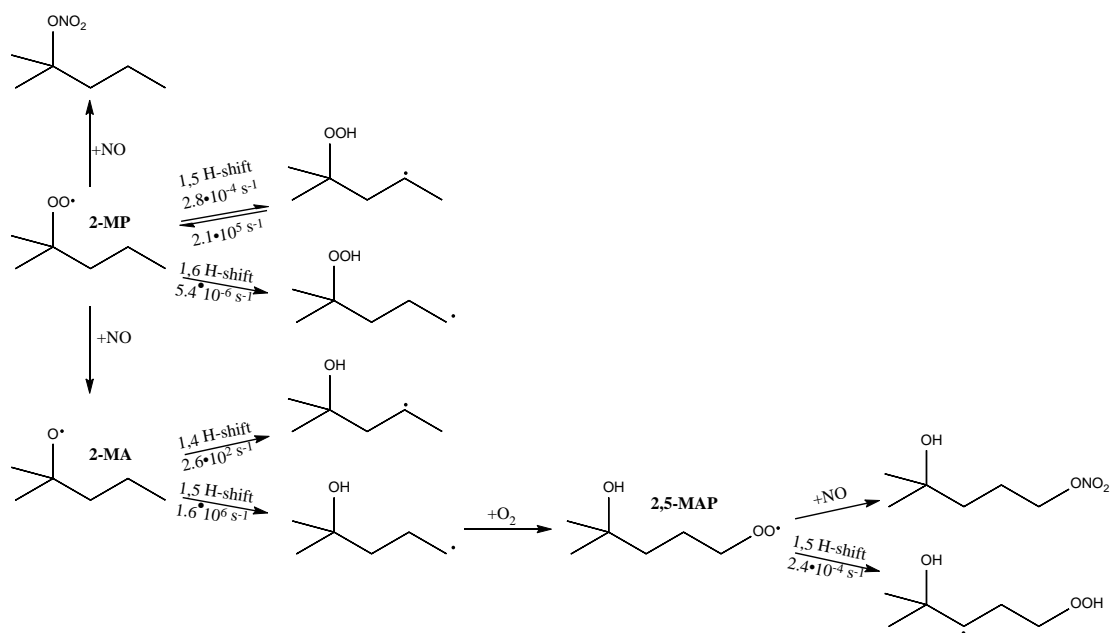
Figure S10. Reactions of 2-MP. Based on the reverse rate coefficient of the 2-MP 1,5 H-shift, O$_2$ addition to the alkyl radical is expected to dominate. The rate coefficients shown are calculated at 298.15 K.

Selected reactions of 2-MP and its products are shown in Figure S7. 2-MP can undergo a 1,5 or 1,6 H-shift. These H-shifts are competing with reaction with NO to form either an organic nitrate or an alkoxy radical. The fastest H-shift of 2-MP is the 1,5 H-shift which has a rate coefficient of $2.8 \cdot 10^{-4} \text{ s}^{-1}$. Because of the slow H-shift rate coefficients, it is likely that 2-MP will react with NO to form an alkoxy radical, 2-MA, or an organic nitrate. We have calculated the rate coefficients of both the 1,4 and 1,5 H-shifts arising from 2-MA.

The 1,5 H-shift is the fastest with a rate coefficient of $1.6 \cdot 10^6$ s^{-1}. This reaction leads to an alkyl radical, which can add O_2 to form a new peroxy radical, 2,5-MAP. The fastest H-shift of 2,5-MAP is likely the 1,5 H-shift, which we calculate to have a rate coefficient of $2.4 \cdot 10^{-4}$ s^{-1}. Thus, bimolecular reaction is expected to dominate under our experimental conditions.

The H-shift reactions of 2,3-MHP are shown in Figure S8. 2,3-MHP only has one fast H-shift, the 1,6-OOH H-shift, which forms 3,2-MHP. The possible 1,4 H-shift of 2,3-MHP abstracting from the C4 position is expected to be slow based on the calculated rate coefficients of the 1,4 H-shift in 3,2-MHP and those calculated by Otkjær et al.,[18] as are the H-shifts that abstract from the methyl groups. That leaves only the 1,6-OOH H-shift, which has a fast forward rate coefficient of $2.3 \cdot 10^2$ s^{-1}. It has a reverse rate coefficient of $3.8 \cdot 10^2$ s^{-1} and, in the absence of fast bimolecular reaction, we expect a rapid interconversion between the 2,3- and 3,2-MHP. 3,2-MHP can undergo a 1,4 H-shift abstracting at C3 or a 1,5 H-shift abstracting at C4. The 1,4 H-shift is expected to be faster than other 1,4 H-shifts due to the OOH group at C3, but we also investigated the 1,5 H-shift because 1,5 H-shifts generally are among the fastest peroxy radical H-shifts.[19-20] We calculate both H-shifts to be relatively

slow, with the fastest forward rate coefficient being $5.3 \cdot 10^{-4}$ s^{-1} for the 1,5 H-shift. Again,

we expect bimolecular reaction to dominate under the experimental conditions.
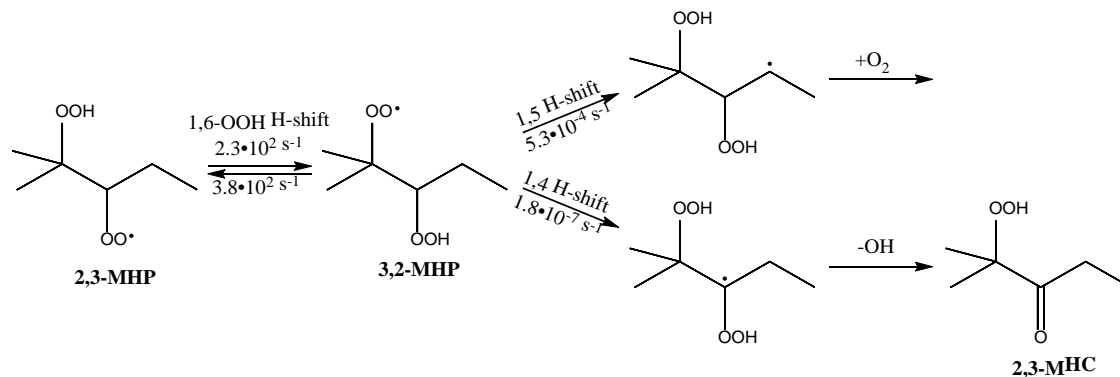
Figure S11. H-shift reactions of 2,3-MHP. Reactions with NO or HO$_2$ are omitted for clarity. The rate coefficients shown are calculated at 298.15 K.

In Figure S9, we show the calculated rate coefficients of the H-shifts of 2,4-MHP. The only H-shift investigated for 2,4-MHP is the 1,7-OOH H-shift, which has forward and reverse rate coefficients of $2.3 \cdot 10^4$ s^{-1} and $7.3 \cdot 10^3$ s^{-1}, respectively. All other H-shifts of 2,4-MHP are expected to be slow. The large rate coefficient for the 1,7-OOH H-shift lead to rapid scrambling between the 2,4- and 4,2-MHP. 4,2-MHP can undergo a 1,5 H-shift, which has a relatively large forward rate coefficient of 0.054 s^{-1}. The reverse reaction was not calculated as the product is expected to decompose promptly, forming a carbonyl and

releasing OH. We expect the 2,4 methyl-hydroperoxy-carbonyl (2,4 MHC) to be a major

product of 2,4-MHP, with the yield depending on $\tau_{bimolecular}$.
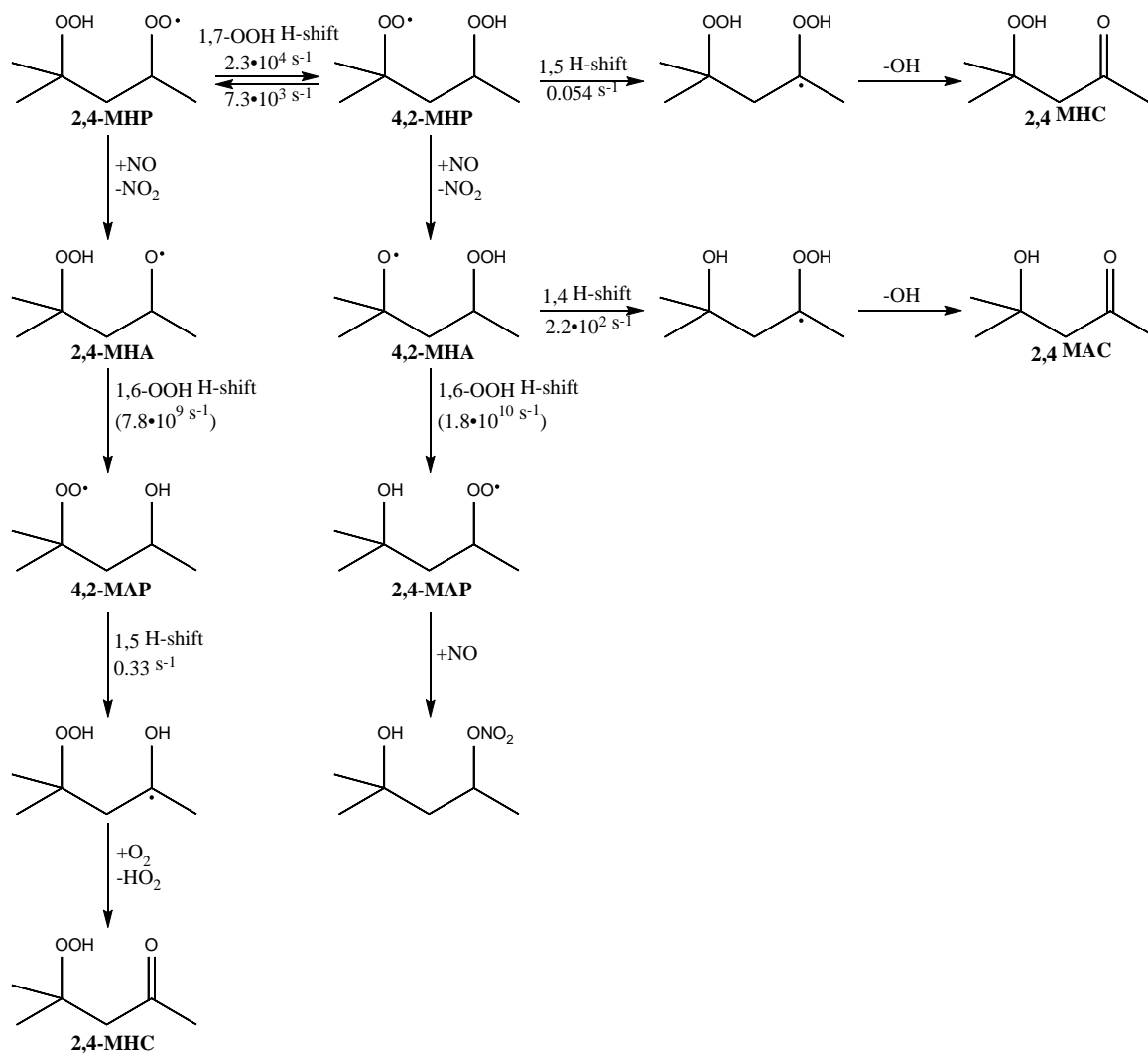
Figure S12. H-shift reactions of 2,4-MHP. Only selected reactions with NO or HO$_2$ are shown for clarity. The rate coefficients shown are calculated at 298.15 K. Rate coefficients in parentheses are only calculated at the ωB97X-D/aug-cc-pVTZ level of theory due to Hartree-Fock convergence issues encountered in the CCSD(T)-F12a/VDZ-F12 calculations.

At high NO concentrations, both 2,4-MHP and 4,2-MHP can react with NO to form

alkoxy radicals, 2,4-MHA and 4,2-MHA, respectively. Both alkoxy radicals undergo a 1,6-

OOH H-shift. We only calculated the rate coefficients of these two H-shifts at the ωB97X-

D/aug-cc-pVTZ level of theory, due to issues with Hartree-Fock convergence for the CCSD(T)-F12a/VDZ-F12 single-point calculation of the energy of the TS. We calculate the 1,6 H-shift of 2,4-MHA to have a rate coefficient of $7.8 \cdot 10^9$ s^{-1}. This leads to the peroxy radical 4,2-MAP. 4,2-MAP undergoes a 1,5 H-shift with a rate coefficient of 0.33 s^{-1}, leading to the formation of a carbonyl (2,4-MHC) through reaction with O$_2$. This is the same carbonyl as the one formed by the 1,5 H-shift of the 4,2-MHP. The other alkoxy radical, 4,2-MHA, undergoes either a 1,4 H-shift to produce a carbonyl, or a 1,6-OOH H-shift. These H-shifts have rate coefficients of $2.2 \cdot 10^2$ s^{-1} and $1.8 \cdot 10^{10}$ s^{-1}, respectively. We expect 4,2-MHA to react via the 1,6-OOH H-shift to form 2,4-MAP, which likely has no fast intramolecular chemistry.

OH-Initiated Oxidation of 2-hydroperoxypentane

As a theoretical complement to the 2-hydroperoxy-2-methylpentane calculations, we studied some of the reactions following OH-initiated oxidation of 2-hydroperoxypentane (see Figure S10).
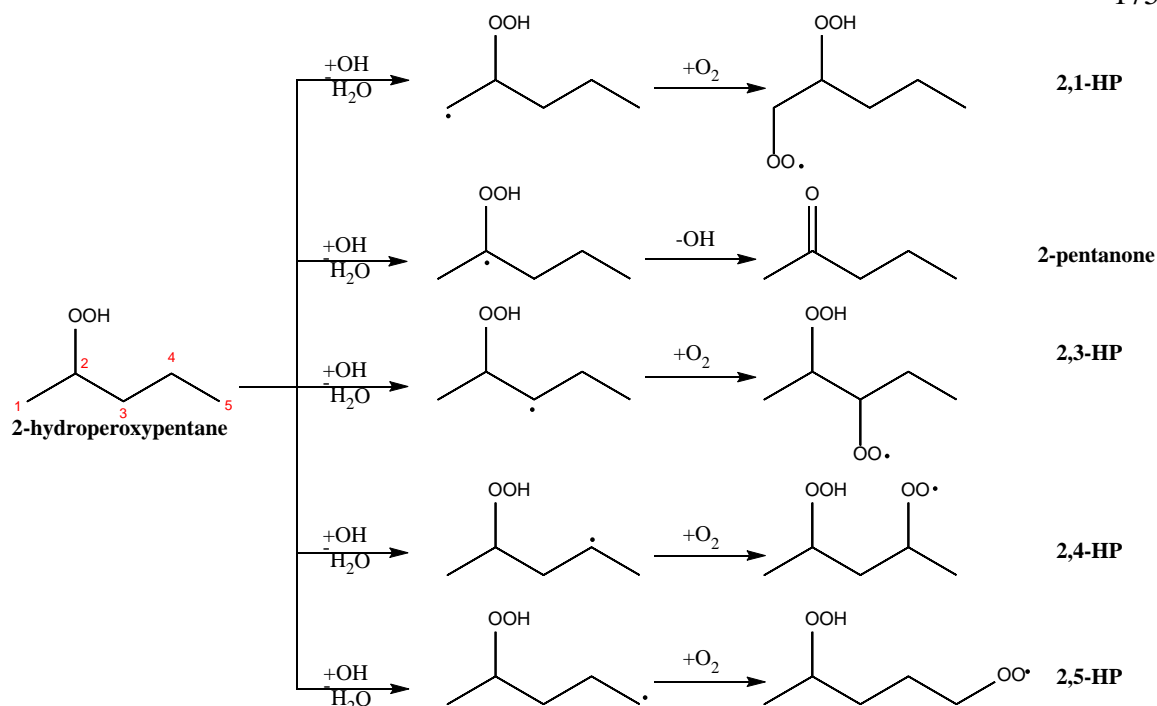
Figure S13. The RO₂ formed following OH-initiated oxidation of 2-hydroperoxypentane. The atom numbering used to name the peroxy radicals is shown in red on 2-hydroperoxypentane.

Abstraction by OH at C2, which yields 2-pentanone, is likely the major reaction but is not of interest here. The most important peroxy radicals in our study are the 2,3- and 2,4-HP, as abstraction at C1 and C5 is expected to be minor. The abstraction of the ROO-**H** likely comprises a significant part of the branching ratio, but the reactions of the resulting peroxy radical are not studied here. Since both 2,3-HP and 2,4-HP have two chiral centers, a total of four diastereomers are produced. We have studied the S,R and S,S diastereomers. The enantiomers are expected to have identical reactivities. The possible H-shift reactions of 2,3-HP are shown in Figure S11.
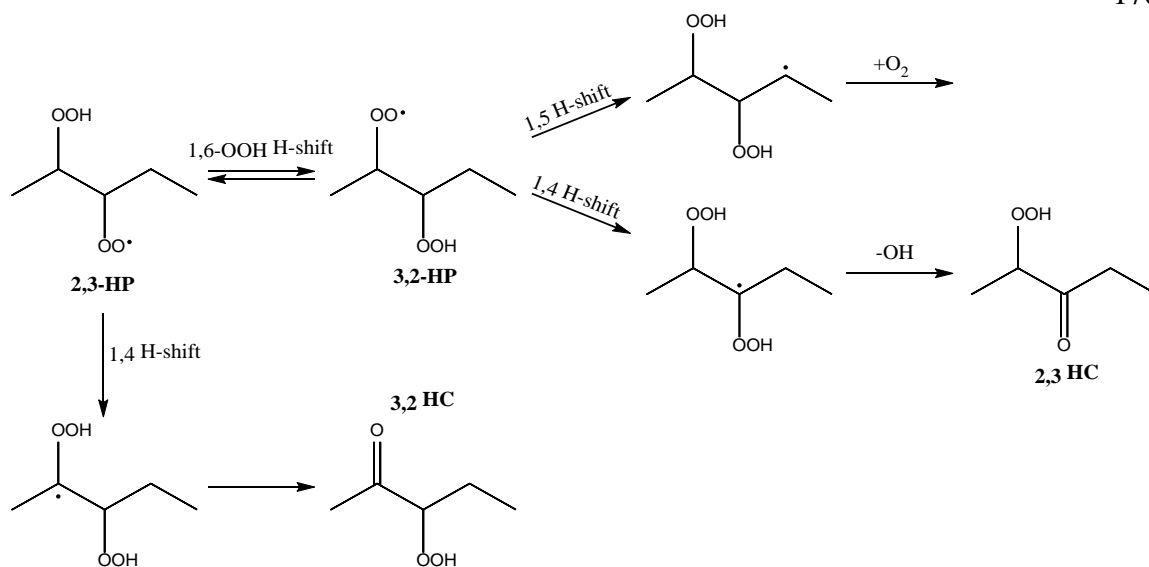
Figure S14. H-shift reactions of 2,3-HP. Reactions with NO or HO₂ are omitted for brevity. The fastest H-shift of 2,3-HP is the 1,6-OOH H-shift, which forms 3,2-HP. It has a forward (and reverse) rate coefficient of 4.4 s⁻¹ (3.3 s⁻¹) for the S,R diastereomer and 13 s⁻¹ (9.6 s⁻¹) for the S,S isomer.

The possible 1,4 H-shift of 2,3-HP is slow for both diastereomers, with the largest rate coefficient of 9.0×10^{-6} s^{-1} for the S,S diastereomer. Both diastereoisomers rapidly, and reversibly, isomerize to form 3,2-HP through the 1,6-OOH H-shift (see Figure S11). 3,2-HP can undergo either a 1,4 or 1,5 H-shift. Both are slow with the largest rate coefficient being the 1,5 H-shift of (S,R) 3,2-HP with a rate coefficient of 6.1×10^{-4} s^{-1}. We expect bimolecular reaction to dominate even with relatively low NO concentrations. The rate coefficients of 2,3-HP and 3,2-HP are shown in Table S3.

Table S4. Calculated rate coefficients in the oxidation of 2-hydroperoxypentane at 298.15 K.

Reactant	H-shift	Isomer	k_f (s^{-1})	k_r (s^{-1})
2,3-HP	1,4	S,R	5.0×10^{-6}	-
		S,S	9.0×10^{-6}	-
	1,6-OOH	S,R	4.4	3.3
		S,S	13	9.6
3,2-HP	1,4	S,R	8.8×10^{-7}	-
		S,S	4.8×10^{-6}	-
	1,5	S,R	6.1×10^{-4}	2.0×10^{5}
		S,S	2.4×10^{-4}	5.4×10^{4}
2,4-HP	1,5	S,R	0.046	-
		S,S	0.12	-
	17-OOH	S,R	6.5×10^{3}	-

		S,S	1.2×10^3	-

In Figure S12 we show the H-shift reactions of 2,4-HP. It can undergo two different, relatively fast H-shifts, the 1,7-OOH and the 1,5 H-shift. The 1,7-OOH H-shift forms a mirror image of the same compound. The 1,5 H-shift leads to the formation of a ketone. The rate coefficients are shown in Table S3.
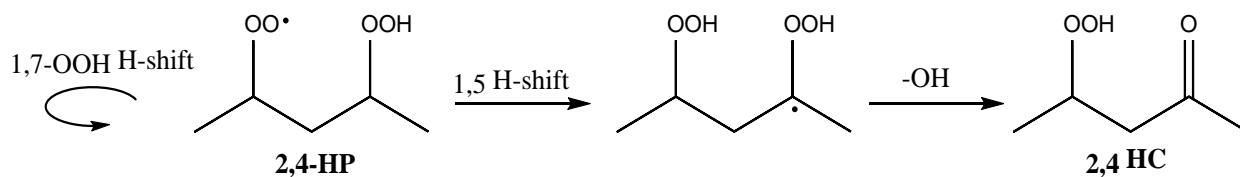
Figure S15. The reactions of 2,4-HP. The curved arrow represents the 1,7-OOH H-shift which, because of symmetry, forms a diastereomer of the same compound. Reactions with NO and HO$_2$ are omitted for brevity.

Temperature Dependencies

The temperature dependencies shown here are obtained by calculating the MC-TST rate coefficients every 5 K between 290-320 K. The MC-TST rate coefficients without tunneling are plotted against $1/T$, while the tunneling corrections are plotted against $1/T^3$. Exponential functions are used to fit the data points. The prefactors of the two exponentials are multiplied to give the factor listed in Table S4. The rate coefficients calculated at 320 K warrant a higher value for the cutoff after B3LYP optimizations to keep the cutoff at a constant value of k_BT, but the error induced by this is likely negligible in the temperature range studied. The expressions in Table S4 and Table S5 yield rate coefficients within 2% of the calculated MC-TST values.

Table S5. Temperature dependencies of the H-shift rate coefficients in the OH oxidation of 2-hydroperoxy-2-methylpentane. They are intended for use in the range 290-320 K.

Reactant	H-shift	Direction	k (s⁻¹)
2-MP	1,5	Forward	$1.4274 \times 10^{12} \times \exp\left(\frac{-11628}{T}\right) \times \exp\left(\frac{7.5299 \times 10^7}{T^3}\right)$
		Reverse	$2.6380 \times 10^{15} \times \exp\left(\frac{-7783.8}{T}\right) \times \exp\left(\frac{7.5299 \times 10^7}{T^3}\right)$
	1,6	Forward	$4.4977 \times 10^{11} \times \exp\left(\frac{-12528}{T}\right) \times \exp\left(\frac{8.1210 \times 10^7}{T^3}\right)$
2-MA	1,4	Forward	$9.4683 \times 10^{11} \times \exp\left(\frac{-7986.6}{T}\right) \times \exp\left(\frac{1.2625 \times 10^8}{T^3}\right)$
	1,5	Forward	$2.9427 \times 10^{11} \times \exp\left(\frac{-4345.7}{T}\right) \times \exp\left(\frac{6.4884 \times 10^7}{T^3}\right)$
2,5-MAP	1,5	Forward	$1.4036 \times 10^{11} \times \exp\left(\frac{-10869}{T}\right) \times \exp\left(\frac{6.5382 \times 10^7}{T^3}\right)$
2,3-MHP	1,6-OOH	Forward	$3.9846 \times 10^{12} \times \exp\left(\frac{-9083.8}{T}\right) \times \exp\left(\frac{1.8194 \times 10^8}{T^3}\right)$
		Reverse	$4.4257 \times 10^{11} \times \exp\left(\frac{-8275.6}{T}\right) \times \exp\left(\frac{1.8194 \times 10^8}{T^3}\right)$
3,2-MHP	1,4	Forward	$1.0845 \times 10^{12} \times \exp\left(\frac{-14830}{T}\right) \times \exp\left(\frac{1.7223 \times 10^8}{T^3}\right)$
	1,5	Forward	$6.6275 \times 10^{12} \times \exp\left(\frac{-11947}{T}\right) \times \exp\left(\frac{7.9513 \times 10^7}{T^3}\right)$
		Reverse	$6.3796 \times 10^{12} \times \exp\left(\frac{-6173.0}{T}\right) \times \exp\left(\frac{7.9513 \times 10^7}{T^3}\right)$
2,4-MHP	1,7-OOH	Forward	$2.0584 \times 10^{11} \times \exp\left(\frac{-6001.6}{T}\right) \times \exp\left(\frac{1.0862 \times 10^8}{T^3}\right)$
		Reverse	$3.0887 \times 10^{10} \times \exp\left(\frac{-5774.1}{T}\right) \times \exp\left(\frac{1.0862 \times 10^8}{T^3}\right)$
4,2-MHP	1,5	Forward	$1.6828 \times 10^{12} \times \exp\left(\frac{-10272}{T}\right) \times \exp\left(\frac{8.9426 \times 10^7}{T^3}\right)$
2,4-MHA	1,6-OOH	Forward	$5.9804 \times 10^{12} \times \exp\left(\frac{-2188.3}{T}\right) \times \exp\left(\frac{1.8363 \times 10^7}{T^3}\right)$
4,2-MHA	1,4	Forward	$4.6678 \times 10^{13} \times \exp\left(\frac{-8320.6}{T}\right) \times \exp\left(\frac{4.8739 \times 10^7}{T^3}\right)$
	1,6-OOH	Forward	$1.9747 \times 10^{12} \times \exp\left(\frac{-1648.7}{T}\right) \times \exp\left(\frac{2.2558 \times 10^7}{T^3}\right)$
4,2-MAP	1,5	Forward	$9.5219 \times 10^{11} \times \exp\left(\frac{-9543.6}{T}\right) \times \exp\left(\frac{8.8195 \times 10^7}{T^3}\right)$

Table S6. Temperature dependencies of the H-shift rate coefficients in the OH oxidation of 2-hydroperoxypentane. They are intended for use in the range 290-320 K.

Reactant	H-shift	Isomer	Direction	k (s^{-1})
2,3-HP	1,4	S,R	Forward	$7.6094 \times 10^{12} \times \exp\left(\frac{-14546}{T}\right) \times \exp\left(\frac{1.8308 \times 10^{8}}{T^{3}}\right)$
		S,S	Forward	$6.1015 \times 10^{12} \times \exp\left(\frac{-14303}{T}\right) \times \exp\left(\frac{1.8310 \times 10^{8}}{T^{3}}\right)$
	1,6-OOH	S,R	Forward	$5.9895 \times 10^{12} \times \exp\left(\frac{-10886}{T}\right) \times \exp\left(\frac{2.2697 \times 10^{8}}{T^{3}}\right)$
			Reverse	$9.3077 \times 10^{11} \times \exp\left(\frac{-10421}{T}\right) \times \exp\left(\frac{2.2697 \times 10^{8}}{T^{3}}\right)$
		S,S	Forward	$3.0704 \times 10^{12} \times \exp\left(\frac{-10075}{T}\right) \times \exp\left(\frac{2.0133 \times 10^{8}}{T^{3}}\right)$
			Reverse	$2.2937 \times 10^{12} \times \exp\left(\frac{-10080}{T}\right) \times \exp\left(\frac{2.0133 \times 10^{8}}{T^{3}}\right)$
3,2-HP	1,4	S,R	Forward	$1.1101 \times 10^{12} \times \exp\left(\frac{-14472}{T}\right) \times \exp\left(\frac{1.8180 \times 10^{8}}{T^{3}}\right)$
		S,S	Forward	$3.9137 \times 10^{12} \times \exp\left(\frac{-14399}{T}\right) \times \exp\left(\frac{1.8655 \times 10^{8}}{T^{3}}\right)$

Reactant	H-shift	Isomer	Direction	k (s^{-1})
	1,5	S,R	Forward	$5.9170 \times 10^{12} \times \exp\left(\frac{-11913}{T}\right) \times \exp\left(\frac{8.3448 \times 10^{7}}{T^{3}}\right)$
			Reverse	$3.0588 \times 10^{12} \times \exp\left(\frac{-5868.6}{T}\right) \times \exp\left(\frac{8.3448 \times 10^{7}}{T^{3}}\right)$
		S,S	Forward	$4.8330 \times 10^{12} \times \exp\left(\frac{-12180}{T}\right) \times \exp\left(\frac{8.7302 \times 10^{7}}{T^{3}}\right)$
			Reverse	$4.1323 \times 10^{11} \times \exp\left(\frac{-5707.4}{T}\right) \times \exp\left(\frac{8.7302 \times 10^{7}}{T^{3}}\right)$
2,4-HP	1,5	S,R	Forward	$1.8270 \times 10^{11} \times \exp\left(\frac{-9818.4}{T}\right) \times \exp\left(\frac{1.0411 \times 10^{8}}{T^{3}}\right)$
		S,S	Forward	$4.3365 \times 10^{11} \times \exp\left(\frac{-9701.6}{T}\right) \times \exp\left(\frac{9.5707 \times 10^{7}}{T^{3}}\right)$
	17-OOH	S,R	Forward	$1.3312 \times 10^{10} \times \exp\left(\frac{-5452.5}{T}\right) \times \exp\left(\frac{9.9596 \times 10^{7}}{T^{3}}\right)$
		S,S	Forward	$1.5651 \times 10^{10} \times \exp\left(\frac{-6117.1}{T}\right) \times \exp\left(\frac{1.0979 \times 10^{8}}{T^{3}}\right)$

Values used in the MC-TST equation at 298.15 K

Table S7. Values of the components of the MC-TST equation used to calculate the rate coefficients in the oxidation of 2-hydroperoxy-2-methylpentane at 298.15 K.

Reactant	Reaction	κ	Q_R	Q_{TS}	Q_P	E_f (kcal/mol)	E_r (kcal/mol)
2-MP	1,5 H-shift	4.63×10^1	6.83×10^8	$5.79E\times10^7$	2.6×10^9	23.1	10.2
	1,6 H-shift	6.60×10^1	6.83×10^8	$2.58E\times10^7$	-	25.2	-
2-MA	1,4 H-shift	1.52×10^2	1.73×10^8	$1.56E\times10^7$	-	15.7	-
	1,5 H-shift	2.34×10^1	1.73×10^8	$6.93E\times10^6$	-	8.95	-
2,5-MAP	1,5 H-shift	3.07×10^1	2.58×10^{10}	$3.58E\times10^8$	-	21.9	-
2,3-MHP	1,6-OOH H-shift	5.05×10^3	1.77×10^9	3.50×10^8	1.06×10^{10}	18.3	17.0
3,2-MHP	1,4 H-shift	4.67×10^2	1.07×10^{10}	1.53×10^9	-	29.1	-
	1,5 H-shift	5.62×10^1	1.07×10^{10}	3.49×10^9	$6.72E\times10^9$	23.6	12.5
2,4-MHP	1,7-OOH H-shift	1.75×10^2	2.44×10^9	1.82×10^8	1.34×10^{10}	13.0	12.7
4,2-MHP	1,5 H-shift	6.70×10^1	1.34×10^{10}	2.36×10^9	-	20.6	-
2,4-MHA	1,6-OOH H-shift	3.56	$2.77E\times10^8$	$1.52E\times10^8$	-	4.36	-
4,2-MHA	1,4 H-shift	8.30	$2.47E\times10^8$	$4.54E\times10^8$	-	15.9	-
	1,6-OOH H-shift	4.82	$2.94E\times10^8$	$7.22E\times10^7$	-	3.55	-
4,2-MAP	1,5 H-shift	5.40×10^1	$4.61E\times10^9$	$3.69E\times10^8$	-	19.0	-

Table S8. Values of the components of the MC-TST equation used to calculate the rate coefficients in the oxidation of 2-hydroperoxypentane at 298.15 K.

Reactant	H-shift	Isomer	κ	Q_R	Q_{TS}	Q_P	E_f kcal/mol	E_r kcal/mol
2,3-HP	1,4	S,R	1.52×10^3	7.48×10^8	5.08×10^8	-	28.8	-
		S,S	1.52×10^3	1.67×10^9	8.92×10^8	-	28.3	-
		S,R	2.85×10^4	7.20×10^8	3.88×10^8	2.56×10^9	22.3	21.7
	1,6-OOH	S,S	9.73×10^3	1.67×10^9	3.43×10^8	1.44×10^9	20.4	20.7
3,2-HP	1,4	S,R	6.97×10^2	2.56×10^9	1.34×10^9	-	29.2	-
		S,S	1.65×10^3	1.42×10^9	5.62×10^8	-	28.6	-
	1,5	S,R	6.18×10^1	2.33×10^9	1.76×10^9	4.02×10^9	24.1	12.2
		S,S	6.54×10^1	1.42×10^9	3.24×10^8	1.02×10^{10}	24.0	11.4
2,4-HP	1,5	S,R	8.13×10^1	1.24×10^{10}	5.99×10^8	-	20.1	-
		S,S	7.76×10^1	7.62×10^9	5.39×10^8	-	19.7	-
	1,7-OOH	S,R	1.23×10^2	1.24×10^{10}	5.55×10^7	-	11.9	-
		S,S	1.72×10^2	7.62×10^9	5.30×10^7	-	13.4	-

Values used for the Eckart Tunneling Correction

Table S9. Components used as input for the calculation of the Eckart tunneling correction in the rate coefficients of the oxidation of 2-hydroperoxy-2-methylpentane.

Reactant	H-Shift	E_f (kcal/mol)	E_r (kcal/mol)	Imag. Freq. v (cm⁻¹)
2-MP	1,5	21.8	8.22	1858
	1,6	23.9	8.40	1950
2-MA	1,4	15.7	24.4	1793
	1,5	8.62	14.4	1647
2,5-MAP	1,5	21.1	7.30	1803
2,3-MHP	1,6-OOH	18.3	17.0	2370
3,2-MHP	1,4	26.4	22.6	1818
	1,5	20.8	8.53	1890
2,4-MHP	1,7-OOH	12.2	12.7	2022
4,2-MHP	1,5	18.8	10.2	1834
2,4-MHA	1,6-OOH	1.80	24.3	1645
4,2-MHA	1,4	11.9	27.8	1297
	1,6-OOH	2.14	23.5	1792
4,2-MAP	1,5	17.8	11.0	1756

Table S10. Components used as input for the calculation of the Eckart tunneling correction in the rate coefficients of the oxidation of 2-hydroperoxypentane.

Reactant	H-Shift	Isomer	E_f (kcal/mol)	E_r (kcal/mol)	Imag. Freq. ν (cm^{-1})
2,3-HP	1,4 H-shift	S,R	26.6	19.0	2027
		S,S	26.6	19.0	2027
3,2-HP	1,6-OOH H-shift	S,R	22.3	20.8	2415
		S,S	20.4	18.7	2367
	1,4 H-shift	S,R	28.3	22.2	1858
		S,S	27.9	19.3	2023
	1,5 H-shift	S,R	20.7	9.1	1877
		S,S	20.8	9.8	1850
2,4-HP	1,5 H-shift	S,R	19.5	13.4	1761
		S,S	19.8	11.1	1824
4,2-HP	1,7-OOH H-shift	S,R	11.6	11.6	1985
		S,S	12.8	12.8	2000

Rate Constants at the ωB97X-D/aug-cc-pVTZ level of theory at 298.15 K

In addition to the rate constants presented in the main manuscript and above (which are calculated using ROHF-ROCCSD(T)-F12a/VDZ-F12//ωB97X-D/aug-cc-pVTZ), we here report the rate constants calculated using ωB97X-D/aug-cc-pVTZ.

Table S11. Rate constants in the oxidation of 2-hydroperoxy-2-methylpentane calculated at the ωB97X-D/aug-cc-pVTZ level of theory at 298.15 K.

Reactant	H-Shift	k_f (s^{-1})	k_r (s^{-1})
2-MP	1,5	7.5×10^{-5}	4.6×10^{6}
	1,6	7.0×10^{-7}	-
2-MA	1,4	4.9×10^{2}	-
	1,5	2.2×10^{6}	-
2,5-MAP	1,5	4.7×10^{-5}	-
2,3-MHP	1,6-OOH	4.0×10^{3}	4.9×10^{3}
3,2-MHP	1,4	2.8×10^{-7}	-
	1,5	8.8×10^{-5}	2.8×10^{6}
2,4-MHP	1,7-OOH	1.2×10^{6}	6.0×10^{5}
4,2-MHP	1,5	3.7×10^{-2}	-
2,4-MHA	1,6-OOH	7.8×10^{9}	-
4,2-MHA	1,4	6.3×10^{3}	
4,2-MHA	1,6-OOH	1.8×10^{10}	
4,2-MAP	1,5	1.3×10^{-1}	1.5×10^{5}

Table S12. Rate constants for reactions in the oxidation of 2-hydroperoxy-pentane calculated at the ωB97X-D/aug-cc-pVTZ level of theory at 298.15 K.

Reactant	H-shift	Isomer	k_T (s^{-1})	k_x (s^{-1})
2,3-HP	1,4	S,R	5.0×10^{-6}	-
		S,S	9.8×10^{-6}	-
	1,6-OOH	S,R	8.1×10^2	6.4×10^2
		S,S	3.5×10^3	2.8×10^3
3,2-HP	1,4	S,R	8.2×10^{-7}	-
		S,S	3.7×10^{-6}	-
	1,5	S,R	2.1×10^{-4}	7.1×10^6
		S,S	7.3×10^{-5}	1.5×10^{-6}
2,4-HP	1,5	S,R	3.8×10^{-2}	-
		S,S	4.6×10^{-2}	-
	1,7-OOH	S,R	8.7×10^4	8.7×10^{-4}
		S,S	7.1×10^{-4}	7.1×10^{-4}

References

1. Teng, A. P.; Crounse, J. D.; Wennberg, P. O., Isoprene Peroxy Radical Dynamics. *J. Am. Chem. Soc.* **2017,** *139* (15), 5367-5377.

2. Praske, E.; Otkjær, R. V.; Crounse, J. D.; Hethcox, J. C.; Stoltz, B. M.; Kjaergaard, H. G.; Wennberg, P. O., Atmospheric Autoxidation Is Increasingly Important in Urban and Suburban North America. *Proc. Natl. Acad. Sci. U.S.A.* **2018,** *115* (1), 64-69.

3. Crounse, J. D.; Paulot, F.; Kjaergaard, H. G.; Wennberg, P. O., Peroxy Radical Isomerization in the Oxidation of Isoprene. *Phys. Chem. Chem. Phys.* **2011,** *13* (30), 13607-13613.

4. Atkinson, R.; Baulch, D. L.; Cox, R. A.; Crowley, J. N.; Hampson, R. F.; Hynes, R. G.; Jenkin, M. E.; Rossi, M. J.; Troe, J., Evaluated Kinetic and Photochemical Data for Atmospheric Chemistry: Volume I - Gas Phase Reactions of O_x, Ho_x, No_x and So_x Species. *Atmos. Chem. Phys.* **2004,** *4*, 1461-1738.

5. Wennberg, P. O.; Bates, K. H.; Crounse, J. D.; Dodson, L. G.; McVay, R. C.; Mertens, L. A.; Nguyen, T. B.; Praske, E.; Schwantes, R. H.; Smarte, M. D., et al., Gas-Phase Reactions of Isoprene and Its Major Oxidation Products. *Chem. Rev.* **2018,** *118* (7), 3337-3390.

6. Teng, A. P.; Crounse, J. D.; Lee, L.; St. Clair, J. M.; Cohen, R. C.; Wennberg, P. O., Hydroxy Nitrate Production in the Oh-Initiated Oxidation of Alkenes. *Atmos. Chem. Phys.* **2015,** *15* (8), 4297-4316.

7. Atkinson, R.; Carter, W. P. L.; Winer, A. M., Effects of Temperature and Pressure on Alkyl Nitrate Yields in the No_x Photooxidations of Normal-Pentane and Normal-Heptane. *J. Phys. Chem.* **1983,** *87* (11), 2012-2018.

8. Garden, A. L.; Paulot, F.; Crounse, J. D.; Maxwell-Cameron, I. J.; Wennberg, P. O.; Kjaergaard, H. G., Calculation of Conformationally Weighted Dipole Moments Useful in Ion-Molecule Collision Rate Estimates. *Chem. Phys. Lett.* **2009,** *474* (1-3), 45-50.

9. Su, T.; Chesnavich, W. J., Parametrization of the Ion-Polar Molecule Collision Rate-Constant by Trajectory Calculations. *J. Chem. Phys.* **1982,** *76* (10), 5183-5185.

10. O'Haver, T. Interactive Peak Fitter. Available at Https://Terpconnect.Umd.Edu/~Toh/Spectrum/Interactivepeakfitter.Htm. Accessed January 8, 2017.

11. Saunders, S. M.; Jenkin, M. E.; Derwent, R. G.; Pilling, M. J., Protocol for the Development of the Master Chemical Mechanism, Mcm V3 (Part a): Tropospheric Degradation of Non-Aromatic Volatile Organic Compounds. *Atmos. Chem. Phys.* **2003,** *3*, 161-180.

12. Eyring, H., The Activated Complex and the Absolute Rate of Chemical Reactions. *Chemical Reviews* **1935,** *17* (1), 65-77.

13. Evans, M. G.; Polanyi, M., Some Applications of the Transition State Method to the Calculation of Reaction Velocities, Especially in Solution. *Transactions of the Faraday Society* **1935,** *31* (0), 875-894.

14. Vereecken, L.; Peeters, J., The 1,5-H-Shift in 1-Butoxy: A Case Study in the Rigorous Implementation of Transition State Theory for a Multirotamer System. *The Journal of Chemical Physics* **2003,** *119* (10), 5159-5170.

15. Møller, K. H.; Otkjær, R. V.; Hyttinen, N.; Kurtén, T.; Kjaergaard, H. G., Cost-Effective Implementation of Multiconformer Transition State Theory for Peroxy Radical Hydrogen Shift Reactions. *J. Phys. Chem. A* **2016,** *120* (51), 10072-10087.

16. Eckart, C., The Penetration of a Potential Barrier by Electrons. *Physical Review* **1930,** *35* (11), 1303-1309.

17. Kwok, E. S. C.; Atkinson, R., Estimation of Hydroxyl Radical Reaction Rate Constants for Gas-Phase Organic Compounds Using a Structure-Reactivity Relationship: An Update. *Atmos. Environ.* **1995,** *29* (14), 1685-1695.

18. Otkjær, R. V.; Jakobson, H. H.; Tram, C. M.; Kjaergaard, H. G., Calculated Hydrogen Shift Rate Constants in Substituted Alkyl Peroxy Radicals. *J. Phys. Chem. A* **2018**, submitted.

19. Jørgensen, S.; Knap, H. C.; Otkjær, R. V.; Jensen, A. M.; Kjeldsen, M. L. H.; Wennberg, P. O.; Kjaergaard, H. G., Rapid Hydrogen Shift Scrambling in Hydroperoxy-Substituted Organic Peroxy Radicals. *J. Phys. Chem. A* **2016,** *120* (2), 266-275.

20. Crounse, J. D.; Nielsen, L. B.; Jørgensen, S.; Kjaergaard, H. G.; Wennberg, P. O., Autoxidation of Organic Compounds in the Atmosphere. *J. Phys. Chem. Lett.* **2013,** *4* (20), 3513-3520.